WRDC-TR-89-4134
UDR-TR-89-81

RESEARCH ON ADVANCED NDE METHODS FOR
AEROSPACE STRUCTURES

AD-A226 858

Brian G. Frock
Robert J. Andrews
Richard W. Martin
Prasanna Karpur
Mark J. Ruddell
Jeffery A. Fox
Edward L. Klosterman
Mary L. Papp

University of Dayton Research Institute
Analytical and Experimental Systems Group
Structural Integrity Division

September 1989

Final Report for 1 September 1986 to 31 August 1989

DTIC
ELECTE
SEP 27 1990
E

NOTICE

WHEN GOVERNMENT DRAWINGS, SPECIFICATIONS, OR OTHER DATA ARE USED FOR ANY PURPOSE OTHER THAN IN CONNECTION WITH A DEFINITELY GOVERNMENT-RELATED PROCUREMENT, THE UNITED STATES GOVERNMENT INCURS NO RESPONSIBILITY OR ANY OBLIGATION WHATSOEVER. THE FACT THAT THE GOVERNMENT MAY HAVE FORMULATED OR IN ANY WAY SUPPLIED THE SAID DRAWINGS, SPECIFICATIONS, OR OTHER DATA, IS NOT TO BE REGARDED BY IMPLICATION, OR OTHERWISE IN ANY MANNER CONSTRUED, AS LICENSING THE HOLDER, OR ANY OTHER PERSON OR CORPORATION; OR AS CONVEYING ANY RIGHTS OR PERMISSION TO MANUFACTURE, USE, OR SELL ANY PATENTED INVENTION THAT MAY IN ANY WAY BE RELATED THERETO.

THIS REPORT HAS BEEN REVIEWED BY THE OFFICE OF PUBLIC AFFAIRS (ASD/CPA) AND IS RELEASABLE TO THE NATIONAL TECHNICAL INFORMATION SERVICE (NTIS), AT NTIS, IT WILL BE AVAILABLE TO THE GENERAL PUBLIC, INCLUDING FOREIGN NATIONS.

THIS TECHNICAL REPORT HAS BEEN REVIEWED AND IS APPROVED FOR PUBLICATION.

THOMAS J. MORAN, Project Engineer
Nondestructive Evaluation Branch
Metals and Ceramics Division
Materials Laboratory

D. M. FORNEY, JR., Chief
Nondestructive Evaluation Branch
Metals and Ceramics Division
Materials Laboratory

FOR THE COMMANDER
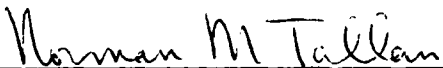
DR NORMAN M. TALLAN, Director
Metals and Ceramics Division
Materials Laboratory

IF YOUR ADDRESS HAS CHANGED, IF YOU WISH TO BE REMOVED FROM OUR MAILING LIST, OR IF THE ADDRESSEE IS NO LONGER EMPLOYED BY YOUR ORGANIZATION PLEASE NOTIFY WRDC/MLLP, WRIGHT-PATTERSON AFB, OH 45433-6533 TO HELP US MAINTAIN A CURRENT MAILING LIST.

COPIES OF THIS REPORT SHOULD NOT BE RETURNED UNLESS RETURN IS REQUIRED BY SECURITY CONSIDERATIONS, CONTRACTUAL OBLIGATIONS, OR NOTICE ON A SPECIFIC DOCUMENT.

REPORT DOCUMENTATION PAGE

Form Approved
OMB No. 0704-0188

1a. REPORT SECURITY CLASSIFICATION	1b. RESTRICTIVE MARKINGS
Unclassified	

2a. SECURITY CLASSIFICATION AUTHORITY	3. DISTRIBUTION/AVAILABILITY OF REPORT
2b. DECLASSIFICATION/DOWNGRADING SCHEDULE	Approved for public release; distribution unlimited

4. PERFORMING ORGANIZATION REPORT NUMBER(S)	5. MONITORING ORGANIZATION REPORT NUMBER(S)
UDR-TR-89-81	WRDC-TR-89-4134

6a. NAME OF PERFORMING ORGANIZATION	6b. OFFICE SYMBOL (If applicable)	7a. NAME OF MONITORING ORGANIZATION
University of Dayton Research Institute		Wright Research and Development Center Materials Laboratory (WRDC/MLLP)

6c. ADDRESS (City, State, and ZIP Code)	7b. ADDRESS (City, State, and ZIP Code)
300 College Park Dayton, Ohio 45469-0001	AFSC Wright-Patterson AFB, Ohio 45433-6533

8a. NAME OF FUNDING/SPONSORING ORGANIZATION	8b. OFFICE SYMBOL (If applicable)	9. PROCUREMENT INSTRUMENT IDENTIFICATION NUMBER
		F33615-86-C-5016

8c. ADDRESS (City, State, and ZIP Code)	10. SOURCE OF FUNDING NUMBERS			
	PROGRAM ELEMENT NO.	PROJECT NO.	TASK NO	WORK UNIT ACCESSION NO.
	62102F	2418	02	32

11. TITLE (Include Security Classification)

Research on Advanced NDE Methods for Aerospace Structures

12. PERSONAL AUTHOR(S)   B.G. Frock, R.J. Andrews, R.W. Martin, P. Karpur, M.J. Ruddell, J.A. Fox, E.L. Klosterman and M.L. Papp

13a. TYPE OF REPORT	13b. TIME COVERED	14. DATE OF REPORT (Year, Month, Day)	15. PAGE COUNT
Final	FROM 9/1/86 TO 8/31/89	September 1989	188

16. SUPPLEMENTARY NOTATION

17. COSATI CODES			18. SUBJECT TERMS (Continue on reverse if necessary and identify by block number)
FIELD	GROUP	SUB-GROUP	NDE, Ultrasonic, Composites, Digital Image Enhancement, Digital Image Restoration

19. ABSTRACT (Continue on reverse if necessary and identify by block number)

This Final Report describes investigations of the capabilities and limitations of several digital ultrasonic NDE techniques for imaging defects in advanced aerospace materials. The goal of these investigations was to determine the feasibility and practicality of transitioning these techniques from the laboratory to field use. Studies of new digital data collection techniques, signal processing, image enhancement and image restoration techniques revealed that their use can significantly improve the resolution of features in ultrasonic images. The use of narrow software gates to collect data from digitized rf A-scans improved the resolution in C-scan images of closely-spaced planes in advanced composite materials. That technique was used to simultaneously generate C-scan images of: (1) material defects in the "dead zones" of the interrogating ultrasonic transducers and (2) material defects throughout the entire thickness of several 32-ply thick, graphite-epoxy composite materials. The depth resolution of ultrasonic B-scan
(continued)

20. DISTRIBUTION/AVAILABILITY OF ABSTRACT	21. ABSTRACT SECURITY CLASSIFICATION
☒ UNCLASSIFIED/UNLIMITED ☐ SAME AS RPT. ☐ DTIC USERS	Unclassified

22a. NAME OF RESPONSIBLE INDIVIDUAL	22b. TELEPHONE (Include Area Code)	22c. OFFICE SYMBOL
Thomas J. Moran	(513) 255-9806	WRDC/MLLP

DD Form 1473, JUN 86   Previous editions are obsolete.   SECURITY CLASSIFICATION OF THIS PAGE

19. Abstract (continued)

images was improved by generating the images from axially deconvolved A-scans and from axially power-spectrum-equalized A-scans rather than from the rf A-scans. Lateral resolution in C-scan images was significantly improved by collecting data for the images from Wiener-deconvolved A-scans and from power-spectrum-equalized A-scans rather than from the rf A-scans. Lateral resolution in C-scan images was further improved by deconvolving the original digitized C-scan data with a two-dimensional Wiener filter and by applying two-dimensional power-spectrum-equalization techniques to the original digitized C-scan data. Leaky Lamb wave ultrasonic methods were used to image simulated defects in bidirectional graphite-epoxy composite materials. The availability of high-speed digitizers on some commercial ultrasonic systems makes it possible to transition some of these digital techniques to field use. Specifically, the use of software gates to collect C-scan image data directly from rf A-scans is recommended for transition. The University of Dayton Research Institute can transition that and other techniques described in this Final Report through its current contract with the WRDC Materials Laboratory.

FOREWORD

This final technical report describes the work accomplished during the period from 1 September 1986 through 31 August 1989 by the University of Dayton Research Institute (UDRI) under Contract Number F33615-86-C-5016 for the WRDC Materials Laboratory. Dr. Thomas J. Moran of the Nondestructive Evaluation Branch, Metals and Ceramics Division was the Contract Monitor.

The efforts reported here were performed by several UDRI employees. Mr. Robert J. Andrews of the UDRI Structural Integrity Division was Principal Investigator for the first year of the contract. Mr. Brian G. Frock of the UDRI Structural Integrity Division was Principal Investigator for the remainder of the contractual period. Dr. Joseph P. Gallagher was Program Manager for the entire period of the contract. The following University employees contributed to the work: Richard W. Martin, Edward Klosterman, Mark J. Ruddell, Prasanna Karpur, Jeffery A. Fox, Mary Papp, Carl Orr, Joyce A. Smith and Dr. J. P. Martino. Mr. David M. Greason and Mark C. Chantell worked as undergraduate student assistants. Mr. Kenneth D. Shimmin and Dr. P. K. Bhagat served as consultants during a portion of the contractual effort. Ms. Joanda D'Antuono, Mrs. Tanya Graham and Mrs. LaVonna Stathes were responsible for typing and assembling the monthly progress reports. Ms. Joanda D'Antuono was responsible for typing and assembling this final report.

TABLE OF CONTENTS

LIST OF ILLUSTRATIONS

LIST OF ILLUSTRATIONS (concluded)

SECTION 1

INTRODUCTION

The studies described in this report were conducted to determine the capabilities and limitations of new ultrasonic techniques for imaging defects in advanced aerospace materials. These studies were made possible by the advent of high-speed digitizers (sampling rates up to 200 MHz) which provided the opportunity to develop new data acquisition capabilities and to obtain significant improvements in existing techniques. Two distinct methods of ultrasonic imaging were investigated: (1) backscatter and (2) leaky Lamb waves. The backscatter imaging studies investigated the capabilities of data collection, signal processing, image enhancement and image restoration techniques for improving defect detection and imaging. Several of the techniques were improved as a result of the studies. Leaky Lamb wave studies were directed toward extending the capabilities of newly developed Lamb wave NDE methods from unidirectional to multi-directional graphite-epoxy composite materials.

One of the classic problems facing inspectors is the necessity to inspect for both near-entry-surface defects and for defects which lie deep within materials. The long "ring" times of ultrasonic transducers require the use of high frequencies for near-entry-surface inspections. However, rough surfaces can severely restrict the maximum usable frequency, especially when focused transducers are required for lateral resolution. High frequencies are also often useless for inspection of thick advanced materials such as composites because of the severe scattering and attenuation losses which occur at the higher frequencies. These severe attenuation and scattering losses force the use of lower frequencies when inspecting many thick materials, with a consequent loss of depth resolution both at the surface and throughout the material. The conflicting requirements of higher frequencies for near-entry-surface inspections and lower frequencies for inspection of thick samples has been circumvented in the past by multiple inspections. One inspection would be performed for near-entry-surface defects using higher frequencies and a second inspection would be conducted for deep defects using lower frequencies. This is a time consuming procedure which is, therefore, undesirable.

Five techniqu- , with potential for improving depth resolution both near the entry surface and deep within thick materials were investigated during the course of this contract. They are: (1) software gating of digitized rf A-scans. (2) entry-surface-echo subtraction, (3) axial Wiener deconvolution, (4) power spectrum equalization and (5) swept-frequency tone-burst generation of ultrasonic waves. Software gating was a new technique for collecting C-scan image data by applying narrow software gates directly to digitized rf A-scans. The technique is general enough to be used to interrogate most engineering materials. During the contractual period covered by this report it was used to image damage in: (1) quasi-isotropic graphite-epoxy composites with planar interfaces and (2) woven composites with nonplanar interfaces. Entry-surface-echo subtraction was used to enhance B-scan images of near-entry-surface defects. The method is applied by subtracting a digitized version of the rf entry-surface echo from all digitized rf A-scans in a B-scan image. Axial or 1-D Wiener deconvolution essentially shortens the received rf pulse echoes, thereby improving the depth resolution in B-scan images and reducing the depth ambiguity in C-scan images. Power spectrum equalization (PSE) also improves depth resolution by shortening the rf pulse echoes. The swept-frequency tone-hurts techniques were investigated because of their capabilities for generating more energy at higher frequencies.

The finite width of ultrasonic beams (even for focused transducers) causes lateral blurring in ultrasonic C-scan images. This is especially true at the lower frequencies required for inspection of thick graphite-epoxy and other composite materials. Quantitative ultrasonic imaging requires removal of at least some of the lateral blur. One edge enhancement and two pseudo restoration techniques were investigated for their blur removal capabilities. The edge enhancement technique is known as Marr-Hildreth enhancement and was tested on C-scan images of the entry surfaces of materials as well as on C-scan images of subsurface planes. The two pseudo restoration techniques are known as two-dimensional Wiener deconvolution and two-dimensional power spectrum equalization. Both restoration techniques were tested on C-scan images of entry surfaces as well as on C-scan images of subsurface planes in graphite-epoxy composites.

1-2

One problem which is commonly encountered by inspectors is that of distinguishing defects from normal background noise in NDE images. Experienced inspectors are often able to distinguish between noise and defects in an image whereas inexperienced inspectors are not. One possible solution to this problem which was investigated during this contract was the use of expert system techniques. The expert system approach was tested on an angle backscatter B-scan image of a graphite-epoxy composite with matrix cracks.

Leaky Lamb wave techniques are capable of imaging defects such as delaminations, ply cuts and porosity in unidirectional graphite-epoxy composites. Ply cuts and porosity are especially difficult to image with other NDE methods. The capabilities of Lamb wave techniques for imaging defects in bidirectional graphite-epoxy composites were investigated during this contract. This represents the first steps toward extending Lamb wave methods to more complex layups.

SECTION 2

SUMMARY

The studies described in this report have demonstrated the usefulness of signal generation, data collection, digital signal processing, digital image enhancement, digital image restoration and expert systems techniques for improving the ultrasonic nondestructive evaluation of advanced composite materials. Application of the techniques have significantly improved the depth resolution in B-scan images and the lateral resolution in C-scan images of graphite-epoxy composites with internal defects. The following paragraphs summarize the capabilities of the techniques discussed in Section 3.

Normal-Incidence Backscatter C-Scan Imaging Using Software-Gated Pulse-Echo rf A-Scans (Page 3-1)

Application of narrow (40 nS) software gates to digitized rf pulse-echoes allowed resolution of closely spaced between-ply delaminations (0.13 mm [0.005 in]) in graphite-epoxy composites with planar interfaces. The high resolution was achieved for near-entry-surface planes and for planes which were deep within the material. Destructive evaluations of impact damage at each interface showed excellent agreement with the ultrasonic images of damage at those interfaces.

The software-gating technique was used to image damage in woven composites which did not have planar interfaces. A large number of adjacent narrow gates provided excellent depth resolution, but required time consuming interpretation. Wide overlapping gates provided acceptable depth resolution and simplified data interpretation.

Generation of C-scan images using the software-gated pulse-echo rf A-scan technique required a high-speed digitizer and a computer for data collection. A high-resolution monitor was required for setting the gates and for displaying the digitized images.

This technique is able to provide high-resolution C-scan images. The scan-time, data-processing and data-storage requirements of this technique are lower than those of any of the other techniques investigated by UDRI during this contractual period. While not the answer for all applications, it should

have broad application potential and is recommended for transition to field use.

Normal-Incidence Backscatter C-Scan Imaging Using Swept-Frequency Tone-Burst Techniques (Page 3-10)

This technique generated more ultrasonic energy over the useful bandwidth of the transducer than the traditional spike-excitation method. The increased energy resulted in higher signal-to-noise ratios during ultrasonic nondestructive evaluation.

Studies described in Section 2 have shown that the technique can be used to image impact damage in quasi-isotropic graphite-epoxy composites. Median-frequency processing of the data acquired at each sampling point allowed defect depth to be encoded in the gray scale of the C-scan images. Low-speed digitizers were used to acquire the envelope-detected data during scanning. The primary disadvantage of the technique was the long time required to: (1) sweep through the entire frequency range and (2) process the data at each sampling point.

B-Scan Image Enhancement Using Entry-Surface-Echo Subtraction (Page 3-20)

This technique significantly improved the visual detection of near-entry-surface echoes that were in the "dead" zone of the transducer. Use of the technique required that the B-scan image consist entirely of digitized rf A-scans stored in a computer. A reference rf entry-surface echo had to be digitized and stored in the computer prior to execution of the subtraction algorithm.

B-Scan Image Restoration Using 1-D Axial Wiener Deconvolution (Page 3-21)

Application of this technique to digitized rf B-scans significantly improved the depth resolution in the B-scan images. The technique improved the depth resolution near the entry surface and within the sample. Implementation of the technique required the use of a high-speed digitizer to digitize the rf A-scans. A reference digitized rf A-scan was required for application of the Wiener deconvolution. One-dimensional Fast Fourier Transform (FFT) software was required for the deconvolutions.

B-Scan Image Restoration Using 1-D Power Spectrum Equalization (Page 3-25)

Applying this technique to digitized rf B-scans improved the depth resolution in the B-scan images. The improvement in depth resolution was not as great as the improvement achieved with the use of axial Wiener deconvolutions. The technique did not, however, require the use of a digitized reference rf A-scan. A high-speed digitizer was required to digitize the rf A-scans for the B-scan images. One-dimensional FFT software was necessary for power spectrum equalization.

C-Scan Image Enhancement Using Marr-Hildreth Operator (Page 3-27)

Use of this two-dimensional, nondirectional edge-enhancement operator improved the visual detection and resolution of features in digitized C-scan images by reducing lateral blur. This operator was used to enhance noisy images as well as near-noise-free images. The moving-window, spatial-domain version executed rapidly and did not require complex computer algorithms such as two-dimensional Fourier transforms. Artifacts can be generated during use of this operator, so some caution is necessary during interpretation of the enhanced images.

C-Scan Image Restoration Using 2-D Lateral Wiener Deconvolution (Page 3-34)

This method improved the visual detection and identification of digitized C-scan image features by reducing the blur caused by the finite beam-width of the ultrasonic transducer. The studies described in Section 2 demonstrated the usefulness of this technique for improving the visual quality of surface and subsurface images of graphite-epoxy composite samples. Use of the technique caused only minimal generation of artifacts. This technique required the use of a digitized reference C-scan image of the ultrasonic transducer's beam-shape. Two-dimensional FFT algorithms were required for implementation of the technique.

C-Scan Image Restoration Using 2-D Power Spectrum Equalization (Page 3-36)

Power spectrum equalization "restored" the C-scan images by using information contained within the digitized images. Image quality was improved through reduction of blur, but the improvement was not as great as the improvement achieved through use of the 3-D Wiener deconvolution method. However, a digitized reference C-scan image of the ultrasonic transducer's

beam shape was not required. Two-dimensional Fourier transforms were required for implementation of the technique. Artifact generation was usually minimal.

Marr-Hildreth Enhancement Versus 2-D Restoration Techniques (Page 3-36)

Marr-Hildreth enhancement reduces blur in images, even in the presence of limited amounts of noise. The technique is easy to implement in the spatial domain, does not require complex software and operates rapidly. Marr-Hildreth enhancement can, however, generate artifacts in an image because it enhances by applying a numeric second derivative.

Restoration techniques also reduce image blur, even in the presence of limited amounts of noise. The techniques require complex software, operate relatively slowly and are usually more difficult to implement. Artifact generation, however, is usually minimal.

C-Scan Image Restoration Using Pseudo 3-D Wiener Deconvolution (Page 3-38)

This method of image "restoration" generated C-scan images by: (1) axial Wiener deconvolution of all digitized rf A-scans in a series of B-scan data files which were stored in computer memory, (2) application of narrow software gates to the axially deconvolved A-scans to generate C-scan data files at specific depths and (3) application of two-dimensional lateral Wiener deconvolutions to the C-scan data files generated from the deconvolved A-scans. The serial application of these three techniques significantly improved the lateral resolution in C-scan images and also improved the ability to image very closely spaced interfaces within test samples. It was also noted that the lateral resolution in the C-scan images generated from the axially-deconvolved rf A-scans was better than that achieved by applying software gates directly to the unprocessed rf A-scans.

All rf A-scans and all axially deconvolved A-scans had to be digitized and stored in a computer. One-dimensional and two-dimensional Fourier transforms were required for application of the pseudo 3-D Wiener deconvolution technique. A digitized reference rf A-scan was required for step 1 (one-dimensional axial deconvolution). A digitized reference C-scan image of the ultrasonic transducer's beam-shape was also required for step 3 (two-dimensional lateral deconvolution).

C-Scan Image Restoration Using Pseudo 3-D Power Spectrum Equalization
(Page 3-43)

Pseudo three-dimensional power spectrum equalization was used to "restore" C-scan images by: (1) one-dimensional power spectrum equalization of all digitized rf A-scans in a series of B-scan files which were stored in computer memory, (2) application of software gates to the power spectrum equalized A-scans to generate C-scan data files and (3) application of two-dimensional power spectrum equalization techniques to the C-scan data files generated from the power spectrum equalized A-scans. The serial application of these three techniques significantly improved the lateral resolution in the resulting C-scan images. It was also demonstrated that the lateral resolution in the C-scan images generated from the power spectrum equalized A-scans was better than the lateral resolution in the C-scan images generated from the rf A-scans. The lateral resolution improvement using pseudo 3-D power spectrum equalization appeared to be comparable to that achieved with pseudo 3-D Wiener deconvolution.

All rf A-scans and all power spectrum equalized A-scans had to be digitized and stored in a computer. One-dimensional and two-dimensional Fourier transforms were required for the power spectrum equalizations. Application of the technique did not require use of a digitized reference rf A-scan or a digitized C-scan image of the ultrasonic transducer's beam-shape.

Comparison of Pseudo 3-D Wiener Restoration and Pseudo 3-D Power Spectrum Equalization (Page 3-45)

The pseudo three-dimensional Wiener restoration technique and the pseudo three-dimensional power spectrum equalization technique appear to provide comparable improvements in subsurface images, at least for the images generated during this contractual period. This is quite different from the results achieved by two-dimensional (lateral) restorations of surface images. In the case of surface images, two-dimensional Wiener restorations were clearly superior to two-dimensional power spectrum equalizations. The reasons for this apparent contradiction are not known at the present time.

Expert System for Angle-Beam Backscatter B-Scan Image Analysis (Page 3-45)

A rule-based feature-classification expert system was developed and applied to the B-scan image of a 16-ply-thick bidirectional graphite-epoxy

composite sample with matrix cracks. The expert system successfully iden-
tified and classified all entry surface and back surface matrix cracks which
had been previously found in the sample. Random noise was eliminated from the
image and two surface irregularities were labeled as unknown features.

Computer Model of Ultrasonic Transducers (Page 3-49)

A computer model was developed which generated B-scan images for pic-
torial illustrations of ultrasonic transducer focusing characteristics. The
model was used to illustrate the effects of frequency content, pulse length,
element diameter and focal length on beam diameter, focal spot size and acous-
tic pulse shape. The program accommodated normal-incidence propagation of the
acoustic pulse across an interface between two materials of differing acoustic
velocity.

A digitized rf A-scan was required as an input to the model.

Leaky Lamb Wave Inspection of Biaxial Composites (Page 3-52)

The study described in this report demonstrated that leaky Lamb wave
techniques could be used to generate C-scan images of simulated defects in
bidirectional graphite-epoxy composites. Simulated delaminations, porosity
and ply cuts were imaged in the bidirectional composite. The median-frequency
signal processing technique was used to encode defect-depth information into
the gray scales of the C-scan images.

SECTION 3

ULTRASONIC NDE TECHNIQUE DEVELOPMENT

Developemental efforts during this contractual period covered a broad
range of ultrasonic NDE techniques. The intent was to improve ultrasonic im-
aging of defects in advanced aerospace materials. Techniques explored
included digital data collection, digital signal processing, digital image en-
hancement and restoration, image analysis using an expert approach, signal
generation and leaky Lamb wave imaging. Section 3 was written to provide an
overview of the applications and capabilities of the techniques investigated.
More fundamental and detailed information can be found in the publications in-
cluded in Appendix A. Further information can be obtained from the
references.

3.1 NORMAL-INCIDENCE BACKSCATTER C-SCAN IMAGING USING SOFTWARE-GATED PULSE-ECHO RF A-SCANS

Ultrasonic C-scan images have traditionally been generated from video-
detected A-scans. The technique is implemented by full-wave rectifying and
low-pass filtering the rf A-scans (pulse echoes) which return from the sample
being inspected. An amplitude threshold is established for entry-surface
tracking and "gates" are set to extract information from temporal locations
along the A-scan. These temporal locations correspond with planes at specific
depths within the sample. The process of thresholding (echo detection) and
gate setting is illustrated in Figure 3-1. The sketches in Figure 3-1 show
video-detected echoes (A-scans) from the entry surface of a multi-ply
graphite-epoxy composite as they appear during an immersion inspection.
Superimposed on the A-scans are the echo-detection threshold and two gates for
extracting information from the interface between the second and third plies
and the interface between the third and fourth plies below the entry surface.

The use of video-detected A-scans is adequate if the planes of interest
are widely spaced and are far enough below the sample's entry surface that the
transducer is no longer "ringing" from the entry-surface echo. However, as
can be seen from the illustrations in Figure 3-1, the technique is inadequate
when the planes of interest lie near the entry surface or when the planes are
close together. The echo from the entry surface, even in a defect-free region
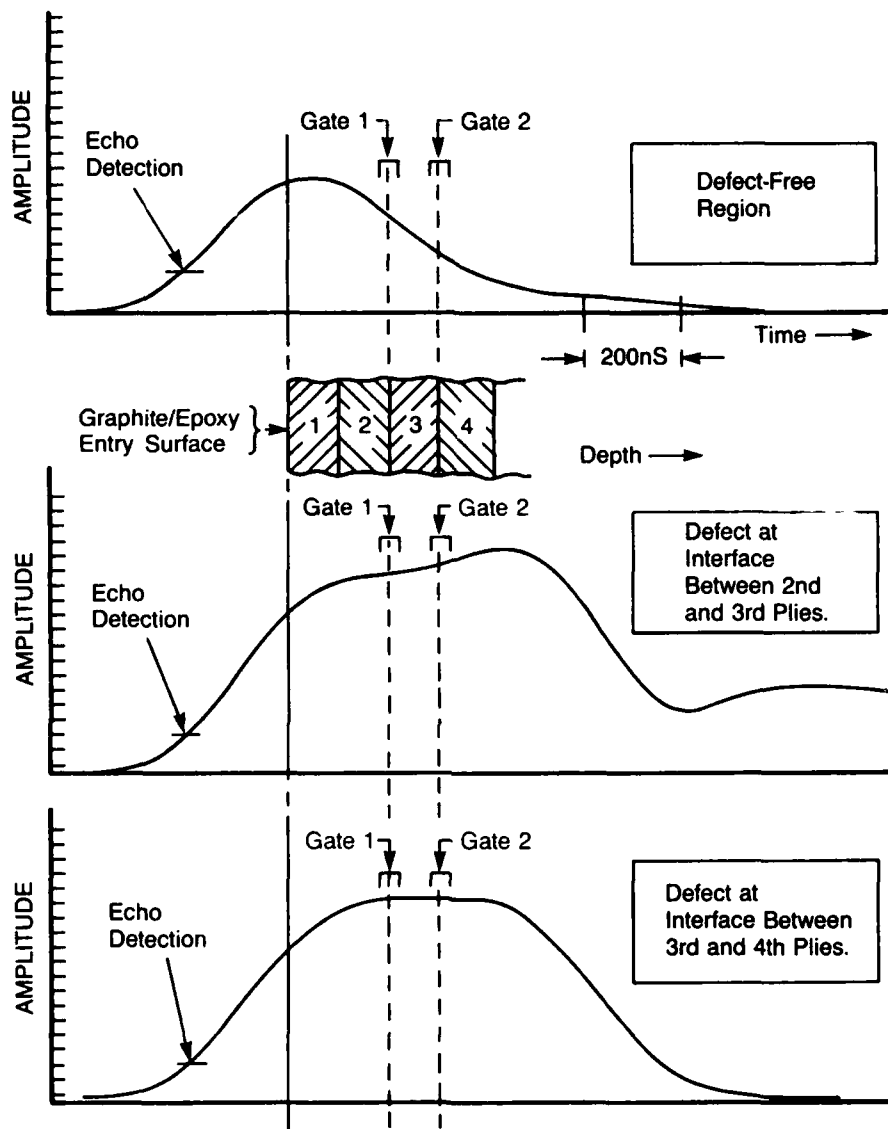
Figure 3-1.   Video-detected A-scans.

(upper plot), "rings" for a long enough time to obscure information from the first two or three ply interfaces. This "ring" time is the so called "dead zone" of an ultrasonic transducer. The lower two plots in Figure 3-1 show video-detected A-scans over regions where there are delaminations at the interface between the second and third plies and at the interface between the third and fourth plies, respectively. The presence of delaminations at either of those two interfaces increases the amplitude of the echo in the region of both gates. Unfortunately, in the case of gate one, the increase in amplitude may be no greater than that which is caused by variations in surface finish. Also, delaminations at either interface cause nearly identical increases in amplitudes in both gates. This makes it virtually impossible to determine whether delaminations are at the interface between the second and third plies or the interface between the third and fourth plies.

Many of the problems discussed in the previous paragraph can be overcome by application of a novel software-gating technique developed at the WRDC Materials Laboratory and implemented by the University of Dayton Research Institute (UDRI)[1,2]. The technique consists of generating C-scan images from data acquired directly from digitized radio frequency (rf) A-scans rather than from the conventional video-detected A-scans. The video detection process (full-wave rectification and low-pass filtering) destroys both the phase and high frequency information that are necessary for interrogating near-entry-surface planes and for interrogating planes that are very close together. Data acquired from the rf A-scans have both the phase and the high frequency information necessary for inspecting near-entry-surface interfaces and closely spaced interfaces.

3.1.1 Composites with Planar Interfaces

The software-gated rf A-scan technique is implemented by first digitizing the (rf) A-scans which are reflected from the material being scanned. As in the case of the video-detected A-scans, a voltage threshold is established for entry-surface tracking (see Figure 3-2) to allow for variations in surface location. Then, a reference is set at the maximum absolute amplitude of the entry-surface echo. Finally, for materials with planar interfaces, narrow software gates are offset from the reference to collect information from planes of interest within the sample. The amount of offset

between the reference and each gate is the round-trip travel time between the entry surface and the plane being inspected by the gate (Figure 3-2). Examples of the type of information which can be collected from any gate are: maximum amplitude (sign included), minimum amplitude (sign included), peak-to-peak amplitude, average amplitude and time-of-flight (for very wide gates). The gates can be made as narrow as desired (within the restrictions of the digitizer -- 5 nS for a 200 MHz digitizer), thus allowing very thin sections of the sample to be inspected. Only the user-specified values from the gates are stored at each discrete scan point. The remainder of the digitized rf waveform is not stored, thus saving memory space.

Some advantages of this technique for imaging planes very near the entry surface of a sample (in the transducer's "dead zone") are illustrated in Figure 3-2. The rf A-scan shown at the top is the entry-surface echo from a defect-free region of a graphite-epoxy composite. Superimposed on the A-scan are the echo detection threshold, gate reference and two gates for inspecting the interfaces between the second and third plies and between the third and fourth plies. Obviously, the "ringing" from the entry-surface echo extends through the interfaces of interest. The values in both gates are near zero. The center rf A-scan shows the echo as it appears when there is a delamination at the interface between the second and third plies. Prior knowledge of the velocity of ultrasound in the material and the depth of the interfaces of interest is used to position the gates at points on the rf A-scans where echoes returning from those interfaces will produce maximum deviations from the "ambient" rf A-scans. The echo from that delamination returns in time to interfere with the echo from the entry surface. The echo from the delamination (the echo is phase reversed) adds to the entry-surface echo to produce the rf A-scan shown in Figure 3-2. The value in gate one is now high in magnitude and positive in sign. The value in gate two is also high in magnitude, but is negative in sign. The bottom rf A-scan in Figure 3-2 shows the echo as it appears when there is a delamination at the interface between the third and fourth plies. Once again the phase-reversed echo has returned in time to interfere with the entry-surface echo. The resultant value in gate one is fairly high in magnitude, but negative in sign while the value in gate two is high in magnitude and positive in sign. Thus, it is possible to determine whether or not an interface near the entry surface is
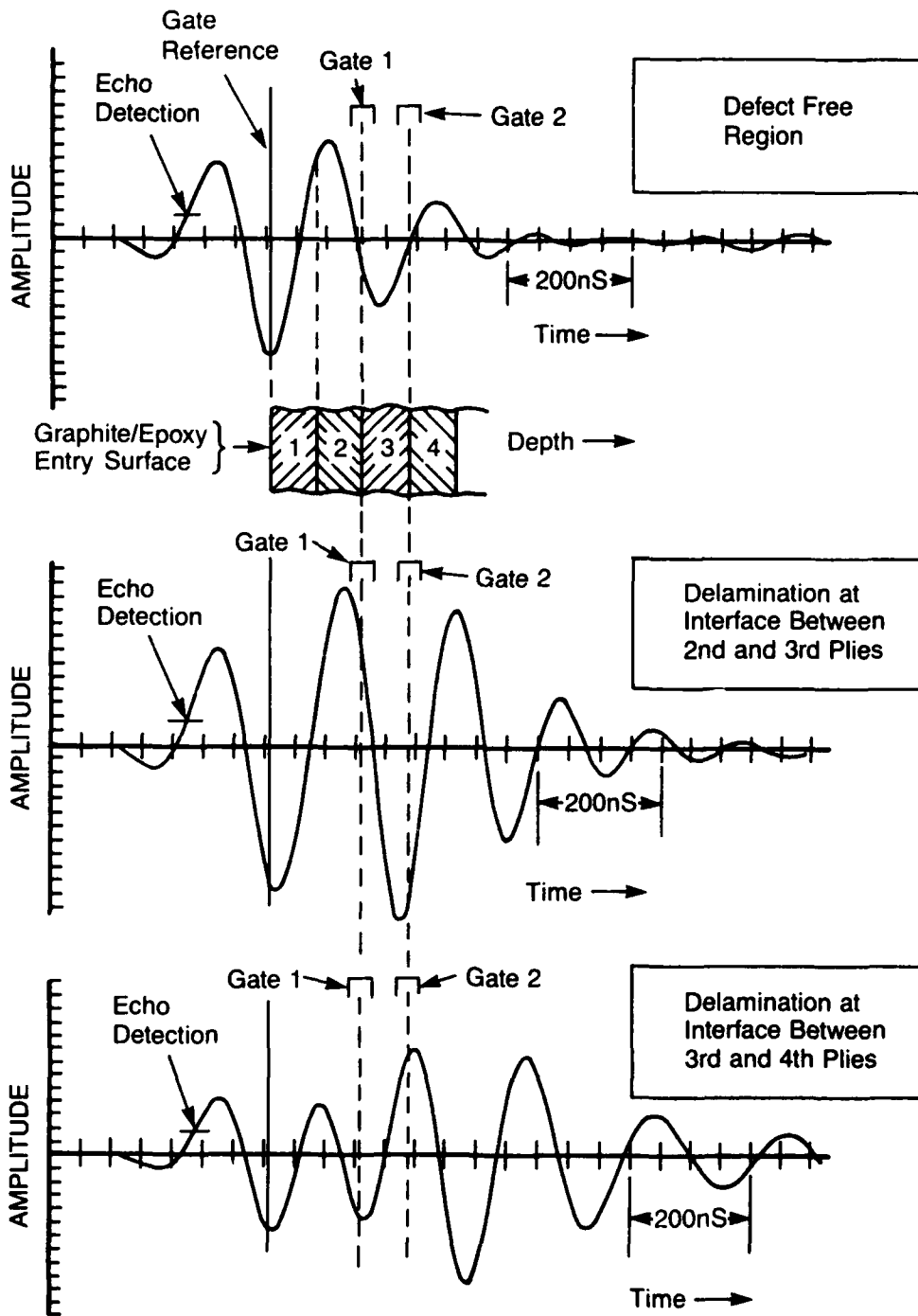
Figure 3-2.   Rf A-scans.

delaminated and, if a delamination is present, it is possible to determine which interface is delaminated.

An example of the type of improvement which can be achieved by use of the software-gating technique is illustrated in the C-scan images of Figure 3-3. Those images are ultrasonic C-scan images of an impact-damaged graphite-epoxy composite sample. Figures 3-3a and 3-3b were generated from data acquired from video-detected A-scans, whereas Figures 3-3c and 3-3d were generated from data acquired from software-gated rf A-scans. Damaged regions in these C-scan images appear as deviations from the general background. In the particular case shown here, the damaged regions are darker than the general background. The gates for Figures 3-3a and 3-3c were set to inspect the interface between the second and third plies and the gates for Figures 3-3b and 3-3d were set to inspect the interface between the third and fourth plies. As was discussed in the preceding paragraphs, gate one (and to a certain extent even gate two) is in the "dead zone" of the ultrasonic transducer used to acquire the data. Damage at each of the inspected interfaces is much more clearly defined in the images generated from the rf A-scans than in the images generated from the video-detected A-scans. Thus, very near-entry-surface defects can be clearly imaged by acquiring information from the rf A-scans.

Published studies have demonstrated the usefulness of the technique for imaging defects at depths well below the entry surface[1,2]. These studies have shown that the technique can resolve closely spaced delaminations (0.13 mm [0.005 in] separation) in quasi-isotropic graphite-epoxy composite panels. Destructive evaluation of impact-damage sites have shown excellent agreement with the ultrasonic images of damage at each interface (please see the publication entitled "Delamination and Crack Imaging in Graphite-Epoxy Composites" in Appendix A of this report). Further technical information on the uses of software gating is available in the article titled "Signal Processing Techniques for Imaging Impact Damage in Composites". That article is also included in Appendix A of this report.
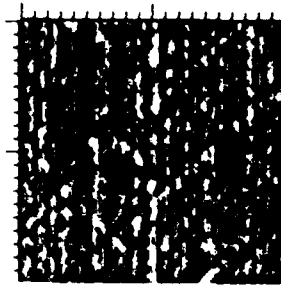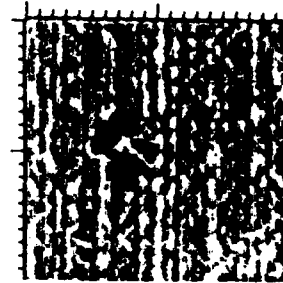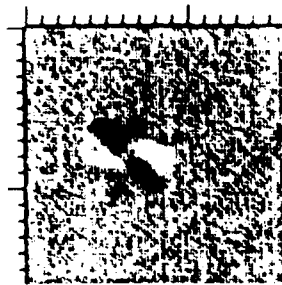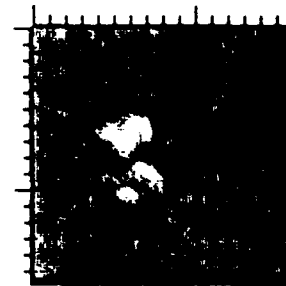
Figure 3-3. C-scan images: (a) Second interface using video-detected A-scans; (b) Third interface using video-detected A-scans; (c) Second interface using rf A-scans; (d) Third interface using rf A-scans.

3.1.2 Composites with Nonplanar Interfaces

The software gating technique proved highly successful for imaging damage in graphite-epoxy composites with nearly planar interfaces. Many useful materials, however, do not have planar interfaces. In woven composites, for instance, the weave pattern produces localized thickness changes which cause the interfaces between plies to vary in depth below the entry surface. That variation in depth makes it extremely difficult to properly set the gates for inspection of individual interfaces. If very narrow gates are used, echoes from specific ply interfaces will drift in and out of the gates, making it impossible to continuously image the interfaces. If very wide gates are used, then echoes from adjacent ply interfaces may drift into and out of individual gates at different times, making it impossible to determine the depths of any detected defects.

The necessity for improved inspections of materials with nonplanar interfaces prompted an experimental investigation of the applicability of software-gating techniques to woven composite materials. The study was conducted on samples with different matrix compositions, weave patterns and numbers of layers. Initial scans of impact-damaged woven composite panels were conducted using the same software gate setups that are commonly used for quasi-isotropic samples, that is, times between gates were set equal to the round-trip travel time for ultrasound in a signal ply and gate widths were set equal to approximately one-third of the time between gates. Comparison of the C-scan image from the back-surface gate with the composite C-scan image generated by superimposing the images from all of the interface gates (Figures 3-4a and 3-4b) revealed that not all of the damage had been imaged by the interface gates. It was assumed that the loss of information was due to the depth variation of the interfaces. Based on that assumption, software-gated C-scans were made using several narrow, adjacent gates. Images from these gates not only confirmed the extent of interface nonplanarity but also indicated that delaminations occurred between perpendicular fiber bundles within a single layer. This was later confirmed through destructive examination.

Although narrow, adjacent gates were used to satisfactorily image the delamination damage, the large number of images produced during a typical scan (four per ply) required substantial manual interpretation. The
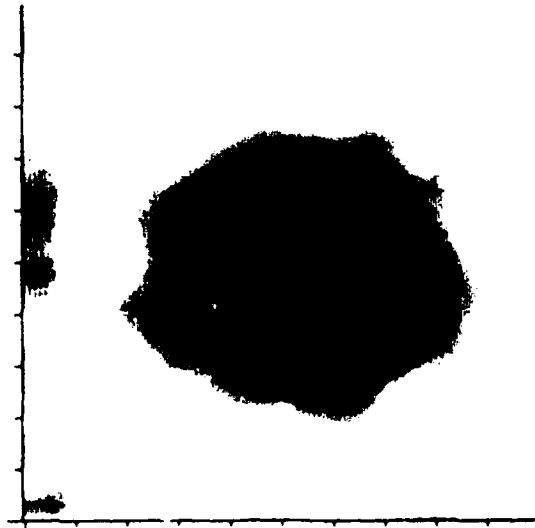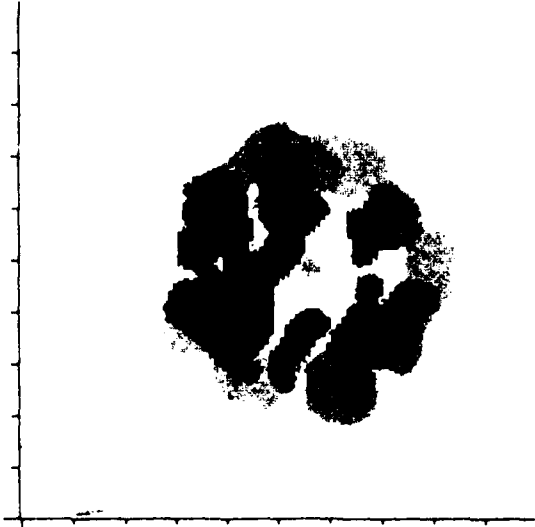
Figure 3-4. Total damage at impact-damage site: (a) Gate over backsurface echo; (b) composite image from narrow interface gates.

next step in this study was to develop a gate setup that could be used to image both interface and intra-ply damage in woven composites with a more manageable quantity of data. This was accomplished by using wide, overlapping gates for each layer (Figure 3-5). The time between gates was set equal to the average round-trip time for ultrasound in a single ply, and gate width was set to 30 nS more than the distance between gates to provide an overlap of two sequential gates at each interface. As a result, damage that appeared in a single image was unique to that gate, and was probably within a single ply. Damage that appeared in two consecutive images was in the gate overlap regions, and was probably an interply delamination.

A composite image made by superimposing the damage detected by the overlapping gates is shown in Figure 3-6. Comparison of Figure 3-6 with Figures 3-4a and 3-4b indicate that more of the damage has been imaged with the wide overlapping gates than with the narrow interface gates. Not all of the damage has been detected, however. It is possible that the undetected damage is very near the surface, where it is virtually indistinguishable from variations in the entry surface. Some entry-surface features are already visible in the composite image. Thus, setting other gates closer to the entry surface would probably not satisfactorily image the remainder of the damage.

Three major conclusions resulted from this investigation. First, ply interfaces in woven graphite-epoxy composites are not sufficiently planar to be imaged reliably with the narrow-software-gate setup used for samples with planar interfaces. Second, a large number of adjacent narrow gates (four gates per ply for the conditions tested), while providing excellent depth resolution, requires time consuming interpretation. Third, wide overlapping gates provide acceptable depth resolution and simplify data interpretation.

3.2 NORMAL-INCIDENCE BACKSCATTER C-SCAN IMAGING USING SWEPT-FREQUENCY TONE-BURST TECHNIQUES

Normal-incidence, swept-frequency, tone-burst techniques were used to generate C-scan images of delamination damage in composite materials[3]. The techniques were studied in an attempt to improve defect imaging in acoustically attenuative materials such as quasi-isotropic and woven graphite-epoxy
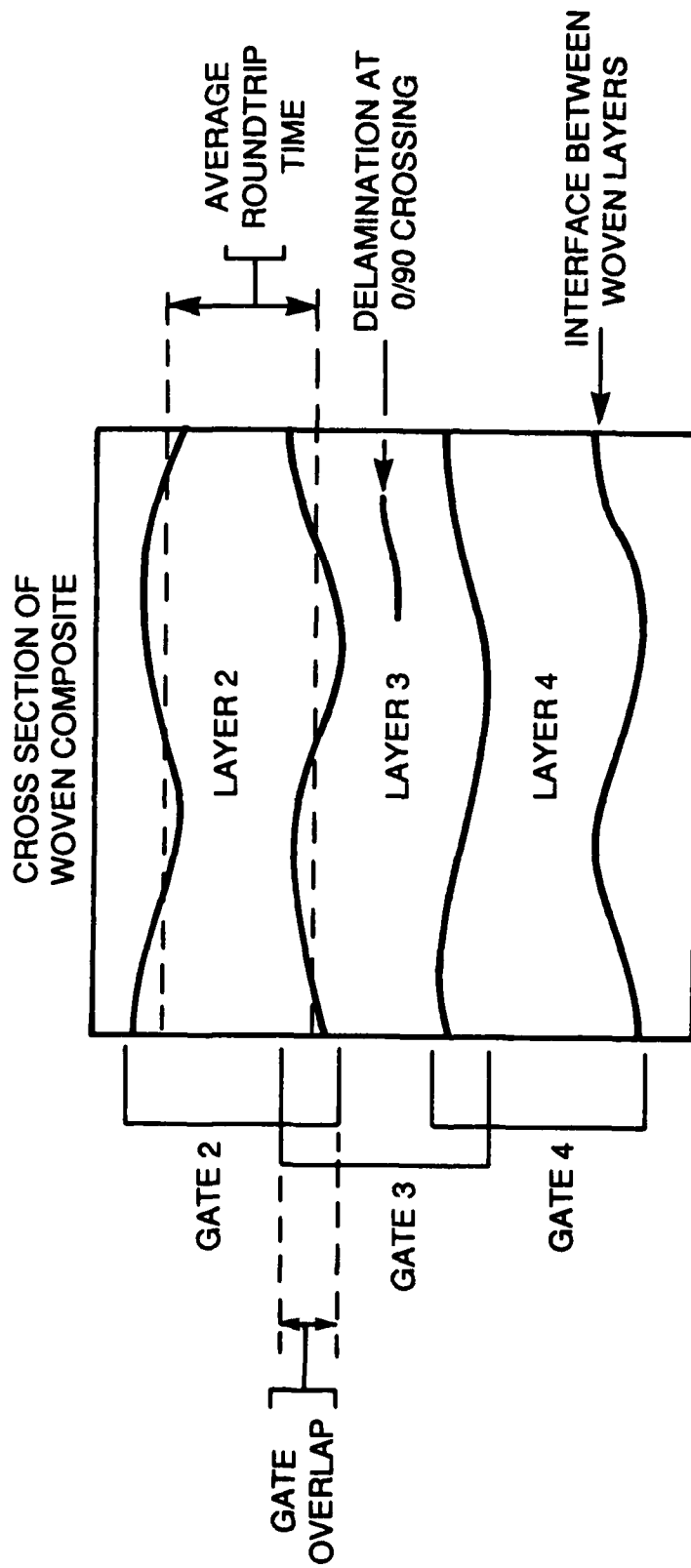
Figure 3-5. Relationship between woven composite interfaces and wide overlapping gates.
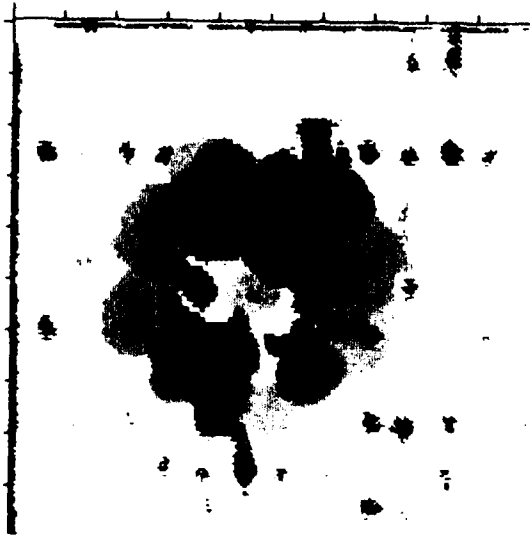
Figure 3-6.   Composite image of damage obtained from
overlapping gate technique.

composites. Normal-incidence methods are less affected by scattering from
fibers than are Lamb wave and angle backscatter methods. Tone-burst methods
generate higher acoustic energy levels than do spike-excitation methods, and
sweeping the frequency while tone bursting allows generation and reception of
energy over the entire usable frequency range of the transducer.

The sample from which data were collected was a 32 ply, quasi-isotropic
graphite-epoxy composite with a 14 joule impact-damage site. Normal-
incidence, immersion techniques were used to acquire all C-scan data, with
ultrasonic waves being generated by applying a swept-frequency tone-burst[4,5]
to an 8 MHz focused transducer. The swept-frequency range was 4 through 12
MHz. The duration of the individual tone burst at each frequency during the
sweep was long enough to allow overlap of the entry-surface and back-surface
echoes. Echoes from internal delaminations (due to the impact) would, there-
fore, also overlap the entry surface echo. The received tone-burst was video-
detected, high-pass filtered and averaged at 128 equally spaced frequencies
during the frequency sweep. Each of the 128 average amplitude values was
digitized, providing an amplitude-versus-frequency curve at each location on
the sample being scanned. The shape, or pattern, of the amplitude-versus-
frequency curve depended on the depth of any delamination which was present.
If a delamination was present, then the amplitude-versus-frequency pattern
would depend upon the phase of the returning echo at each frequency during the
sweep. The phase of the returning echo (at each frequency) would, in turn,
depend on the depth of the delamination.

Since a digital C-scan image requires a single value for each location
on the sample, it was necessary to reduce the amplitude-versus-frequency pat-
terns produced at each point to a single value which would be representative
of that pattern. The first step in reducing the pattern to a single, unique
value was the calculation of its Fourier transform. While calculating the
Fourier transform of amplitude versus frequency data may seem to be a meaning-
less exercise (amplitude versus frequency is already a Fourier transform), it
can be thought of as the first in a series of steps in a pattern recognition
technique. If there were no defects at the sampling location, the amplitude-
versus-frequency pattern which resulted from the interference of the entry-
and back-surface echoes would have many peaks and valleys (Figure 3-7a). This

would appear very similar to a high frequency time-domain waveform added to a very low frequency time-domain waveform. Thus, its Fourier transform would have a peak in the high frequency region and a peak in the very low frequency region as does Figure 3-7b which is the Fourier transform of the data in Figure 3-7a. If there were a defect near the entry surface, then the amplitude-versus-frequency pattern which resulted from the interference of the entry-surface and defect echoes would have fewer peaks (Figure 3-8a). This would appear similar to a low frequency time-domain waveform added to a very low frequency time-domain waveform. Thus, its Fourier transform would have a peak in the low frequency region and a peak in the very low frequency region. This is exactly what is seen in Figure 3-8b which is the Fourier transform of the data in Figure 3-8a.

The Fourier transform of the amplitude-versus-frequency data was the starting point for two distinct methods for generating the C-scan image data. The first method used band-pass filtering and divided the Fourier-transformed data into four frequency bands. The average value in each of the frequency bands was used to produce a C-scan image. This resulted in four C-scan images representing the presence or absence of defects in four wide depth ranges. The second method generated C-scan images from the median frequency of the Fourier-transformed data[4]. This median frequency was strongly affected by the location of the peaks in the Fourier-transformed data and was thus very sensitive to the depth of the defect. This second method produced a single C-scan image with defect depth encoded in the gray levels.

Four C-scan images produced by the band-pass filter method (method one) are shown in Figure 3-9. Those images show the typical impact-damage pattern of delaminations at each depth[1,2]. The depth resolution is about two plies. The C-scan image which resulted from application of the median-frequency method (method two) to the same data are shown in Figure 3-10. Since the median frequency is proportional to defect depth, the gray levels in the image are also proportional to depth. White results from a low median frequency and thus is indicative of a near-entry-surface delamination. Progressively darker shades of gray represent progressively deeper delaminations. The highest median-frequency values are black in Figure 3-10 and indicate reflections from
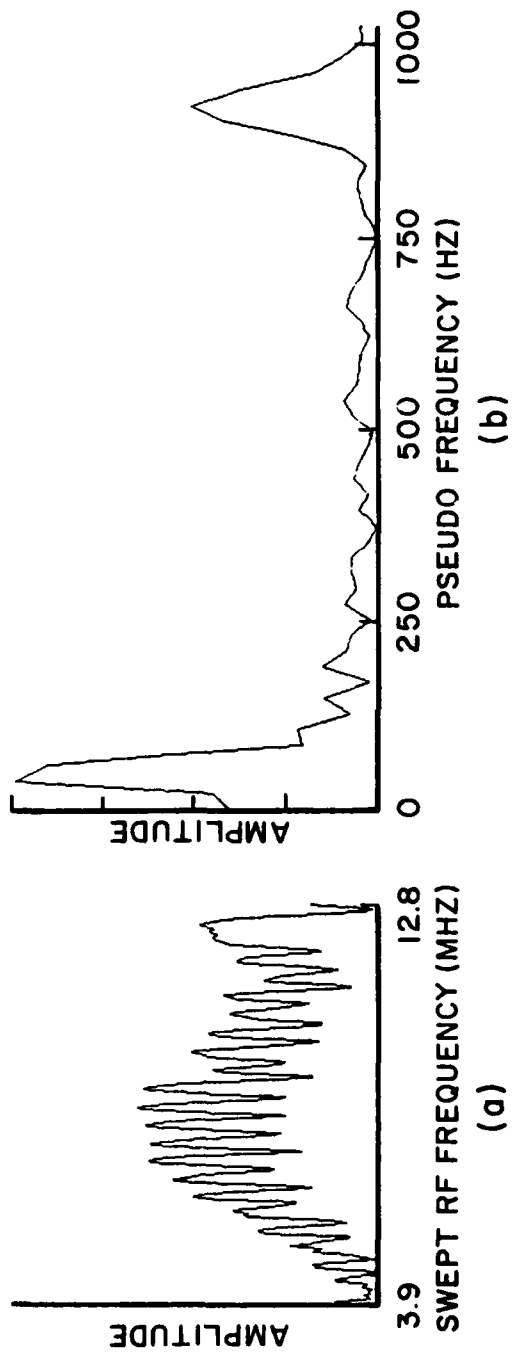
Figure 3-7.   Swept-frequency, tone-burst signals from defect-free region: (a) Amplitude-versus-frequency pattern; (b) Fourier transform of "a".
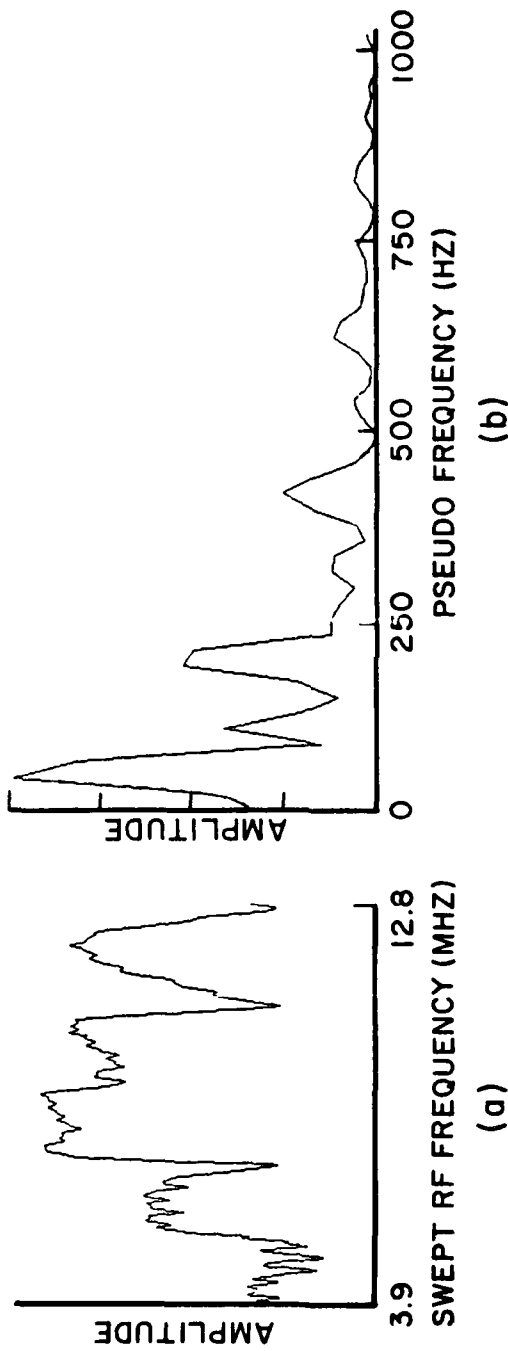
Figure 3-8.   Swept-frequency, tone-burst signals from mid-level delamination site:
(a) Amplitude-versus-frequency pattern; (b) Fourier transform of "a".
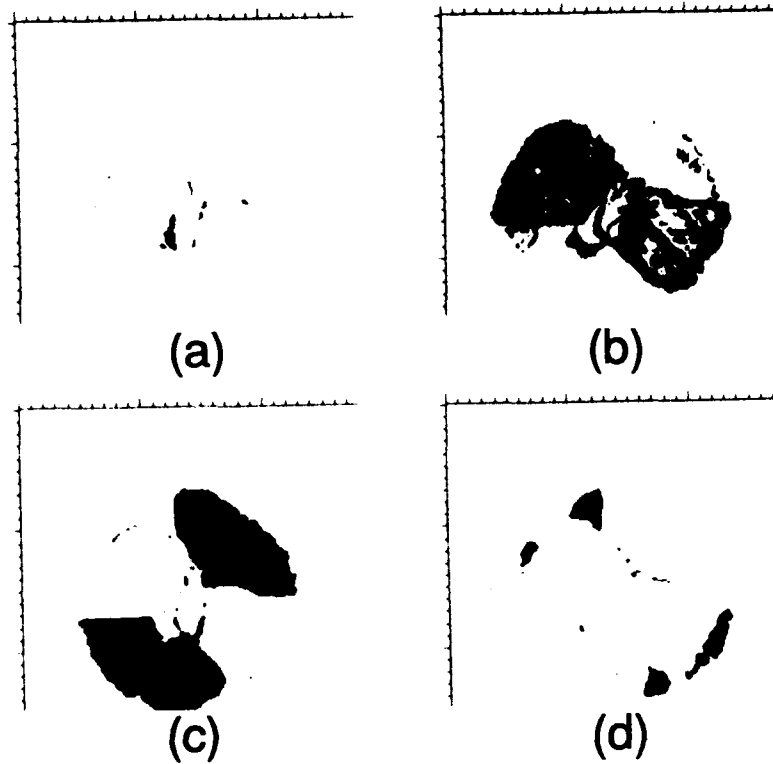
Figure 3-9. Images of impact-damage site obtained by band-pass filtering the Fourier transform of the swept-frequency, tone-burst signal: (a) Upper level (nearest to entry surface); (b) Upper-middle level; (c) Lower-middle; (d) Lowest level (nearest to back surface).
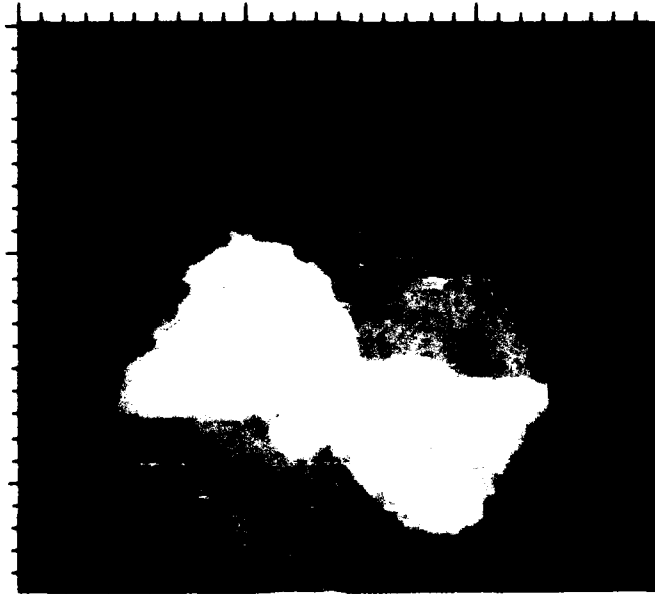
Figure 3-10.   Image of impact-damage site obtained by applying
median-frequency processing to the Fourier
transform of the swept-frequency, tone-burst signal.

the back surface of the plate (defect-free regions). The direction of fiber tows have also been imaged in Figure 3-10.

This study demonstrated that delamination damage in quasi-isotropic, graphite-epoxy composites can be imaged using the normal-incidence, swept-frequency, tone-burst technique. In addition, the study demonstrated that the median-frequency signal processing technique encodes the depths of defects in the gray levels of the image. The swept-frequency, tone-burst technique has two major advantages over other techniques. First, greater acoustic energy can be transferred to the test sample with tone-bursting than impulse-excitation methods, resulting in higher signal-to-noise ratios. Also, because envelope-detection methods are used during the frequency sweep, low-speed (5 KHz) analog-to-digital converters can be used to digitize the amplitude versus frequency data. These low-frequency A/D converters are lower in cost and generally have greater resolution and dynamic ranges[3] than higher speed digitizers. The primary disadvantage of the swept-frequency, tone-burst technique and the median-frequency signal processing method is that considerable time is required to capture and process the signal at each scan point. This results in very long scanning times. More detailed information about the swept-frequency, tone-burst technique is available in the article entitled "Swept Frequency Ultrasonic Imaging in Composite Plates" which is included in Appendix A of this report.

3.3 DIGITAL ENHANCEMENT AND RESTORATION OF ULTRASONIC BACKSCATTER IMAGES

There are no ultrasonic inspection or imaging systems that can generate perfect images of samples being tested. The long "ring" times of ultrasonic transducers cause uninspectable or "dead" zones near the entry surfaces of samples undergoing inspection and general depth-wise blurring in ultrasonic B-scan images[6,7]. This depth-wise blurring leads to uncertainty in the location and extent of any subsurface defects. The finite beam width (point-spread function) of any ultrasonic transducer results in lateral blurring of features in ultrasonic C-scan images. The lateral blurring makes it nearly impossible to accurately determine the size of any defect which may have been imaged. The blurring of image features (whether depth-wise or lateral) generally becomes worse at lower ultrasonic frequencies because of the corresponding

increase in wavelengths. Unfortunately, it is often necessary to use the lower frequencies (with the consequent degradation in image quality) when inspecting thick composite materials or when inspecting materials with rough surfaces.

The blurring caused by the inspection system and the necessity for using low frequencies to inspect thick composite samples led to the investigation of digital image enhancement and image restoration techniques for improving the visual detection and resolution of image features. The digital image enhancement and restoration techniques selected for study were those which had been successfully used in other disciplines[8-12]. The goals of the investigations were to determine the capabilities and limitations of those selected enhancement and restoration techniques for reducing system-introduced blur in the digitized ultrasonic NDE images.

In the discussions which follow, the term, enhancement, will refer to those methods which attempt to improve the visual "quality" of an image without any prior knowledge of the degradation process. The term, restoration, will be used for those methods which attempt to recreate the "true" image of a feature by removing the degrading effects of the imaging system.

3.3.1 B-Scan Image Enhancement Using Entry-Surface-Echo Subtraction

Defects which are very close to the entry surface of a sample may not be visible in B-scan images because of the long "ring" time of ultrasonic transducers. The computer program, REFSUB, enhances radio frequency (rf) B-scan images of near-entry-surface defects by subtracting a reference rf A-scan from every A-scan in the B-scan. For B-scans obtained from samples with smooth entry surfaces, the rf entry surface echoes will be nearly identical, except in regions where there are near-entry-surface defects. Thus, subtraction of the reference rf A-scan from the A-scans in the B-scan image leaves only background noise and the back-surface echoes except where there is a defect echo. The defect echo is then more easily visually detectable.

REFSUB does not operate in real time. Rather, the rf A-scans used to generate the B-scan image must be digitized and stored in a computer prior to the use of REFSUB. A reference rf A-scan must also be digitized and

stored in the computer. One of the rf A-scans in the B-scan file can be used as the reference A-scan or the reference rf A-scan can be obtained from a separate source. If the reference A-scan is obtained from a separate source, then it too must be digitized and stored in the computer prior to the use of REFSUB. The user is required to adjust the echo amplitude of the reference A-scan to the same level as the amplitude of one of the echoes in the rf B-scan by specifying a multiplicative constant. The program automatically removes any d.c. offset in the waveforms and automatically aligns the waveforms to account for small shifts in location of the sample's entry surface before subtraction. A user selected amplitude threshold is used by the program to accomplish the waveform alignment prior to subtraction.

Figures 3-11a and 3-11b show the results of applying REFSUB to data acquired from a flat aluminum plate which has a slot milled from the back to within 0.33 mm (0.013 in) of the entry surface. A 3.5 MHz transducer was used to generate the ultrasonic waves for the B-scan inspection. Figure 3-11a shows the rf B-scan image prior to application of REFSUB. The loss of the back-surface echo image is the only indication that a defect may be present. However, the near-entry-surface defect is clearly visible after the entry-surface echo has been removed by the use of REFSUB (Figure 3-11b).

3.3.2   B-Scan Image Restoration Using 1-D Axial Wiener Deconvolution

A technique known as axial Wiener deconvolution[7] can be used to reduce the "ring" time of ultrasonic transducers. The technique effectively reduces the length of the ultrasonic pulse as illustrated in Figure 3-12. Figure 3-12a shows a typical rf pulse echo (A-scan) and Figure 3-12b shows the result of applying the axial Wiener deconvolution technique to the rf A-scan in Figure 3-12a. The "ringing" has been reduced and the pulse length has been shortened. The result of applying the axial Wiener deconvolution technique to all rf A-scans in a B-scan is an improvement in the depth resolution as shown in Figure 3-13. Figure 3-13a shows a B-scan image generated from radio frequency (rf) A-scans of a delaminated graphite-epoxy composite sample. The entry surface echo is clearly seen as a thick, black line with light colored lines above and below. Echoes from the delaminations are thick, white lines. The B-scan image generated from axially Wiener deconvolved A-scans is shown in Figure 3-13b. The black line denoting the entry–surface echo and the light
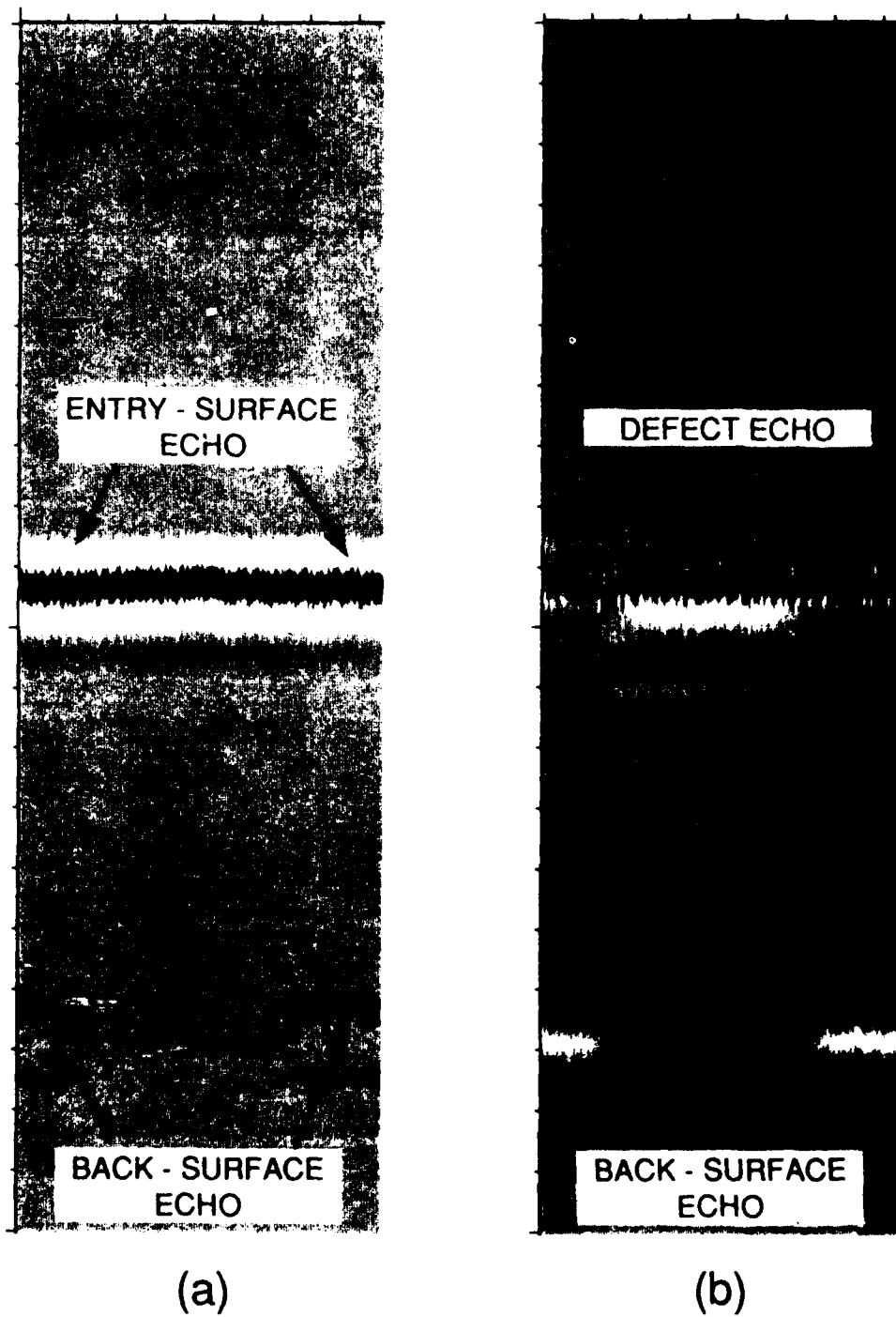
Figure 3-11.   B-scan images of slot milled 0.33 mm below entry
surface of aluminum sample: (a) From rf A-scans;
(b) After entry-surface-echo subtraction.
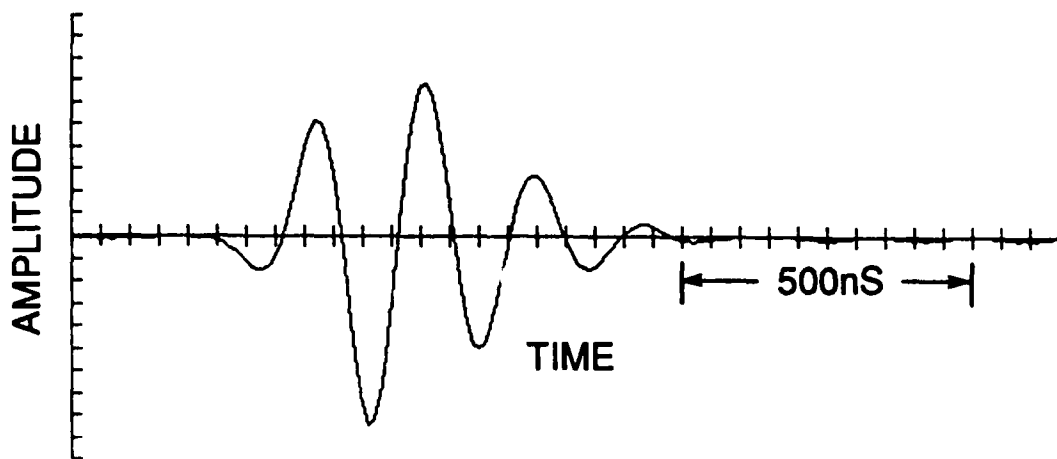
(a)
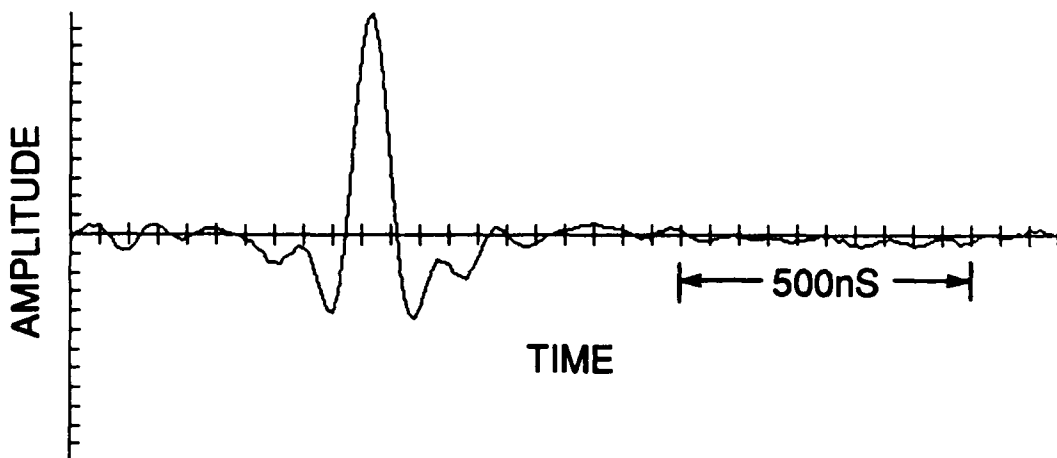
(b)

Figure 3-12.   Ultrasonic pulse length reduction by axial Wiener
deconvolution: (a) Unprocessed rf pulse (A-scan);
(b) Wiener deconvolution of "a".
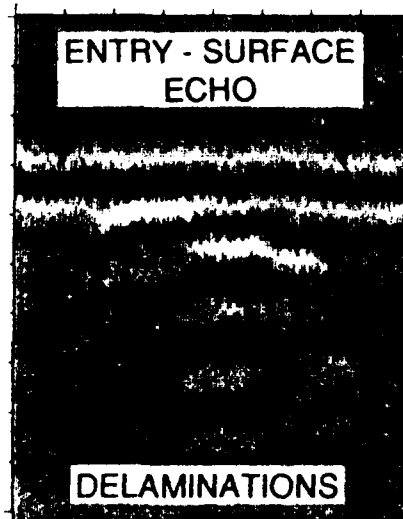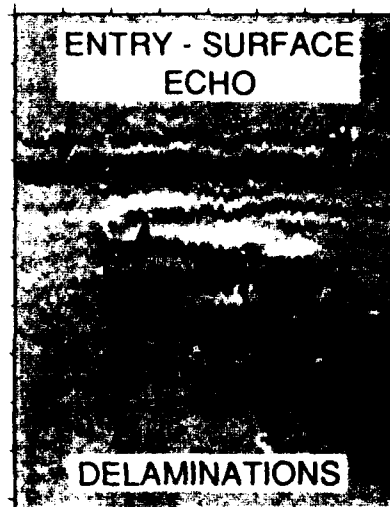
Figure 3-13.   B-scan images of impact-damage site in graphite-epoxy
composite: (a) From rf A-scans; (b) From axially
Wiener-deconvolved A-scans.

lines which denote the delaminations are thinner in Figure 3-13b, demonstrating the improvement in resolution which can be expected through application of the axial Wiener deconvolution technique.

Implementation of the technique currently requires that a reference rf A-scan (pulse echo) be digitized and stored in a computer and that all rf A-scans required for a B-scan image be digitized and stored in the computer. One-dimensional Fourier transformation software must also be available. The axial Wiener deconvolutions can then be performed in the computer and the results can be used to generate a B-scan image with enhanced depth resolution. The current technique requires considerable computer storage and is not performed in real time. However, the use of high-speed, dedicated digital signal processing (DSP) chips should make it possible to perform the deconvolution during data collection. The practical applications of this technique are discussed in the articles titled "Signal Processing Techniques for Imaging Impact Damage in Composites" and "Imaging of Impact Damage in Composite Materials" which are included in Appendix A of this report.

3.3.3   B-Scan Image Restoration Using 1-D Power Spectrum Equalization

The use of the Wiener deconvolution technique requires a reference rf A-scan which is representative of the pulse at the depth within the material being inspected. For near-entry-surface inspections this reference A-scan can be obtained from a thick, flat plate[13]. For inspections deep within a complex material such as a quasi-isotropic, graphite-epoxy composite a usable reference rf A-scan may not be obtainable.

The difficulty of obtaining a suitable reference for axial Wiener deconvolutions of certain rf A-scans led to the investigation of the use of a technique known as power spectrum equalization (PSE)[14]. This technique makes use of information contained within the B-scan image itself to construct a filter which "restores" the image. Application of the technique to the data for the B-scan image in Figure 3-13a produced the image in Figure 3-14. The depth resolution in the image of Figure 3-14 is significantly better than that in Figure 3-13a. Application of the PSE technique requires that the B-scan image be digitized and that one-dimensional Fourier transformation software be available to perform the power spectrum equalization. Detailed technical information about this technique is contained in the article
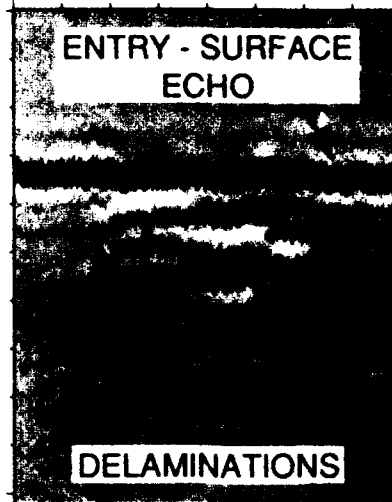
Figure 3-14.   B-scan image produced by power spectrum
                equalization of data used to generate
                Figure 3-13a.

"Ultrasonic Image Restoration by Pseudo Three-Dimensional Power Spectrum Equalization" which is included in Appendix A of this report.

3.3.4   C-Scan Image Enhancement Using Marr-Hildreth Operator

3.3.4.1   Sources of Degradation in C-scan Images

A major degradation in lateral resolution in ultrasonic C-scan images is the blur caused by the finite width of the ultrasonic beam[15]. This is illustrated in Figure 3-15. Figure 3-15a shows a computer simulation of a "perfect" disk-shaped object. Figure 3-15b shows a C-scan image of an ultrasonic beam, generated by scanning a small diameter steel sphere. Figure 3-15c shows the blurred image which would result if the "perfect" disk-shaped object of Figure 3-15a were ultrasonically scanned with the transducer beam of Figure 3-15b. Note that the image of the disk-shaped object is now blurred and is wider than the original object. It is this blur-ring and expansion that must be reduced in order to quantify the shape and size of defects which have been imaged by ultrasonic C-scanning techniques. There are other sources of C-scan image degradation, such as, surface rough-ness, but the emphasis in this report will be on the removal of the blur introduced by the finite beam width of the ultrasonic transducer.

3.3.4.2   Marr-Hildreth Operator

Previous publications[16,17] have demonstrated the usefulness of digital image enhancement techniques for improving visual detec-tion and resolution of features in NDE images. Many of those techniques were used to enhance the appearance of the edges of features by removing blur. Two of the major advantages of the more popular edge enhancement operators are their ease of implementation and their execution speed. Their major disad-vantages are that they emphasize "noise" as well as edges, and some are directionally dependent operators which tend to suppress features that are not aligned in the "preferred" direction.

The nondirectional Marr-Hildreth operator was actually developed for detection of intensity changes[18] in optical images. As Marr and Hildreth demonstrated, this operator is capable of simultaneously emphasizing the edges and suppressing "noise" in digital images. The Marr-Hildreth operator's ease of implementation, rapidity of execution, lack of "preferred"
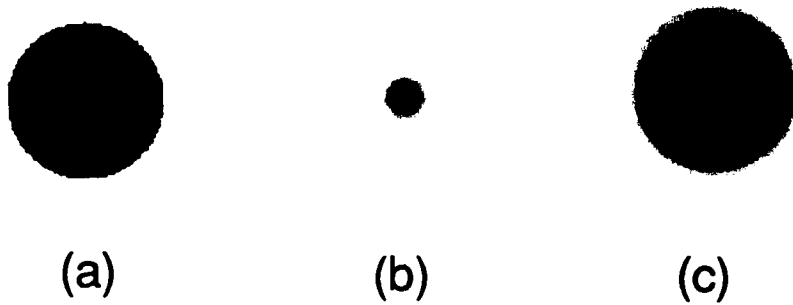
Figure 3-15.   Blurring of object due to finite beam width of
                ultrasonic transducer: (a) Disk-shaped object;
                (b) Ultrasonic beam; (c) Blurred image of disk-
                shaped object.

orientation and ability to enhance edges in the presence of noise make it useful for rapid enhancement of images prior to attempting more difficult and time-consuming techniques. The operator is the two-dimensional second derivative (Laplacian) of a two-dimensional Gaussian. The equation in rectangular coordinates is:

$$MH = A * \left\{ \left(\frac{X-\mu_x}{\sigma_x^2}\right)^2 + \left(\frac{Y-\mu_y}{\sigma_y^2}\right)^2 - \frac{1}{\sigma_x^2} - \frac{1}{\sigma_y^2} \right\} e^{-\frac{1}{2}\left[\left(\frac{X-\mu_x}{\sigma_x}\right)^2 + \left(\frac{Y-\mu_y}{\sigma_y}\right)^2\right]} \tag{1}$$

where μ_x and μ_y define the location of the central element in the moving-window[17] implementation of this operator, σ_x and σ_y are the standard deviations in the X-direction and the Y-direction, and "A" is a constant. Use of large values for the standard deviations will provide considerable noise suppression, but will locate and emphasize only very broad edges. Narrow edges may be suppressed along with the noise. Use of small values for the standard deviations will locate and emphasize very narrow edges, but will also provide less noise suppression.

For all of the studies discusses in this report, the Marr-Hildreth enhancement was implemented as a so-called moving-window, spatial-domain convolution operation[17,19]. This moving-window, spatial-domain convolution methodology will not be discussed here. Rather, the interested reader is referred to the article titled "Digital Image Enhancement for Ultrasonic Imaging of Defects in Composite Materials" which is included in Appendix A of this report.

3.3.4.3   Application of the Marr-Hildreth Operator

An optical image of the surface of a graphite-epoxy composite is shown in Figure 3-16a. The major feature in that image is a weave pattern which is actually the impression of the bleeder cloth used during fabrication of the sample. An unenhanced and two digitally enhanced ultrasonic C-scan images of the composite sample's surface are also shown in Figure 3-16. Digital data for the original C-scan image (Figure 3-16b) were acquired with a low frequency (3 MHz) acoustic-microscope transducer. The images in Figures 3-16c and 3-16d are digital enhancements of Figure 3-16b
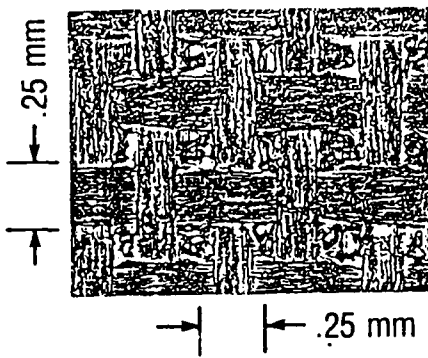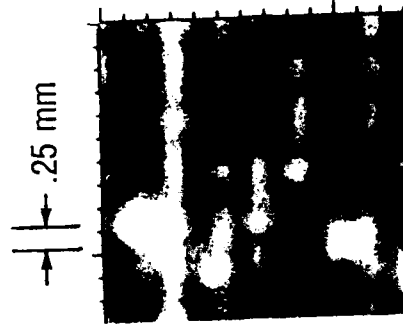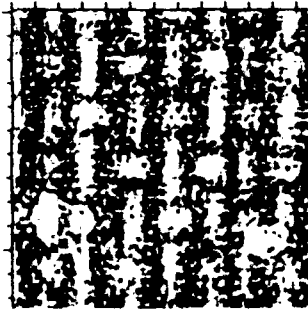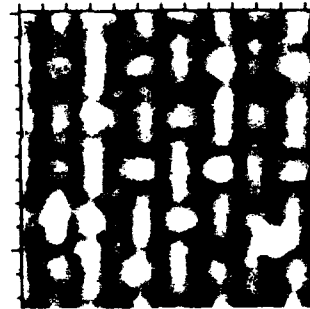
Figure 3-16. Images of graphite-epoxy composite surface:
(a) Optical; (b) Ultrasonic C-scan; (c) Marr-Hildreth
enhancement of "b" with $\sigma = 1$; (d) Marr-Hildreth
enhancement of "b" with $\sigma = 2$.

using Marr-Hildreth operators with standard deviations of 1 pixel and 2 pixels, respectively. Note that in each case the blur has been reduced and the weave pattern has been made visible over the entire image. However, the use of the smaller standard deviation has resulted in a "noisier" image (Figure 3-16c). The Marr-Hildreth operator can also be used to enhance a "noisy" image as demonstrated in Figure 3-17. The image in Figure 3-17a was generated by adding computer generated noise to the digitized ultrasonic C-scan image in Figure 3-16b. Images "b" and "c" in Figure 3-17 shows the results of enhancing the image in Figure 3-17a by using Marr-Hildreth operators with standard deviations of 1 and 2 pixels, respectively. The image in Figure 3-17b is too "noisy" to allow visual interpretation of any features. The image in Figure 3-17c has been sufficiently "deblurred" and the noise has been sufficiently suppressed to allow visual recognition of the weave pattern everywhere in the image.

Another example of Marr-Hildreth enhancement of a blurred ultrasonic C-scan image is shown in Figure 3-18. Figure 3-18a is an optical image of a steel ruler. The rulings are separated by 0.25 mm (0.010 in). Digital data for the C-scan image in Figure 3-18b were acquired with the same transducer as that used to acquire the data for the C-scan image in Figure 3-16b. Both the numerals and the rulings are blurred beyond legibility in the ultrasonic C-scan image of Figure 3-18b. The results of applying a Marr-Hildreth operator to the data of Figure 3-18b are shown in Figure 3-18c. The numerals are now legible in Figure 3-18c, but the rulings are not clear. The lack of simultaneous visibility of numerals and rulings is caused by a relatively large contrast variation over the image as a whole, and very small contrast variations between the rulings and the general background in the vicinity of the rulings. This problem of contrast variations was overcome by applying a variable-gain filter (designed to emphasize features in low-contrast regions of an image) to the image data of Figure 3-18c. The results of applying the variable-gain filter to the image data in Figure 3-18c are shown in Figure 3-18d. Both the numerals and the rulings are clearly visible in Figure 3-18d. More information about the implementation of the moving-window, spatial-domain Marr-Hildreth convolution operator is provided in the articles titled "Marr-Hildreth Enhancement of NDE Images" and "Improving Ultrasonic NDE Images with Pseudo Wiener Filtering and Marr-Hildreth

.25 mm

(a)   (b)   (c)
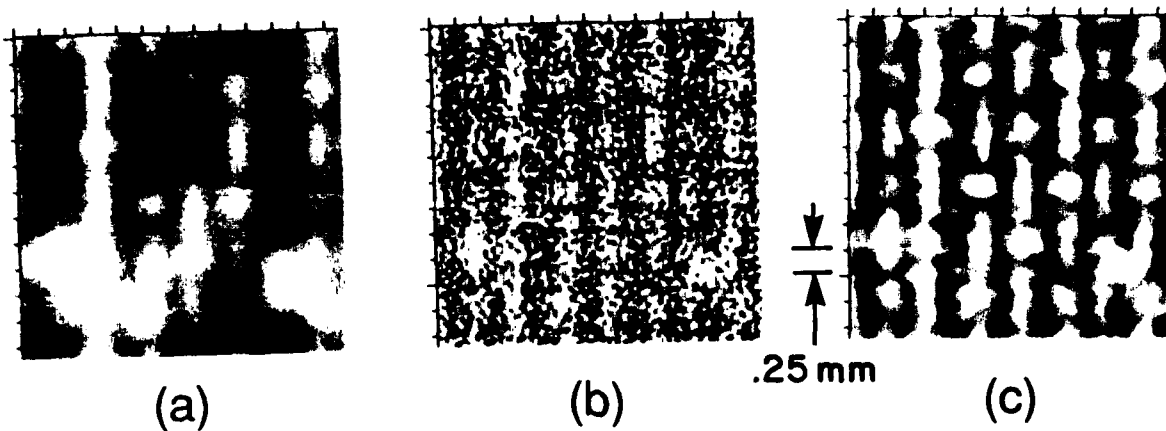
Figure 3-17.   "Noisy" images of graphite-epoxy composite: (a) Computer-
                generated noise added to image in Figure 3-16a; (b) Marr-
                Hildreth enhancement of "a" with σ = 1; (c) Marr-Hildreth
                enhancement of "a" with σ = 2.

3-32
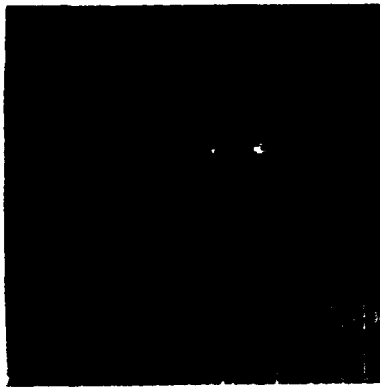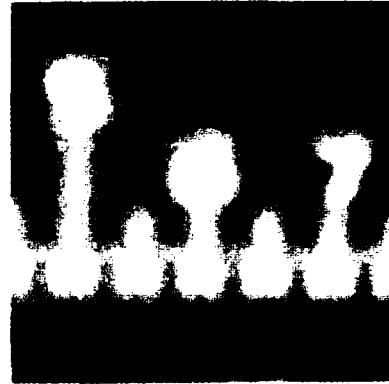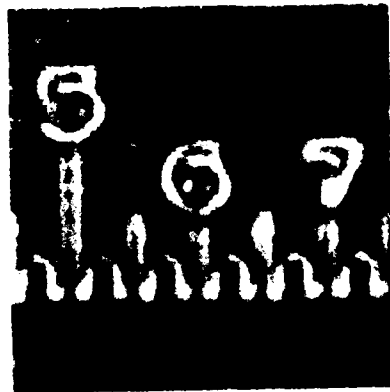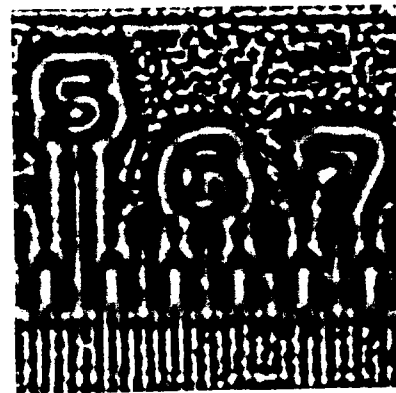
Figure 3-18.   Images of ruler: (a) Optical; (b) Ultrasonic;
(c) Marr-Hildreth enhancement of "b"; (d) Variable
gain enhancement of "c".

Enhancement Techniques" both of which are included in Appendix A of this report.

3.3.5   C-Scan Image Restoration Using 2-D Lateral Wiener Deconvolution

If the major source of blur in an ultrasonic C-scan image is due to the finite diameter of the ultrasonic beam and if sufficient knowledge of the beam diameter and beam shape are available, the image can be at least partially restored by a technique known as two-dimensional Wiener deconvolution[8,9]. This is a two-dimensional equivalent of the one-dimensional axial Wiener deconvolution described previously in Subsection 3.3.2. The two-dimensional technique effectively reduces the diameter of the ultrasonic beam, thereby reducing the lateral blur in C-scan images. Application of the technique requires a reference C-scan image of the ultrasonic beam (technically referred to as a point-spread function) and a digitized ultrasonic C-scan image. The technique can then be applied to remove some of the effects of the broad ultrasonic beam from the C-scan image.

An indication of the effectiveness of this technique for "restoring" ultrasonic C-scan images is demonstrated in Figure 3-19. Figure 3-19a shows the effects of using the two-dimensional Wiener deconvolution technique to remove the ultrasonic-beam-introduced blur from the C-scan images of the ruler shown in Figure 3-18b. The reference image of the ultrasonic beam was obtained by first generating a C-scan image of a very small diameter ball in water with the same ultrasonic transducer that was used to scan the steel ruler. A two-dimensional Gaussian was then fit to the C-scan image and the two-dimensional Gaussian was used as the reference in the deconvolution procedure. Both the numerals and the rulings are legible in Figure 3-19a, but some apparent blur remains due to overall image contrast problems. The same variable gain filter which was applied to the Marr-Hildreth image data in Figure 3-18c was applied to the image data of Figure 3-19a to generate the data for the image in Figure 3-19b. Both numerals and rulings are clearly visible in Figure 3-19b.

Technical details of two-dimensional Wiener filtering and further details regarding its implementation are provided in the articles entitled "Two-Dimensional Pseudo Wiener Filtering in Ultrasonic Imaging for Nondestructive Evaluation Applications" and "Improving Ultrasonic NDE Images
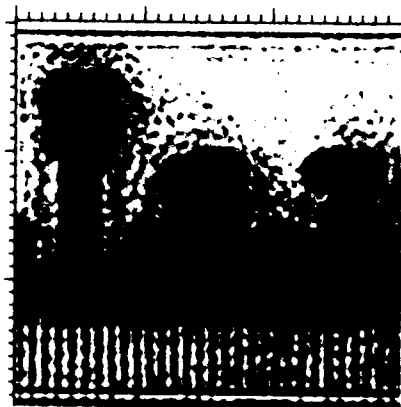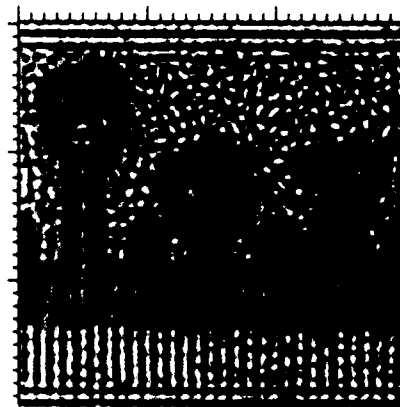
(a)   (b)

Figure 3-19.   Pseudo-Wiener restoration: (a) Pseudo-Wiener
                restoration of image in Figure 3-18b; (b) Variable
                gain enhancement of "a".

with Pseudo Wiener Filtering and Marr-Hildreth Enhancement Techniques" which are included in Appendix A of this report. More technical details about Wiener filtering are also available in the references in the former article.

3.3.6   C-Scan Image Restoration Using 2-D Power Spectrum Equalization

The power spectrum equalization technique[14] which was applied to B-scan images was also applied to the ultrasonic C-scan image of the steel ruler. The intent was to improve lateral resolution by removing the blur caused by the transducer, but without using any knowledge of the transducer's beam width. The results of applying power spectrum equalization to the image data of Figure 3-18b are shown in Figure 3-20a. The resolution of the numerals has been improved, but in Figure 3-20a the improvement is not sufficient to resolve both the numerals and the rulings. Application of the variable gain filter to the image data in Figure 3-20a produced the results in Figure 3-20b. Now, both the numerals and the rulings are visually resolvable.

The improvement in lateral resolution achieved by use of this technique is not as great as that obtained by application of the two-dimensional lateral Wiener deconvolution technique. It does not, however, require as much prior information (knowledge of the beam's shape and diameter) as does the two-dimensional lateral Wiener deconvolution technique. Interested readers should review the article, "Ultrasonic Image Restoration by Pseudo Three-Dimensional Power Spectrum Equalization" included in Appendix A of this report for more technical details.

3.3.7   Marr-Hildreth Enhancement Versus 2-D Restoration Techniques

The results of applying Marr-Hildreth enhancement (Figure 3-18d) and two-dimensional lateral Wiener deconvolution (Figure 3-19b) to the ultrasonic C-scan images of the steel ruler are very similar. Implementation of the two-dimensional lateral Wiener deconvolution requires more information (knowledge of the transducer's beam diameter) and more complex software (two-dimensional Fourier transforms) than does implementation of the moving-window, spatial-domain Marr-Hildreth convolution operator. Also, the implementation of the Wiener filter in the two-dimensional Fourier domain is more difficult than is the implementation of the moving-window, spatial-domain Marr-Hildreth
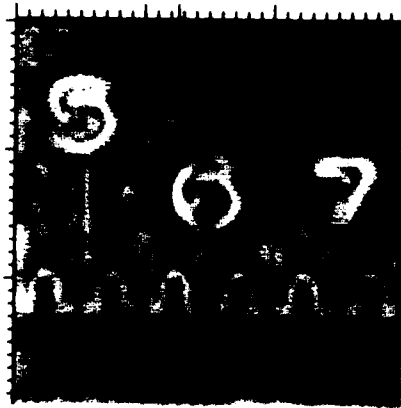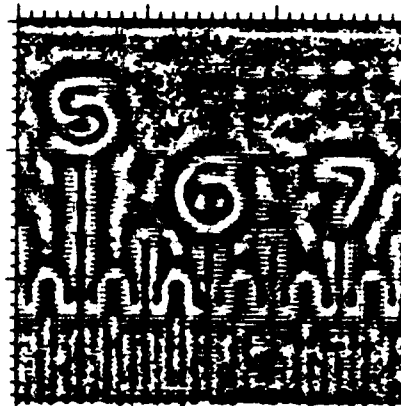
(a)   (b)

Figure 3-20.   Power spectrum equalization: (a) Power spectrum
                equalization of the image in Figure 3-18b;
                (b) Variable gain enhancement of "a".

convolution operator. Power spectrum equalization, while not requiring knowledge of the beam diameter, does require more complex software for implementation. Also, as can be seen by comparing Figures 3-18d, 3-19b and 3-20b, the resolution improvement is less than can be achieved with Marr-Hildreth enhancement or Wiener filtering.

Why, then, should one ever use the two-dimensional lateral Wiener deconvolution technique or the power spectrum equalization technique? The answer lies in the fact that the Marr-Hildreth operator enhances edges in features by applying a numeric second derivative to the image data. Any regions of constant intensity or constant change in intensity will be set to zero when the Marr-Hildreth operator is used. This may severely distort an image. The two-dimensional lateral Wiener deconvolution, however, attempts to restore the degraded image to the "true" image. This is illustrated by the images in Figures 3-21b and 3-21c. Figure 3-21b is the result of applying the Marr-Hildreth operator to the blurred image of Figure 3-21a. Instead of a restoration of the disk-shaped object of Figure 3-21a, the "enhancement" has created the image of a ring-shaped object. However, application of the two-dimensional lateral Wiener deconvolution technique has more faithfully restored the disk-shaped object (see Figure 3-21c). Thus, for rapid screening operations where some distortions can be tolerated, the Marr-Hildreth operator can be used. However, if artifacting is a serious problem, and if a "restoration" of the image is required, then it is necessary to use other techniques such as lateral Wiener deconvolution or power spectrum equalization.

3.3.8 <u>C-Scan Image Restoration Using Pseudo 3-D Wiener Deconvolution</u>

The success achieved with the individual software-gating[1,2], one-dimensional axial Wiener deconvolution[13] and two-dimensional lateral Wiener deconvolution[15] efforts led to another study which combined these three techniques. The study experimentally investigated the capabilities and limitations of the serial application of those three techniques for simultaneously reducing depth-wise ambiguities and improving lateral resolution in ultrasonic C-scan images. The major motivation for the study was the need to improve resolution in C-scan images of closely spaced planes in thick graphite-epoxy composite materials. The complex nature of acoustic wave
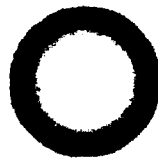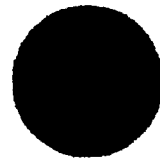
(a)   (b)   (c)

Figure 3-21.   Image enhancement versus restoration: (a) Original blurred image; (b) Marr-Hildreth enhancement of "a"; (c) Pseudo-Wiener restoration of image in "a".

propagation in the graphite-epoxy composites makes determination of reference signals for axial and lateral deconvolutions difficult in thick samples. Thus, this initial study was conducted on C-scan images of planes near the entry surface of the sample. It was assumed that the reference waveform from a flat glass plate in water would be adequate for axial deconvolutions of rf waveforms reflected from near-entry-surface planes. It was also assumed that the beam width or point-spread function (PSF) derived from C-scans of a point reflector in water would provide an acceptable approximation to the transducer's actual beam width in planes near the entry surface of the graphite-epoxy composite. If the study proved successful for planes near the entry surface, then further studies could be conducted to determine whether or not the technique could be extended to planes deep within composite samples. If unsuccessful for near-entry-surface planes, then there would be little chance of successfully enhancing images of planes which lie deep within the sample.

The serial combination of the three signal processing techniques was applied to data collected from an impact-damaged 32-ply-thick, quasi-isotropic, graphite-epoxy composite. A low-frequency (3.5 MHz), 12.7 mm (0.5 in) diameter 51 mm (2.0 in) focal length transducer was used to inspect the sample. The low-frequency (long-wavelength) transducer was selected because long wavelengths will be necessary when the study is extended to thicker samples. The investigation consisted of: (1) digitizing and storing rf A-scans, (2) axially deconvolving the rf A-scans, (3) applying software gates to the rf A-scans and to the axially deconvolved A-scans to generate C-scan images, and (4) using two-dimensional Wiener deconvolutions to reduce the effects of the transducer's finite beam width in the C-scan images. C-scan images were generated of the interface between the second and third plies and of the interface between the third and fourth plies below the entry surface. Because of the long wavelengths associated with the 3.5 MHz transducer, these two interfaces were separated by a round-trip travel distance of about one-third of a wavelength.

The results of applying axial Wiener deconvolutions to rf A-scans have already been shown in the B-scan images of Figure 3-13. The improvement in depth resolution achieved via the pulse shortening which

results from the axial deconvolution is apparent from comparison of the images in Figure 3-13 and has been discussed in the section on image enhancement and resolution. The lateral resolution improvements in C-scan images which result from generating the images from axially deconvolved A-scans and from reduction of beam width by lateral Wiener deconvolution of the C-scan images are demonstrated in Figure 3-22. The C-scan images in that figure are of the interface between the third and fourth plies below the entry surface. The delamination damage present at this interface is shown as the lightest gray region in the figure. The improvements in lateral resolution due to the various processing techniques are evident in that figure.

Five major conclusions resulted from this experimental study. First, B-scan images generated from axially deconvolved A-scans have better depth resolution than B-scan images generated from rf A-scans. This conclusion is in agreement with those of other researchers[6,7]. Second, C-scan images generated by applying software gates to axially deconvolved A-scans have better lateral resolution than C-scan images generated by applying software gates to rf A-scans. The reason for this improvement in lateral resolution is still under investigation. Third, the use of two-dimensional lateral Wiener deconvolutions to reduce the effects of the transducer's finite beam width significantly improves the lateral resolution in C-scan images. Fourth, the greatest improvement in lateral resolution results from the lateral deconvolution of C-scan images generated from axially deconvolved A-scans. Fifth, the reference beam width (diameter of the PSF) required for two-dimensional lateral deconvolution of C-scan images generated from axially deconvolved A-scans was smaller than the reference beam width required for two-dimensional lateral deconvolution of C-scan images generated from rf A-scans. The reason for this difference in reference beam widths is still under investigation. For more detailed information on this topic please read the article titled "Blur Reduction in Ultrasonic Images Using Pseudo Three-Dimensional Wiener Filtering" in Appendix A of this report.
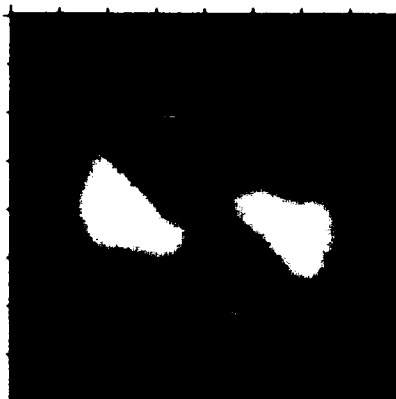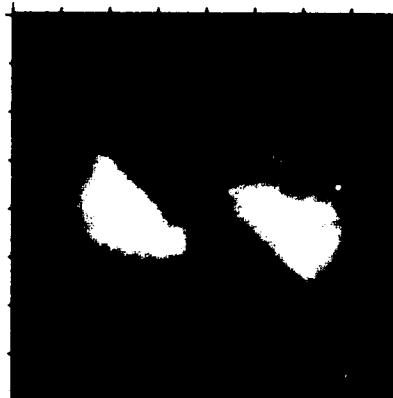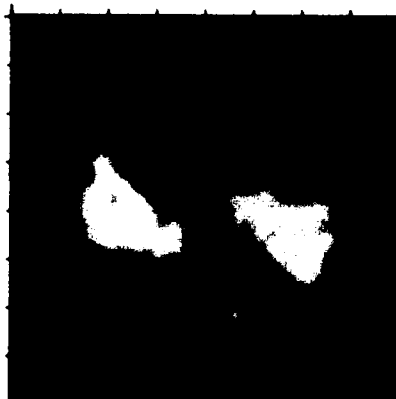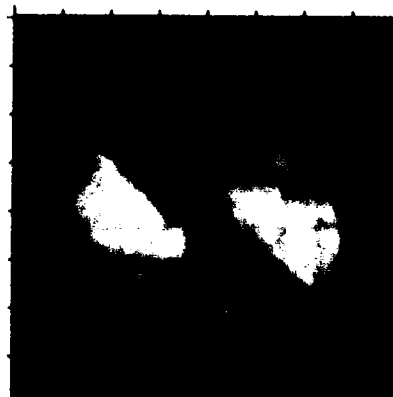
Figure 3-22.   C-scan image of interface between third and fourth
plies below the entry surface: (a) From rf A-scans;
(b) From axially Wiener deconvolved A-scans; (c)
lateral Wiener deconvolution of "a"; (d) Lateral
Wiener deconvolution of "b".

3.3.9 C-Scan Image Restoration Using Pseudo 3-D Power Spectrum Equalization

The power spectrum equalization technique discussed earlier in this report (Subsections 3.3.3 and 3.3.6) was applied to the rf B-scan data collected from the impact-damaged sample. Information regarding data collection and storage are given in Subsection 3.3.8.

One-dimensional power spectrum equalization was first applied to the rf A-scan lines in all of the B-scan images. Software gates were then applied to those unprocessed and processed B-scans to generate C-scan images of the interface between the third and fourth plies below the entry surface. Damaged areas (delaminations) at this interface appear as the lightest gray regions in the figure. The C-scan image generated from the unprocessed B-scans is shown in Figure 3-23a (identical to Figure 3-22a) and the C-scan image generated from the power spectrum equalized B-scan data is shown in Figure 3-23b. Two-dimensional power spectrum equalization was then applied to the image data used to generate Figures 3-23a and 3-23b. The results are shown in Figures 3-23c and 3-23d, respectively.

Comparison of the image in Figure 3-23b with that in Figure 3-23a reveals that the lateral resolution has been improved by power spectrum equalization of the rf A-scans prior to generating the C-scan image. Application of two-dimensional power spectrum equalization to the image data of Figure 3-23b yielded further marginal improvements in the lateral resolution as is evident from Figure 3-23d. Application of two-dimensional power spectrum equalization to the C-scan image data of Figure 3-23a (generated by gating the rf A-scans) yielded improvements in lateral resolution as can be seen in Figure 3-23c. The best lateral resolution (Figure 3-23d) was obtained by the serial combination of: (1) one-dimensional power spectrum equalization of the rf A-scans, (2) generating C-scan images from the processed A-scans, and (3) two-dimensional power spectrum equalization of the C-scan images generated from processed A-scans. For more information please see the article, "Ultrasonic Image Restoration by Pseudo Three-Dimensional Power Spectrum Equalization." This article is included in Appendix A.
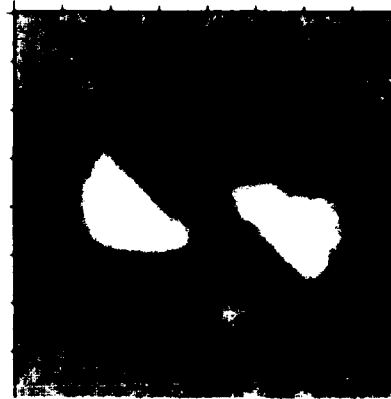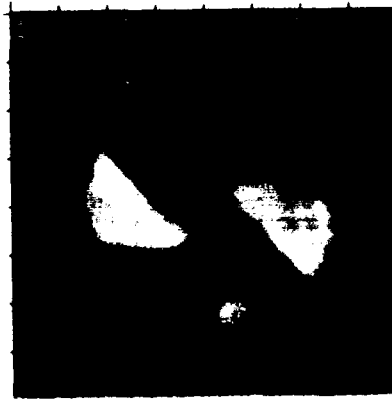
Figure 3-23.   C-scan image of interface between third and fourth
                plies below the entry surface: (a) From rf A-scans;
                (b) From power spectrum equalizaed A-scans; (c)
                Lateral power spectrum equalization of "a"; (d)
                Lateral power spectrum equalization of "b".

3.3.10 Comparison of Pseudo 3-D Wiener Restoration and Pseudo 3-D Power Spectrum Equalization

Direct comparison of equivalently processed images (Figure 3-23b with 3-22b, 3-23c with 3-22c and 3-23d with 3-22d) reveals that the improvements in visual resolution are approximately the same for the two techniques (Wiener deconvolution and power spectrum equalization). The damaged areas appear slightly larger in the Wiener restored images than the damaged areas in the images restored with power spectrum equalization. Since the sample has not been destructively examined, it is not known which of the two methods provides the "best" estimate of the damaged regions.

The comparable resolution improvement produced by the two techniques is in direct contrast to that observed in the restoration of ultrasonic images of the ruler (Figures 3-19b and 3-20b). In that case, the Wiener processing provided superior improvement in resolution. The reasons for this contradiction are not known at this time. It may be that the ultrasonic beam has been distorted by passing through the upper layers of the graphite-epoxy composite. If the beam has been distorted, the reference beam acquired by scanning the ball in water would no longer be a valid approximation of the beam in the material. This would lead to a "poorer" restoration by the Wiener deconvolution process.

3.4 EXPERT SYSTEM FOR ANGLE-BEAM BACKSCATTER B-SCAN IMAGE ANALYSIS

A rule-based expert system technique was developed to identify and classify features in ultrasonic B-scan images of graphite-epoxy composite samples. The approach was essentially one of pattern recognition in which symbolic reasoning and rules-of-thumb were used to identify and classify the important features. An extension of such a system could allow an inexperienced NDE field-level inspector to apply the knowledge of many experts to routine inspections. This "expert" knowledge should result in more reliable inspections.

Data for development of the expert system were acquired from a 16 ply graphite-epoxy composite with a $[90_4/0_4]_s$ bidirectional layup. The sample was approximately 60 mm (2.4 in) long by 25 mm (1.0 in) wide and had several matrix cracks in the entry and back surfaces plies. A 10 Mhz, 13 mm (0.5 in)

diameter, 76 mm (3.0 in) focal length transducer was used to generate the ultrasonic pulses. The transducer was inclined at an angle of 20 degrees from normal incidence during collection of the angle-beam backscatter data. A typical 16 gray-level B-scan image of the sample is shown in Figure 3-24.

The pattern recognition process involved several steps. First, the B-scan image was thresholded from the gray scale into a binary image. Next, each image component was labeled (assigned a number) to distinguish it from other image features. Various statistics were then computed for each labeled image component including location, angle of axis of least inertia, Euler number, area, perimeter, elongation ratio and intensity[21,22]. These statistics were used as inputs to a set of rules which identified and classified the image features as either a top-surface-connected crack, bottom-surface-connected crack, delamination, surface-roughness noise, random noise or unknown. The rules were determined by finding typical values for these statistics from known cracks and other defects in the same material and under the same test conditions.

The program's output (Figure 3-25) was in the form of an image where each image component was identified by a gray-level code. All noise components in Figure 3-25 were set to white (background color) and, therefore, are not visible. Top-surface-connected cracks were set to the lightest gray (image components 10, 13, 15, 17, 18, 33, 35 and 36) while the top-surface reflection was set to the next darker gray. Bottom-surface-connected cracks were set to a darker gray (image components 22, 34, 37, 39 and 44) while unknown image features were set to black (image components 28 and 53). An estimate of the actual locations of the top and bottom surfaces are shown by two nearly horizontal black lines. Clearly, the image of Figure 3-25 is easier to interpret than is the image of Figure 3-24.

The expert system developed from this effort successfully identified and classified all entry surface and back surface matrix cracks which had been previously found in the sample[23]. In addition, random noise was eliminated from the image and two surface irregularities were labeled as unknown features. More information on this study is available in Appendix A in the article titled "Application of Pattern Recognition Techniques to B-scan Analysis."
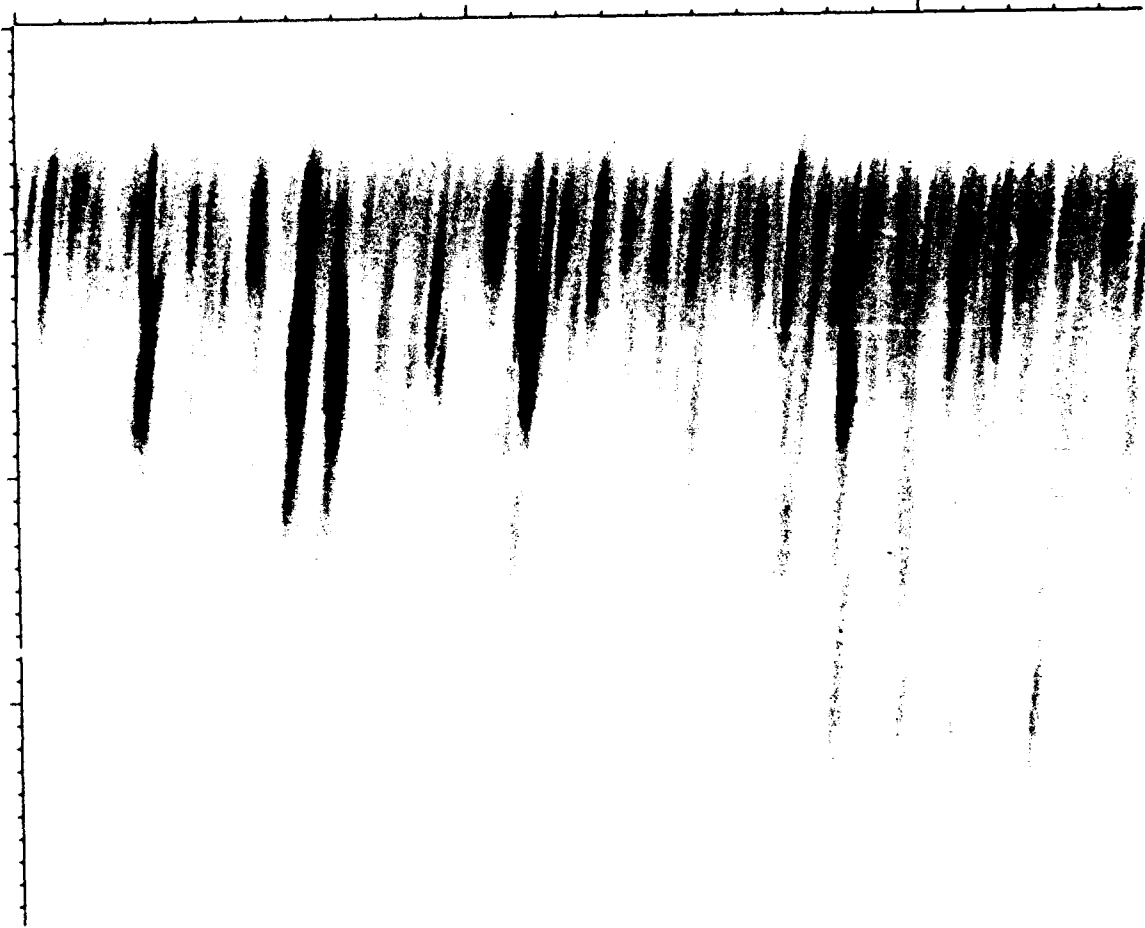
Figure 3-24. Angle-beam, backscatter B-scan image of graphite-epoxy composite with matrix cracks in entry-surface and back-surface plies.
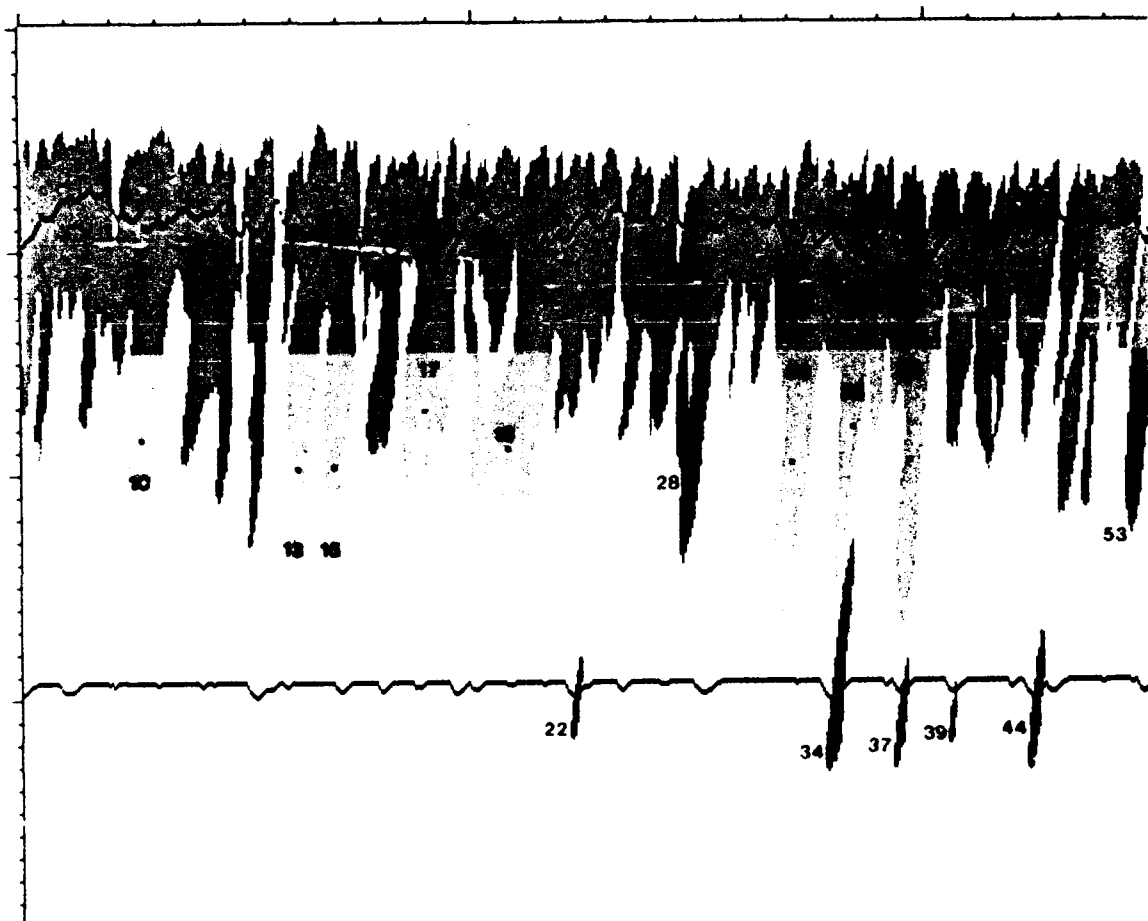
Figure 3-25.   Results of applying pattern recognition processing to
the B-scan image of Figure 3-24.

3.5 COMPUTER MODEL OF ULTRASONIC TRANSDUCERS

TRANS_SIM is an ultrasonic transducer modeling program which generates B-scan images for pictorial illustrations of transducer focusing characteristics. The modeling program can be used to illustrate the effects of frequency, pulse length, element diameter and focal length on beam diameter, focal spot size and acoustic pulse shape.

The user-supplied inputs required by TRANS_SIM are: a digitized rf A-scan, diameter and focal length of the transducer, number of discrete points required to adequately model the transducer's element, acoustic velocity of the target material(s) and distance to the target plane. The output from the program is a B-scan image in which the vertical axis represents time and the horizontal axis represents distance along the specified target plane parallel to the transducer's face. Amplitude variations are represented by variations in gray or color scale. This B-scan output format allows the user to make rapid visual observations of the beam diameter in the target plane.

The ultrasonic transducer is modeled as a linear array of equally spaced points, each of which is the source of a finite-length ultrasonic pulse. This differs from TRANS_SIM's predecessor, FOCUS[23], which used only single-frequency, continuous waves for modeling purposes. Focusing is accomplished by a time delay technique which causes pulses from all source points to arrive in proper phase at the focal point. The media in which the pulse travels are assumed to have zero attenuation, but the pulse amplitude from each point decreases as a consequence of hemispherical spreading. TRANS_SIM allows for propagation of the acoustic pulse in one medium or across an interface between two media of different acoustic velocities. In the case of two materials, the transducer is oriented normal to the interface. Thus, the target plane at which the resultant pulse is calculated is always perpendicular to the transducer's central axis.

Figure 3-26 shows an rf pulse input for the program. The center frequency of this pulse is 10 MHz. Figure 3-27 shows two different outputs using the waveform of Figure 3-26. Figure 3-27a shows the amplitude (gray scale) versus time and position (parallel to the transducer's face) for a 13 mm (0.5 in) diameter, 76 mm (3.0 in) focal length transducer. Figure 3-27b is an analogous plot for a 25 mm (1.0 in) diameter, 76 mm focal length transducer.
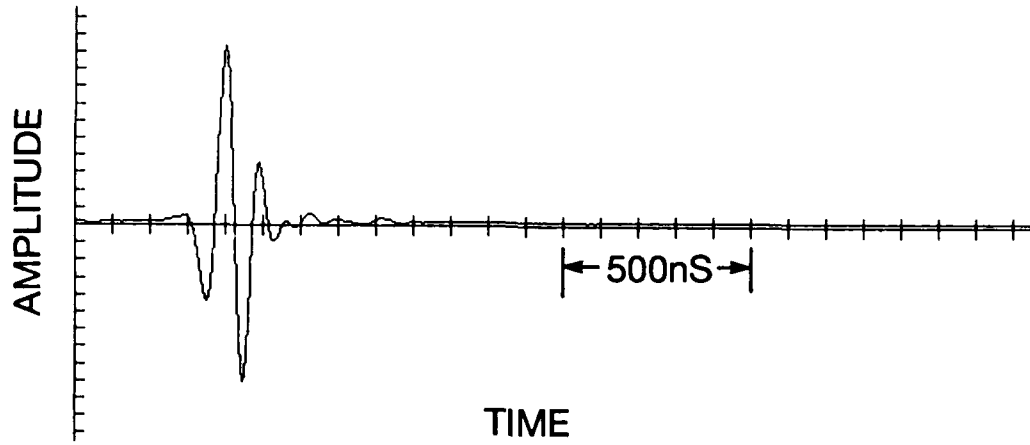
Figure 3-26.   Typical rf A-scan (10 MHz) used as input to the
                transducer simulation program, TRANS_SIM.
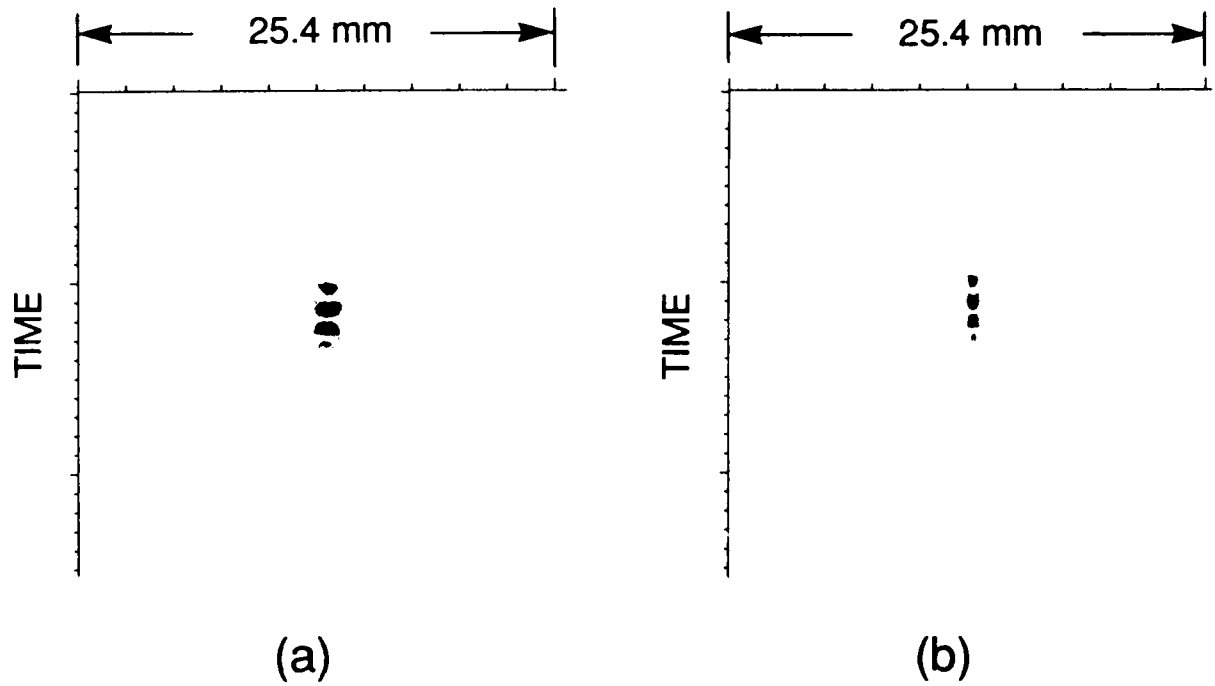
Figure 3-27.   Rf B-scan outputs from the transducer modeling program,
                TRANS_SIM showing amplitude (gray levels) versus time
                and position at the transducer's focal point: (a) 10 MHz,
                12.7 mm diameter, 76 mm focal length transducer; (b) 10 MHz,
                25.4 mm diameter, 76 mm focal length transducer.

Note that the 25 mm diameter transducer produces a beam with a smaller width at the focal plane.

3.6   LEAKY LAMB WAVE INSPECTION OF BIAXIAL COMPOSITES

Experimental and theoretical studies have demonstrated that Lamb waves are sensitive to a variety of defects in unidirectional graphite-epoxy composite materials[24-26]. Some of the defects in unidirectional composites which have been successfully imaged with Lamb wave techniques include: delaminations, porosity, fiber misorientation, ply drops, variations in fiber volume and debonding of composite structures[24-26]. However, most graphite-epoxy composites in use today are multi-directional. Thus, Lamb-wave imaging techniques must be extended to multi-directional composites before they can be transitioned to field use. The study described here represents the first steps of that extension, i.e., the investigation of the applicability of Lamb wave techniques to biaxial (two-directional) graphite-epoxy composites[27].

The transducer configuration (Figure 3-28) and the instrumentation setup (Figure 3-29) used for the study were those which had proven to be the most successful in a previous Lamb wave study[26]. Lamb waves were generated by the swept-frequency tone-burst technique which had been shown by that study to yield better signal-to-noise ratios than other Lamb wave generation techniques. High quality C-scan images were then generated by applying the median-frequency signal processing technique[26] to the data collected at each discrete sampling point. The median-frequency technique was chosen because it produces C-scan images in which shades of gray correspond to depths of the imaged defects.

The sample used for the study was a 24 ply bidirectional graphite-epoxy composite with a $[0_2/90_2]_{3s}$ stacking sequence. Artificial defects consisting of internal ply cuts, simulated delaminations and regions of high porosity were intentionally placed in the sample to test the leaky Lamb wave imaging capabilities.

A Lamb wave C-scan image of the bidirectional sample is shown in Figure 3-30a. All defects on the left side of the image were between the eighth and ninth plies and all defects on the right side of the image were located between the sixteenth and seventeenth plies. Both defects at the top of the
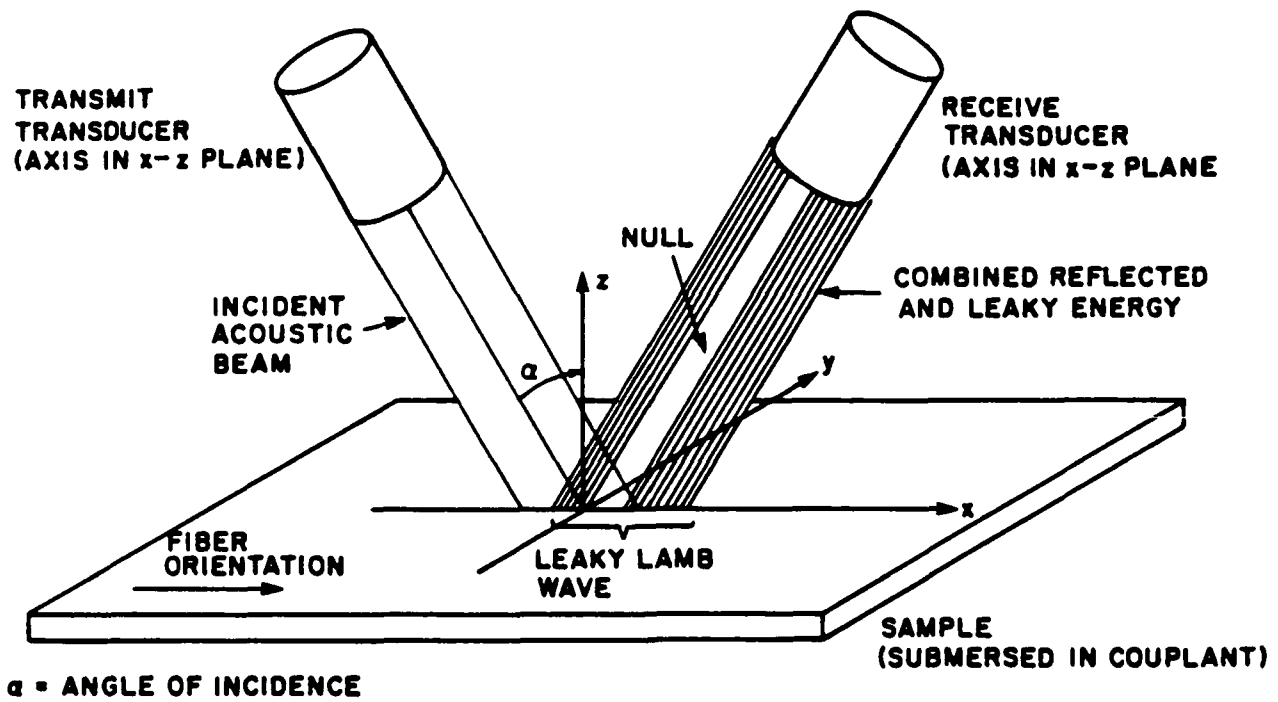
Figure 3-28. Transducer configuration for leaky Lamb wave inspection.
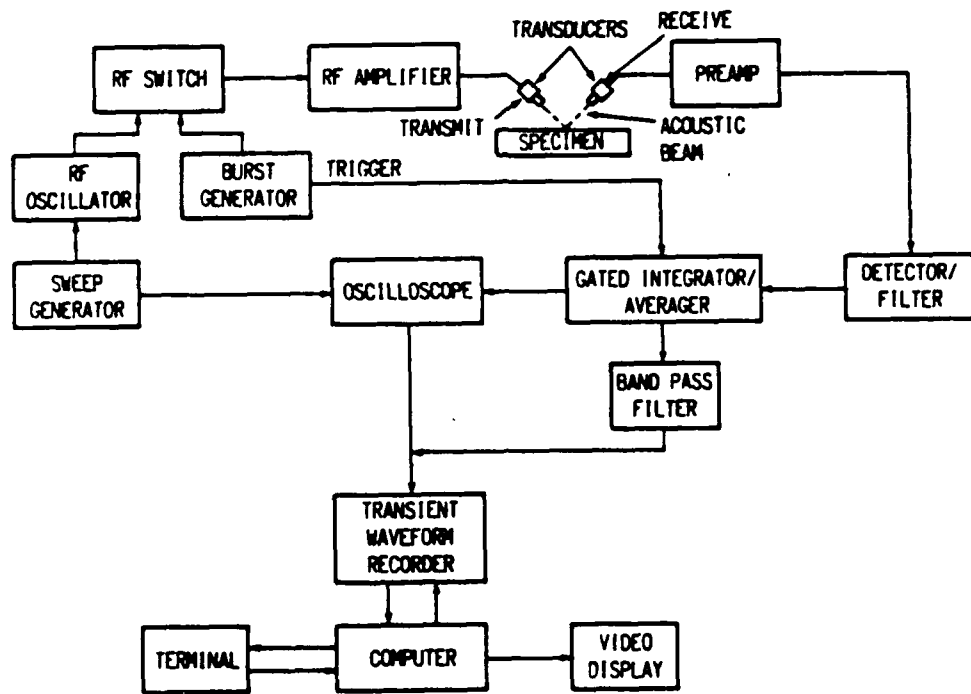
Figure 3-29. Leaky Lamb wave instrumentation.

image were 12.7 mm (0.5 in) diameter simulated delaminations. The next pair of defects from the top were 6.4 mm (0.25 in) diameter simulated delaminations. The third set of defects (from the top of the image) were 12.7 mm diameter regions of simulated porosity and the bottom-most defects were 12.7 mm wide by 3.2 mm (0.125 in) long ply cuts. The deeper simulated delaminations (top two imaged defects on the right side of Figure 3-30a) are a darker shade of gray than are the corresponding shallower simulated delaminations (left side of Figure 3-30a). This encoding of depth in shades of gray is a consequence of using the median-frequency signal processing technique for image generation. Defect-free regions of the panel are black because they represent the maximum panel thickness. The porosity and ply cuts do not conform to the same gray-scale pattern because they interact with only a small portion of the ultrasonic beam.

A normal-incidence C-scan image of the same panel is shown in Figure 3-30b. The data were acquired by pulse-echo techniques using a 10 MHz, 76 mm (3.0 in) focal length, 12.7 mm (0.5 in) diameter transducer. This normal-incidence technique imaged the delaminations, but did not image the porosity or the ply cuts. Also, gray scale is not proportional to defect depth in Figure 3-30b.

This study has demonstrated that leaky Lamb waves can be used to image simulated delaminations, porosity and ply cuts in bidirectional graphite-epoxy composites. Also, the median-frequency signal processing technique has been successfully applied to Lamb wave data acquired from bidirectional composites. The interested reader is referred to the article, "Leaky Plate Wave Inspection of Biaxial Composites," in Appendix A.

BETWEEN 8th & 9th PLIES BETWEEN 16th & 17th PLIES BETWEEN 8th & 9th PLIES BETWEEN 16th & 17th PLIES

12.7 mm SIMULATED DELAMINATIONS

6.4 mm SIMULATED DELAMINATIONS

6.4 mm SIMULATED POROSITY

12.7 x 3.2 mm PLY CUTS

(a)

(d)
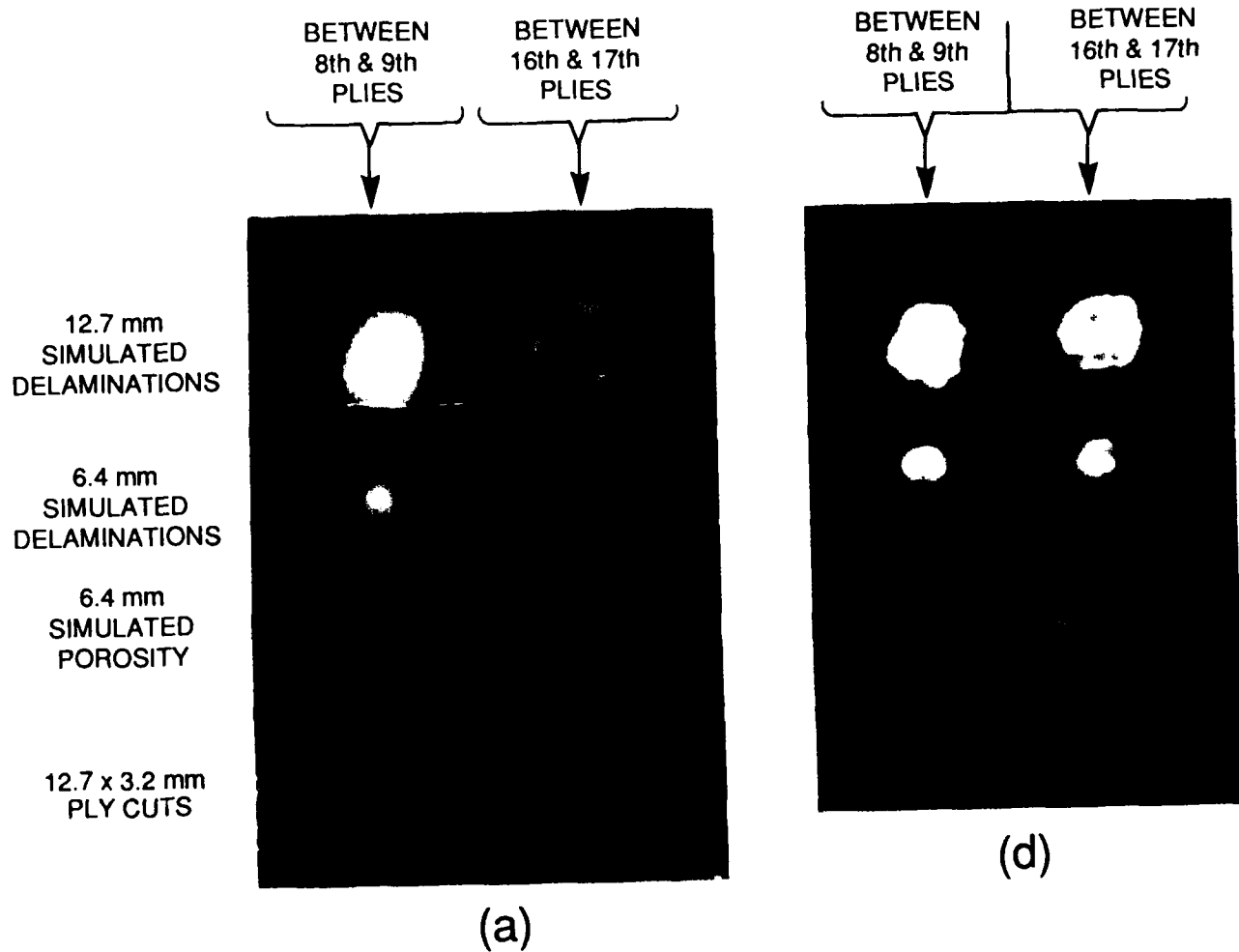
Figure 3-30.   Ultrasonic C-scan images of bidirectional test panel using:
(a) Leaky Lamb waves with median-frequency signal processing;
(b) Normal-incidence, pulse-echo techniques.

SECTION 4

RECOMMENDATIONS

Significant improvements in ultrasonic imaging of defects have been achieved by using the techniques described in Section 3 of this report. Improvements in depth resolution have resulted from use of software gating, entry-surface-echo subtraction, axial Wiener deconvolutions and one-dimensional power spectrum equalization techniques. Lateral resolution has been improved by spatial-domain implementation of Marr-Hildreth enhancement techniques, and Fourier-domain implementation of two-dimensional Wiener deconvolutions and two-dimensional power spectrum equalization. Leaky Lamb wave techniques have been used to image defects in bidirectional graphite-epoxy composites.

Significant progress has been made, but much still remains to be accomplished. The improvements in depth and lateral resolution must be applied to defects which lie far (as much as 2 cm) below the entry surfaces of advanced aerospace materials such as graphite-epoxy composites and metal-matrix composites. Leaky Lamb wave techniques must be extended to more complex layups in graphite-epoxy composites and must be extended to metal-matrix composites if they are to reach the practical applications phase. Many of the techniques need to be modified or incorporated in digital signal processing (DSP) chips to allow their use in high-speed NDE data acquisition and near-real-time processing applications. The following recommendations specifically address the needs discussed above.

Transition the Technqiue for Generating C-Scan Images from Software-Gated Rf A-Scans

Use of this techniqe provides: (1) excellent depth resolution, (2) the ability to detect and image features in the "dead zone" of a transducer and (3) the ability to simultaneously image features in the "dead zone" of the transducer and deep within a material. Thus, the technique should have broad applicability in field inspection applications. The availability of high-speed digitizers (up to 500 MHz) in certain commercial ultrasonic instruments makes it both possible and practical to use this technique in inspection

situations outside the laboratory. We are, therefore, recommending that this technique be transitioned to field use.

Improve the Depth Resolution in Images of Thick Aerospace Materials

The axial Wiener deconvolution technique should be extended to improve depth resolution of ultrasonic imaging techniques in thick aerospace materials. To do this, methods must be developed for obtaining reference waveforms for deconvolving echoes from deep within quasi-isotropic graphite-epoxy composites, woven fabric composites and metal-matrix composites.

The one-dimensional axial power spectrum equalization technique should also be extended to improve depth resolution of ultrasonic imaging techniques in thick aerospace materials. The improvements in depth resolution obtained by using power spectrum equalization methods should be compared with analogous improvements obtained through use of axial Wiener deconvolutions.

Improve the Lateral Resolution in Images of Thick Aerospace Materials

Digital image enhancement and restoration techniques should be applied to ultrasonic C-scan images of planes which lie far below the entry surfaces of advanced aerospace materials. Techniques such as Marr-Hildreth enhancement, two-dimensional Wiener deconvolutions and two-dimensional power spectrum equalization should be tested for their ability to reduce blur in those C-scan images. Methods for estimating the correct sizes for the standard deviations in the Marr-Hildreth operator must be developed. Special consideration must be given to methods for obtaining a suitable reference C-scan image of the ultrasonic beam shape (point-spread function) at the required depths in the materials being examined. This reference C-scan image is required for two-dimensional Wiener deconvolutions.

Pseudo three-dimensional methods for improving depth and lateral resolution must be developed for improving ultrasonic images of regions which lie far below the entry surfaces of aerospace materials. Pseudo three-dimensional Wiener deconvolution and pseudo three-dimensional power spectrum equalization are two methods which should be developed for that purpose.

Entry-surface features are often superimposed on the ultrasonic C-scan images of planes far below the entry surface. Techniques need to be developed to remove those entry-surface features from images of subsurface planes.

Literature sources should be reviewed to determine the most suitable methods for initial investigations of entry-surface feature removal techniques.

Extend Leaky Lamb Wave Methods to More Complex Materials

Leaky Lamb wave techniques have been used to image simulated defects in bidirectional graphite-epoxy composite materials. However, most practical applications require more complex stacking sequences. Thus, for practical applications the leaky Lamb wave techniques must be extended to include graphite-epoxy composites with more complex stacking sequences such as quasi-isotropic layups. The leaky Lamb wave techniques must also be extended to other materials, e.g., metal-matrix composites.

Increase Data-Acquisition Speed

The speed of the software-gated rf A-scan data acquisition technique must be increased. To achieve the speed increase, the technique of stopping the scanning motion during waveform digitization must be replaced with waveform digitization during continuous-motion scanning. Faster methods for transferring data from the digitizer to memory must also be explored.

Axial Wiener deconvolution and power spectrum equalization of rf A-scans should be implemented in digital signal processing (DSP) chips. This would allow the deconvolution and power spectrum equalization techniques to be implemented during scanning. Software gates could then be applied to the processed waveforms to obtain C-scan image data, thus eliminating the necessity for storing thousands of digitized rf waveforms in the computer.

Combine Information from Different NDE Sources

Studies should be conducted to develop algorithms for combining information from a variety of NDE methods. The combination of data from different NDE techniques should provide more information about material properties and defects than data from a single NDE technique. Ultrasonics, thermal wave imaging and X-ray computed tomography are candidate NDE methods for developing hybrid information.

REFERENCES

1. Buynak, C.F. and Moran, T.J., "Characterization of Impact Damage in Composites," in <u>Review of Progress in Quantitative Nondestructive Evaluation</u>, edited by D.O. Thompson and D.E. Chimenti (Plenum Press, New York, 1987), Vol. 6B, pp 1203-1211.

2. Buynak, C.F., Moran, T.J., and Martin, R.W., "Delamination and Crack Imaging in Graphhite-Epoxy Composites," in <u>Materials Evaluation</u>, Vol. 47 (4), April 1989, pp 438-441.

3. Martin, R.W and Chimenti, D.E., "Swept Frequency Ultrasonic Imaging in Composite Plates," to be published in <u>Review of Progress in Quantitative NDE</u>, edited by D.O. Thompson and D.E. Chimenti (Plenum Press, New York, 1990), Vol. 9.

4. Martin, R.W and Chimenti, D.E., "Signal Processing of Leaky Lamb Wave Data for Defect Imaging in Composite Laminates," in <u>Review of Progress in Quantitative NDE</u>, edited by D.O. Thompson and D.E. Chimenti (Plenum Press, New York, 1987), Vol. 6A, pp 815-824.

5. Martin, R.W and Chimenti, D.E., "Leaky Plate Wave Inspection of Biaxial Composites," in <u>Review of Progress in Quantitative NDE</u>, edited by D.O. Thompson and D.E. Chimenti (Plenum Press, New York, 1989), Vol. 8B, pp 1663-1670.

6. McRae, K.I. and Zala, C.A., "Improved Axial Resolution of Ultrasonic B-scans by L1-Norm Deconvolution," in <u>Review of Progress in Quantitative NDE</u>, edited by D.O. Thompson and D.E. Chimenti (Plenum Press, New York, 1988), Vol. 7A, pp 747-755.

7. Liu, C.N., Fatemi, M., and Waag, R.C., "Digital Processing for Improvement of Ultrasonic Abdominal Images," <u>IEEE Transactions on Medical Imaging</u>, Vol. MI-2, June 1983, pp 361-370.

8. Castleman, K.R., <u>Digital Image Processing</u> (Prentice-Hall, Englewood Cliffs, New Jersey, 1979).

9. Gonzalex, R.C. and Wintz, P., <u>Digital Image Processing</u> (Addison-Wesley, Reading, Massachusetts, 1977).

10. Andrews, H.C. and Hunt, B.R., <u>Digital Image Restoration</u> (Prentice-Hall, Englewood Cliffs, New Jersey, 1977).

11. Lee, J., "Digital Image Enhancement and Noise Filtering by Use of Local Statistics," <u>IEEE Transactions on Pattern Analysis and Machine Intelligence</u>, Vol. PAMI-2 (2), March 1980, pp 165-168.

12. Davis, L.S., "A Survey of Edge Detection Techniques," <u>Computer Graphics and Imaging Processing</u>, Vol. 4 (3), September 1975, pp 248-270.

13. Frock, B.G., Martin, R.W., Moran, T.J., and Shimmin. K.D., "Imaging of Impact Damage in Composite Materials," in <u>Review of Progress in Quantitative NDE</u>, edited by D.O. Thompson and D.E. Chimenti (Plenum Press, New York, 1988), Vol. 7B, pp 1093-1099.

14. Iraca, D., Landini, L., and Verrazzani, L. "Power Spectrum Equalization for Ultrasonic Image Restoration," <u>IEEE Transactions on Ultrasonics, Ferroelectrics and Frequency Control</u>, Vol. 36 (2), March 1989, pp 216-222.

15. Karpur, P. and Frock, B.G., "Two-Dimensional Pseudo-Wiener Filtering in Ultrasonic Imaging for Nondestructive Evaluation Applications," in <u>Review of Progress in Quantitative NDE</u>, edited by D.O. Thompson and D.E. Chimenti (Plenum Press, New York, 1989), Vol. 8A, pp 743-750.

16. Tom, V.T., Merenyi, R.C., Carlotto, M.J., and Heller, W.G., "Advanced Enhancement Techniques for Digitized Images," in <u>Proceedings of the 15th Symposium on Nondestructive Evaluation</u>, edited by D.W. Moore and G.A. Matzkanin, April 1985, pp 68-72.

17. Frock, B.G. and Martin, R.W., "Applications of Digital Image Enhancement Techniques to the Ultrasonic NDE of Composite Materials," in <u>Acoustical Imaging</u>, edited by H.W. Jones (Plemum Press, New York, 1987), Vol. 15, pp 461-469.

18. Marr, D. and Hildreth, E., "Theory of Edge Detection," in <u>Proceedings of the Royal Society of London B</u>, Vol. 207, 1980, pp 187-217.

19. Venetsanopoulos, A.N and Cappellini, V., "Real-Time Image Processing," in <u>Multidimensional Systems, Techniques and Applications</u>, edited by S.G. Tzafestas (Marcel Dekker, Inc., New York, 1986), pp 345-399.

20. Tom, V.T., "Adaptive Filter Techniques for Digital Image Enhancement," in <u>Digital Image Processing</u>, SPIE, Vol. 528, 1985, pp 29-42.

21. Winston, P.H. and Horn, B.K.P., <u>LISP</u>, Second Edition (Addison-Wesley Publishing Company, 1984), pp 151-167.

22. Martin, R.W., "Application of Pattern Recognition Techniques to B-scan Analysis," in <u>Review of Progress in Quantitative NDE</u>, edited by D.O. Thompson and D.E. Chimenti (Plemun Press, New York, 1988), Vol. 7A, pp 777-784.

23. Andrews, R.J., et al., "Research on Advanced NDE Methods for Aerospace Structures," AFWAL-TR-87-4007, Final Report, April 1987.

24. Chimenti, D.E. and Bar-Cohen, Y., "Signal Analysis of Leaky Lamb Wave Spectra for NDE of Composites," <u>1985 IEEE Ultrasonic Proceedings</u>, edited by B.R. McAvoy, (IEEE Publishing, New York, 1986) pp 1028-1031.

25. Chimenti, D.E. and Nayfeh, A.H., "Leaky Lamb Waves in Fibrous Composites Laminates", _Journal of Applied Physics_, Vol. 58, No. 12, (December 1985), pp 4531-4538.

26. Martin, R.W. and Chimenti, D.E., "Signal Processing of Leaky Lamb Wave Data for Defect Imaging in Composite Laminates," in _Review of Progress in Quantitative NDE_, edited by D.O. Thompson and D.E. Chimenti (Plenum Press, New York, 1987), Vol 6A, pp 815-824.

27. Martin, R.W. and Chimenti, D.E., "Leaky Lamb Wave Inspection of Biaxial Composites," in _Review of Progress in Quantitative NDE_, edited by D.O. Thompson and D.E. Chimenti (Plenum Press, New York, 1989), Vol 8B, pp 1663-1670.

APPENDIX A

PUBLICATIONS DESCRIBING RESULTS OF
NDE TECHNIQUE DEVELOPMENT EFFORTS

LIST OF ARTICLES

Delamination and Crack Imaging in Graphite-Epoxy Composites

by C. F. Buynak,* T. J. Moran,* and R. W. Martin†

Abstract

Damage and defects in composites present a unique problem to the materials community. Impact damage can produce significant degradation of the material's structural integrity, with no external evidence of the subsurface defects. Ultrasonic inspection, using a software gating method, has provided a significantly increased capability of producing images of individual delaminations and defects in graphite-epoxy laminates. Advanced digitization capabilities enable investigation of the discrete locations (typically, interfaces) in a composite material for ply delaminations, cracks, and other defects.

To correlate the results obtained using the nondestructive ultrasonic method described above, destructive analyses were conducted on 32-ply, quasi-isotropic, graphite-epoxy composite panels. Thermal elimination of the epoxy matrix component, following the penetration of a gold chloride marker dye into the impact-affected regions, allowed the specimen's layers (0.005 in. [0.13 mm] thick) to be individually removed to reveal the dye-marked areas that were damaged by a calibrated impact load. Impact damage is displayed, using a C-scan format, as a function of its depth through the graphite-epoxy composite. This paper fully demonstrates the capabilities of the software gating method by showing that the impact-defect images correlate almost perfectly with the destructive macrophotos of the individual ply-interface damage zones.

Keywords: *acoustics, composite materials, delamination imaging, deply, graphite-epoxy, imaging, impact damage, nondestructive evaluation, signal processing, ultrasonic testing.*

INTRODUCTION

Some of the most critical flaws encountered during the service life of a composite component can result from impact damage due to foreign objects. Impact damage can produce significant degradation of the material's structural integrity. Destructive sectioning[1] or deplying[2] of impact-damaged laminates has shown that very often the damage is comprised of many delaminations, each of different size, shape, and ply-interface orientation through the thickness. Unfortunately, the extent of the delamination damage typically may not be identifiable from visual surface evidence. The seriousness of this problem has led to much work in both the nondestructive evaluation and mechanics communities to characterize and assess the effects of such damage.

In typical field applications, nondestructive methods such as the "coin-tap," through-transmission, and pulse-echo ultrasonic methods have been used to determine the extent of

*AFWAL/Materials Laboratory, NDE Branch, AFWAL/MLLP, Wright-Patterson AFB, OH 45433-6533, (513) 255-9802.
†University of Dayton Research Institute, Dayton, OH 45469-0001.

internal delamination damage. These methods were useful only in determining the outline of the maximum extent of all superimposed delaminations; they gave no indication of the depth and magnitude of the individual delaminations. Therefore, a technique was needed to nondestructively determine not only the maximum extent of delamination damage, but also the size and depth of individual delaminations.

More advanced ultrasonic instrumentation than is currently in common laboratory and field use can provide some damage detail as a function of depth by using multiple time gates (a hardware or software function that isolates the signal returning at a specified time delay relative to a reference) on the detected and filtered signal. However, even this instrumentation is not adequate to completely characterize the delamination pattern resulting from impact. The advent of high-speed transient recorders with the ability to efficiently digitize, store, and transfer large amounts of data has provided the capability of capturing and analyzing the entire signal without reducing the information content through the detection and filtering process. Methods have been adopted that use postprocessing of these stored waveforms to map out delaminations on individual layers. However, the large data storage requirements of such methods make them impractical for all but laboratory applications on relatively small specimens. It was found that considerably better resolution, especially in the near-surface region, is obtainable using relatively simple signal-processing methods.[3,4] This paper will report on a new ultrasonic method to nondestructively produce and display images of the damage on a ply-by-ply basis; this method requires that only a limited amount of data be collected and stored during a single scan, allowing the method to be used in both the laboratory and the field. We will discuss the equipment and procedures required for its implementation as well as the limitations inherent in its application.

SPECIMENS AND DEFECTS

To demonstrate the efficacy of our new ultrasonic methodology on a problem of practical interest, impacted specimens of graphite-epoxy composite were chosen which had multiple delaminations present as their principal flaws. The laminates used in this study were 32-ply [0/+45/−45/90]₄ₛ quasi-isotropic panels. The flat laminate panels were Hercules IM6/3501-6 graphite-epoxy composite. A 10 ft-lb (14 J) impact-energy level was selected. For this panel thickness (32 plies), this energy level is known to produce significant internal damage while displaying minimal surface deformation. These panels were impacted using the pendulum impact apparatus developed by Sjoblom.[5]

EXPERIMENTAL NONDESTRUCTIVE EVALUATION PROCEDURE

The impacted specimens were ultrasonically scanned using a specialized laboratory scanning system.[4] The specimen is scanned in a raster pattern, using a focused ultrasonic transducer. A relatively long focal length, 75–150 mm in water, is used to produce a narrow, collimated beam in the material; this procedure will give good lateral resolution. In contrast to conventional systems, the entire ultrasonic waveform is digitized at each point. No attempt is currently made to retain the entire waveform in memory because this would produce intolerably large data files. Instead, one uses prior knowledge about the material and the defects or properties being sought to select only one data point for each layer or material location of interest. For the case of a planar laminated specimen and a delamination-type defect, it is known that the defects will produce reflections that are out of phase with the input waveform and delayed in time by some integer multiple n of the round-trip transit time t for an ultrasonic wave in a single layer. Thus, the largest peak of a signal reflected from the nth interface in the composite will occur at a time delay equal to nt relative to the largest peak of the front-surface reflection (point R in Figure 1). The software gating method is based upon the fact that the principle of linear superposition holds and the maximum deviation from the relative background level will occur at time nt for a flaw in the nth layer (point indicated by the arrow in Figure 1 for a third-layer flaw); scan data collected at this point will result in an image of the flaw.

SOFTWARE DESCRIPTION

Software gating and normal hardware gating are similar in that both use time delays and gated windows to extract information from a portion of a waveform. However, software gating provides more precise control of gate positions and gate widths and greater time stability. Software gating uses less hardware, thereby reducing electrical noise or interference and also cost when a large number of gates are used.

To implement a software gated C-scan, a front-surface tracking threshold, reference point, and individual gate-delay starting and ending times must be defined. First, a radio frequency (rf) A-scan of the specimen must be digitized and its waveform displayed on the monitor. The operator then positions the cursor to a point on the slope of the front-surface echo of the waveform that represents the amplitude of a detection threshold that will indicate the location of the front surface of the specimen (point F in Figure 1). When this threshold is exceeded, the front-surface tracking algorithm will define that point in time as the location of the front surface. The location of the front-surface tracking position is determined for each rf A-scan. Front-surface tracking provides an adjustable software-generated time delay for each rf A-scan to compensate for specimen curvature and misalignments of the scan axis with the orientation of the specimen. This allows the software gates to maintain a consistent depth throughout the course of the entire C-scan. The operator must define the polarity of the waveform at the threshold as either positive- or negative-going and must also define the method of locating the threshold. The location may be found either by comparing single points on the waveform to the threshold value or by calculating and comparing a two-point moving-average value of the waveform to the threshold value. The moving-average method is usually best because this usually eliminates false threshold detection due to random single-data-point noise spikes.

Another important feature of the front-surface tracking algorithm is the ability to detect bad A-scan data due to an incorrect digitizer trigger, extreme amounts of noise, or nonspecular reflection of the sound wave. If the front-surface tracking threshold cannot be found or if the threshold is found so late in time that it would cause the last of the software gates to not be included in the digitized A-scan area, then the
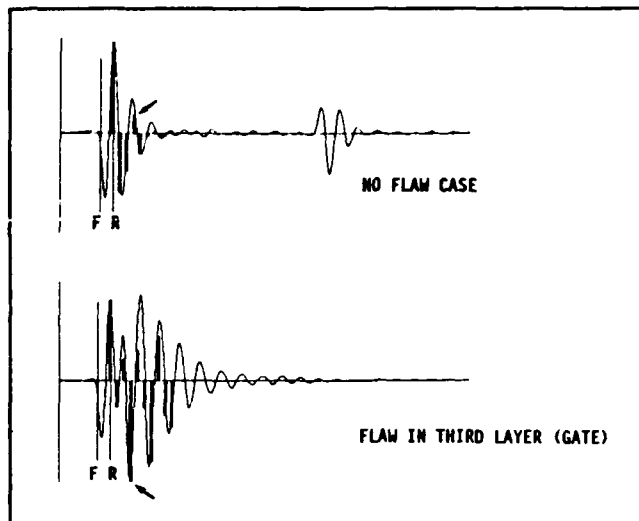
Figure 1 — Software gates and reference points for signals from flawed and unflawed locations.

scanning movement is stopped and the A-scan redigitized up to ten times in an effort to obtain correct data. If all attempts fail, then the operator is notified and asked to choose if (1) the scan should be aborted or (2) data from the previous correct A-scan should be substituted for the current A-scan data and the scanning continued. These checks provide a high confidence factor for the validity of the software gated data.

After the front-surface tracking is set, the reference point must be defined. The reference point is chosen to be the time at which the largest peak in the front-surface reflection occurs. This point is used because the corresponding peaks in reflections from known depths in the material (i.e., at ply interfaces) will occur at known times relative to the peak value of the front-surface echo (or at multiples of the round-trip transit time of the ultrasound in a single ply). This point is used as the zero point in time for computing the positions of the software gates that follow it. The reference point is defined as a fixed time delay after the front-surface tracking position and is determined by moving the cursor along the waveform to the desired position and depressing a key. The image generated from data collected at the reference point provides information on surface conditions of the specimen (i.e., presence of dents, scratches, other anomalies) that might affect the data collected on lower levels.

The operator then selects the number of software gates desired for the scan. This can be any number from 1 to 160 software gates in our present system. The gate locations may be selected by one of several methods. One method allows the operator to move the cursor along the waveform and depress a key at the starting and ending points of each software gate. The gates can be in any location or of any width and can overlap if desired. Another method of locating software gates is by calculated time delays in nanoseconds from the reference point. The operator can enter the location and width in nanoseconds of each individual gate or can specify equal spacing between all gates and the widths of all gates in a single command. For example, in a 32-ply panel, the number of gates is set to 33 and the reference point is set at the peak of the front-surface echo. The spacing between gates is then set to the round-trip travel time between adjacent ply interfaces, and the gate widths are set to a narrow range (i.e., 10–30 ns) to allow for small variations in thickness of individual plies. Usually, 512 data points are digitized on each A-scan. When the scan is completed, the result will be 32 data files, with each being a C-scan at each ply interface. The A-scan data points are not required to be saved, thus saving valuable disk and memory space.

One of several methods is selected to compute the data value in each of the software gates. These methods are mean value, peak value, minimum value, and peak-to-peak values of all data points within the gates. Peak value or minimum value (whichever is opposite to the stored reference) is most often the one of choice to detect the delamination reflections that are out of phase with the reference, but the selection depends upon the intentions of the scan. The number of data points in a gate is determined by the width of the gate in nanoseconds divided by the digitizing interval, which is usually 5 ns (200 MHz digitizing rate). The minimum and maximum data values for each of the gates' data files are also stored and used later by the C-scan display program to expand the data ranges and enhance the images.

The current system configuration is not optimized for rapid data acquisition. For example, 200 lines (200 points per line), with 33 gates and 0.015 in. (0.38 mm) step-size scans, took approximately 2 h and 15 min; 1 h and 15 min of this time was used to store the data, with the data-acquisition process stopped at the end of each line. This data storage time can be eliminated through the use of a control computer capable of processing the data as it is acquired, bringing the acquisition time down to approximately 1 h, which is comparable to the time required by conventional C-scans.
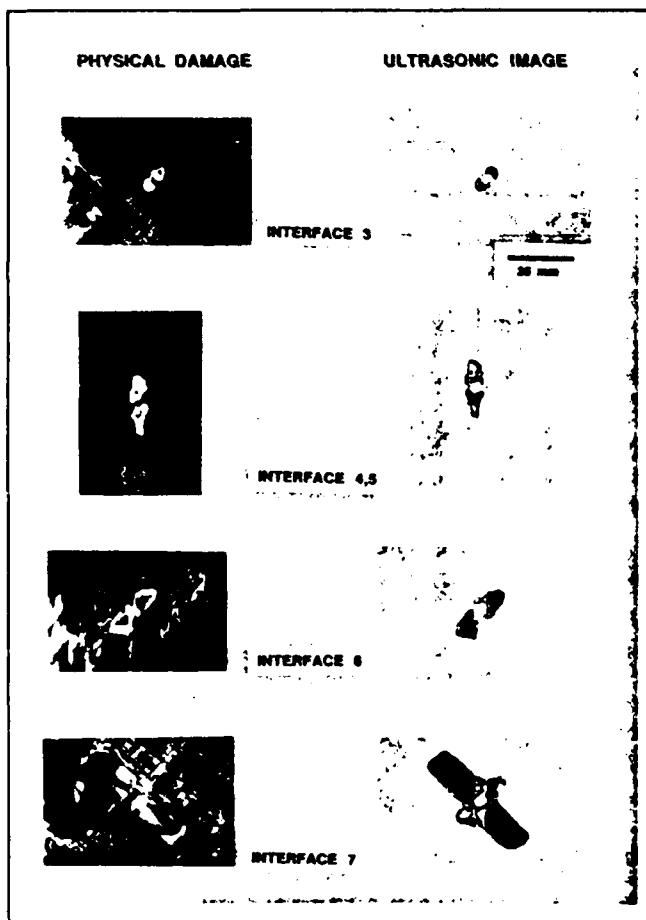
Figure 2—Ultrasonic and destructive images of delaminations produced by a 10 ft lb impact on interfaces 3; 4,5; 6; 7; where the interface number corresponds to the lower ply number. Ultrasonic data were taken with a 10 MHz, 3 in. focus transducer, 200 lines (200 points per line), 0.015 in. (0.38 mm) step size with 33 software gates. (Delaminations are shown in color, background in gray scale.) The photographs of the gold chloride residue on the surface of the graphite are of relatively poor quality because of the low contrast between the dye markings and the fiber background.
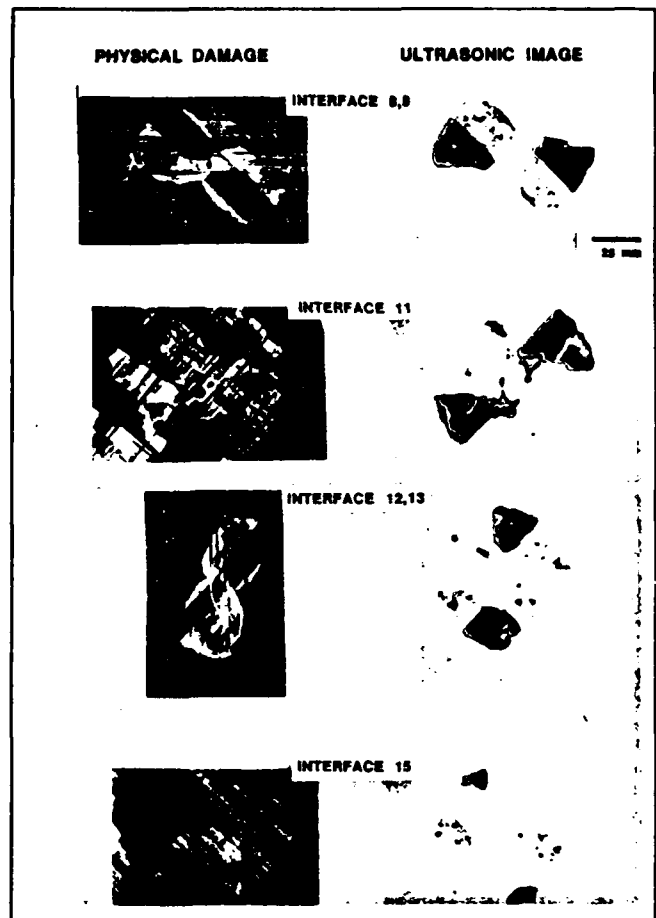
Figure 3—Ultrasonic and destructive images of delaminations on interfaces 8,9; 11; 12,13; 15. Same specimen and experimental conditions as in Figure 2.

Figure 4—Ultrasonic image of interface 7 in an 8 by 8 in. (20 by 20 cm) panel containing nine impacts. Same experimental parameters as before, with the number of data points increased to 512 by 512.

A-5

EXPERIMENTAL RESULTS

Low-velocity impact events have a distinct effect on each interface within a laminate material because such forces propagate through these materials. The size, shape, and orientation of the resultant damage are directly related to the orientation of the material's graphite fibers. As noted, the software gated ultrasonic method enables the inspector to image defects simultaneously on all depths of interest with single-ply resolution. Figures 2 and 3 display the ultrasonic images of the delaminations at the first eight interfaces in the specimen described above; the images show significant features resulting from a single 10 ft-lb (14 J) impact. Figure 2 shows the results of the damage identified in the third, (fourth,) fifth, sixth, and seventh interfaces. (Note that fiber orientation in the fourth and fifth layers is identical, nullifying any distinct interface that existed between them in the layup procedure before curing or eliminating the possibility of a delamination occurring there now because they exist as a singular unit.) These images explicitly demonstrate the ability of this technique to acquire and display data representing the intricate matrix-damage features, especially in the near-surface region. As one views the resulting images of the material's deeper layers (Figure 3), the screening effect of the delaminations on the upper layers is very evident. The images viewed in each successive layer display only lateral growth, not hidden by any previous delaminations, of the delamination "footprint." This is especially evident as one progresses deeper into the specimen (Figures 2 and 3). In the near-surface interface between plies 1 and 2, the force of the impact had no large delamination effect. Imaging in this area produced a small ($\approx$1/8 in. [$\approx$3.2 mm] dia) spot due to the impression from the impactor. This is why this interfacial image is not displayed here. Subsequent layers begin to show more detailed and interesting delaminations between layers of the graphite-epoxy composite. Some of these are not fully evident in the C-scans because of the shielding from the upper-level delaminations. In spite of the physical limitation of this ultrasonic inspection technique, excellent detailing of these material defects can be discerned.

To verify the accuracy of the software gating technique, the gold chloride marker-dye technique described by Freeman[6,7] was used to display the accurate correlation of the software gated ultrasonics data with the actual delamination damage that occurred as a result of the impact event. Following the nondestructive inspection and data acquisition, the destructive analysis was done by pyrolyzing the specimen, which had been treated with the gold chloride solution at the damage site. Upon cooling to room temperature, the individual ply layers of the composite panel were carefully separated for individual inspection. The locations where matrix damage (i.e., delaminations) occurred had a residual deposit from the gold chloride marker-dye solution. Within the composite specimen, several significant features of the impact damage became evident. The gold chloride solution was able to penetrate into the delaminations between the inner layers; this would not be possible if the delaminations were isolated on single plies. Transverse cracks[3] resulting from the impact permit delaminations to propagate through several plies. These cracks connect adjacent delaminations and allow the fluid marker dye to flow freely into the spaces created by the delaminations. After pyrolysis, one is physically able to follow the path of the destructive impact forces. The residual salt of the gold chloride dye has marked the damage path, allowing analysis of how the impact energy disturbed the material's internal structure.

The photographs of the individual layers, also shown in Figures 2 and 3, demonstrate the incredibly accurate correlation that exists between the ultrasonically generated images and the gold chloride-marked delaminations showing the actual matrix damage. (Note: the several interfaces that showed no significant damage ultrasonically showed no physical damage that would not have been masked by delaminations on upper layers.) This almost perfect replication of the damaged

zone is especially significant in the near-surface region, which has traditionally been the most difficult for ultrasound to inspect. Figures 2 and 3 permit a parallel analysis of the ultrasonic nondestructive images and the photographs of dye-marked destructive physical damage. Unique shapes and orientations of delaminations are evident at each of the different interfaces. The −45 degree linear edges of interface 7 show signs of an abrupt stop of the delamination but, through the transverse cracks, the delamination is continued in the next level (interface 8,9). At this interface, it has spread out from the crack. Most of the impact energy has continued the delamination along the lower ply direction but some has also caused delamination along the perpendicular direction. Similar features are also shown on the interface 12,13 photograph and ultrasonic image. We found that it was possible to directly image these transverse cracks by using the software gated method in conjunction with the acoustical backscatter method developed earlier.[8,9] These finer details of the material's impact-stress responses explicitly demonstrate the power of this inspection technique.

The capability of investigating the discrete failure occurrences of a destructive event that produces few or no external features enables the materials development community to understand exactly what has occurred in a damaged material. For example, Figure 4 displays the delaminations evident at the seventh interface for an 8 by 8 in. (20 by 20 cm) flat laminate graphite-epoxy panel with the same layup as before, but containing nine different impact sites. The impact activity was essentially identical for all nine impacts (10 ft-lb [14 J] load, 50 mm support ring on the back surface). Because of anomalies on the surface of this specimen, the surface tracking-gate feature of the methodology was essential to keep each gate synchronized with the topography of the front surface. This figure shows the similarities and differences in how this material disperses the energy of the impact. All the images in Figure 4 have delaminations in the same orientation (−45 degrees), that of the ply direction under the delamination. Each delamination has the same rectangular shape for this ply layup. This correlates with other impacts in other specimens of the same layup (see Figure 2, interface 7).

An example of the use of this methodology for materials behavior specialists is the information obtainable on the variability of the material response for nominally identical impact events. In Figure 4, it can be seen that there is considerable variability in the sizes of the individual delaminations. The radial extent of the delamination can vary up to 16 percent and the width can vary over 70 percent. Destructive gold chloride deply analysis was also performed on part of the specimen and is shown in Figure 5. Once again, near-perfect correlation was found with the images from the software gating nondestructive technique.

Figure 5 — Destructive image of the delamination seen in the upper right of Figure 4.

8. Hall, J. E., and J. D. Awtrey, "Real-Time Image Enhancement Using 3 × 3 Pixel Neighborhood Operator Functions," *Optical Engineering*, Vol. 19, No. 3, May/June 1980, pp 421–424.
9. Hall, E. L., R. P. Kruger, S. J. Dwyer, D. L. Hall, R. W. McLaren, and G. S. Lodwick, "A Survey of Preprocessing and Feature Extraction Techniques for Radiographic Images," *IEEE Transactions on Computers*, Vol. C-20, No. 9, Sep. 1971, pp 1032–1044.
10. Venetsanopoulos, A. N., and V. Cappellini, "Real-Time Image Processing," in *Multidimensional Systems, Techniques and Applications*, ed. S. G. Tzafestas, 1986, pp 345–399. Marcel Dekker, New York, NY.
11. Marr, D., and E. Hildreth, "Theory of Edge Detection," *Proceedings of the Royal Society of London B*, Vol. 207, No. 1167, 29 Feb. 1980, pp 187–217.
12. Moran, T. J., R. L. Crane, and R. J. Andrews, "High-Resolution Imaging of Microcracks in Composites," *Materials Evaluation*, Vol. 43, No. 5, Apr. 1985, pp 536–540.
13. Martin, R. W., and R. J. Andrews, "Backscatter B-Scan Images of Defects in Composites," in *Review of Progress in Quantitative Nondestructive Evaluation*, Vol. 5, 1986, pp 1189–1198. Plenum Press, New York, NY.

Authors

Brian Frock is a research engineer with the University of Dayton Research Institute. He received a B.A. degree in physics and mathematics from Wilmington College, Wilmington, OH, in 1965, an M.S. degree in physics from the University of Dayton in 1968, and an M.S. degree in engineering management from the University of Dayton in 1981. His research activities include image analysis, application of digital signal-processing technique for image enhancements, and design of experiments for ultrasonic data acquisition. Before joining the Research Institute in 1985, Frock worked in NDE, instrumentation, and process control at Armco Inc. for twelve years.

Richard Martin is an associate research engineer with the University of Dayton Research Institute. He earned a B.S. degree in electrical engineering in 1970 and a B.S. degree in business administration in 1972. Both degrees were received from Ohio University, Athens, OH. His responsibilities include design and implementation of hardware and software for computer control of ultrasonic data-acquisition systems as well as software development for digital signal processing, image analyses, and image enhancements. Previously, Martin was responsible for the system hardware and software design and development for microprocessor-controlled slip-ring and bearing torque experiments.

CONCLUSIONS

The significant quantitative capability of software gating of digitized ultrasonic data has been thoroughly demonstrated in this paper. The method has the ability to resolve closely spaced delaminations (0.005 in. [0.13 mm] separation), a result almost impossible using conventional low-frequency ultrasonic methods. Precision capabilities are most obviously demonstrated in the near-surface region, which was previously entirely inaccessible to low-frequency ultrasonic interrogation. Ultrasonic images match the dye-marked delaminations on individual layers almost perfectly, even down to the finest details of the impact-damage artifacts. The software gated ultrasonics allowed location and precise imaging of unshadowed delaminations that the gold chloride penetrant was able to mark.

Acknowledgments

References

1. Liu, D., L. S. Lillycrop, L. E. Malvern, and C. T. Sun, *Experimental Techniques*, Vol. 11, No. 20, 1987.
2. Guynn, E. G., and T. K. O'Brien, "The Influence of Lay-up and Thickness on Composite Impact Damage and Compression Strength," AIAA/ASME/ASCE/AHS 26th Structures, *Structural Dynamics and Materials Conference* (Part 1), Apr. 1985, pp 187–196.
3. Buynak, C. F., and T. J. Moran, "Characterization of Impact Damage in Composites," in *Review of Progress in Quantitative Nondestructive Evaluation*, Vol. 6B, ed. D. O. Thompson and D. E. Chimenti, 1987, pp 1203–1211. Plenum Press, New York, NY.
4. Buynak, C. F., T. J. Moran, and S. L. Donaldson, "Characterization of Impact Damage in Composites," *SAMPE Journal*, Mar./Apr. 1988, Vol. 24, No. 2, pp 35–39.
5. Sjöblom, P., SAMPE International Symposium, Vol. 32, 1987, p 529.
6. Freeman, S. M., "Correlation of X-Radiograph Images with Actual Damage in Graphite/Epoxy Composites by the Deply Technique," Composites in Manufacturing 3 Conference, Vol. EM84-101, 1984, pp 1–13. Manufacturing Engineers, Dearborn, MI.
7. Smith, B. T., J. S. Heyman, J. G. Moore, S. J. Cucura, and S. M. Freeman, "Correlation of the Deply Technique with the Ultrasonic Imaging of Impact Damage in Graphite/Epoxy Composites," in *Review of Progress in Quantitative Nondestructive Evaluation*, Vol. 5B, ed. D. O. Thompson and D. E. Chimenti, 1986, pp 1239–1244. Plenum Press, New York, NY.
8. Bar-Cohen, Y., and R. L. Crane, "Acoustical-Backscattering Imaging of Subcritical Flaws in Composites," *Materials Evaluation*, Vol. 40, No. 9, Aug. 1982, pp 970–975.
9. Moran, T. J., R. L. Crane, and R. J. Andrews, "High-Resolution Imaging of Microcracks in Composites," *Materials Evaluation*, Vol. 43, No. 5, Apr. 1985, pp 536–540.

Authors

Charles F. Buynak is a materials engineer with the Nondestructive Evaluation Branch of the Materials Laboratories at the USAF Wright Aeronautical Laboratories. He holds B.S. degrees in materials science engineering and chemistry and an M.B.A. in management from Wright State University, Dayton, OH. Buynak's current research interests include ultrasonic methods for application to characterization of low-velocity impact damage in composite materials.

Thomas J. Moran is leader of the in-house nondestructive evaluation research effort in the USAF Wright Aeronautical Laboratories/Materials Laboratory. He earned a B.S. in electronic physics in 1964 at St. Joseph's College, Philadelphia, PA, an M.S. in physics at the University of Pennsylvania, Philadelphia, in 1965, and a Ph.D. in physics in 1971 at Rutgers University, New Brunswick, NJ. His current research interests involve application of advanced signal-processing techniques to ultrasonic inspection of composites.

Richard W. Martin is an associate research engineer with the University of Dayton Research Institute. He earned a B.S. degree in electrical engineering in 1970 and a B.S. degree in business administration in 1972, both from Ohio University, Athens. His responsibilities include design and implementation of hardware and software for computer control of ultrasonic data-acquisition systems as well as software development for digital signal processing and image enhancement.

SIGNAL PROCESSING TECHNIQUES FOR IMAGING IMPACT DAMAGE IN COMPOSITES

B. G. Frock, R. W. Martin
The University of Dayton
Research Institute
Dayton, Ohio   USA

T. J. Moran
AFWAL/Materials Laboratory
Wright-Patterson AFB, Ohio   USA

ABSTRACT

Three different signal processing techniques
have been applied to the ultrasonic
interrogations of impact damaged quasi-
isotropic graphite/epoxy composites. The
capabilities of the techniques for imaging the
extent of impact damage near the entry surface
in composite materials are discussed and
compared. The first technique uses multiple
gates to acquire data from the rectified and
filtered versions of the ultrasonic pulse echo
A-scans. The second technique uses multiple
software gates to digitize and store data
directly from the Rf A-scans while the sample is
being raster scanned. The third technique uses
multiple software gates to digitize and store
data from the results of Wiener deconvolutions
of the Rf A-scans. Application of the third
technique requires that the Rf waveforms be
digitized and stored in the computer.

Significantly less blurring is present in images
generated from gated Rf A-scans than in images
generated from rectified and filtered A-scans.
Even less blurring is present in images
generated from Wiener deconvolved A-scans than
in images generated from gated Rf A-scans. The
Wiener deconvolution process also reduces the
background noise level. These reductions in
depth-wise blurring and background noise level
lead to significant improvements in the ability
to define the extent of damage near the entry
surface of a graphite/epoxy composite panel.

ULTRASONIC C-SCAN IMAGING TECHNIQUES can be used
to determine the boundaries of impact damage at
interfaces in graphite/epoxy composites. If
conventional methods are used, the C-scan images
are generated from data acquired at specific
"gated" locations along rectified and low-pass
filtered A-scans. Placing the gates at temporal
locations which correspond with interfaces
should allow the integrity of the interfaces to
be examined. However, if the interfaces are
closely spaced, as is the case for quasi-
isotropic graphite/epoxy composites, the
information from adjacent layers will be blurred
together. There are two reasons for this
blurring. First, the duration of the Rf pulse
from the transducer is finite and may extend
(ring) through several interfaces. Second, the
process of rectifying and low-pass filtering the
A-scans causes additional temporal or depth-wise
blurring and destroys phase information. The
combination of these effects results in blurring
at and below the first interface. This blurring
makes precise definition of the boundaries of
damage at specific interfaces very difficult.

These blurring effects can be reduced by
acquiring data directly from the Rf waveform.
Although the echoes from adjacent interfaces may
still overlap, the C-scan images which are
generated from Rf signals that are gated at the
interface locations are less affected by depth-
wise blurring than are the C-scan images
generated from the rectified and low-pass
filtered A-scans[1,2]. Significant depth-wise
blurring may still exist at lower frequencies,
however, leading to imprecision in the
definitions of the boundaries of damaged regions.

The application of the one-dimensional
Wiener filter deconvolution process to Rf A-scans
decreases the finite time duration of the Rf
echoes and, thus, decreases the depth-wise
blurring. Collecting data from gates placed at
the appropriate locations along the axially
deconvolved A-scans should allow more precise
definitions of the boundaries of the damage at
specific ply interfaces. The boundary definition
should be more precise than that which is
achievable with either the gated rectified and
filtered A-scans or the gated Rf A-scans.

WIENER FILTER DECONVOLUTION

The deconvolution technique utilized for
this work is known as constrained deconvolution

or Wiener filtering[3-6]. It assumes that the measured signal from the reflector, y(t), is a convolution of the overall system response, h(t), and the flaw response, s(t), or

$$y(t) = h(t) * s(t) \qquad (1)$$

where h(t) is obtained by recording a reference waveform from a planar reflector. The measured signals, y(t) and h(t), are transformed into the frequency domain and the flaw spectral response is calculated from

$$S(\omega) = \frac{Y(\omega)H^*(\omega)}{|H(\omega)|^2 + K^2} \qquad (2)$$

where $H^*(\omega)$ is the complex conjugate of $H(\omega)$ and K is a constant. Noise in $S(\omega)$ is minimized when $H(\omega)$ is zero or very small by setting K to a predetermined percentage of the maximum amplitude of $H(\omega)$.

SAMPLE

The sample used in this study is a 32-ply thick, quasi-isotropic graphite/epoxy composite. Prior to ultrasonic inspection, it had been intentionally damaged by a 5.4 joule impact from a 12.7 mm diameter stainless steel ball on a pendulum impacter.

DATA COLLECTION

A computer controlled ultrasonic immersion C-scanning system was used to collect data at each of 6400 discrete points in a 40 mm by 40 mm square area surrounding the impact damage site. The separation between discrete data collection points was 0.5 mm in each planar direction. A 5 MHz center frequency, 12 mm diameter, 76 mm focal length transducer was used for all data collection, with excitation for the transducer provided by a broadband spike pulse.

GATED RECTIFIED/FILTERED A-SCANS - Data from a gate on the rectified and low-pass filtered A-scans were digitized and stored using 8-bit resolution at each of the 6400 discrete sampling points around the damage site. The gate was positioned at the approximate location of the interface between the second and third plies (about 0.25 mm below the entry surface), and the average value in the gate was digitized and stored at each of the discrete locations. A rectified and low-pass filtered A-scan with the gate superimposed is shown in Fig. 1.

RF A-SCANS - Rf A-scans (512 points long) were digitized and stored using 8-bit resolution at all 6400 discrete points around the damage site. These digitized Rf A-scans were used for direct generation of C-scan images from the Rf data and for axial Wiener deconvolutions[6] followed by C-scan image generation. A reference A-scan (Rf echo from the front surface of a flat plexiglas plate) was collected and stored for use during the Wiener deconvolution process. The reference echo and its Fourier amplitude spectra are shown in Fig. 2.
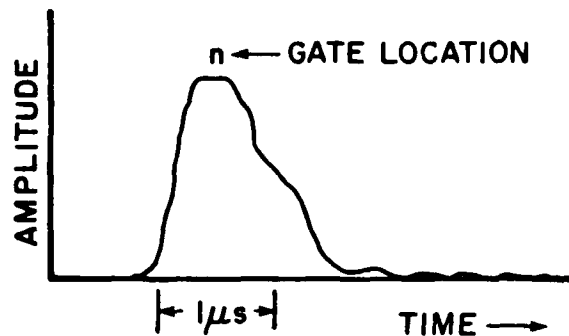
(a)
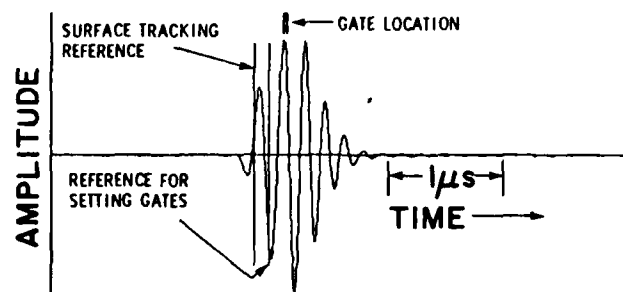
(b)
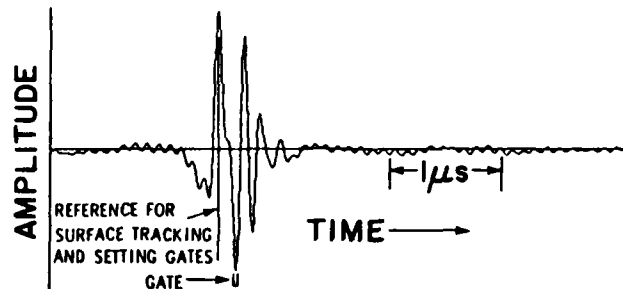
(c)

Fig. 1. Gating for C-scan image generation:
(a) rectified and filtered A-scan;
(b) rf A-scan; (c) deconvolved A-scan.

(a)

FREQUENCY (MHz)
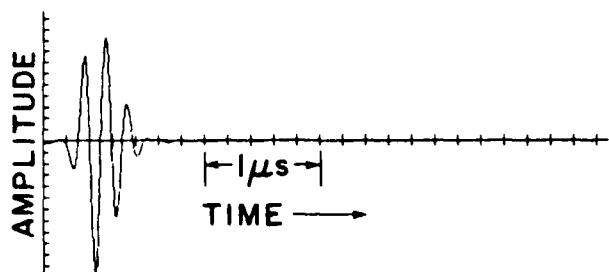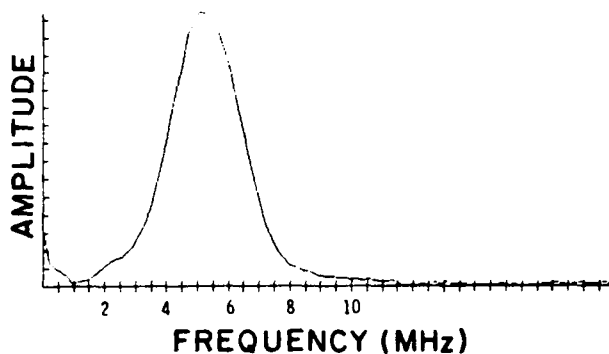
(b)

Fig. 2. Reference A-scan: (a) rf A-scan;
(b) Fourier amplitude spectra of "a".

C-SCAN IMAGE GENERATION

GATED RECTIFIED AND FILTERED A-SCANS - C-scan images were generated in the standard manner from the gated data after completion of the scan.

GATED RF A-SCAN METHOD - This technique is analogous to gating the raw Rf A-scan during scanning, except that in the present case the Rf A-scan had already been digitized and stored in the computer. Peak signal levels were collected and stored from a gate located over a 40 nanosecond-wide region of the A-scan (see Fig. 1a). This location corresponded with the location of the interface between the second and third plies. The C-scan image generated from that data provided information concerning the structural integrity of the interface.

GATED WIENER DECONVOLVED A-SCAN METHOD - All 6400 of the Rf A-scans were deconvolved using a Wiener filter of the form given in Eq. (2). The amplitude cut-off, K, was set at 0.5% of the maximum amplitude of $H(\omega)$ because of the very low noise level of the Rf A-scans. Phase reversal of the echoes from the delaminated interfaces yielded a negative-going spike in the deconvolved

A-scan at the echo return locations. Thus, the minimum value of the portion of the deconvolved A-scan which was within an appropriately placed 40 nanosecond-wide gate (see Fig. 1b) was collected from each of the 6400 deconvolved A-scans and stored in the computer. A C-scan image of the interface between the second and third plies was then generated from the data[7].

RESULTS

C-scan images of the interface between the second and third plies (measured from the entry surface) are shown in Fig. 3. The images in
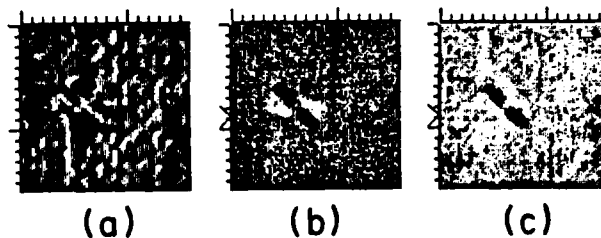
Fig. 3. C-scan images: (a) from rectified and filtered A-scan; (b) from rf A-scan; (c) from deconvolved A-scan.

Fig. 3a, 3b and 3c were generated from the rectified and filtered A-scans, the gated Rf A-scans and the Wiener deconvolved A-scans, respectively. The delamination between the second and third plies is difficult to resolve from the background in the C-scan image generated from the rectified and filtered A-scans (Fig. 3a). However, that delamination is easily resolved in the C-scan images generated from the gated Rf A-scans and from the Wiener deconvolved A-scans as the dark somewhat peanut-shaped object. The lighter regions on either side of the second-to-third ply interface delamination in the gated Rf and Wiener deconvolved images are "precursors" of the delaminations at the interface between the third and fourth plies. These "precursors" are more evident in the C-scan image generated directly from the Rf A-scans and are a result of the "ringing" of the transducer. This "ringing" is partially removed by the deconvolution process.

Plots of the individual pixel amplitudes along selected horizontal lines in the C-scan images are shown in Fig. 4. Figure 4 demonstrates that the general signal-to-background level is significantly higher for the C-scan image generated from gated Rf A-scans than is the signal-to-background level for the C-scan image generated from gated rectified and filtered A-scans. The signal-to-background level is even higher for the C-scan image generated from the gated Wiener
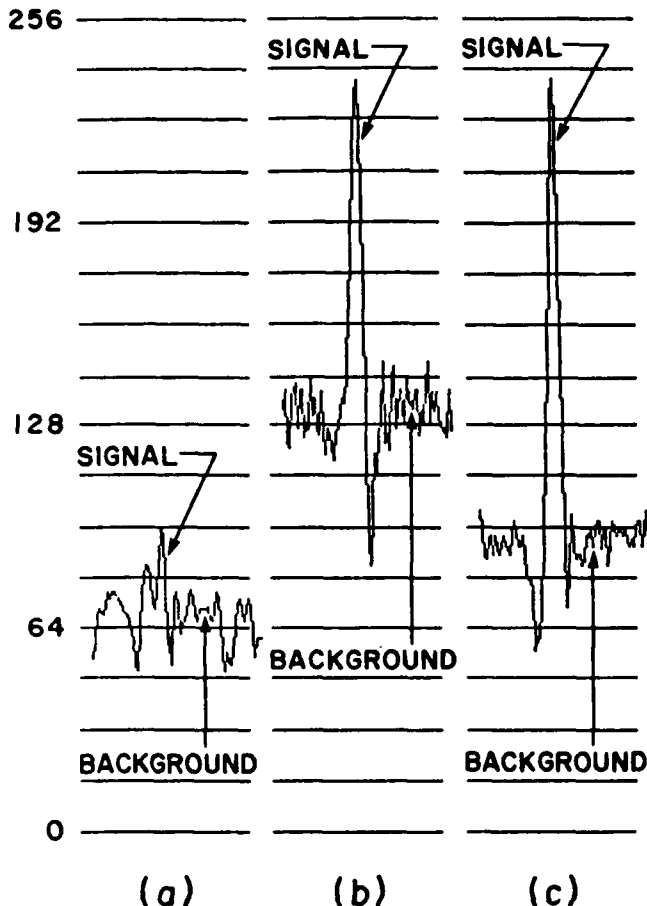
Fig. 4. Pixel amplitude plots from line 45 of
C-scan images: (a) from rectified and
filtered A-scan; (b) from rf A-scan;
(c) from deconvolved A-scan.

deconvolved A-scans than is the signal-to-background level for the C-scan image generated from the gated Rf A-scans. In these cases, the "signal" is defined as the pixel amplitude in the delaminated region and the "background" is defined as the pixel amplitude everywhere else. The higher signal-to-background level greatly improves the ability to precisely define the boundaries of the damaged regions at the interrogated interface.

The rectified and filtered A-scans, the Rf A-scans, and the axially deconvolved A-scans from two locations (one "signal" and one "background") along line 35 of the C-scan images are shown in Figs. 5 and 6. The locations of the "gates" are superimposed on each of the A-scans. The dynamic range of the portion of the Rf A-scan which lies within the gated region is significantly larger than the dynamic range of the portion of the rectified and filtered A-scan which lies within the gated region. The dynamic range of the portion of the deconvolved A-scan which lies within the gated region is greater than the dynamic range of the portion of the Rf A-scan which lies within the gated region. It is these differences in the
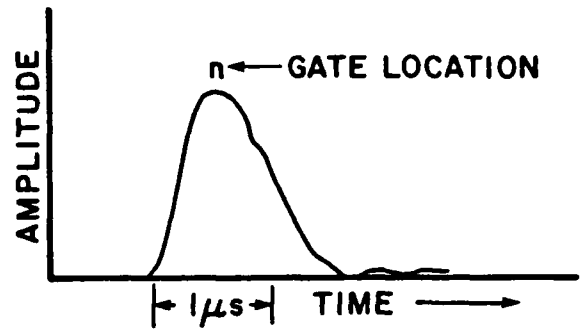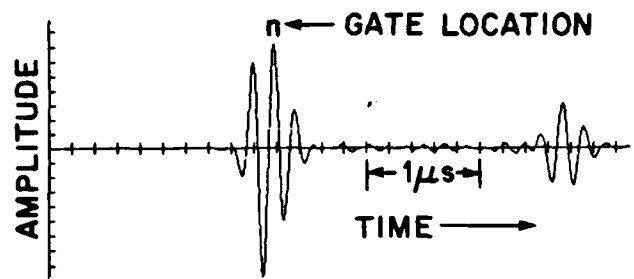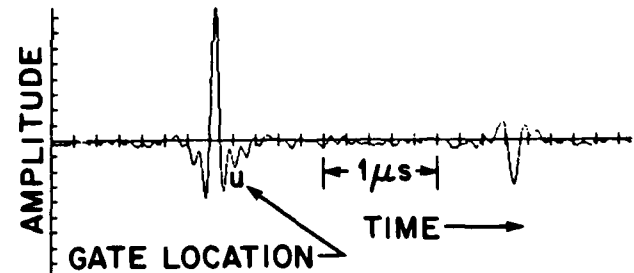
Fig. 5. A-scans from background region of
C-scans: (a) rectified and filtered
A-scan; (b) rf A-scan; (c) deconvolved
A-scan.

dynamic ranges which cause the different signal-to-background levels in the C-scan images generated from the three different types of A-scans.

A second advantage of the C-scans generated from Wiener deconvolved A-scans relative to the C-scans generated from the gated Rf A-scans is the lowered "noise" level which is superimposed on the "signal" and "background" regions of the images. This can be seen in the pixel amplitude plots in Fig. 4 and the Fourier amplitude spectra in Fig. 7. The Fourier amplitude spectra are from line number ten (a "background"

A-11
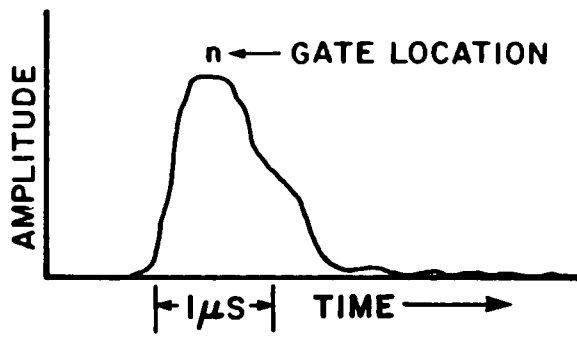
(a)
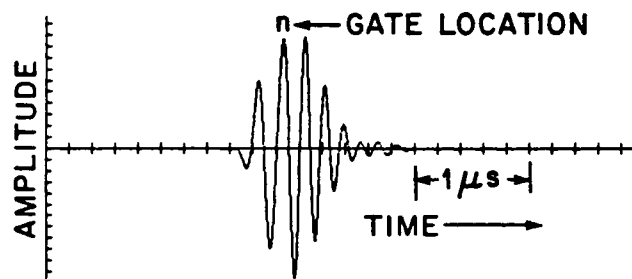
(b)
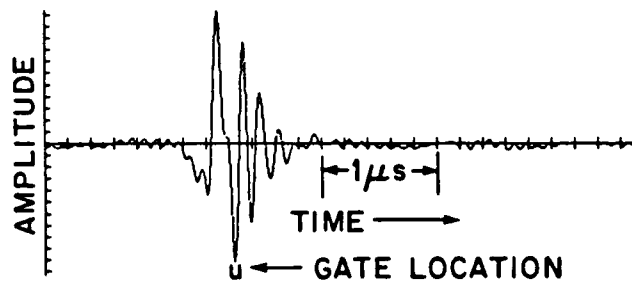
(c)

Fig. 6. A-scans from signal region of C-scans:
(a) rectified and filtered A-scan;
(b) rf A-scan; (c) deconvolved A-scan.

(a)

(b)

Fig. 7. Fourier amplitude spectra of line 10
from C-scans in Fig. 3: (a) from image
in Fig. 3b; (b) from image in Fig. 3c.

region) of the C-scan images in Fig. 3. The
Fourier amplitude spectra of line 10 of the
C-scan data generated from the Rf A-scans has
more energy in the high spatial frequency region
than does the spectra of line ten of the
C-scan data generated from the deconvolved
A-scans. The lower noise level allows for a
more precise definition of the delaminated
regions and for better visual definition of
other features such as the fiber tows.

CONCLUSIONS

The signal-to-background level ratio in the
C-scan image generated from the gated Rf A-scans
is significantly greater than is the signal-to-
background level ratio in the C-scan image
generated from the gated rectified and filtered
A-scans. This is primarily due to the temporal
blurring and loss of phase information which
results from rectification and low-pass
filtering. The higher signal-to-background
level ratio in the C-scans generated from gating
the Rf A-scans allows for a more precise
definition of the boundaries of the delamination
in those C-scan images.

Deconvolution removes some of the "ringing"
in bandwidth-limited ultrasonic pulses. This
decreased "ringing" in the deconvolved waveforms
leads to a greater dynamic range between the
"signal" regions and the "background" regions of
C-scan images generated from these deconvolved
waveforms than for C-scan images generated
directly from the Rf waveforms. The
deconvolution process also performs some
smoothing which results in less "noise" being
superimposed on the "signal" and "background"

regions of the C-scan images generated from the deconvolved waveforms. The greater dynamic range and the noise suppression which result from the deconvolution process allow more precise visual and machine definition of the boundaries of damaged regions in impacted graphite/epoxy composites.

ACKNOWLEDGMENTS

REFERENCES

1. Buynak, C. F. and T. J. Moran, "Review of Progress in Quantitative NDE," 6B, 1203-1211, edited by D. O. Thompson and D. E. Chimenti, Plenum Press, New York (1987).

2. Buynak, C. F., Moran, T. J. and S. Donaldson, Sampe Journal 24 (2), 35-39 (March/April 1988).

3. Neal, S. and D. O. Thompson, "Review of Progress in Quantitative NDE," 5A, 737-745, edited by D. O. Thompson and D. E. Chimenti, Plenum Press, New York (1986).

4. Furgason, E. S., Twyman, R. E., and V. L. Newhouse, "Proceedings DARPA/AFML Review of Progress in Quantitative NDE," AFML-TR-78-55, 312 (1978).

5. Murakami, Y., Kuri-Yakub, B. T., Kino, G. S., Richardson, J. M. and A. G. Evans, Applied Physics Letters 33 (8), 685-687 (October 1978).

6. Liu, C. N., Mostafa, F. and R. C. Waag, IEEE Transactions on Medical Imaging MI-2, 66-75 (June 1983).

7. Smith, B. T., Heyman, J. S., Moore, J. G. and S. J. Cucura, "Review of Progress in Quantitative NDE," 5B, 1239-1244, edited by D. O. Thompson and D. E. Chimenti, Plenum Press, New York (1986).

SWEPT FREQUENCY ULTRASONIC IMAGING IN COMPOSITE PLATES

Richard W. Martin
University of Dayton Research Institute
Dayton, Ohio 45469

Dale E. Chimenti
Air Force Materials Laboratory
Wright-Patterson Air Force Base, Ohio 45433

INTRODUCTION

Conventional ultrasonic C-scan imaging normally employs focussed transducers excited by high-voltage impulsive signals. The reflected wave train, containing information about the internal features of the test piece, is translated, either through analog or digital means, to an intensity (or color) and plotted as a function of transducer position on the sample. While this method is certainly effective for many inspections, it is not the only way, or perhaps even the best way, to obtain this kind of information. The purpose of this paper will be to describe an alternate means to acquire ultrasonic C-scan data using a swept-frequency tone-burst imaging technique which presents several important advantages over more conventional means.

This technique has been applied in the standard C-scan geometry to normal incidence reflection waveforms from various types of defects or material discontinuities in fiber-reinforced composites. We use digital signal processing methods to analyze the reflection data and, subsequently, to generate C-scan images which represent defect size, depth, and (x,y) location. The defects in this study consist of impact-generated delaminations in both woven and quasi-isotropic graphite-epoxy plates.

Ultrasonic inspection of composites is a large and active field to which many investigators have contributed over the past dozen years. In addition to an extensive literature on modeling and measurements, much has been written on the application aspects of this problem. While there is not sufficient space here for a full review of the field, recent theoretical contributions have substantially extended appreciation of guided wave behavior in layered plates of anisotropic materials, both in vacuum and immersed in a fluid [1-4]. These calculations have responded to the growing body of experimental results [1,4-6], only a few of which are cited here. Moreover, much applied work has appeared [6-14] on this topic because of its importance to manufacturing quality assurance and in-service NDI.

INSPECTION GEOMETRY

The beam of a focussed (75 mm focal length, 12.5 mm diameter) ultrasonic transducer (8 MHz center frequency) is directed at normal incidence onto the surface of a plate immersed in water. The

transducer is excited with a radio frequency (rf) tone-burst whose frequency is swept over the range of about 4 to 12 MHz in 25 milliseconds. The modulation of the rf signal is provided by a 20 Hz triangular waveform which linearly ramps the frequency of the rf generator during each half cycle. Therefore, the rf is essentially constant in frequency over each tone burst, but varies from burst to burst. Tone burst frequency modulation enables us to acquire the test specimen's ultrasonic reflection properties over the full transducer bandwidth. The duration of an individual tone burst (5-30 μsec) is chosen to excite the sample in a quasi-cw fashion (ie. to allow overlap among multiple front and back surface reflections). The resulting constructive and destructive interference of the reflected signal leads to a pattern of peaks and nulls generated in the rf spectrum.

The transducer is operated in the Transmit/Receive mode to acquire the reflected signal from each tone burst. The received signal is amplified, video-detected and filtered. The rf envelope is then sampled and averaged by a boxcar integrator, as shown in Fig. 1, whose aperture is placed in the overlap region of the signal. The output of the integrator is proportional to the signal envelope amplitude and represents the spectral magnitude characteristics of the sample. After filtering to remove any artifacts of the frequency sweep, the signal is sampled with a digitizer at a rate of several kHz. Although the instrument used in this study has a vertical resolution of only 8 bits, at such low sampling rates digitizers capable of much higher resolution could be substituted.

Capturing the rf reflection spectrum as a time domain signal permits further processing to recover a more familiar representation. Results for a 32-ply [0/45/-45/90]s4 quasi-isotropic layup are shown in Fig. 2. The rf amplitude spectrum, indicated as a pseudo time-domain signal, and its 128-point discrete Fourier transform are recorded for a defect-free region of the specimen. The spacing and regularity of the resonances are characteristic of undamaged composite. Its FFT in Fig. 2(b) shows a large peak in a region of the pseudo frequency spectrum we have arbitrarily denoted band #5. This peak near 900 Hz may be taken as indicative of defect-free material. In the data of Fig. 3, acquired over an impact delamination, the pseudo time signal and its transform show the effect of a mechanical discontinuity at about the 8th ply. Many fewer resonances are seen, and the first peak in the pseudo frequency spectrum occurs near 200 Hz.

One important advantage of the swept-frequency tone burst technique is that much greater average acoustic power can be coupled to the test sample than with conventional impulse excitation methods, resulting in a comparatively higher S/N ratio. In fact, acoustic amplitude, expressed as a voltage, is the significant factor determining the signal-to-noise ratio. Making broad assumptions about the experimental conditions, we can estimate the advantage of quasi-cw excitation. Let us take the impulse as triangular and 40 nsec in duration with a maximum height of 500 V. The swept-frequency waveform is 12.5 Vrms and is sampled by the boxcar integrator for an aperture of 10 microsec. Since the transducer characteristics and inspection geometry are identical in each case, the equivalent charge available for signal acquisition is 20 μVsec for each impulse and 125 μVsec for each tone burst. The bursts are repeated at a rate of 2 to 8 kHz. The higher figure substantially improves the rf spectral details in the boxcar output. Each pixel in the method of this paper consists of tone bursts for 25 msec, during which the rf is swept to scan the transducer spectrum.
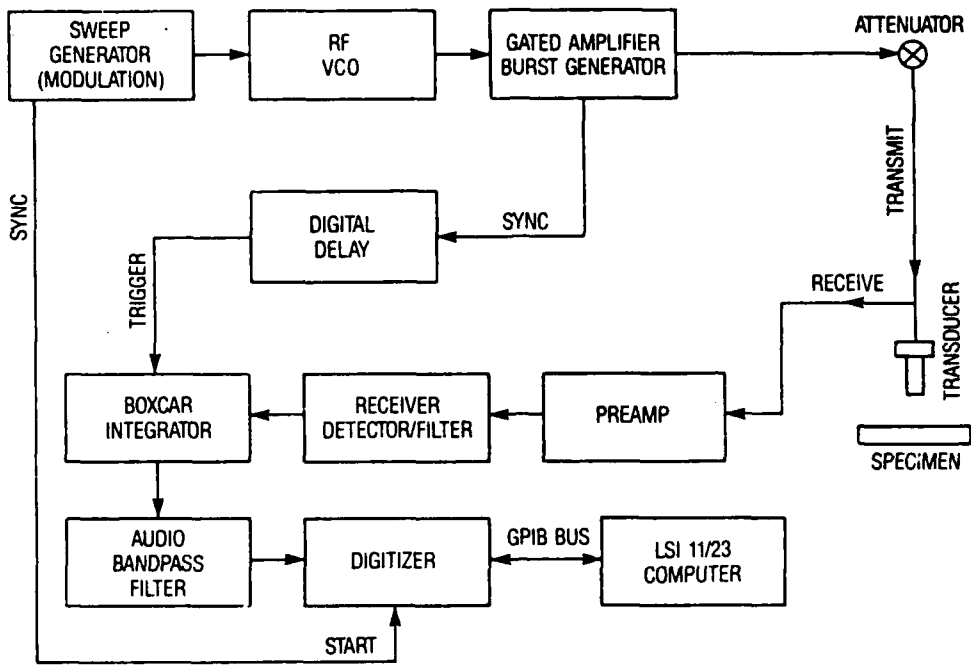
Figure 1.   Swept Frequency Tone Burst Instrumentation.

(a)

(b)
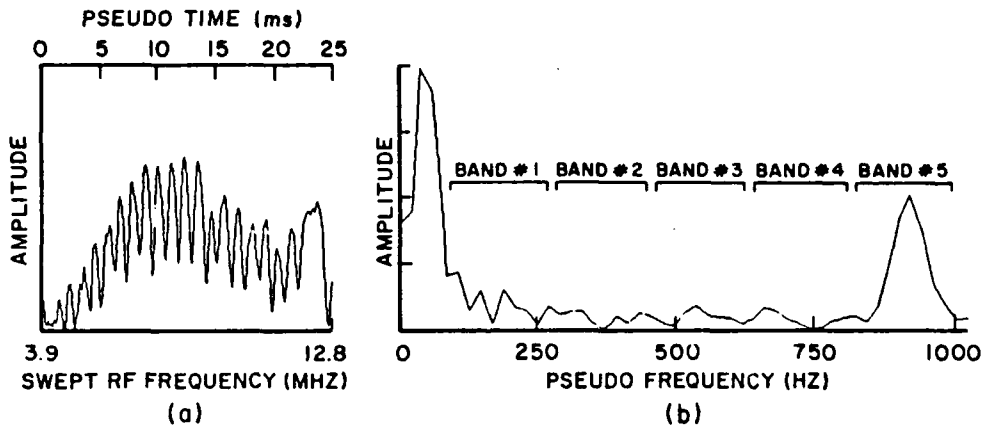
Figure 2.   Swept frequency signal amplitudes (a) and
corresponding FFT (b) of a defect-free region in a
quasi-isotropic composite plate.

(a)

(b)
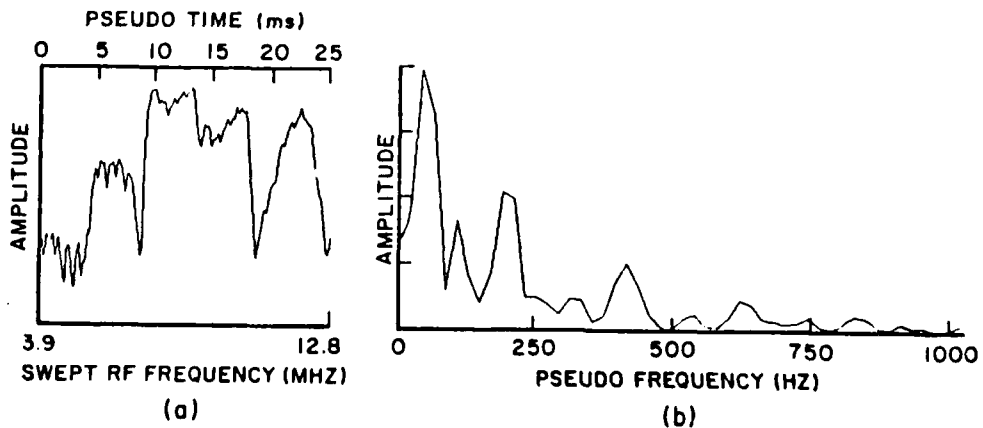
Figure 3.   Swept frequency signal amplitudes (a) and
corresponding FFT (b) of a delaminated region in a
quasi-isotropic composite plate.

A-16

Naively, one could compare the total charge ratio for swept-frequency and impulse excitation, $(125/20) \times (8 \times 25/1) = 1250$. This result ignores any averaging which could be done on the impulse signal during the 25 msec frequency sweep. However, instrument limitations prevent either the digital acquisition of such a large amount of data or the rapid transfer of acquired data to computer memory for summation and storage, or both. With readily available instruments, the maximum number of rf time-domain records is about 64, corresponding to 32k channels. At DMA transfer rates using the IEEE-488 protocol, this data would still require at least 200 msec to reach computer memory for accumulation, in addition to the data gathering time. Averaging multiple rf impulses reduces the advantage of the swept-frequency method to a factor of 20, but then slows the impulse scan rate to fewer than five pixels per second. In practice, averaging of rf waveforms is seldom done, because it is complicated, expensive, and time consuming. Moreover, this comparison ignores any nonlinear behavior induced by the large amplitude impulse voltage.

DIGITAL SIGNAL PROCESSING

The envelope of the rf signal is digitized at 5120 samples/sec to obtain 128 data points during the 25 millisecond sweep time (Figs. 2(a) and 3(a)). Then a FFT of the resulting pseudo time signal is computed to determine the pseudo frequency characteristics of the interference pattern. Two methods have been utilized to obtain image data from the FFT magnitude spectrum. Both rely on the shift in frequency of the magnitude spectrum towards lower frequencies in the presence of delaminations. In thick (ie, defect-free) material there are many nulls, as in Fig. 2(a), and the FFT magnitude spectrum indicates this with a large peak near 900 Hz (Fig. 2(b)). In material that is effectively thinner because of mechanical decoupling due to delaminations, there are fewer nulls (Fig. 3(a)). This condition produces a peak which is lower in frequency in the FFT magnitude spectrum (200 Hz and harmonics) and the absence of the peak at 900 Hz (Fig. 3(b)). Herein lies a second important advantage of swept-frequency tone burst imaging. Digitizing at about 5 ksample/sec requires a relatively inexpensive A/D converter compared to the one needed for 50 or 200 Msample/sec capture of a rf time-domain waveform. In addition, kHz sampling rates would permit use of instruments having increased vertical resolution and much higher dynamic range, typically by 24 dB or greater.

The first image generation method employs bandpass filtering techniques which are implemented by integrating the signal within specific bands in the FFT magnitude spectrum. Figure 2(b) shows the location of five frequency bands chosen for this purpose. A peak in band #1 would indicate the presence of a delamination near the entry surface of the specimen and would result in a high value for that filter. Likewise, the presence of delaminations in bands #2, #3 or #4 would indicate respectively deeper delaminations and produce high amplitudes in these filters. The peak in band #5 represents the backsurface of the specimen, so this band will have a large amplitude only for defect-free material. The value of a particular filter at each (x,y) scan point is assigned to a single pixel in a C-scan format. In this manner, C-scan images can be generated for various depths depending upon the filter band selected. Experimental results will be discussed in a later section.

The second image generation method also derives a single value calculated from the pseudo time domain signal, one which characterizes the entire FFT magnitude spectrum at each (x,y) scan point. The median

frequency [8,9] is that frequency which divides the area of the rf
magnitude spectrum equally. The median frequency of each (x,y) scan
point is mapped to a corresponding pixel, creating a C-scan type image
format. Median frequency imaging encodes depth into the grey scale of
the image. In defect-free material, the largest number of interference
nulls will be observed (assuming constant plate thickness), and the
median frequency is consequently high. In material that is effectively
thinner because of mechanical decoupling due to delaminations, there
are fewer nulls and the median frequency is lower in proportion to the
defect's proximity to the sound entry surface. Median frequency
spectral processing provides a wide dynamic range of response to
defects while preserving sensitivity to small or weak flaws. The defect
depth can be estimated and resolved to within the equivalent frequency
resolution of the FFT. This outcome and the appearance of Figs. 2(a)
and 3(a) are to be expected. Although we have treated the boxcar output
in Fig. 1 as a (pseudo) time domain signal, it is nonetheless clearly
the rf magnitude spectrum of the plate reflectance. Its FFT will
produce a low frequency (slow time) replica of the plate's impulse
response. Therefore, the back surface appears at the right-hand side of
Fig. 2(b), and a near-surface delamination appears on the left of Fig.
3(b). Results presented in the next section will demonstrate this
capability. Median frequency image representation was originally
applied to modulated tone-burst leaky Lamb wave generation and is
described in previous publications [7-9].

RESULTS

Two graphite-epoxy composite specimens have been investigated in
this study. The first specimen is a 32-ply quasi-isotropic (QI) plate
with a [0/+45/-45/90]s4 layup. The thickness of this sample is 6.85 mm.
It contains delaminations caused by a 13.56 joule (10 ft-lb) impact

(a)   (b)

(c)   (d)
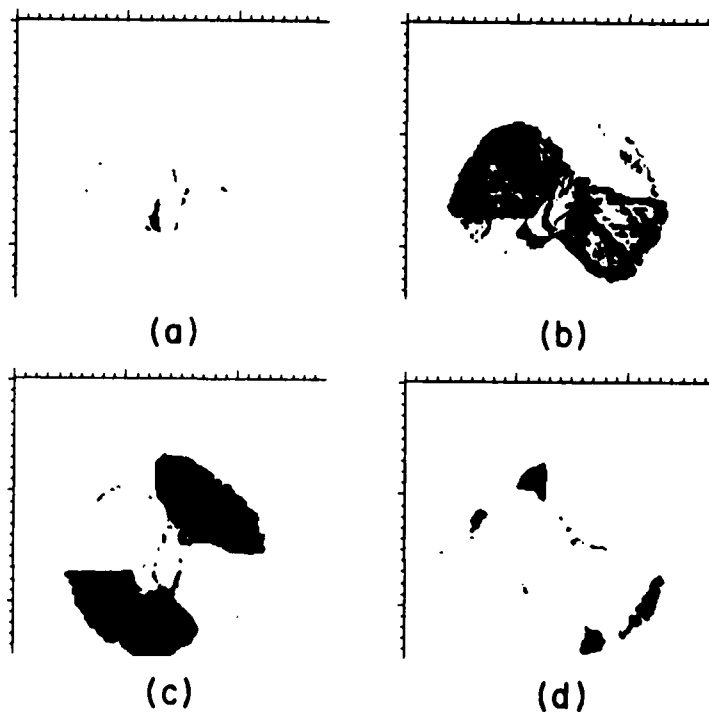
Figure 4.   Digital bandpass filtered images of the swept-
             frequency signal separated into 4 bands. The highest
             amplitudes in each image are thresholded to black to
             emphasize the delaminations.

A-18

force. The second specimen is a 14-layer woven plate 4.88 mm thick having a simple weave pattern. It has multiple layer delaminations which were induced by an impact force of 2.7 joule (2 ft-lb). Both specimens were subjected to low velocity impacts with a 12.7 mm diameter stainless steel ball on a pendulum impacter to induce delaminations.

C-scan images of delamination damage at 4 different depths in the QI plate were obtained by digital bandpass filtering and are shown in Fig. 4. A 71mm by 71 mm area of this specimen is imaged. Using the frequency bands shown in Fig. 2(b), the image was thresholded into a binary B&W image with the highest amplitudes in each image encoded as black to emphasize the delaminations. We see the typical damage pattern for impacts, where delaminations are oriented in the ply direction at each depth. The area of delamination generally increases with depth [10,11]. Frequency band #1, Fig. 4(a), corresponds to near-surface delamination in a +45 degree ply. Frequency band #2 (Fig. 4(b)) shows delaminations in deeper +45 and 0 degree plies, as does frequency band #3 (Fig. 4(c)) which indicates damage in 90 and -45 degree plies. The deepest delaminations imaged are shown in frequency band #4 (Fig. 4(d)) and are of 0 and +45 degree plies. The depth resolution in these images is about 2 plies, limited by the density of points in the discrete Fourier transform.

The results of applying median frequency (Mfreq) processing to the data from the QI plate are shown in Fig. 5. In this image, Mfreq is encoded as grey scale levels and is proportional to defect depth. White indicates low Mfreq and near-surface delaminations. Light grey through dark grey indicate progressively higher median frequencies and areas of deeper delamination. The highest Mfreq are represented as black in the figure and indicate reflections from the back surface of
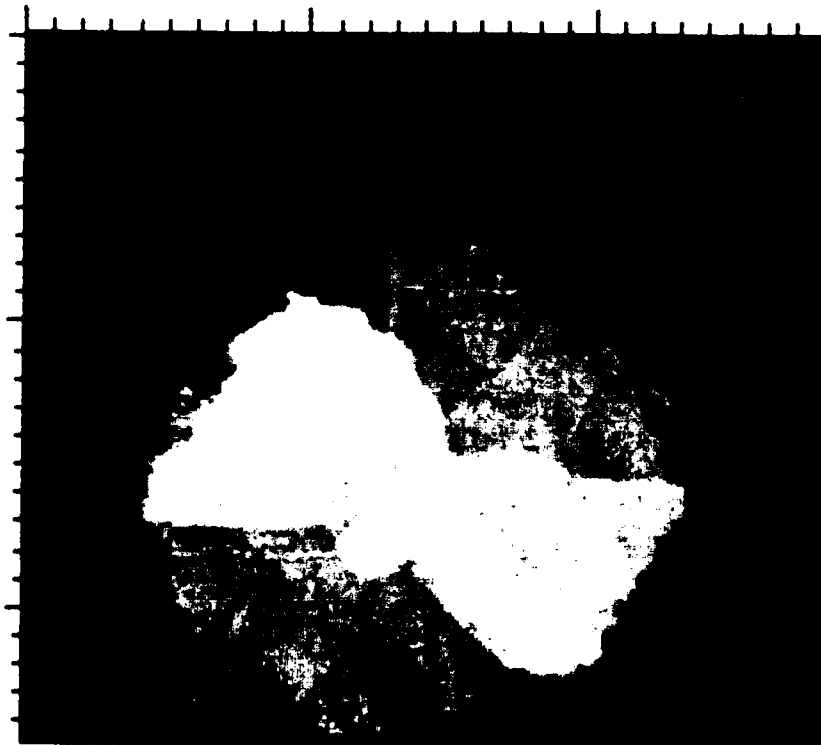
Figure 5. Median-frequency processed image from impacted quasi-isotropic plate. Defect depth encoded as grey scale. White shows near-surface delaminations; black is defect-free material.

A-19
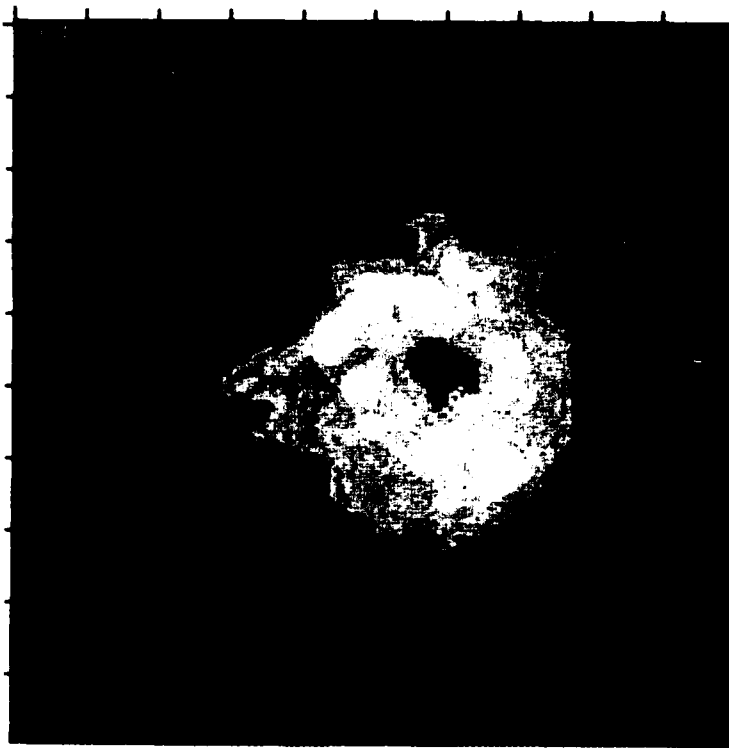
Figure 6. Median frequency processed image of impacted
           woven plate. Defect depth is encoded as grey scale;
           white shows near-surface delaminations. Dark grey
           shows deeper delaminations; black is defect-free
           material.

the plate (defect-free material). Reflected sound from inhomogeneities
in various plies generates linear features along that fiber direction
in the image of Fig. 5, indicating the ply layup.

    Median frequency processed data from the woven plate is shown in
the image of Fig. 6. A 25 mm by 25 mm area of this material has been
scanned. The median frequency is encoded as discrete grey scale levels
proportional to delamination depth, as in the previous figure. As
expected for this type of composite failure mode, increased
delamination area with depth is again evident, but with no obvious
orientation as in the QI case. The superposition of the weave pattern
can be seen on both the delamination and defect-free areas. The impact
point can be seen as a grey area near the center of the delamination
area. The higher S/N achievable in the swept-frequency tone burst
method was essential in obtaining a clear image in this highly
attenuative material.

CONCLUSIONS

    The relative depths of delaminations and other defects in complex
laminates such as woven and quasi-isotropic composites can be
determined utilizing swept-frequency techniques and median frequency
signal processing. Because many modes are excited, swept-frequency
techniques have a high sensitivity to many types of defects at all
depths. These techniques are equally applicable to leaky Lamb wave
applications. Also, much greater average acoustic amplitude can be
excited in the test sample with quasi-cw swept-frequency techniques
than with impulse excitation methods, resulting in a comparatively
higher S/N ratio. Lastly, only a low speed (5000 samples/sec) A/D
converter is required to digitize the envelope of the rf signal

A-20

utilizing the described techniques. In addition to being much lower in cost, low speed digitizers usually also offer much greater vertical resolution and dynamic range, which can be of significant value in image enhancement.

ACKNOWLEDGEMENTS

REFERENCES

1. A. H. Nayfeh and D. E. Chimenti, "Ultrasonic wave reflection from liquid-coupled orthotropic plates with application to fibrous composites", J. Appl. Mech. 55, 863 (1988).

2. S. K. Datta, A. H. Shah, R. L. Bratton, and T. Chakraborty, "Wave propagation in laminated composite plates", J. Acoust. Soc. Am. 83, 2020 (1988).

3. Y. Li and R. B. Thompson, "Propagation of guided waves in orthotropic plates", in Review of Progres in ONDE, Vol. 8A, eds. D. O. Thompson and D. E. Chimenti, (Plenum Press, New York, 1989), p. 189.

4. A. K. Mal and Y. Bar-Cohen, "Ultrasonic characterization of composite laminates", Wave Propagation in Structural Composites, (ASME, New York, 1988) AMD-Vol 90, p. 1.

5. D. E. Chimenti and A. H. Nayfeh, "Ultrasonic Reflection and Wave Propagation in Multilayered Composite Plates", in Review of Progress in ONDE, Vol. 8A, eds. D. O. Thompson and D. E. Chimenti, (Plenum Press, New York, 1989), p. 221.

6. P. B. Nagy, L. Adler, D. Mih, and W. Shephard, "Single mode Lamb wave inspection of composite laminates", in Review of Progress in ONDE, op. cit., Vol. 8B, (1989) p. 1535.

7. D. E. Chimenti and Y. Bar-Cohen, "Signal analysis of leaky Lamb wave spectra for NDE of composites", in Proceedings of 1985 IEEE Ultrasonics Symposium, ed. B. R. McAvoy, (IEEE, New York, 1986) p. 1028.

8. R. W. Martin and D. E. Chimenti, "Signal Processing of Leaky Lamb Wave Data for Defect Imaging in Composite Laminates," in Review of Progress in ONDE, op. cit., Vol. 6A, (1987) p. 815.

9. R. W. Martin and D. E. Chimenti, "Leaky Plate Wave Inspection of Biaxial Composites", Review of Progress in ONDE, op. cit., Vol 8B, (1989) p 1663.

10. B. G. Frock, R. W. Martin, T. J. Moran, and K. O. Shimmin, "Imaging of Impact Damage in Composite Materials", Review Of Progress in ONDE, op. cit., Vol 7B, (1988) p 1093.

11. C. F. Buynak, T. W. Moran and R. W. Martin, "Delamination and Crack Imaging in Graphite/Epoxy Composites," Materials Eval. 47, 438 (1989).

12. L. H. Pearson and W. J. Murri, in Review of Progress in ONDE, op. cit., Vol. 5B, (1986) p. 1093.

13. W. R. Rose, S. I. Rokhlin, and L. Adler, in Review of Progress in ONDE, op. cit., Vol. 5B, (1986) p. 1111.

14. Y. Bar-Cohen and D. E. Chimenti, "Nondestructive evaluation of composites by leaky Lamb waves", in Review of Progress in ONDE, op. cit., Vol. 5B, (1986) p. 1199.

IMAGING OF IMPACT DAMAGE IN COMPOSITE MATERIALS

B. G. Frock and R. W. Martin[†]

University of Dayton Research Institute
Dayton, Ohio 45469

T. J. Moran

AFWAL/Materials Laboratory
Wright-Patterson AFB, Ohio 45433

K. D. Shimmin[‡], Systran Corp.

4126 Linden Avenue
Dayton, Ohio 45432

INTRODUCTION

Conventional ultrasonic C-scan images are generated from information acquired within "gates" placed at specific temporal locations on low-pass filtered and rectified versions of A-scans. Placing the gates at temporal locations which correspond with interfaces allows the integrity of the interfaces to be examined. However, if the interfaces are closely spaced, as is the case for quasi-isotropic graphite/epoxy composites, the information from upper layers is blurred into the layers below because of the finite time duration of the ultrasonic pulse. This creates a low signal-to-background-level ratio, which causes blurring at and below the first interface.

The blurring effects can be reduced by acquiring data from the rf waveform. The C-scan images which are generated from rf signals that are gated at the interface locations are less affected by depth-wise blurring than are the C-scan images generated from low-pass filtered and rectified signals [1]. The finite time duration of the ultrasonic pulse, however, still results in the overlapping of echoes from delaminations at adjacent interfaces and between the entry surface echo and echoes from delaminations at near-entry-surface interfaces. This overlapping of echoes results in some blurring and imprecision in the definitions of the boundaries of delaminated regions in impact damaged, quasi-isotropic graphite/epoxy composites.

The use of the Wiener filter to deconvolve the overlapping echoes suppresses some of the "ringing" in the ultrasonic pulse. Collecting data from gates placed at the appropriate locations along the deconvolved signals should increase the signal-to-background-level ratio, and should allow a more precise definition of the boundaries of the marginal damage at specific ply interfaces.

1093

WIENER FILTER DECONVOLUTION

The deconvolution technique utilized for this work is known as constrained deconvolution or Wiener filtering [2-4]. It assumes that the measured signal from the reflector, y(t), is a convolution of the overall system response, h(t), and the flaw response, s(t), or

$$y(t) = h(t) * s(t) \tag{1}$$

where h(t) is obtained by recording a reference waveform from a planar reflector. The measured signals, y(t) and h(t), are transformed into the frequency domain and the flaw spectral response is calculated from

$$S(\omega) = \frac{Y(\omega)H^*(\omega)}{|H(\omega)|^2 + K^2} \tag{2}$$

where $H^*(\omega)$ is the complex conjugate of $H(\omega)$ and K is a constant. Noise in $S(\omega)$ is minimized when $H(\omega)$ is zero or very small by setting K to a predetermined percentage of the maximum amplitude of $H(\omega)$. In addition, high-pass filtering and low-frequency smoothing are also performed to minimize the sidelobes generated by the rectangular windowing created by setting the response to zero.

SAMPLE

The sample used in this study is a 32-ply thick, quasi-isotropic graphite/epoxy composite. Prior to ultrasonic inspection, it had been intentionally damaged by a 5.4 joule impact from a 12.7 mm diameter stainless steel ball on a pendulum impacter.

DATA COLLECTION

A computer controlled ultrasonic immersion scanning system was used to collect 512 point, 8-bit, rf A-scans at each of 6400 discrete points in a 40.6 mm by 40.6 mm square area surrounding the impact damage site. The spatial separation between data collection points was 0.51 mm in both planar directions. All 6400 A-scan lines were stored in the computer memory for later processing. A 5 MHz center frequency, 12.7 mm diameter, 76.2 mm focal length transducer was used for all data collection. Excitation for the transducer was a broadband spike pulse. A reference waveform (rf echo from the front surface of a flat plexiglas plate) was collected and stored for use during the deconvolution process. The reference echo and its Fourier amplitude spectra are shown in Fig. 1.

C-SCAN IMAGE GENERATION

Gated A-Scan Method

This technique is analogous to gating the raw rf waveform during scanning, except that in the present case the rf waveforms had already been digitized and stored in the computer. Peak signal levels were collected and stored from 40 nanosecond-wide regions of the waveform (see Fig. 2a) which corresponded with the locations of the interfaces between plies. The C-scan image generated from that data provided information concerning the structural integrity of the interfaces.

1094

A-23
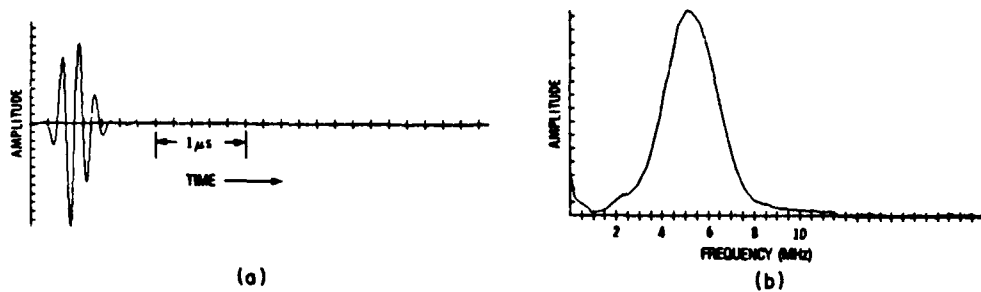
Fig. 1.   Reference waveform: (a) rf A-scan; (b) Fourier amplitude spectra
of rf A-scan in "a".
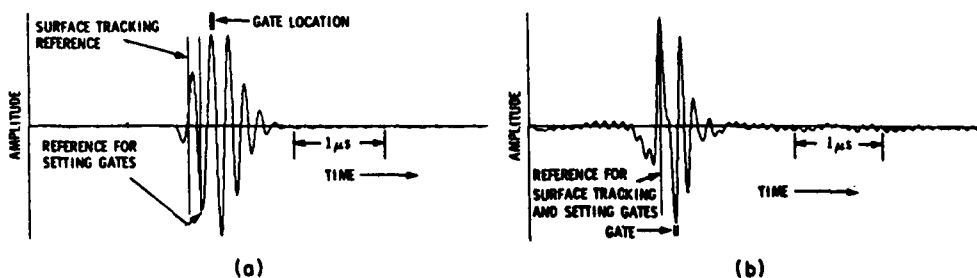
Fig. 2.   Gating for C-scan image generations: (a) rf A-scan;
(b) deconvolved A-scan.

Deconvolution Method

All 6400 of the rf A-scans were deconvolved using a Wiener filter of
the form given in Eq. (2). The amplitude cut-off was set at 0.05% because
of the very low noise level of the rf A-scans. Examination of the Fourier
amplitude spectra of the reference waveform (Fig. 1b) led to the choice of
12 MHz for the high frequency cut-off and 1 MHz for the low-frequency and
interpolation cut-off. Phase reversal of the echoes from the delaminated
intérfaces yielded a negative-going spike in the deconvolved waveform at
the echo return locations. Thus the minimum values of the portions of the
deconvolved waveforms which fell within appropriately placed 40 nanosecond-
wide gates (see Fig. 2b) were collected from each of the 6400 waveforms and
stored in the computer. A C-scan image of the interface between the second
and third plies was then generated from the data [5].

RESULTS

C-scan images of the interface between the second and third plies
(measured from the entry surface) are shown in Fig. 3. The image in Fig. 3a

1095

A-24
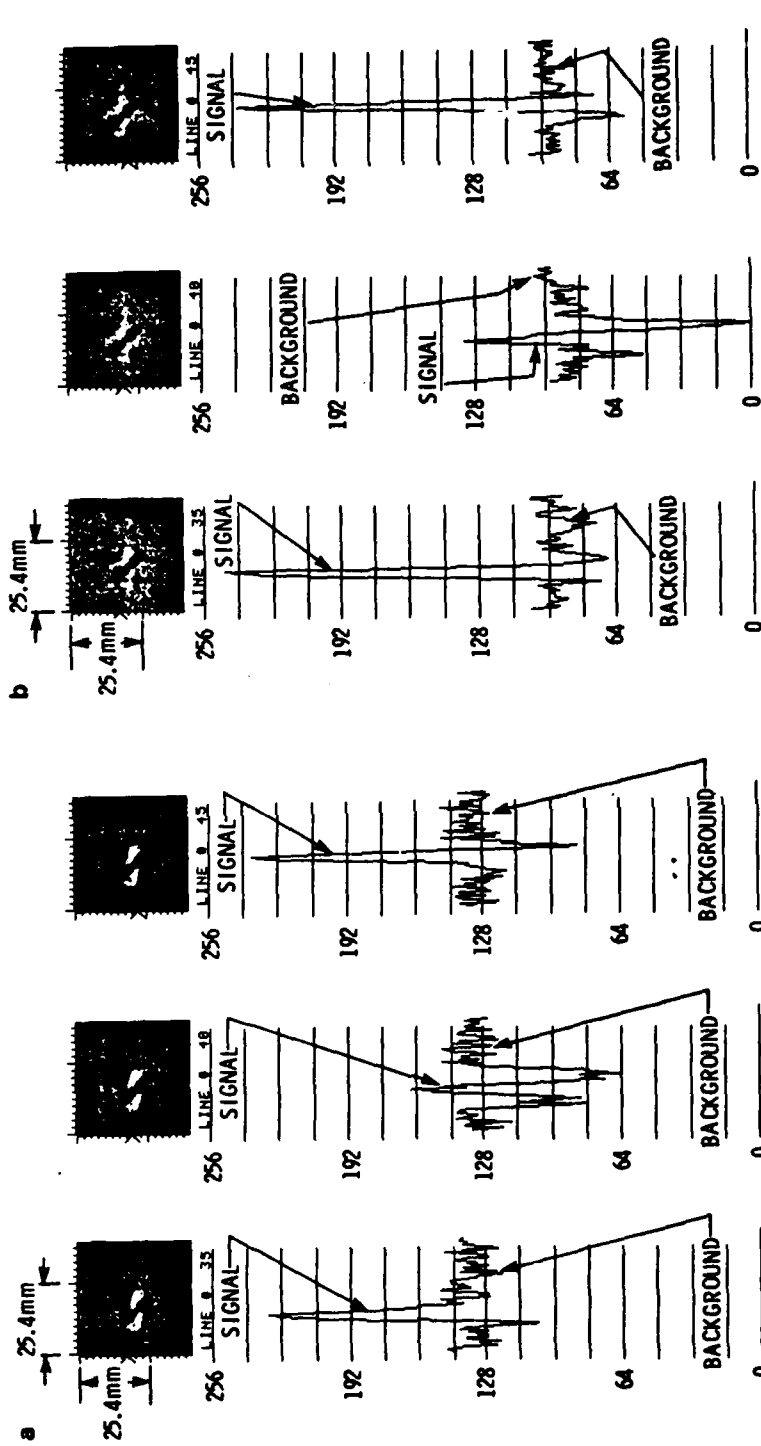
Fig. 3. C-scan images with pixel amplitude plots: (a) from gated rf A-scan; (b) from gated deconvolved A-scan.

was generated directly from the rf A-scans while the image in Fig. 3b was generated from the deconvclved waveforms. The delamination at the interface between plies two and three is the dark (black) somewhat peanut-shaped object lying along a diagonal which, if extrapolated would extend from the upper left corner to the lower right corner of each C-scan image. The lighter regions on either side of the second-to-third ply interface delamination are "precursors" of the delaminations at the interface between the third and fourth plies. These "precursors" are more evident in the C-scan image generated directly from the rf A-scans and are a result of the "ringing" of the transducer. This "ringing" is partially removed by the deconvolution process.

Plots of the individual pixel values along selected horizontal lines in the C-scan images are also shown in Fig. 3a and Fig. 3b. The major advantages which result from the deconvolution process are evident from these plots. First, the general signal-to-background level is higher for the C-scan image which was generated from the deconvolved waveforms than is the signal-to-background level for the C-scan image which was generated from the rf A-scans. In these cases the "signal" is defined as the pixel amplitudes in the delaminated region and the "background" is defined as the pixel amplitudes everywhere else. The higher signal-to-background level greatly improves the ability to precisely define the boundaries of the damaged regions at the interrogated interface. Second, the general "noise" level which is superimposed on the "signal" and "background" regions is significantly higher in the C-scan image which was generated directly from the rf A-scans. This can be seen in the pixel amplitude plots in Fig. 3a and Fig. 3b and also in the Fourier amplitude spectra in Fig. 4. The Fourier amplitude spectra are from line number ten (a "background" region) of the C-scan images in Fig. 3. The Fourier amplitude spectra of line 10 of the C-scan data generated from the rf A-scans has more energy in the high spatial frequency region than does the spectra of line 10 of the C-scan data generated from the deconvolved waveforms. The lower noise level allows for a more precise definition of the delaminated regions and for better visual definition of other features such as the fiber tows.

The raw rf waveforms and the deconvolved waveforms for two locations (one "signal" and one "background") on line 35 of the C-scan images are shown in Fig. 5. The locations of the "gates" are superimposed on each of the waveforms. The dynamic range of the portion of the deconvolved waveform which lies within the gated region is greater than the dynamic range of the portion of the rf waveform which lies within the gated region. It is this difference in dynamic ranges which results in the difference in signal-to-background levels in the two types of C-scan images.

CONCLUSIONS

Deconvolution removes some of the "ringing" in bandwidth-limited ultrasonic pulses. This decreased "ringing" in the deconvolved waveforms leads to a greater dynamic range between the "signal" regions and the "background" regions of C-scan images generated from these deconvolved waveforms than for C-scan images generated directly from the rf waveforms. The deconvolution process also performs some smoothing which results in less "noise" being superimposed on the "signal" and "background" regions of the C-scan images generated from the deconvolved waveforms. The greater dynamic range and the noise suppression which result from the deconvolution process allow more precise visual and machine definition of the boundaries of damaged regions in impacted graphite/epoxy composites.

1097

Fig. 4. Fourier amplitude spectra of line 10 from C-scans in Fig. 3:
(a) from image in Fig. 3a; (b) from image in Fig. 3b.
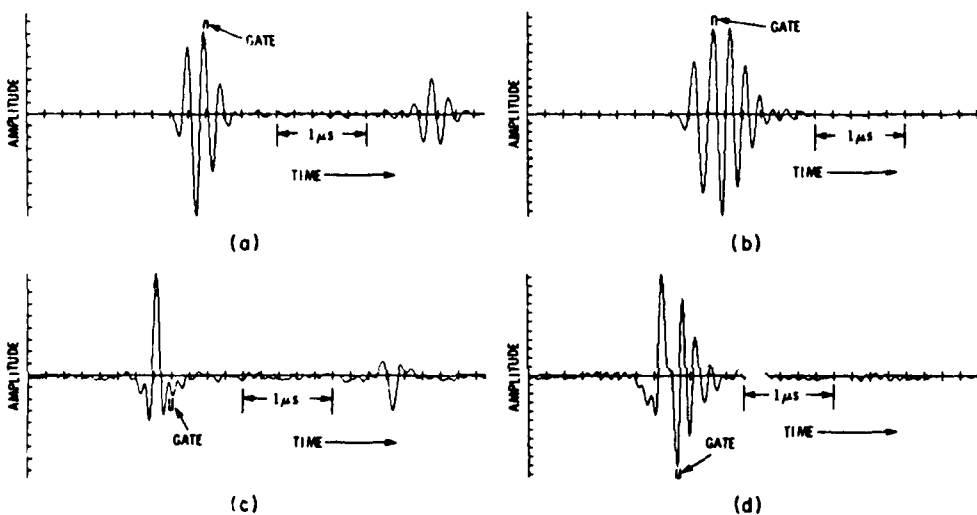
Fig. 5. A-scans at two locations on line 35 of C-scan images in Fig. 3:
(a) rf A-scan in background region; (b) rf A-scan in signal
(delaminated) region; (c) deconvolution of rf A-scan in "a";
(d) deconvolution of rf A-scan in "b".

1098

A-27

REFERENCES

1. C. F. Buynak and T. J. Moran, in Review of Progress in Quantitative NDE, edited by D. O. Thompson and D. E. Chimenti (Plenum Press, New York, 1987), Vol. 6B, pp. 1203-1211.

2. S. Neal and D. O. Thompson, in Review of Progress in Quantitative NDE, edited by D. O. Thompson and D. E. Chimenti (Plenum Press, New York, 1986), Vol. 5A, pp. 737-745.

3. E. S. Furgason, R. E. Twyman and V. L. Newhouse, in Proceedings DARPA/AFML Review of Progress in Quantitative NDE, AFML-TR-78-55, May 1978, p. 312.

4. Y. Murakami, B. T. Khuri-Yakut, G. S. Kino, J. M. Richardson and A. G. Evans, in Applied Physics Letters 33 (8), 15 October 1978, pp. 685-687.

5. B. T. Smith, J. S. Heyman, J. G. Moore and S. J. Cucura, in Review of Progress in Quantitative NDE, edited by D. O. Thompson and D. E. Chimenti (Plenum Press, New York, 1986), Vol. 5B, pp. 1239-1244.

1C99

ULTRASONIC IMAGE RESTORATION BY PSEUDO THREE-DIMENSIONAL

POWER SPECTRUM EQUALIZATION

Prasanna Karpur and Brian G. Frock
University of Dayton
Research Institute
300 College Park Avenue
Dayton, OH 45469-0001

ABSTRACT

Image restoration techniques such as Wiener filtering and inverse filtering require a knowledge of the Point Spread Function (PSF) of the imaging system. However, when internal structure of the material is being imaged, the material acts as an interfering filter which distorts the PSF of the imaging system thereby making it ineffective to use a PSF measured at the surface of the object being imaged for image restoration and resolution enhancement purposes. Power Spectrum Equalization (PSE) technique overcomes the need for an a priori knowledge of the PSF by deriving the restoration filter from the power spectrum of the degraded image itself. This paper describes the implementation of a Pseudo three-dimensional filter wherein a digitized three-dimensional A-scan data block is acquired from an impact damaged graphite-epoxy composite. Subsequently, each A-scan signal in the three-dimensional data block is restored by PSE leading to restored B-scan images from which C-scan images are constructed at various depths in the material. The C-scans so obtained are further restored using a two-dimensional PSE. The resulting restored C-scan and B-scan images are compared with unprocessed C-scan and B-scan images. Also, C-scans obtained from unprocessed RF-signals are processed by two dimensional PSE.

Considerable improvements in both the C-scan and B-scan images have been obtained by this technique, although the improvement obtained for B-scan images is superior to that obtained for C-scan images. The C-scans obtained from the processed B-scans show a good resolution enhancement. A further two dimensional processing of these C-scan images shows additional marginal improvements.

INTRODUCTION

Ultrasonic signal analysis and image processing play important roles in the field of NDE. Many methods of ultrasonic imaging such as A-scan, B-scan and C-scan are available. Using such images, NDE tests and analysis can be performed. However, the images are limited by the resolution limits of the imaging system which are established by many factors such as the bandwidth of the transducer, frequency of interrogation, diffraction effects, etc. One of the results of such resolution limits is the blurring of the images.

Blurring of an ultrasonic image masks the features of the object being imaged. In addition to producing diffused edges and blurred features, the resolution limit of the imaging system also obscures the presence of targets or features spaced closer than the resolution limit of the system. As a result, images of a material such as a composite, wherein thin laminates are closely spaced, will not provide meaningful results if the objective is to separate the features such as impact damage at each laminate interface of the composite material.

There are various methods such as inverse filtering, Wiener filtering, etc. [1,2,3], which are useful to improve the resolution limits of an image and to restore the blurred features. However, many of the techniques require an a priori knowledge of the blur function or the Point Spread Function (PSF) of the imaging system. With an a priori knowledge of the PSF, the imaging process can be represented by Figure 1 and equation (1) wherein the spectral distortions of the PSF, due to the wave-material interaction, have been ignored. As a result, linear operators such as an inverse filter can be applied for image restoration.

$$i(z) = h_1(z) * f(z) + n(z) \qquad (1)$$

where i(z) is the image/signal formed by the imaging system with an impulse response of $h_1(z)$, f(z) is the transfer function of the object which is assumed to have no spectral distortion of $h_1(z)$ and n(z) is additive noise.

The imaging process as shown in Figure 1 is an accurate representation only when the material being interrogated is homogeneous, isotropic and has negligible attenuation. Under these conditions, the PSF of the imaging system stays relatively undistorted during propagation in the material, thereby permitting the use of a known PSF (measured in water) for image restoration. However, the PSF approach is often rendered inappropriate because of the anisotropy and dispersion of the material being imaged.

Imaging of anisotropic, inhomogeneous, dispersive and/or thick material can not be represented by a simple block diagram as shown in Figure 1. The effect of material anisotropy or large frequency dependent attenuation is the progressive distortion of the power spectrum of the PSF as the wavefront travels in the material. The degree of distortion of the PSF is a function of many factors such as the severity of anisotropy, inhomogeneity, frequency dependent attenuation and thickness of the material. The spectral distortion of the PSF and the resulting image formation can be represented by [4] the block diagram in Figure 2 and equation (2) below:

$$i(z) = h_1(z) * h_2(z) * f(z) + n(z) \qquad (2)$$

where $h_2(z) * f(z)$ is the object transfer function when the spectral distortions are not ignored. As a result of the distortional effect of the object, there is a need for an image/signal restoration technique which can perform the restoration when the degree and the nature of the distortion of the PSF is unknown. Power Spectrum Equalization (PSE) is one such technique which does not need an estimate of the PSF for the restoration/enhancement operation.

POWER SPECTRUM EQUALIZATION

Power spectrum equalization (PSE) technique [4,5] is a useful method of image restoration when the PSF is unknown due to the spectral distortions of the PSF. The PSE filter is a phaseless filter and is

Impulse Response
of the Imaging System
$h_1(z)$

Object Transfer Function
$f(z)$

$+$

Resultant Image
$i(z)$

Additive Noise
$n(z)$
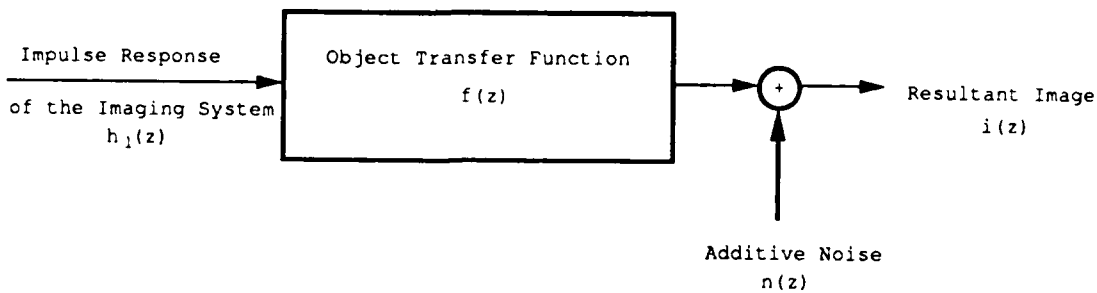
Figure 1   Block diagram showing the imaging process
when the object being imaged is assumed to
be ideal, ie., does not distort the spectrum
of the propagating wave front.

Object Being Imaged

Power Spectral
Distortion Due
to Wave
Propagation
$h_2(z)$

Object Transfer
Function
(Distortional
Effect Ignored)
$f(z)$

Impulse Response
of the Imaging System
$h_1(z)$

$+$

Resultant Image
$i(z)$

Additive Noise
$n(z)$
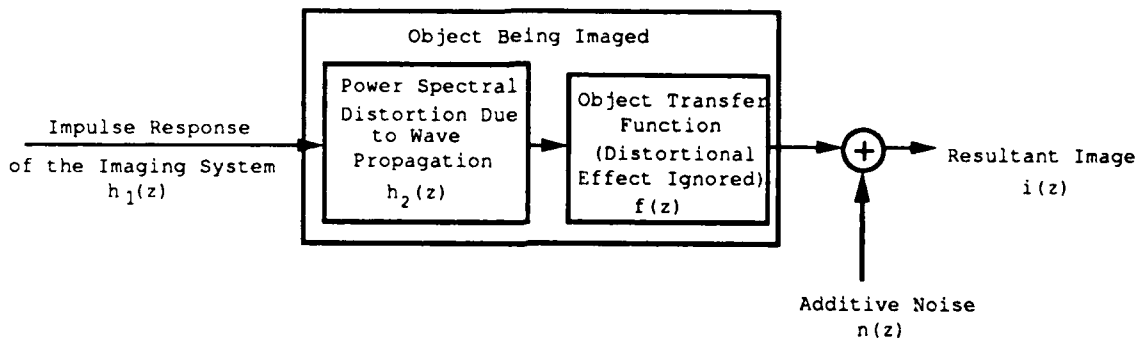
Figure 2   Block diagram showing the imaging process
when the distortional effect of the object
being imaged is not ignored.

derived from the distorted power spectrum of the signal/image itself
thereby eliminating the need for an a priori knowledge of the PSF.

Power spectrum equalization is performed by a linear phaseless
restoration filter synthesized in the frequency domain. The distorted
power spectrum of the image is used to derive the restoration filter
with the imposed condition that,

$$L(u,v)\ I(u,v) = F'(u,v)$$

where $F'(u,v)$ is the complex frequency spectrum of the restored object,
$L(u,v)$ is the PSE filter and $I(u,v)$ is the complex spectrum of the
image. Assuming that the spectral distortion due to wave-material
interaction is limited to amplitude distortion, the linear restoration
filter can be derived by constraining the power spectrum of the object
to be equal to the power spectrum of the estimated object (eqn. 3):

$$P_f(u,v) = P_f'(u,v) \tag{3}$$

where $P_f(u,v)$ is the object power spectrum given by $F^2(u,v)$ and $P'_f(u,v)$
is the power spectrum of the estimated object. With a further
simplifying assumption that the object can be represented by a
combination of delta impulse functions, it can be shown [4] that,

$$L(u,v) = \frac{1}{[H^2(u,v)\,P_f(u,v)+N]^{1/2}} = \frac{1}{[P_i(u,v)+N]^{1/2}} \tag{4}$$

A-31

where a constant N is included in the denominator as an estimate of the noise-to-signal ratio of the image and $P_i(u,v)$ is the power spectrum of the image. Hence the complex spectrum of the estimated object is given by equation (5) below:

$$F'(u,v) = L(u,v)\, I(u,v) = \frac{I(u,v)}{[P_i(u,v)+N]^{1/2}} \qquad (5)$$

EXPERIMENTAL SAMPLE

The sample used in this study is a 32-ply thick, quasi- isotropic, graphite-epoxy composite. The separation between ply interfaces in this sample is approximately 0.14 mm. Prior to ultrasonic inspection, the sample was intentionally damaged by a 5.4 Joule impact from a 12.7 mm diameter stainless steel ball on a pendulum impactor.

DATA COLLECTION

A computer controlled ultrasonic immersion scanning system was used to collect 256 point, 8-bit rf A-scans at 200 by 200 discrete points in a 20.3 mm by 20.3 mm square area surrounding the impact damage site. The spatial separation between data collection points was 0.10 mm in both planar directions. All 40,000 A-scan lines were stored in the computer memory for later processing. A 3.5 MHz center frequency, 12.7 mm diameter, 50.8 mm focal length transducer was used for all data collection. Excitation for the transducer was a broadband spike pulse.

RESULTS

The PSE operator shown in equation (4) has been implemented in both 1-D and in 2-D to process the rf signals in the B-scans and the C-scans obtained from the 3-D B-scan data.

Figure 3a shows a B-scan image produced at about the middle of the impact damage of the sample. The image shows the top surface of the sample (dark band across the image) and the delaminations because of the impact damage. Although some of the deeper delaminations and some reverberating echoes are clearly visible, a delamination immediately below the top surface is completely obscured by the front surface echo. Figure 3b shows the result of 1-D PSE processing of each rf scan contained in the B-scan. The resolution enhancement obtained in Figure 3b can be seen by the clearly visible impact damage layer immediately following the top surface of the composite material.

C-scan images were generated by applying narrow software gates to the rf A-scans contained in a series of 200 B-scans obtained on the scan grid mentioned before. Similar C-scans were also generated using the PSE processed B-scans (such as the one shown in Figure 3b). The gates were set to interrogate the third ply interface below the entry surface. Figures 4a and 4b show the C-scans of the impact damaged 3-ply interface obtained from unprocessed A-scans and processed A-scans, respectively. The improvement of the lateral resolution obtained in Figure 4b is noticeable compared to Figure 4a.

The C-scans shown in Figures 4a and 4b were further processed by using a 2-D PSE filter shown in equation (4) and the results are shown in Figures 5a and 5b respectively. Although improved lateral resolution is apparent compared to Figures 4a and 4b, the enhancement is not as effective as that obtained by 1-D processing.
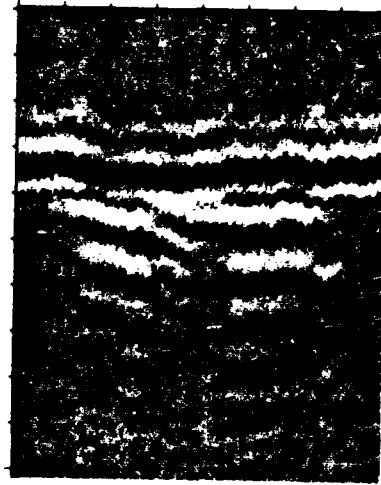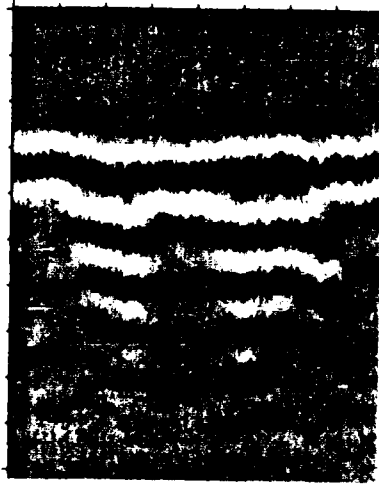
Figure 3a   Unprocessed B-scan of an impact damaged Composite material. The section is through the middle of the impact damage.

Figure 3b   The B-scan image shown in Figure 3a after power spectrum equalization. The impact damage close to the top surface is clearly visible.
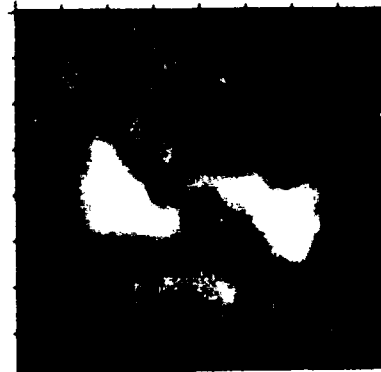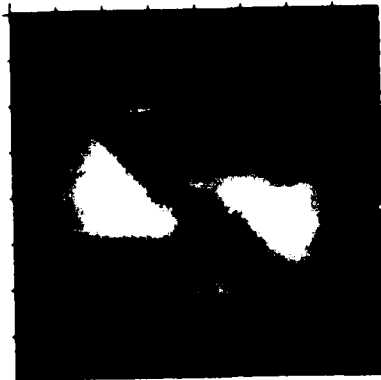
Figure 4a   C-scan image of the impact damage at the third ply interface. The C-scan is obtained from the unprocessed rf signals in the B-scans such as the one in Figure 3a.

Figure 4b   C-scan image of the impact damage at the third ply interface. The C-scan is obtained from the 1-D PSE processed rf signals in the B-scans such as the one in Figure 3b.
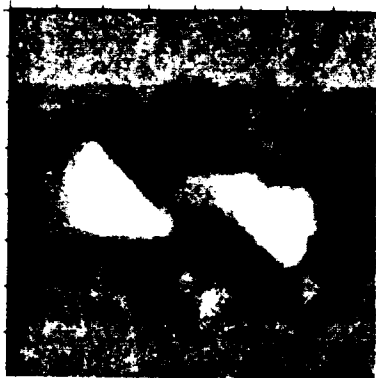
Figure 5a   Result of a 2-D PSE processing of the C-scan image shown in Figure 4a.

Figure 5b   Result of a 2-D PSE processing of the C-scan image shown in Figure 4b.

CONCLUSIONS

Power spectrum equalization has been shown to be a useful method of image restoration in anisotropic, inhomogeneous materials which distort the power spectrum of the propagating wave field due to attenuation. It has been observed that the enhancement obtained in B-scan images is far superior to that obtained in C-scan images. C-scan images obtained from PSE processed B-scan images show good enhancement. Also, they show further marginal improvement after a subsequent 2-D PSE processing.

ACKNOWLEDGEMENTS

REFERENCES

1. Burgoyne B., Pavkovich J. and Kino G.S., "Digital Filtering of Acoustical images", Vol.11, Plenum Press, New York, pp:131-166, 1981.
2. Frock B.G., Martin R.W., Moran T.J. and Shimmin K.D., "Imaging of Impact Damage in Composite Materials", Review of Progress in Quantitative Nondestructive Evaluation, Vol. 7, 1987.
3. Karpur P. and Frock B.G., "Two Dimensional Pseudo-Wiener Filtering in Ultrasonic Imaging for Nondestructive Evaluation Applications", Review of Progress in Quantitative Nondestructive Evaluation, Vol. 8, pp:743-750, 1988.
4. Iraca D., Landini L. and Verrazzani L., "Power Spectrum Equalization for Ultrasonic Image Restoration", IEEE Transactions on Ultrasonics, Ferroelectrics and Frequency Control, Vol.36, No. 2, pp:216-222, March 1989.
5. Andrews H.C. and Hunt B.R., Digital Image Restoration, Prentice-Hall Inc., 1977.

Digital Image Enhancement for Ultrasonic Imaging of Defects in Composite Materials

by B. G. Frock and R. W. Martin*

Abstract

Two classes of digital image enhancement techniques — thresholding and spatial-domain convolutions — have been applied to digitized ultrasonic immersion C-scan data. Two of the most popular thresholding techniques — equal percent of range and histogram equalization — are described, and images are generated by applying both techniques to the same data. Three different spatial-domain convolution techniques are discussed: edge enhancement by blurred image subtraction, edge enhancement by first-difference approximations to the gradient, and pseudo Marr-Hildreth methods for line/edge enhancement. The usefulness of these techniques for improving the visual detection and resolution of features in images is demonstrated with before-enhancement and after-enhancement images for each of the techniques described.

Keywords: composite materials, data analysis, digital analysis, immersion ultrasonic testing, image enhancement, nondestructive evaluation, ultrasonic testing.

INTRODUCTION

Typical industrial ultrasonic C-scan images often fail to display all of the information available. This is a result both of the necessity to set breakpoints (threshold values) for the gray levels before display and of variations in material attenuation, thickness, surface roughness, etc. that result in the need for use of considerably different amplitudes to obtain edge information. Because of these factors, outlines of the features may be very poorly defined and the features may be difficult to resolve from the background.

Digitizing and storing the C-scan amplitude information allows these problems to be overcome because the digital image-enhancement techniques[1-11] that have been so well developed in other disciplines can now be applied to ultrasonic nondestructive evaluation (NDE) data. Threshold values for converting amplitude information into gray or color levels can be selected after scanning has been completed, and the image can be redisplayed with many different threshold settings to improve visual detection and resolution of features in the image. A second type of digital image-enhancement technique — spatial-domain convolutions — can also be applied to digitized NDE data. These techniques, which actually modify the amplitude values of the data, can be used to suppress noise, enhance edges, reduce blur, make many features in the image simultaneously visible, and, in general,

improve the visual detection and resolution of features in the image.

SAMPLE

A 16-ply graphite-epoxy composite specimen with a $[0_4/90_4]_s$ stacking sequence was used for this study. The sample was 2.5 in. (63.5 mm) long, 1 in. (25.4 mm) wide, and 0.10 in. (2.54 mm) thick. There were cure cracks in both of the 0 degree ply layers and also in the 90 degree ply layer, as illustrated in the dye-enhanced x-radiograph of Figure 1. Note in particular the cracks labeled 2 and 3 in Figure 1. These cracks lie close together and will be used to illustrate the improvements in visual resolution of features that can be expected from the application of specific digital image-enhancement techniques.
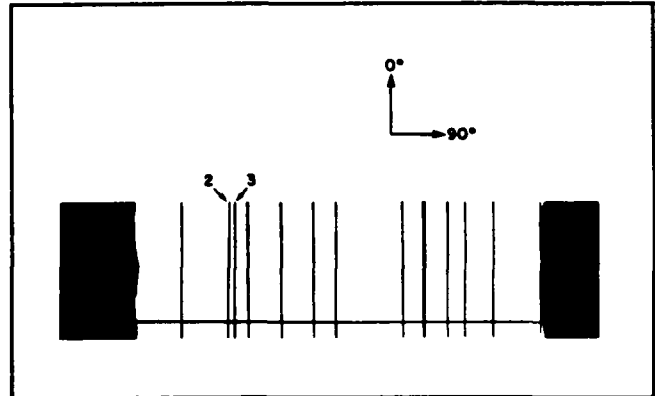
Figure 1 — X-radiograph of cure crack sample.

DATA COLLECTION

Data for all images were collected using computer-controlled,[12,13] normal-incidence, ultrasonic-immersion C-scanning techniques. Three different focused transducers were used to collect the data presented in this paper. The first transducer had a 25 MHz center frequency, a 0.25 in. (6.35 mm) dia, and a focal length in water of 1 in. (25.4 mm). The second transducer had a 10 MHz center frequency, a 0.50 in. (12.7 mm) dia, and a focal length in water of 3.0 in. (76.2 mm). The final transducer had a center frequency of 3.5 MHz, a 0.50 in. (12.7 mm) dia, and a focal length in water of 2 in. (50.8 mm). The location of the focal plane within the sample

*University of Dayton Research Inst., Structural Integrity Div., 300 College Park, Dayton, OH 45469-0001; (513) 255-9813.

differed for the different C-scans and will be specified as the individual images are presented and discussed.

Data were collected at uniformly spaced discrete locations during the raster scanning of the sample. These discrete points were separated by 0.005 in. (0.127 mm) in both the x and the y directions. All data were acquired from the rectified and low-pass filtered version of the back-surface echo. The average value of that version of the back-surface echo was digitized (using 12-bit resolution) and stored for each discrete location during scanning.

Noise-free data were acquired by using high gain in the preamplifier stage and low gain in subsequent amplifier stages. Noisy data were generated by using low gain in the preamplifier stage and high gain in subsequent amplifier stages.

DIGITAL IMAGE ENHANCEMENT

Thresholding Techniques

The method of setting breakpoints for assigning amplitude values to gray or color levels for image generation is referred to as thresholding. In addition to allowing conversion of the data values into gray or color levels, thresholding can serve also as a method for compressing the amplitude range of the data. The data acquired for this paper were digitized using 12-bit resolution, which corresponds to 4096 distinct amplitude values within the anticipated amplitude range. The image display device, however, had only four bits of resolution, which is equivalent to 16 gray or color levels. Thus, for purposes of display with the equipment available, the data had to be compressed from 4096 potential values to just 16.

There are many ways to set the breakpoints for thresholding, two of which—equal percent of range and histogram equalization—will be presented here. Regardless of the actual technique employed for setting the threshold, the conversion of amplitude values to gray levels remains essentially the same. All pixels (individual picture elements) with amplitude values between zero and the first threshold will be white. Those pixel elements with values between the first and second thresholds will be the lightest gray, and so on.

Equal-percent-of-range thresholding[2] consists of dividing the total range of pixel amplitudes into equally spaced intervals (in this case 16 intervals). This is illustrated in the histogram of image amplitudes in Figure 2. The vertical tick marks along the lower horizontal axis in Figure 2 represent the locations of the amplitude thresholds between different gray levels. Thus, those pixel elements with amplitudes between 0 and 100 would be white, those pixel elements with amplitudes between 100 and 200 would be the lightest gray and so on, with those pixel elements with amplitude values between 1500 and 1600 being black. Figure 2 also serves to illustrate a major weakness of equal-percent-of-range thresholding. This technique is particularly inefficient for converting data into an image when the histogram of amplitude values is highly peaked or skewed. In the present case, half of the gray levels would be used on only about 5 percent of the data (those pixels with amplitudes between 0 and 800). This leaves only eight gray levels to display almost 95 percent of the data.

Histogram equalization[2] is often a better technique to use with histograms of this type. The histogram-equalization technique sets the thresholds such that there are a nearly equal number of pixel elements within each gray level. When this technique is applied to the histogram of Figure 2, the thresholds will be located as shown along the upper horizontal axis of Figure 2. The vertical tick marks along the upper horizontal axis represent the locations of the thresholds. Most of the thresholds are located in the region of the histogram with the highest density of pixels and very few thresholds are located in the sparse regions of the histogram. In fact, all pixel elements with amplitude values between 0 and 850 now lie within one level. This is a much more efficient technique for displaying data with highly peaked and/or skewed histograms.

The results of applying the two thresholding techniques to image data are presented in Figures 3a and 3b. These images were generated from the data in Figure 2. The top image is displayed using equal-percent-of-range thresholding, and the bottom image is displayed using histogram-equalization thresholding. More visual information is made available to the viewer through the use of the histogram-equalization display format. The vertical lines defining the cracks are still visible and the narrow vertical and horizontal lines (due to the surface
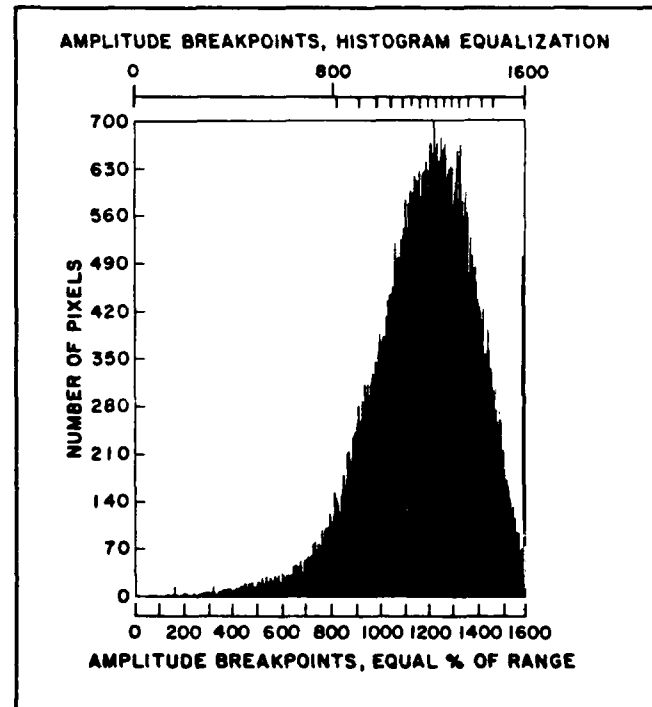

Figure 2—Data amplitude histogram showing thresholding for image generation.
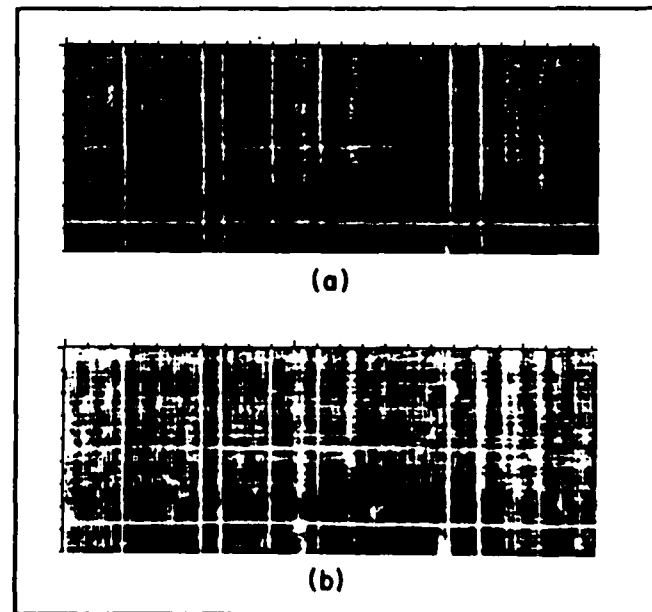

Figure 3—Effects of thresholding techniques on displayed image using 25 MHz transducer: (a) equal percent of range; (b) histogram equalization.

A-36

148	153	150	148	165	180	175	180	188
153	151	145	153	168	183	185	175	181
150	145	153	145	160	175	181	185	185
152	152	150	150	163	180	183	181	175
145	150	148	150	168	185	180	183	182

(a)

-1	0	1
-2	0	2
-1	0	1

(b)

|								
*	*	*	*	*	*	*	*	*
*	-11	-1	68	122	65	-6	9	*
*	-4	0	50	120	79	13	-4	*
*	2	-4	53	125	73	10	-10	*
*	*	*	*	*	*	*	*	*

(c)
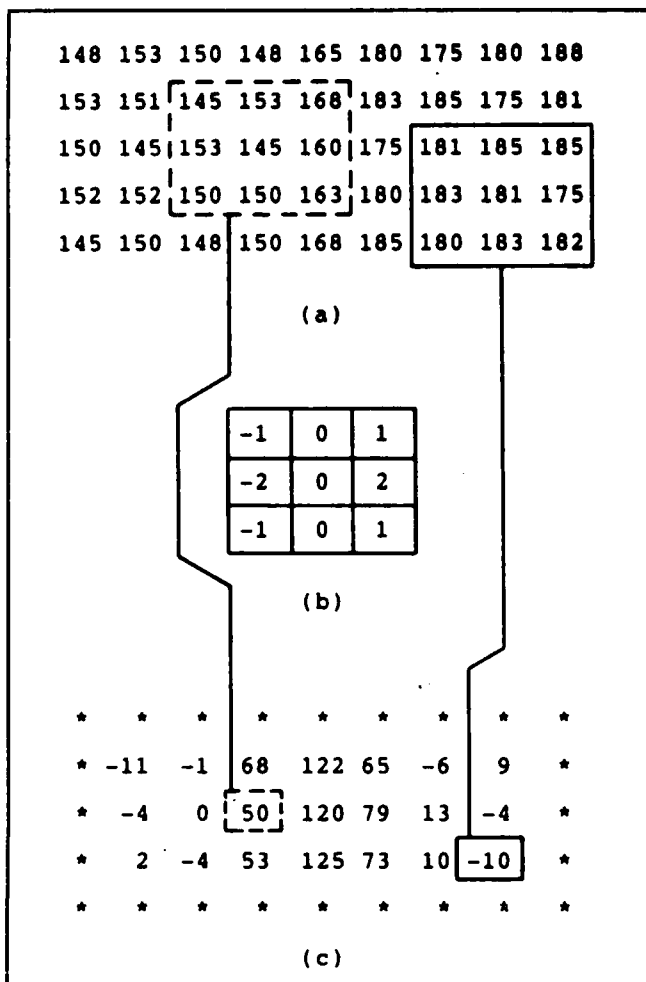
Figure 4—Moving-window operator: (a) portion of original image data; (b) Sobel first-difference edge-enhancement operator with multipliers; (c) transformed image data.


(a)

(b)
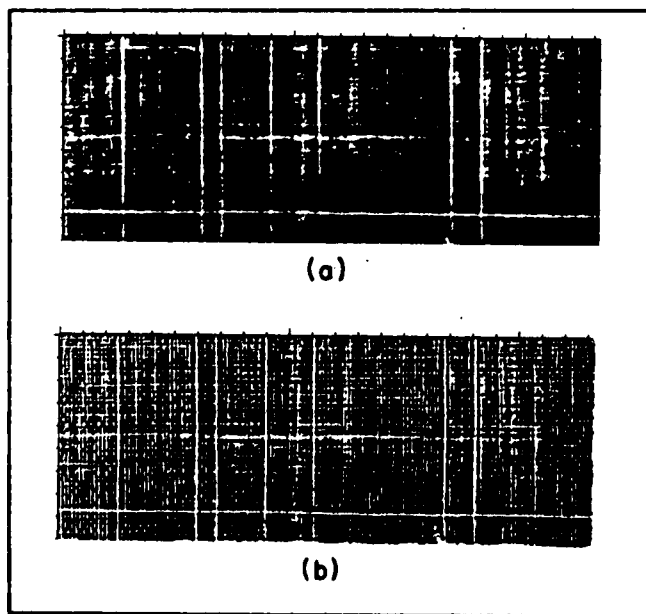
Figure 5—Blurred image subtraction: (a) image resulting from blurring the data used to generate the images in Figure 3; (b) image resulting from subtracting the blurred data from the original data.

topography of the sample) are more clearly visible in the image displayed using histogram-equalization thresholding. A comparison of the images in Figure 3 with the dye-enhanced x-radiograph of Figure 1 reveals that not all the cure cracks are visible in the images generated from the ultrasonic C-scan data. This is due to the location of the focal plane and to the very short acoustic depth of field of the transducer used for the data collection. The 25 MHz transducer was used for data collection, with the focal plane set at the top surface of the sample. Those cracks in the upper 0 degree plies are sharply imaged; those in the lower 0 degree plies are out of focus and are too blurred to be visually resolved.

Spatial-Domain Convolutions Using Moving Windows

With the exception of histogram equalization, all of the digital image-enhancement techniques illustrated here were implemented through the use of spatial-domain convolutions. These techniques actually modify (transform) the amplitude values of the original data through the use of a moving window. The technique is illustrated in Figure 4. The pixel amplitude values in a region of an image are shown in Figure 4a. Note that the data values on the left side of Figure 4a are lower than those on the right side; i.e., there is a step in the center of this set of values. A 3 by 3 moving-window spatial-domain convolution operator (in this case a Sobel[3] vertical edge detector) is shown in Figure 4b. The values in the nine window elements of Figure 4b are multipliers used to modify the original data. The moving-window technique is implemented by placing the 3 by 3 window over a 3 by 3 region of the original image data and multiplying the data in the original image by the values of the multipliers in the window. The resulting nine values are then summed to yield the single new value, which is placed in the appropriate location of the transformed image (Figure 4c). The window then shifts by one pixel column and the transformation is repeated. The process of transformation and shifting is continued until the entire image has been processed.

The results of applying the edge detector of Figure 4b to the data in Figure 4a are shown in Figure 4c. The data values are very small on both the right and left sides of Figure 4c, and the values along a vertical line through the center of the data are quite large. Thus, the Sobel edge detector of Figure 4b has enhanced the edge that separates the low values on the left side of Figure 4a from the high values on the right side of Figure 4a.

Edge enhancement by blurred image subtraction[1] is a standard technique for improving edge definition in digitized images. It is implemented by first blurring an image with a smoothing filter, which attenuates the higher spatial frequencies in the image, thus emphasizing the lower spatial frequencies. The low-spatial-frequency image data are then subtracted from the original image data. The result is a high-spatial-frequency image in which the edges are sharpened and bands (different gray levels) are created on both sides of an edge.[1] This banding aids the visual detection of the edges[9] and improves features detection. The enhancement of the high spatial frequencies also tends to make more features in the image simultaneously visible. The smoothing operation can be accomplished with a moving-window Gaussian filter in which the central pixel element in the transformed image is replaced by the Gaussian weighted average of all pixel elements in the corresponding window of the original image.

An example of the blurred-image-subtraction technique is presented in Figure 5. The original image is shown in Figure 3. The top image in Figure 5a is the Gaussian blurred image, and the image in Figure 5b is the difference image. Features in Figure 5a are obviously more blurred than those in Figure 3. In Figure 5b, the crack features are sharpened with bands (different gray levels) on each side of the edges. In addition, the very narrow vertical and horizontal lines (surface topographic features) are now visually detectable and resolvable over the entire image.

The edge-enhancement-by-first-difference technique[1,2,6,7,10] uses a moving window that is a numerical approximation of a spatial first derivative of the pixel amplitudes. In this technique, the amplitude of the central pixel element within the window in the original image is replaced by the sum of the first differences of pixel amplitudes across an oriented line within the moving window. Thus, the resulting image is everywhere a numeric first derivative of the original image. Images that are useful for feature identification and that are also visually pleasing can be generated by using a diagonal edge-enhancement operator that is actually the sum of vertical and horizontal Sobel first-difference edge-enhancement windows. The images that result from the application of the diagonal first-difference edge-enhancement window have sharpened edges and directionally dependent shading, which creates a three-dimensional appearance in the enhanced image.

The results of applying the diagonal first-difference operator to image data acquired with the 10 MHz transducer are shown in Figure 6. Figure 6a is an image of the unenhanced data displayed using the histogram-equalization technique for setting the gray-level breakpoints. All the cure cracks in the sample are now visible because of the longer acoustic depth of field associated with this transducer. Note in particular that both cracks 2 and 3 are visible in this image, although they are somewhat blurred together. The first-difference edge-enhanced version of the image in Figure 6a is shown in Figure 6b. The image in Figure 6b has a pseudo three-dimensional appearance, which produces the illusion that the cracks are elevated above the background. In addition, all the cracks are more distinct and cracks 2 and 3 are visually more easily resolved than in the original image (Figure 6a).

Edge enhancement with a pseudo Marr-Hildreth operator is a two-stage implementation of the technique developed by Marr and Hildreth[11] for locating lines and edges in images. The actual Marr-Hildreth operator is generated by taking the Laplacian (a second-order differential) of a two-dimensional Gaussian. The Marr-Hildreth operator is an optimal tradeoff between Gaussian smoothing for noise suppression and Laplacian high-spatial-frequency emphasis for line or edge detection. The widths of the edges detected or enhanced by this technique are controlled by the values of the standard

deviations in the two-dimensional Gaussian. Very coarse edges are located by using large standard deviations in the Gaussian; very fine or narrow edges are located by using small standard deviations in the Gaussian. Examples of the Marr-Hildreth operator are shown in Figure 7. The multipliers for a 7 by 7 Marr-Hildreth operator with a standard deviation of 0.75 pixel are given in Figure 7a, and a sketch of a one-dimensional operator is shown in Figure 7b.
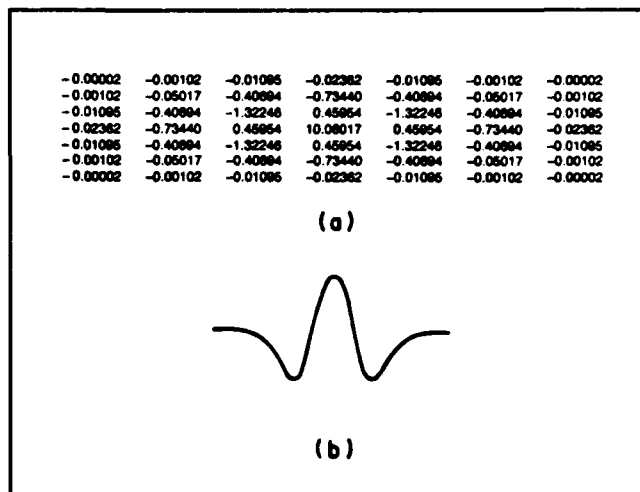
Figure 7—Marr-Hildreth operator with a standard deviation of 0.75 pixel: (a) multipliers; (b) shape of one-dimensional Marr-Hildreth operator.

In the usual application of the technique, smoothing and differentiation take place in a single stage. This implementation requires a larger window size than could be implemented on the authors' computer system. The technique was, therefore, implemented in two stages by first applying a Gaussian filter to the original data and then applying a Laplacian filter to the Gaussian-filtered data. In the results presented in this paper, the pseudo Marr-Hildreth enhanced data were further enhanced through the use of the first-difference diagonal edge-enhancement operator. This significantly improved the visual detectability and resolution of features in the resultant image.

The usefulness of the pseudo Marr-Hildreth technique for enhancing an image generated from noisy data is illustrated in Figure 8. The original noisy image is shown in Figure 8a. The results of applying a 3 by 3 Sobel-type diagonal edge-enhancement operator to the original noisy data without prior noise suppression are shown in Figure 8b. Noise dominates both images, and cracks 2 and 3 are very difficult to resolve even in the enhanced image. The results of applying an edge-enhancing operator after applying a pseudo Marr-Hildreth operator (with its Gaussian filtering) are shown in Figure 8c. Noise is less dominant in the image presented in Figure 8c and cracks 2 and 3 are now visually resolvable, but they are difficult to distinguish from surface topography.

A second very useful application of the pseudo Marr-Hildreth operator is illustrated in Figure 9. The image in Figure 9a was generated from unenhanced data acquired with the 3.5 MHz transducer focused on the back surface of the sample. The images of the cracks are very blurred because of the relatively large focal-spot size of the transducer. Note in particular that cracks 2 and 3 are not visually resolvable in this image. Figure 9b shows the results of applying the 5 by 5 pseudo Marr-Hildreth operator (standard deviation = 0.67 pixel) to the original image data. Much of the blurring of the edges has been removed, and cracks 2 and 3 can just barely be resolved visually. The results of applying a 5 by 5 first-difference edge-enhancement operator to the image data of
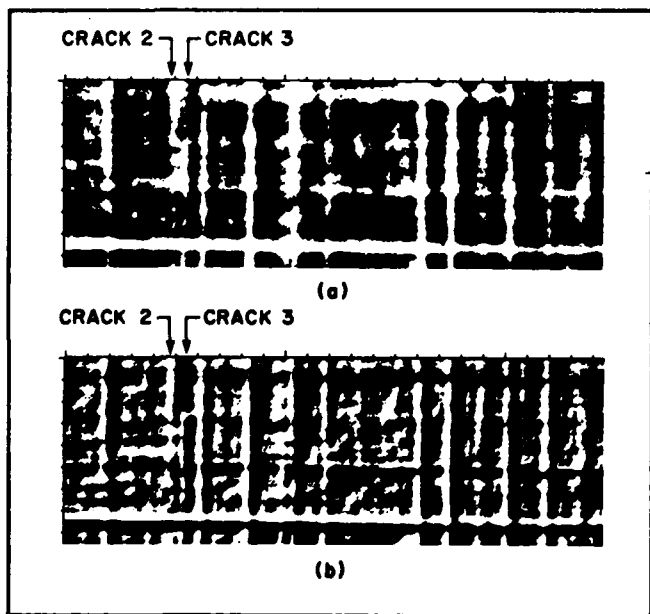
Figure 6—Edge enhancement by diagonal first-difference operator: (a) image from original data using 10 MHz transducer; (b) diagonal first-difference edge enhancement of 6a.

Figure 9b are shown in Figure 9c. All the cracks in that image are much less blurred than they are in the original image of Figure 9a.

SUMMARY

The application of relatively simple digital image-enhancement techniques to ultrasonic C-scan data can significantly improve the detection and resolution of features in images. Images of features can be made more distinct, many features can be made visible simultaneously, noise can be suppressed to allow enhancement of noisy images, and blur can be reduced in those cases in which the blur is due to the use of transducers with large focal-spot sizes.

The reduction of blur with its consequent improvement in feature resolution is especially important for the inspection of thick samples of graphite-epoxy composites. The attenuation of ultrasonic energy at the high temporal frequencies is so large that only frequencies below about 5 MHz can be used to inspect samples that are more than approximately 0.25 in. (6.35 mm) in thickness. At these relatively low frequencies, however, narrow spot sizes are very difficult to achieve, even with focused transducers. The blurring that results from the use of larger focal-spot sizes makes visual detection and resolution of small features very difficult. Thus, digital image-enhancement techniques such as those presented in this article become very important for improving the visual detection of small features in thick samples.

Finally, it must be noted that digital image-enhancement techniques, although useful for improving feature detection and resolution in many images, are not the ultimate solution. As is evident in some of the images presented in this paper (particularly Figure 8), it is sometimes difficult to distinguish between cure cracks and other features in the image even after enhancement techniques have been applied.
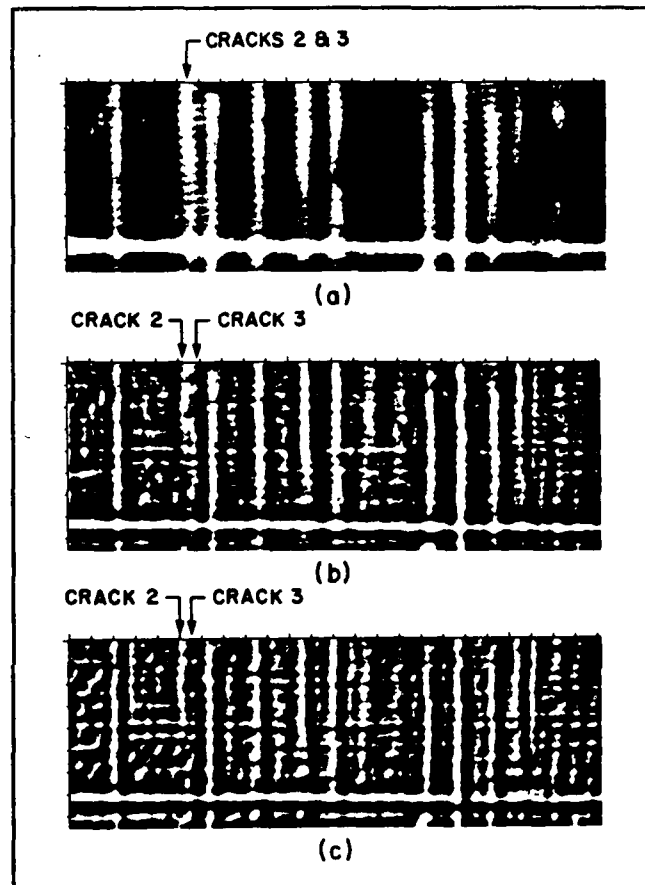
Figure 9—Improved resolution by multistep processing: (a) image from original data; (b) pseudo Marr-Hildreth enhancement of 9a; (c) diagonal first-difference edge enhancement of 9b.

Figure 8—Edge enhancement of noisy data: (a) image from original noisy data; (b) diagonal first-difference edge enhancement of 8a without prior noise suppression; (c) diagonal first-difference edge enhancement after application of pseudo Marr-Hildreth operator to 8a.

References

1. Castleman, K. R., Digital Image Processing, 1979, pp 52–135. Prentice-Hall, Englewood Cliffs, NJ.
2. Gonzalez, R. C., and P. Wintz, Digital Image Processing, 1977, pp 115–182. Addison-Wesley, Reading, MA.
3. Frei, W., and C. Chen, "Fast Boundary Detection: A Generalization and a New Algorithm," IEEE Transactions on Computers, Vol. C-26, No. 10, Oct. 1977, pp 988–998.
4. Andrews, H. C., and B. R. Hunt, Digital Image Restoration, 1977, pp 113–208. Prentice-Hall, Englewood Cliffs, NJ.
5. Lee, J., "Digital Image Enhancement and Noise Filtering by Use of Local Statistics," IEEE Transactions on Pattern Analysis and Machine Intelligence, Vol. PAMI-2, No. 2, Mar. 1980, pp 165–168.
6. Davis, L. S., "A Survey of Edge Detection Techniques," Computer Graphics and Image Processing, Vol. 4, No. 3, Sep. 1975, pp 248–270.
7. Rosenfeld, A., and M. Thurston, "Edge and Curve Detection for Visual Scene Analysis," IEEE Transactions on Computers, Vol. C-20, No. 5, May 1971, pp 562–569.

A–39

8. Hall, J. E., and J. D. Awtrey, "Real-Time Image Enhancement Using 3 × 3 Pixel Neighborhood Operator Functions," *Optical Engineering*, Vol. 19, No. 3, May/June 1980, pp 421–424.
9. Hall, E. L., R. P. Kruger, S. J. Dwyer, D. L. Hall, R. W. McLaren, and G. S. Lodwick, "A Survey of Preprocessing and Feature Extraction Techniques for Radiographic Images," *IEEE Transactions on Computers*, Vol. C-20, No. 9, Sep. 1971, pp 1032–1044.
10. Venetsanopoulos, A. N., and V. Cappellini, "Real-Time Image Processing," in *Multidimensional Systems, Techniques and Applications*, ed. S. G. Tzafestas, 1986, pp 345–399. Marcel Dekker, New York, NY.
11. Marr, D., and E. Hildreth, "Theory of Edge Detection," *Proceedings of the Royal Society of London B*, Vol. 207, No. 1167, 29 Feb. 1980, pp 187–217.
12. Moran, T. J., R. L. Crane, and R. J. Andrews, "High-Resolution Imaging of Microcracks in Composites," *Materials Evaluation*, Vol. 43, No. 5, Apr. 1985, pp 536–540.
13. Martin, R. W., and R. J. Andrews, "Backscatter B-Scan Images of Defects in Composites," in *Review of Progress in Quantitative Nondestructive Evaluation*, Vol. 5, 1986, pp 1189–1198. Plenum Press, New York, NY.

Authors

Brian Frock is a research engineer with the University of Dayton Research Institute. He received a B.A. degree in physics and mathematics from Wilmington College, Wilmington, OH, in 1965, an M.S. degree in physics from the University of Dayton in 1968, and an M.S. degree in engineering management from the University of Dayton in 1981. His research activities include image analysis, application of digital signal-processing technique for image enhancements, and design of experiments for ultrasonic data acquisition. Before joining the Research Institute in 1985, Frock worked in NDE, instrumentation, and process control at Armco Inc. for twelve years.

Richard Martin is an associate research engineer with the University of Dayton Research Institute. He earned a B.S. degree in electrical engineering in 1970 and a B.S. degree in business administration in 1972. Both degrees were received from Ohio University, Athens, OH. His responsibilities include design and implementation of hardware and software for computer control of ultrasonic data-acquisition systems as well as software development for digital signal processing, image analyses, and image enhancements. Previously, Martin was responsible for the system hardware and software design and development for microprocessor-controlled slip-ring and bearing torque experiments.

MARR-HILDRETH ENHANCEMENT OF NDE IMAGES

B.G. Frock†
University of Dayton
Research Institute
Dayton, Ohio 45469

P. Karpur ‡
Systran Corporation
4126 Linden Avenue
Dayton, Ohio 45432

INTRODUCTION

Previous publications [1-5] have demonstrated the usefulness of digital image enhancement techniques for improving visual detection and resolution of features in NDE images. Many of the techniques are high-pass spatial domain convolution filters [6] which are used to enhance the appearance of edges by removing blur. Two of the major advantages of the more popular edge enhancement operators are their ease of implementation and their rapidity of execution [7]. This makes them very useful for rapid "screening" of images. Their major disadvantages are that they emphasize "noise" as well as edges, and some are directionally dependent operators which tend to suppress features that are not aligned in the "preferred" direction.

The problems of preferred orientation and noise enhancement can be minimized if "restoration" techniques such as Wiener deconvolutions [8] are applied. Unfortunately, these techniques are usually computationally intensive and, when applied in the two-dimensional Fourier domain, require highly specialized software that may be expensive or difficult to implement. Implementation of the two-dimensional Wiener deconvolution technique in small computers often requires that the size of the image be severely restricted.

The Marr-Hildreth operator was developed for detection of the intensity changes [9] in images. As Marr and Hildreth demonstrated, this bandpass operator is an optimal tradeoff between the high spatial frequency emphasis necessary for edge enhancement and the high spatial frequency attenuation necessary for noise suppression. Since it can be implemented as a convolution operator in the spatial domain, it can be applied without highly specialized software. The convolution should execute rapidly so long as the "size" of the Marr-Hildreth operator is small. The ease of implementation, rapidity of execution, lack of "preferred" orientation and ability to enhance edges in the presence of noise should make it useful for rapid enhancement of images prior to attempting more difficult and time-consuming techniques.

MARR-HILDRETH OPERATOR

This operator is the two-dimensional second derivative (Laplacian) of a two-dimensional Gaussian. The equation in rectangular coordinates is:

$$MH = A^* \left\{ \left(\frac{X-\mu_x}{\sigma_x^2}\right)^2 + \left(\frac{Y-\mu_y}{\sigma_y^2}\right)^2 - \frac{1}{\sigma_x^2} - \frac{1}{\sigma_y^2} \right\} e^{-\frac{1}{2}\left[\left(\frac{X-\mu_x}{\sigma_x}\right)^2 + \left(\frac{Y-\mu_y}{\sigma_y}\right)^2\right]} \quad (1)$$

where μ_x and μ_y are the mean values in the X-direction and the Y-direction, σ_x and σ_y are the standard deviations in the X-direction and the Y-direction, and "A" is a multiplicative constant. The shapes and extents of the filters in the frequency and spatial domains are controlled by the values of the standard deviations as is illustrated in Fig. 1. Small values for the standard deviations produce a narrow operator in the spatial domain and a broad operator in the frequency domain. This narrow spatial domain operator places more emphasis on the higher frequencies. A narrow spatial domain operator will be very effective for removing blur from an image, but may amplify high spatial frequency noise. Large values for the standard deviations result in a broad operator in the spatial domain and a narrow operator in the frequency domain. The broad spatial domain operator places more emphasis on the lower frequencies. Such an operator will remove less blur from an image, but will also not amplify high frequency noise.
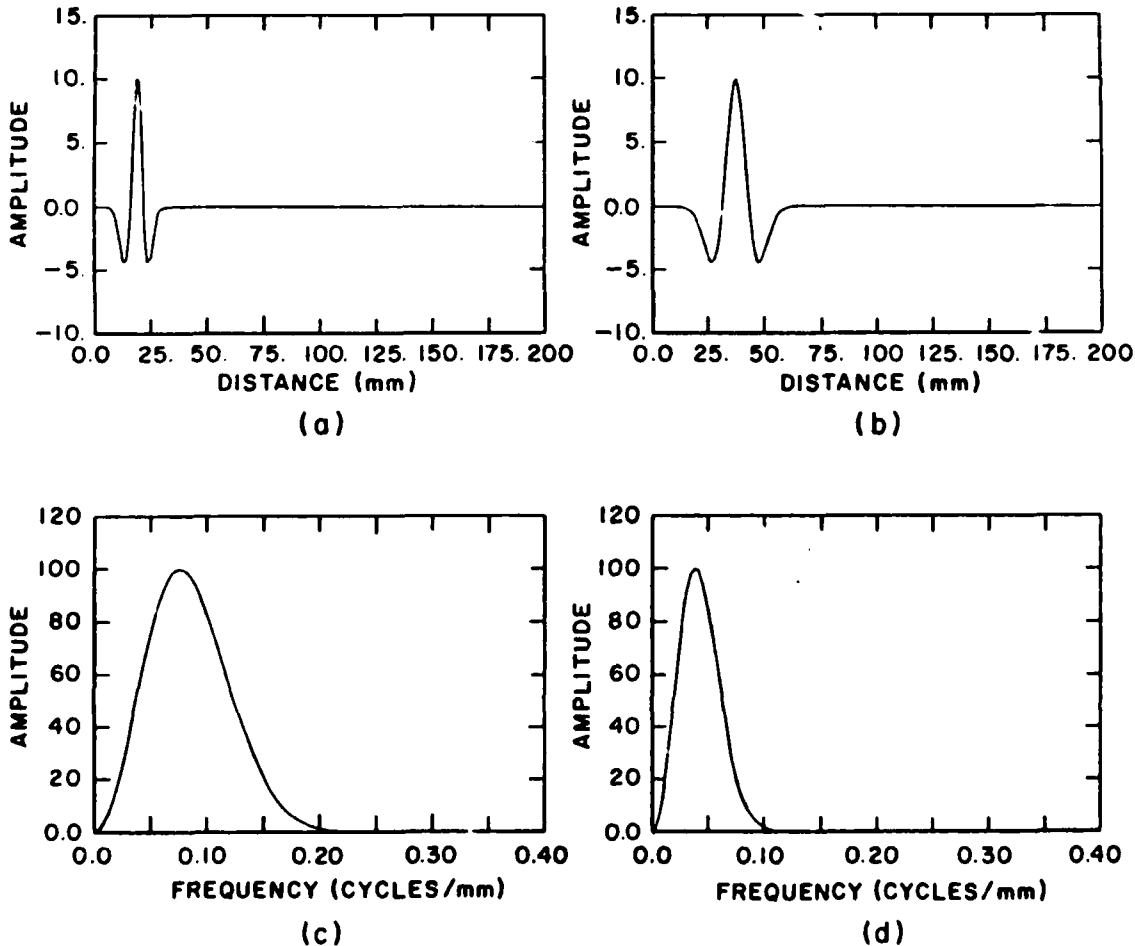
Fig. 1. Marr-Hildreth convolution operators: (a) Spatial Domain, $\sigma = 3$; (b) Spatial Domain, $\sigma = 6$; (c) Fourier amplitude spectra of "a"; (d) Fourier amplitude spectra of "b".

DATA ACQUISITION

Experimental Data

Ultrasonic C-scan data were acquired from a 32-ply thick graphite epoxy composite panel. A computer controlled, immersion C-scanning technique was used to acquire, digitize and store ultrasonic data from 40,000 discrete points on the sample. These discrete points were separated by 0.025mm in the two orthogonal directions. The sample was insonified with a Precision Acoustic Device's low-frequency (3MHz) acoustic microscope transducer excited with a spike pulse and focused on the entry surface of the sample. Data were collected from a 120ns wide gate located over the first negative going cycle of the rf entry surface echo. The minumum value (sign included) in that gate was digitized and stored at each of the 40,000 discrete sampling points. The C-scan images generated from this data were essentially topographic maps of the sample's entry surface with depth variations encoded in the amplitude values at the discrete points. A magnified optical image of the sample's surface is shown in Fig. 2. The major surface topographic feature in the image is the weave pattern, i.e., the impression of the bleeder cloth used during fabrication.
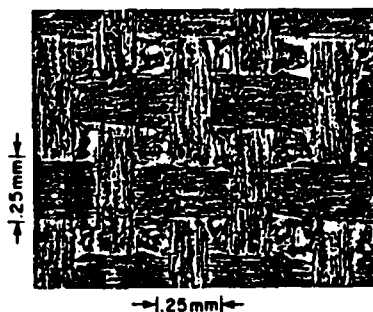
Fig. 2.   Optical microscope image of graphite/epoxy sample's surface
(Magnification = 50X).

Simulated Noise

Noisy data were generated by adding computer simulated noise to the nearly-noise-free experimental ultrasonic data. The amplitude of the noise was Gaussian distributed with the standard deviation set at 3.3% of the maximum amplitude value of the experimental data set.

One-Dimensional Simulated Data

Simulated studies of one-dimensional data were undertaken to help determine some of the capabilities and limitations of the Marr-Hildreth convolution operator. The studies consisted of simulating a sensor's point spread function with a one-dimensional Gaussian, and then convolving the point spread function with a one-dimensional "ideal" image feature to produce a simulated sensor-generated image. This simulated image was then convolved with Marr-Hildreth operators and the results were compared with results obtained by Wiener deconvolution of the Gaussian point spread function from the simulated sensor image.

RESULTS

Experimental Nearly-Noise-Free Data

Unenhanced ultrasonic data were used to generate the image in Fig. 3a. This image of the sample's entry surface is very blurred, and only portions of the weave pattern are visually resolvable. The results of applying

Marr-Hildreth operators with different standard deviations (1.0 and 2.0 pixels) to the image data of Fig. 3a are shown in Figs. 3b and 3c. The weave pattern on the sample's surface is visually resolvable in both of these enhanced images. The effects of choosing different values for the standard deviations are also clearly evident in these images and in the pixel amplitude plots in Figs. 3e and 3f. The amplitude plots are from horizontal line 45 of each of the images in Figs. 3a, 3b and 3c. The Marr-Hildreth operator with the smaller standard deviation removes more blur, but also tends to emphasize more noise in the image. The use of a Marr-Hildreth operator with a larger standard deviation generates images with less noise, but less blur is removed form the images. The Marr-Hildreth convolutions were implemented as discrete 13 x 13 moving window operations. When performed on a MicroVax computer, the convolution operations on the 40,000 point images required about 200 seconds per image.

LINE #45   LINE #45

(a)   (b)   .25mm   (c)

192   192   192

128   128   128

64   64   64

Pixel Amplitudes   Pixel Amplitudes   Pixel Amplitudes
0 Line #45   0 Line #45   0 Line #45

(d)   (e)   (f)
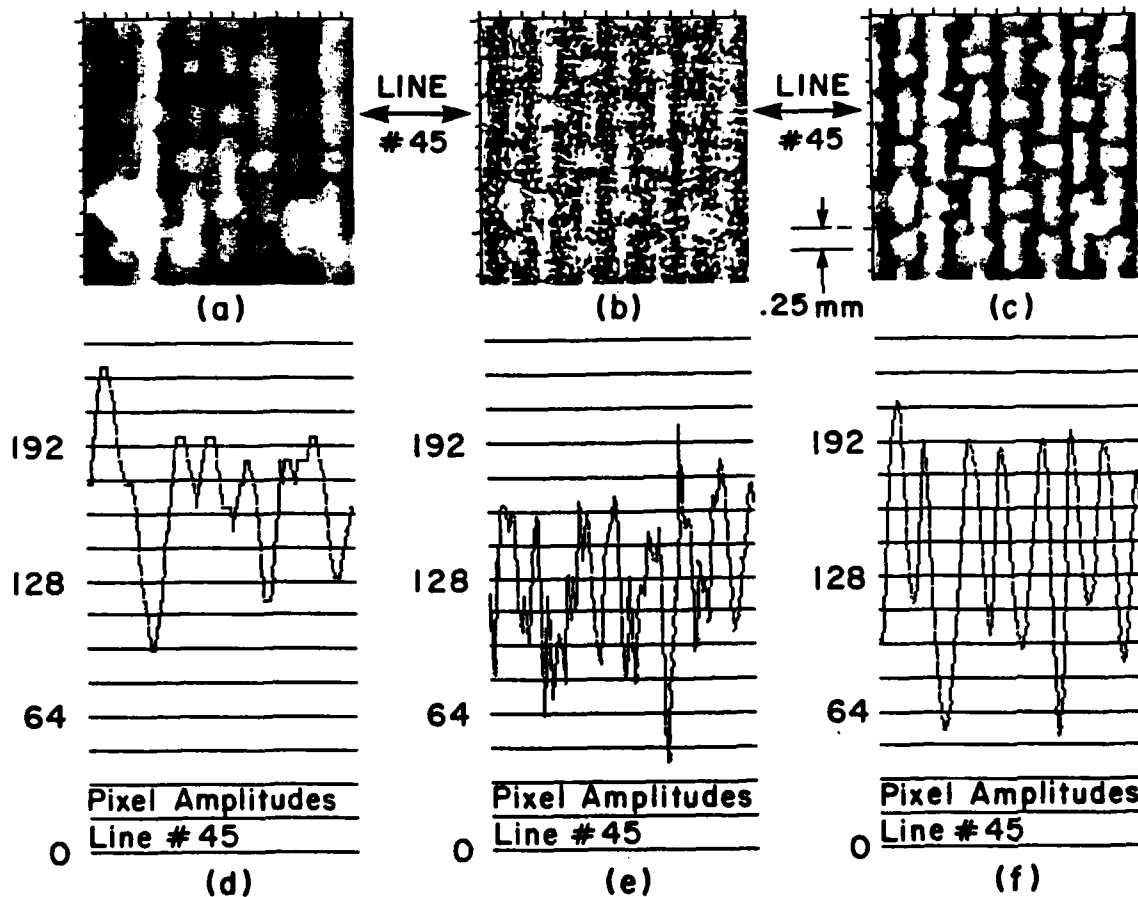
Fig. 3.   Ultrasonic images of graphite/epoxy sample's surface:
           (a) Original data; (b) Marr-Hildreth operator (σ=1) convolved
           with "a"; (c) Marr-Hildreth operator (σ=2) convolved with "a";
           (d) through (f) Pixel amplitudes along lines 45 of "a" through
           "c".

A two dimensional Fourier domain Wiener filter deconvolution [8] was applied to a portion of the ultrasonic data for comparative purposes. The point spread function of the transducer was generated from scans of a thin wire (0.076mm). The results of the Wiener deconvolution are displayed in Fig. 4a. This deconvolved image is visually similar to the images resulting form Marr-Hildreth convolutions (see Fig. 3). A plot of the pixel amplitudes from horizontal line 45 of the image in Fig. 4a is shown in Fig. 4b. This amplitude plot is also quite similar to that resulting from Marr-Hildreth convolutions (see Fig. 3).

(a)   (b)
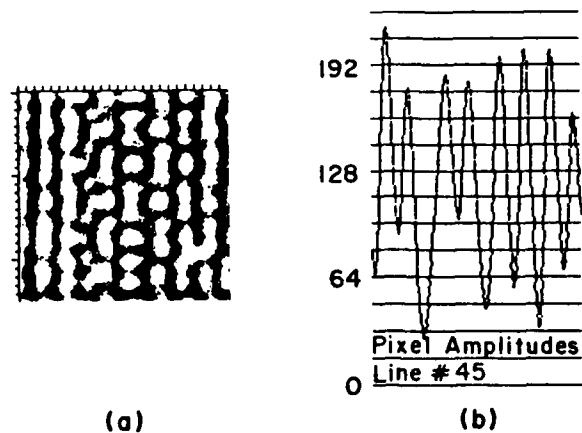
Fig. 4.   Weiner deconvolution of data in Fig. 3a: (a) Deconvolved image;
           (b) Pixel amplitude plot from horizontal line 45 of "a".

Noisy Data

     The results of adding Gaussian noise to the image in Fig. 3a are
shown in Fig. 5a. The noise appears as isolated light and dark "speckles"
in the image. Marr-Hildreth operators with different standard deviations
(1 and 2 pixels) were convolved with the "noisy" data. The resulting
images are presented in Figs. 5b and 5c. Amplitude plots from horizontal
line number 45 for each of the images in Fig. 5 are also shown in Fig. 5.
The narrower Marr-Hildreth operator (σ = 1) reduces the blur, but
emphasizes the noise which is present in the data. The broader Marr-
Hildreth operator (σ = 2) removes less blur, but also generates results
with less noise. The amplitude plots in Figs. 5d, 5e, and 5f substantiate
the visual interpretations of the images in Figs. 5a, 5b, and 5c.
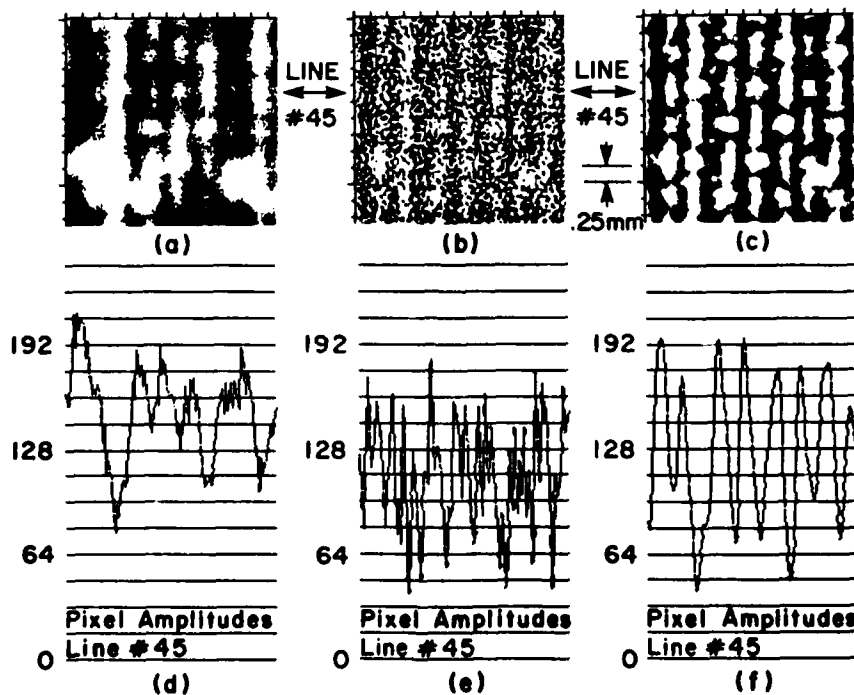

Fig. 5.   "Noisy" image of graphite/epoxy sample's surface: (a)
           Unenhanced; (b) Marr-Hildreth operator (σ = 1) convolved
           with "a"; (c) Marr-Hildreth operator (σ = 2) convolved
           with "a"; (d) through (f) Pixel amplitudes along lines 45
           of "a" through "c".

A-45

One-Dimensional Simulated Data

The Gaussian point spread function, an "ideal" image and the simulated sensor generated image are shown in Figs. 6a, 6b, and 6c respectively. The standard deviation of the point spread function was 5 mm and the "ideal" image consisted of 30 adjacent impulse spikes. Fig. 7a shows the results of convolving the Marr-Hildreth operator ($\sigma = 3$) with the simulated sensor generated image of Fig. 6c. The results of Wiener deconvolution of the point spread function (Fig. 6a) from the simulated sensor generated image of Fig. 6c are shown in Fig. 7b. The results of convolving the Marr-Hildreth operator with the simulated sensor generated image are illustrated in Fig. 7a. Some of the artifacts which might result from application of a Marr-Hildreth convolution operator are evident in Fig. 7a. There are deep negative troughs present on the outer edges of the feature, and there is a shallow trough in the center of the feature. The "deep" negative troughs on either side of the "feature" will appear in an image as dark colored bands at the boundaries of the "feature". This banding actually helps the visual/neural system detect [10] the "feature". The shallower trough which has been created in the center of the image "feature" might well result in the visual misinterpretation of the image "feature" as being two smaller features rather than the boundaries of a single larger feature.

(a)

(b)

(c)
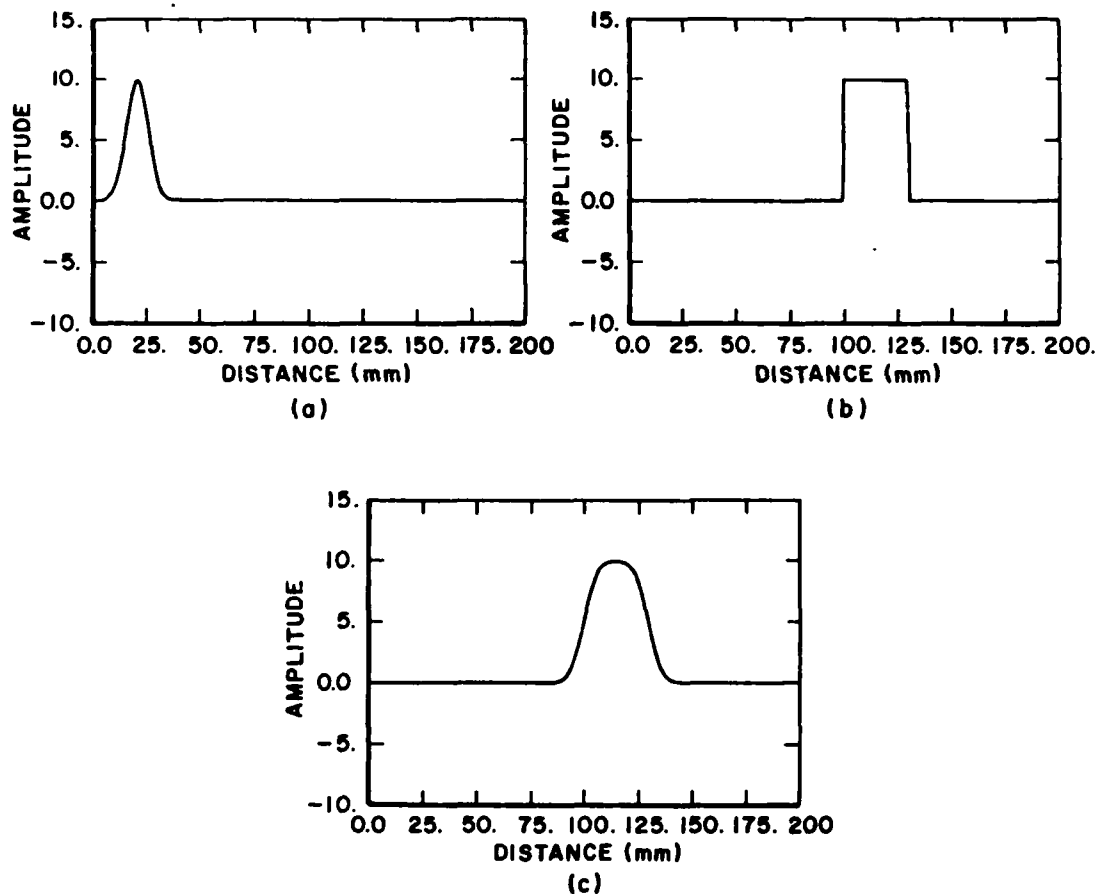
Fig. 6. Simulated feature: (a) Simulated point spread function of sensor; (b) Ideal feature; (c) Simulated sensor generated feature ("a" convolved with "b").
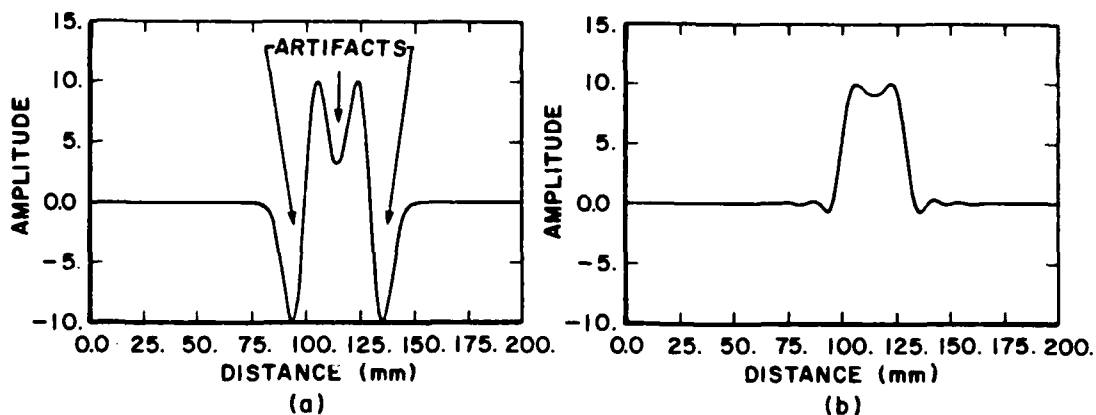
Fig. 7.   Enhancement of a simulated sensor generated image: (a) Marr-
          Hildreth operator (σ=3) convolved with Fig. 6c; (b) Wiener
          deconvolution of Fig. 6c.

CONCLUSIONS

    We have shown that the Marr-Hildreth operator can be used to remove
blur in ultrasonic NDE images even in the presence of noise. It is easily
implemented as a spatial domain convolution operator, and, as such does
not require sophisticated or highly specialized software for its appli-
cation. The spatial domain convolution executed rapidly, and in the case
of the image data examined in this study, produced results similar to
those achieved with a two-dimensional Fourier domain Wiener filter. We
have also demonstrated that artifacting can occur with the application of
the Marr-Hildreth operator and have attempted to explain how that art-
ifacting might affect the visual interpretation of a Marr-Hildreth enhanced
image. Despite this artifacting, the Marr-Hildreth operator can serve as
a useful tool for the rapid enhancement of NDE images prior to the appli-
cation of more sophisticated and time-consuming enhancement techniques.

ACKNOWLEDGEMENTS

REFERENCES

1.   B.G. Frock and R.W. Martin, "Applications of Digital Image
     Enhancement Techniques for Improved Ultrasonic Imaging of Defects in
     Composite Materials," Review of Progress in Quantitative NDE, Vol. 6A,
     edited by D.O. Thompson and D.E. Chimenti, (Plenum Press, New York,
     New York, 1987), pp. 781-789.

2.   M.J. Closier, "Automatic Product Analysis Using X-Rays," NDT
     International, April 1981, pp. 59-65.

3.   M.H. Jacoby, R.S. Loe and P.A. Dondes, "Computer Evaluation of Real-
     Time X-Ray and Acoustic Images," SPIE, Applications of Digital Image
     Processing IV, Vol. 359, 1982, pp. 273-277.

4. J. Boutin and C. Forget, "Powerful Image Analysis Techniques for Quantitative Measurements of Materials," Metal Progress, April 1988, pp. 24-25.

5. R.S. Gilmore, R.E. Joynson, C.R. Trzaskos and J.D. Young, "Accoustic Microscopy: Materials Art and Materials Science," Review of progress in Quantitative NDE, Vol. 6A, edited by D.O. Thompson and D.E. Chimenti, (Plenum Press, New York, New York, 1987), pp. 553-562.

6. L.S. Davis, "A Survey of Edge Detection Techniques," Computer Graphics and Image Processing, 4, 1975, pp. 248-270.

7. A.N. Vcnetsanopoulos and V. Cappellini, "Real-Time Image Processing," Multidimensional Systems, Techniques and Applications, edited by S.G. Tzafestas (Marcel Dekker, Inc., New York, New York, 1986), pp. 345-399.

8. R.C. Gonzalez and P. Wintz, Digital Image Processing (Addison-Wesley Publishing Company, Reading, Massachusetts, 1977), pp. 210-211.

9. D. Marr and E. Hildreth, "Theory of Edge Detection," Proceedings of the Royal Society of London B, Vol. 207, 1980, pp. 187-217.

10. E.L. Hall, R.P. Kruger, S.J. Dwyer, D.L. Hall, R.W. McLaren and G.S. Lodwick, "A Survey of Preprocessing and Feature Extraction Techniques for Radiographic Images," IEEE Transactions on Computers, Vol. C-20, No. 9, September 1971, pp. 1032-1044.

IMPROVING ULTRASONIC NDE IMAGES WITH PSEUDO WIENER FILTERING AND MARR-HILDRETH ENHANCEMENT TECHNIQUES

P. Karpur and B. Frock

INTRODUCTION

Nondestructive evaluation (NDE) is the process of assuring manufacturing integrity and in-service reliability of engineering materials and products without affecting the form or the usefulness of the material being tested. Nondestructive evaluation is used in various industries such as aerospace, aviation, defense, nuclear, construction, metals and nonmetals, etc. The diverse types of products which need to be tested require the use of many methods of NDE. Of the many types of NDE techniques currently being used, this paper will discuss only ultrasonics, and, in particular, ultrasonic C-scan imaging techniques. C-scan images are views of specific planes within a material. Unfortunately, these views are often blurred by the finite dimensions of the ultrasonic transducer's point-spread function. We will discuss two methods for removing much of this blur and will illustrate some of their advantages and disadvantages with images generated from both real and simulated data.

ULTRASONIC NDE

The most common methods of ultrasonic inspection are the pulse echo and through-transmission techniques. While the pulse echo technique is implemented by using the same transducer for both transmitting and receiving the signals, the through-transmission technique is implemented by using separate transducers for transmission and reception. The received ultrasonic signal will carry information about the material through which it has passed and also about any anomalies that might be present in the material. Such information carried by the received wavefront can be used to detect, locate, classify and size the anomaly as well as to characterize the material.

The information resulting from the nondestructive test is usually presented in the form of A-scans (Fig. 1a), B-scans (Fig. 1b) or C-scans (Fig. 1c). An A-scan is an amplitude trace with respect to time. A B-scan is made by compiling many A-scans together and is useful for imaging a vertical section of the material. A C-scan is obtained by displaying the amplitudes received from a particular depth within the material and over a plane parallel to the motion of
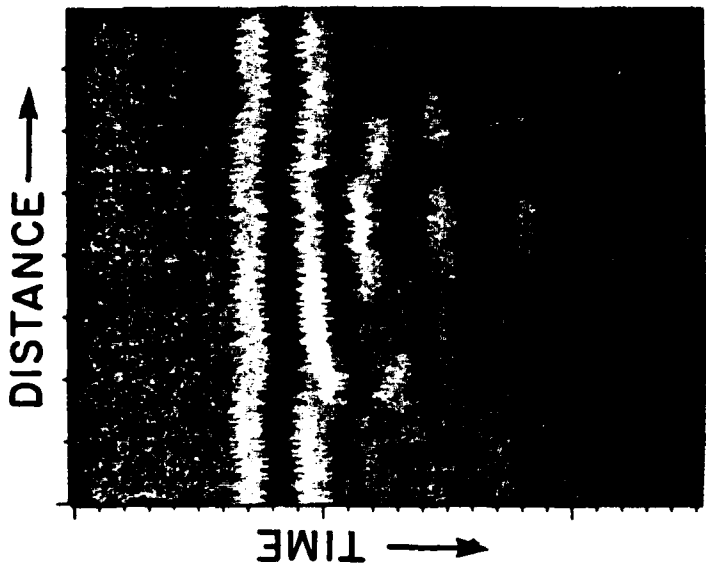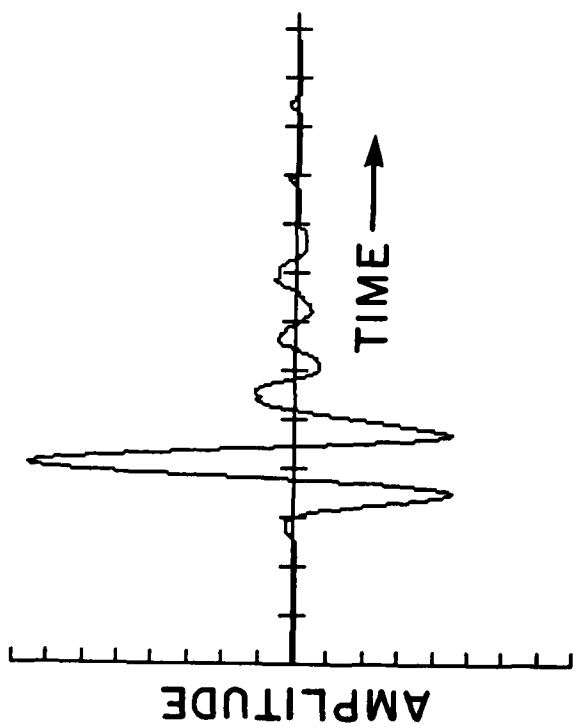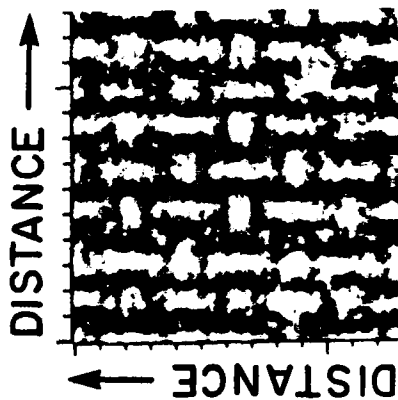
Fig. 1. Ultrasonic scans: (a) Rf A-scan; (b) B-scan and (c) C-scan.

the transducer. The remainder of this paper concentrates on the processing of C-scan images. The techniques discussed are also applicable, in principle, to the B-scan images.

C-SCAN, POINT-SPREAD FUNCTION AND IMAGE BLURRING

C-scan images provide a close representation of the object which is being imaged. However, the images are often 'blurred' because of the point-spread function (PSF) or the transfer function of the transducer being used for the imaging as illustrated in Fig. 2. The blurring effect is due to the fact that the ultrasonic beam being used is a spreading wavefront rather than a 'pencil beam'. Hence the ultrasonic image loses the sharp, well defined clarity which is possible in an optical image. Such a blurring process is described as 'convolution' in signal processing terminology. Deconvolution or deblurring can be performed using many signal and image processing techniques.

(a)   **(b)**   **(c)**
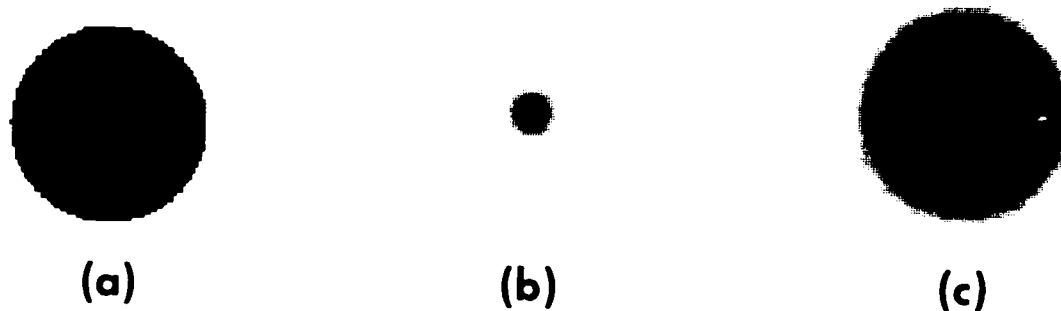
Fig. 2.   Simulated blurring of disk-shaped object: (a) Original disk-shaped object; (b) Point-spread function and (c) Blurred image of disk-shaped object.

IMAGE PROCESSING FOR IMAGE ENHANCEMENT AND DEBLURRING

Image enhancement and deblurring can be performed by many techniques such as Marr-Hildreth filtering, Wiener filtering and deconvolution. The first two techniques will be discussed next.

Marr-Hildreth Filtering

The Marr-Hildreth operator is an edge enhancement filter. The edges appear in ultrasonic images as a change in the local mean value of the image amplitude. The Marr-Hildreth operator is the Laplacian of a Gaussian function represented by the equation below:

$$\nabla^2 G(x,y) = \frac{1}{\pi \sigma_x \sigma_y} \left[\left(\frac{x-\mu_x}{\sigma_x^2}\right)^2 + \left(\frac{y-\mu_y}{\sigma_y^2}\right)^2 - \frac{1}{\sigma_x^2} - \frac{1}{\sigma_y^2} \right] \mathrm{Exp}\,(\zeta) \tag{1}$$

where,

$$\zeta = -\frac{1}{2}\left[\left(\frac{x-\mu_x}{\sigma_x}\right)^2 + \left(\frac{y-\mu_y}{\sigma_y}\right)^2\right]$$

From the equation, it can be seen that the filter finds the rate of change of the slope of the image surface. Thus, any sudden change in slope is enhanced more than a gradual change. This results in enhanced and sharp edges. Figure 3 shows a three-dimensional view of a Marr-Hildreth operator.
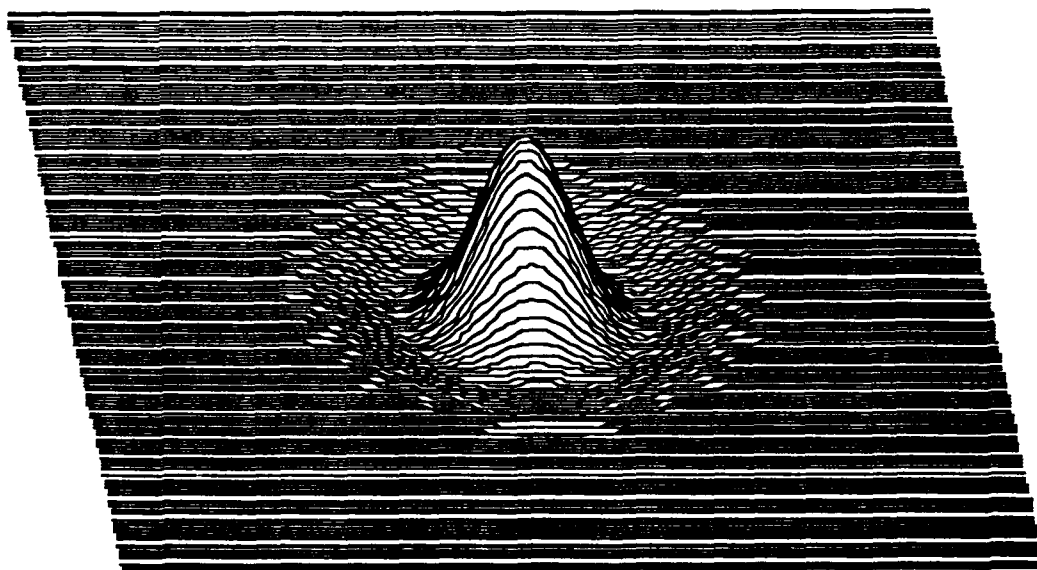
Fig. 3.   Spatial domain image of Marr-Hildreth operator.

Wiener Filtering

Wiener filtering, in the frequency domain, is represented by the following equation:

$$\text{Pseudo-Wiener Filter} = \frac{H^{\cdot}(w_x, w_y)}{|H(w_x, w_y)|^2 + A} \qquad (2)$$

The equation shows that the filter is similar to a deconvolution filter but for the presence of an additive constant term, 'A', in the denominator. The constant term serves as an estimate of the noise content of the image. Since the Wiener filtering process is almost an inverse of the convolution process which produced the blur of the image, Wiener filtering results in an object estimate rather than an edge enhancement. Figure 4 shows a Wiener filter in the spatial domain.
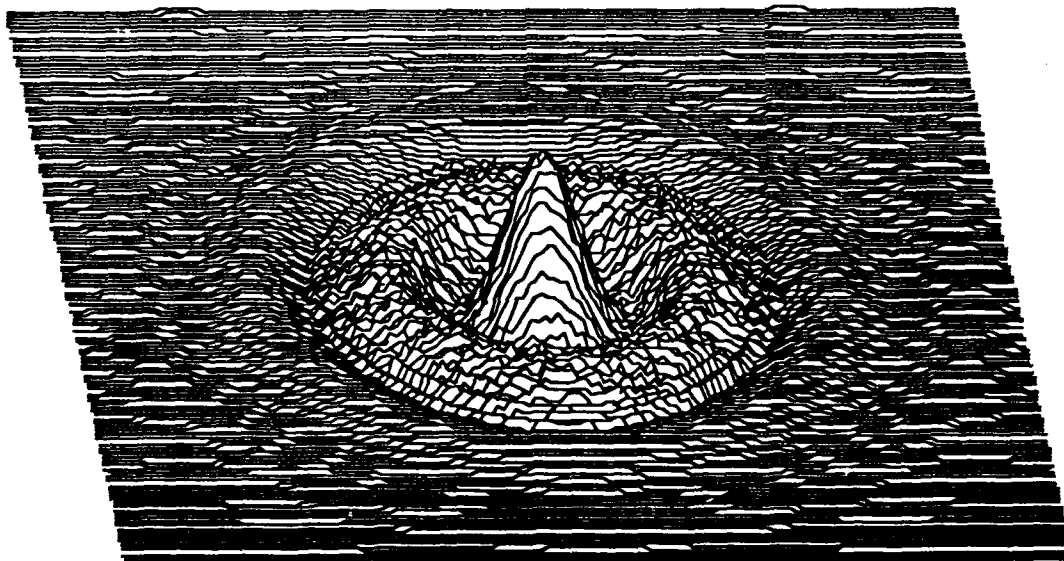
Fig. 4.   Spatial domain image of Wiener filter.

RESULTS

Images of a Penny

Figure 5a shows an ultrasonic C-scan image of part of the monument side of a penny, with each pixel in the image representing a 0.025mm (0.001 inch) by 0.025mm area of the penny. The blurring of the letters in the phrase, "E PLURIBUS UNUM", are illustrative of the problems caused by the relatively large focal spot sizes of ultrasonic transducers. This blurring was significantly reduced by the use of a Marr-Hildreth spatial domain convolution operator with both standard deviations set to 2.25 pixels (see Fig. 5b). All letters in "E PLURIBUS UNUM", while still blurred, are legible. Further deblurring and improvement in legibility of the letters were achieved by application of a variable gain filter to the Marr-Hildreth convolved data (see Fig. 5c). The gain applied by this filter to each image pixel is dependent upon the local contrast, with higher gain being applied in low contrast regions. Thus, features in low contrast regions of the image are emphasized. Unfortunately, noise in the image is also emphasized by this filter.

Results of Fourier domain Wiener filtering of the original image data are shown in Fig. 5d. Legibility of the letters is better than in the original image, but the improvement is not as good as was achieved by use of the combination of Marr-Hildreth convolution and variable gain filtering. Application of the variable gain filter to the Wiener filtered data further improved the legibility of the image features. The letters in this image (Fig. 5e) are as easily recognizable as those in the image generated by post filtering of the Marr-Hildreth convolved data (Fig. 5c).

Images of a Ruler

An optical image and an unenhanced ultrasonic C-scan image of part of a stainless steel ruler are presented in Figs. 6a and 6b respectively. The rulings (clearly visible in the optical image) are separated by 0.25mm (0.010 inch). Even though each pixel in the ultrasonic image represents 0.050mm (0.002 inch), the sensor induced blurring prevents resolution of the rulings and the numerals. Application of the Marr-Hildreth operator followed by variable gain filtering
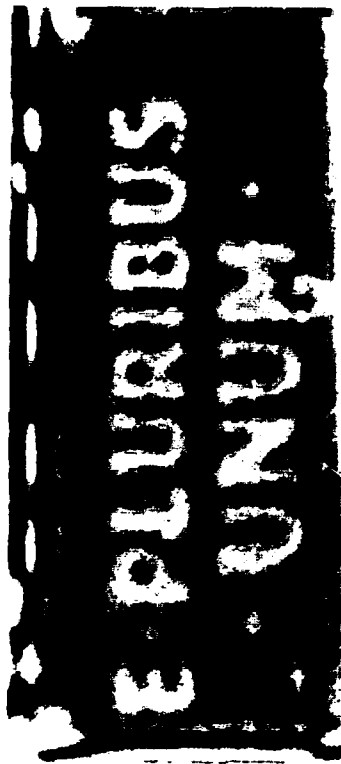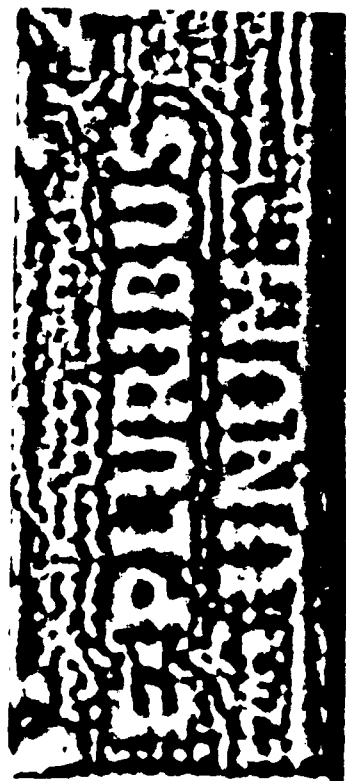
Fig. 5. Images of penny: (a) Ultrasonic C-scan; (b) Marr-Hildreth enhancement of "a"; (c) Wiener filtering of "a"; (d) Variable gain filtering of "b" and (e) Variable gain filtering of "c".

A-55

reduces the blurring sufficiently to allow visual resolution of the numerals and the rulings (see Fig. 6c).

Figure 6d shows an image of the ruler after Fourier domain Wiener filtering followed by variable gain filtering. Again, blurring has been significantly reduced and both numerals and rulings are visually identifiable.
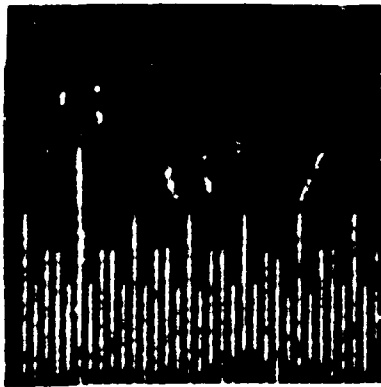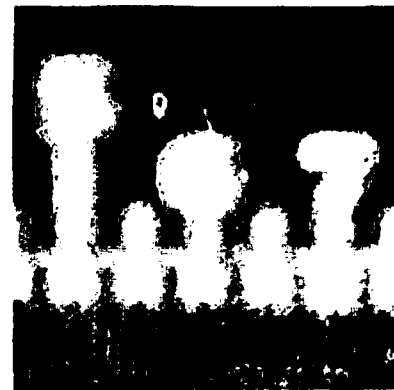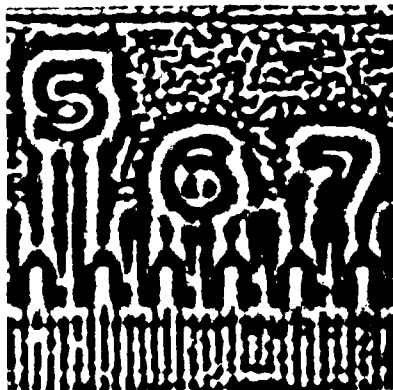
Fig. 6.   Images of ruler: (a) Optical; (b) Ultrasonic C-scan; (c) Variable gain filtering after Marr-Hildreth enhancement of "b" and (d) Variable gain filtering after Wiener filtering of "b".

Graphite/Epoxy Composite Surface Image

An optical image and an ultrasonic C-scan image of the surface of a graphite/epoxy composite are shown in Figs. 7a and 7b respectively. The optical image clearly illustrates the weave pattern resulting from the use of a bleeder cloth during fabrication. The weave pattern is only partially visible in the ultrasonic image, however, and is blurred even in those parts of the image where it is visible. Application of the Marr-Hildreth operator (with standard deviations of 1.5 pixels) significantly reduces the blur and yields an image (Fig. 7c) in which the weave pattern is everywhere visible.

Wiener filtering of the ultrasonic C-scan data also reduces blur and yields an image (Fig. 7d) in which the weave pattern is everywhere visible. In this case, Marr-Hildreth convolution yields an image which more closely resembles the optical image.

Noisy Images

Both Marr-Hildreth convolution and pseudo-Wiener deconvolution techniques can be applied to images with significant amounts of noise, but the images which result will be somewhat degraded when compared with near-noise-free images. Figure 8a shows a noisy, unenhanced ultrasonic C-scan image of the penny. The "noise" was introduced by adding randomly generated, Gaussian distributed amplitude values to the C-scan data used to generate Fig. 5a. The standard deviation of the Gaussian noise amplitude distribution was chosen to be 25 percent of the maximum amplitude value in the original image data. Figure 8b shows the results of Marr-Hildreth convolution followed by variable gain filtering. The results of pseudo-Wiener deconvolution followed by variable gain filtering are presented in Fig. 8c. The letters are visually identifiable, but the noise has resulted in considerable visual degradation in the enhanced images (see Figs. 5d and 5e).

Advantages/Disadvantages of the Techniques

The implementation of the Marr-Hildreth convolution operator in the spatial domain is relatively straight forward and requires no special transformation

(a)

(b)

(c)

(d)

.25 mm
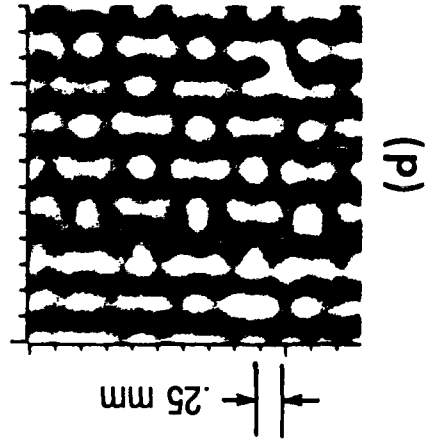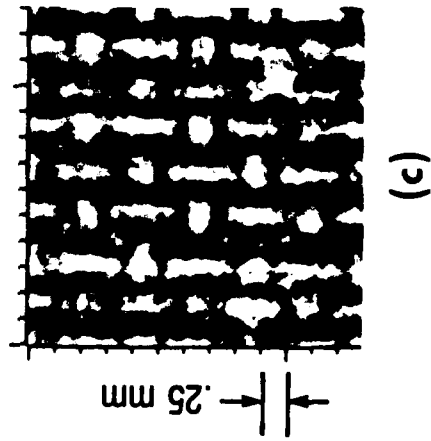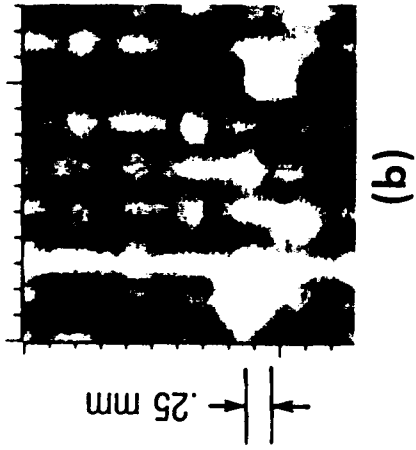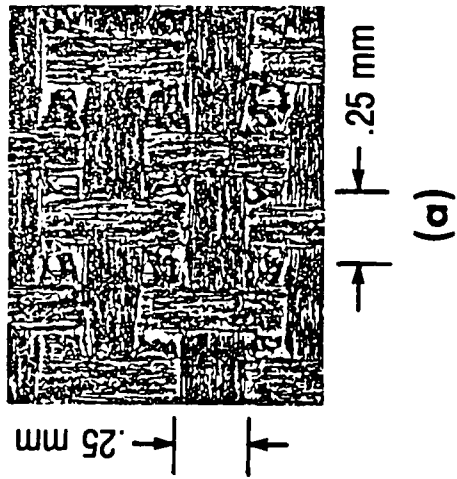
Fig. 7. Images of surface of graphite/epoxy composite: (a) Optical; (b) Ultrasonic C-scan; (c) Marr-Hildreth enhancement of "b" and (d) Wiener filtering of "b".
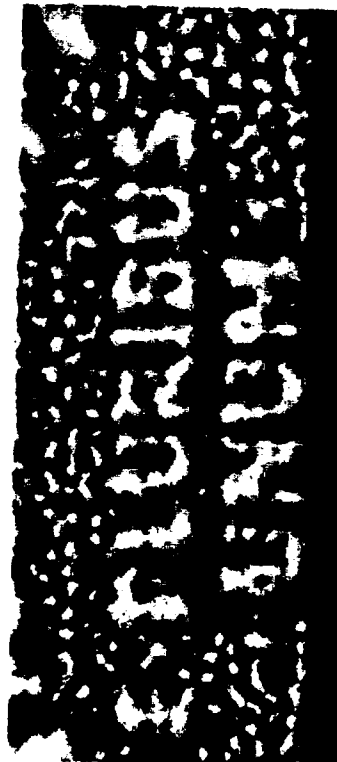
Fig. 8. Noisy image of penny: (a) Noisy ultrasonic C-scan; (b) Variable gain filtering after Marr-Hildreth enhancement of "a" and (c) Variable gain filtering after Wiener filtering of "a".

software. Also, as long as the operator size is not large, the execution time is short, even without special devices such as array processors. By contrast, the Fourier domain implementation of the Wiener filter is much more complex and requires specialized software, i.e., two-dimensional Fourier transformation software. Execution times are generally much longer than for the Marr-Hildreth spatial domain operators, and, in cases such as have been presented in this paper, Wiener filtering does not offer any visually apparent advantages over the Marr-Hildreth convolution operation.

There is, however, a very significant difference between the two techniques. The Marr-Hildreth operator enhances edges of image features by differentiation, whereas the Wiener filter provides estimates of the actual features in the image. This difference is illustrated in the images of Fig. 9. Figure 9a is a computer generated image of a "perfect" disk-shaped reflector. Figure 9b shows the same disk as it might appear in an ultrasonic C-scan image with blurring from the finite point-spread function of the ultrasonic transducer. Figures 9c and 9d show the results of applying a spatial domain Marr-Hildreth convolution operator and a Fourier domain Wiener filter respectively to the blurred image of Fig. 9b. The images in Figs. 9c and 9d are significantly different. Both techniques have removed some of the "sensor induced" blur, but application of the Marr-Hildreth operator has produced a ring-shaped artifact at the perimeter of the disk. This artifact is the result of the numerical second derivative which the Marr-Hildreth operator performs on the image data. Because of this differentiation, regions of constant intensity (or constant change in intensity) are set to zero. Both the background and the interior of the disk are of constant intensity. Those regions are transformed to zero intensity by the convolution, whereas the edges are set to high intensity values, resulting in the ring-shaped image. The Wiener filter, however, produces an estimate of the "actual" object while deblurring the image of that object. There is some characteristic ripple superimposed on the deblurred image, but that ripple is minimal in this case.
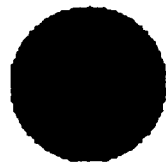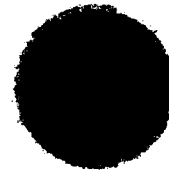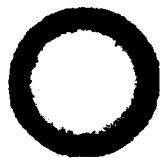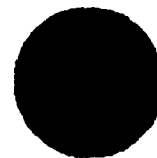
Fig. 9. Artifacting: (a) Disk-shaped object; (b) Blurred image of "a"; (c) Marr-Hildreth enhancement of "b" and (d) Wiener filtering of "b".

SUMMARY

We have demonstrated that the spatial domain Marr-Hildreth convolution operator and Fourier domain Wiener filter can be used to remove some of the sensor induced blur in ultrasonic C-scan images. This reduction in blur may lead to significant improvements in visual detection and identification of features in the images. Implementation of the spatial domain Marr-Hildreth operator is considerably simpler than is the implementation of the Fourier domain Wiener

A-61

filter. Also, execution times for Marr-Hildreth convolutions are usually much shorter than those for the Wiener filtering operation. We have also demonstrated that significant artifacting can result from application of the Marr-Hildreth operator due to the differentiation that this operator performs. The Wiener filter, however, does provide an estimate of the object which is present in the image. The Marr-Hildreth operator with its rapid execution times can be used for rapid screening enhancements, with Wiener filtering used in cases where an object estimate is required.

ACKNOWLEDGMENTS

TWO DIMENSIONAL PSEUDO-WIENER FILTERING IN ULTRASONIC

IMAGING FOR NONDESTRUCTIVE EVALUATION APPLICATIONS

Prasanna Karpur
Visiting Scientist
NDE Branch, Materials Laboratories, AFWAL/MLLP
Wright Patterson Air Force Base, OH 45433

Brian G. Frock
University of Dayton Research Institute
Dayton, OH 45066

ABSTRACT

This paper deals with the use of a two dimensional pseudo-Wiener filter for ultrasonic image enhancement. Experimental results are presented to demonstrate the effectiveness of the technique for the improvement of the lateral resolution and image enhancement of ultrasonic images in materials such as graphite/epoxy composites and stainless steel. The difficulties encountered in the implementation of the filter will be delineated. Methods of overcoming some of these 'implementational hurdles' will be suggested.

INTRODUCTION

Ultrasonic imaging and image analysis have grown to be powerful tools in the fields of nondestructive evaluation (NDE) and noninvasive diagnostic medicine. While B-scan imaging is the most frequently used approach in medical applications [1], both the B-scan and C-scan imaging techniques are utilized in the field of NDE [2]. In both the B-scan and C-scan imaging methods, the resolution of the imaging transducer and the background material noise impose severe limitations on the applicability of ultrasonic imaging, especially in materials such as composites. The material noise can be most often effectively overcome by a signal processing technique such as Split Spectrum Procesing [3-5]. The limitation on the resolution aspect of the imaging process can be reduced to an extent by using one of the many deconvolution techniques [6-10]. Wiener filtering technique [8,11,12] is one such resolution enhancement method of signal/image processing.

WIENER FILTERING

Parametric Wiener filtering has been traditionally used for image enhancement [13,14]. It is a modified version of the back propagation filter [15]. A back propagation

743

filter does not account either for any noise content of the image or for the finite bandwidth of the Point Spread Function (PSF) of the imaging system. As a result, it can be unstable when the amplitude of the transfer function of the PSF is very small at certain frequencies. This would result in a corrupted object estimate. A parametric Wiener filter achieves its stability in the presence of noise by minimizing the effective noise-to-signal ratio (NSR) of the estimated object while simultaneously minimizing the error between the image and the reblurred estimated object [13]. The Fourier domain representation of such a parametric Wiener filter is given by

$$\text{Fourier Wiener Filter} = \frac{H^*(w_x, w_y)}{|H(w_x, w_y)|^2 + [P(w_x, w_y)]} \tag{1}$$

where, $H(w_x, w_y)$ is the transfer function of the imaging system (or the PSF) and $P(w_x, w_y)$ is the noise-to-signal ratio (NSR) matrix. The symbol '*' stands for complex conjugation. From equation 1, it is obvious that the NSR is a function of frequency. However, the NSR matrix is difficult to estimate in practical applications.

A pseudo-Wiener filter overcomes the need for the use of frequency dependent noise characteristics by approximating the noise term with a frequency independent constant. Thus, the NSR matrix in the denominator of equation 1 can be replaced by an estimated constant as in equation 2 below:

$$\text{Pseudo-Wiener Filter} = \frac{H^*(w_x, w_y)}{|H(w_x, w_y)|^2 + A} \tag{2}$$

where, A is a constant approximating the noise characteristics of the image. The constant, 'A', in the denominator of equation 2 has a stabilizing effect on the filter operating characteristics. When $|H(w_x, w_y)|=0$, the constant, 'A', ensures that the pole of the filter is not reached. In practice, A can be a fraction of H(0,0), assuming H(0,0) is the maximum magnitude in the transfer function [12].

EXPERIMENTAL PROCEDURE

Experiments have been conducted to demonstrate the performance of Wiener filtering for resolution enhancement applications. A DEC PDP-11/23 computer in conjunction with a LeCroy transient recorder was used for the data acquisition while a DEC Microvax-GPX computer was used for the image processing. The PDP-11/23 computer also controls the stepper motor driven axes of an immersion tank in which the samples being tested were submerged. The stepper motor controlled carriage was used to position and move the transducer to acquire an ultrasonic C-scan image of the specimen being tested.

The point spread function, h(x,y), whose transfer function is used in equation 2, was obtained by C-scan imaging a ball bearing placed in water. However, since the 'ball bearing' method of determination of the PSF slightly overestimates the beam width (as a function of the diameter of the ball bearing), the 2-D PSF obtained by C-scanning the ball bearing was modified by digital processing to conform to the beam width calculated
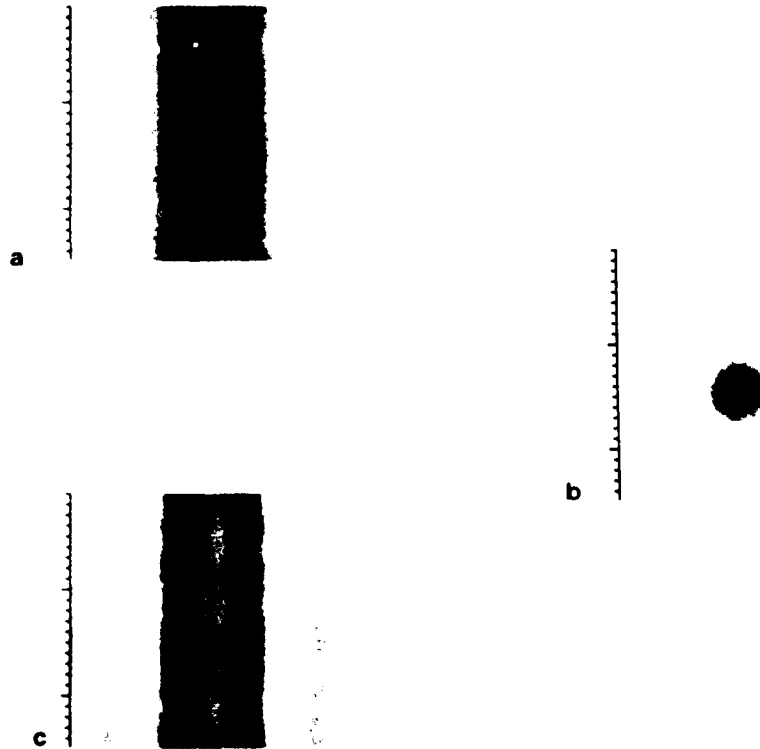
Figure 1 a   Surface image of a stainless steel plate. The image shows
               a pair of unresolved, narrow and closely spaced (1 mm) slots.
Figure 1 b   The PSF of the transducer used to obtain the image in Figure 1 a.
Figure 1 c   Result of Wiener filtering the image in Figure 1 a using the
               PSF in Figure 1 b. The pair of slots are clearly resolved.

from a lateral scan of a wire of 0.08 mm diameter.

Three samples from two different types of materials were used for the experiment.
The first sample was a stainless steel plate (229 mm long, 76 mm wide and 9,5 mm
thick) which had several pairs of narrow and closely spaced slots cut into one of the
surfaces. The second sample was a graphite/epoxy composite (171 mm long, 117 mm
wide and 5 mm thick) which was used for entry surface imaging. The final sample was a
graphite/epoxy composite (64 mm long, 25 mm wide and 3 mm thick) with internal cure
cracks. All data were acquired using ultrasonic immersion C-scanning technique.

RESULTS

The results of Wiener filtering of the 2-D images will be presented under two
headings: 1. Stainless steel block with slots and, 2. Composite material.

Stainless Steel Block with Slots

Figure 1a shows an image of one of the pairs of slots on the top surface of the
steel plate. The slots were of 0.1 mm width each and were separated by 2 mm. The
image (represents 6.35 mm by 6.35 mm of the material) was obtained using a transducer
of center frequency of 3.5 MHz whose PSF is shown in Figure 1b. The image in Figure-

745

a   b

Figure   2 a   Internal image of a pair of slots in a stainless steel plate.The slots are 10.35 mm inside the material and are separated by 2 mm.

Figure   2 b   Result of Wiener filtering the image in Figure 2 a using a PSF obtained by C-scanning a ball bearing. The image shows a marginal improvement in resolution.

1a was Wiener filtered using the PSF in Figure 1b and with the constant A=0.004 times H(0,0) of the PSF in the frequency domain, which was found to be the most suitable value (also reported by Burgoyne et. al.[12]). The result of Wiener filtering is shown in Figure 1c which clearly shows the two resolved slots.

The effect of material-wave interaction on Wiener filtering was studied by imaging the slots from the back surface of the sample. The slots were approximately at a depth of 10.3 mm from the surface of entry. Figure 2a (represents 6.35 mm by 6.35 mm of the material) shows the images of the slots before processing while Figure 2b shows the image after processing. The PSF used for the processing was again that obtained from a C-scan of a ball bearing in water. The result of Wiener filtering shows some resolution enhancement but not as much improvement as was obtained in Figure 1c, perhaps because of the use of a PSF in water which ignores the effect of material on the PSF.

Composite Material

Figure 3a is the entry surface image of a graphite/epoxy composite material (represents 3.175 mm by 3.175 mm of the material). The image has been obtained using a 3.0 MHz low frequency acoustic microscope transducer whose PSF is shown in Figure 3b. The Wiener filtered image (A=0.004[H(0,0)]) is presented in Figure 3c which clearly shows the weave pattern of the bleeder cloth impression found on the top surface of the composite.

Internal cure cracks in a composite have been imaged and is shown in Figure 4a (represents 6.35 mm by 6.35 mm of the material). The cure cracks have been confirmed earlier by using dye enhanced X-ray radiographic techniques. The image shows three internal cracks in the epoxy of the composite material. Figure 4b shows the Wiener filtered image of the cure cracks. As in the case of the steel plate with slots, 'inside the material' image enhancement is not as effective as in the case of surface imaging. Nevertheless, there is a noticeable resolution improvement.
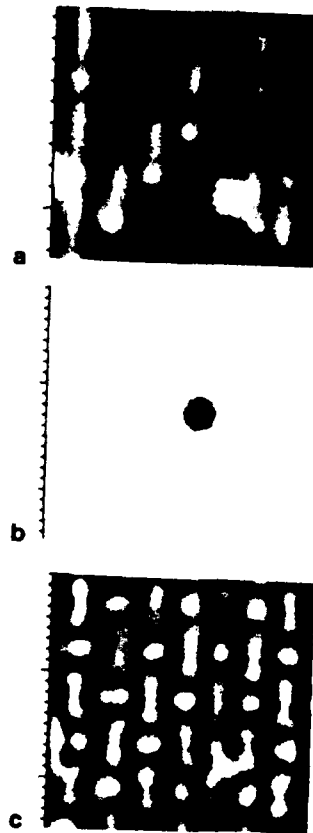
Figure 3 a   Surface image of a graphite/epoxy composite plate. The image shows a blurred pattern of the impression left by the bleeder cloth.

Figure 3 b   The PSF of the transducer used to obtain the image in Figure 3 a.

Figure 3 c   Result of Wiener filtering the image in Figure 3 a using the PSF in Figure 3 b. The bleeder cloth impression is clearly visible.

DISCUSSION

The images presented here demonstrate the potential of Wiener filtering in image processing applications of ultrasonic NDE. However, there is a need for caution during the implementation of the filter since there are several implementational 'pit falls' to be avoided.

First, one of the major factors affecting the Wiener operation is, as in any other Fourier domain method, the presence of any abrupt changes in amplitude along the edges. This can produce a discontinuity because of the underlying assumption of the Fourier method that the image is repetitive in spacial domain. Although such a problem can be alleviated to a certain extent by using a suitable window function, it should be remembered that such a windowing alters the amplitude ratios of the very image being 'protected' from spurious high frequency contents. Another method of reducing an edge discontinuity would be to subtract the average edge amplitude from the entire image and to perform a lowpass filtering of the Wiener filtered image. It is necessary to have the cut off frequency of the ⁻ᵗer high enough to include most of the frequencies contained in the original image and narrow enough to reject any spurious high frequency components. Such a lowpass filtering also eliminates the effect of any division by very small numbers (equation 2) outside the bandwidth of the PSF.

747

A-67

Figure 4 a Internal images of the cure cracks in a graphite/epoxy composite.
Figure 4 b Result of Wiener filtering the image in Figure 4 a using a PSF obtained
        by C-scanning a ball bearing.

Second, 'wrap around error' [13,14], which again stems from the assumption of
the Fourier method that the image repeats itself in the spacial domain, affects the object
estimate obtained by Wiener filtering. One of the standard methods used [14] to avoid
the wrap around error is to 'zero pad' the image and the PSF. However, such a technique
will be successful only if the edge amplitudes are zero-valued. Otherwise, spurious high
frequency components are introduced in the frequency domain. The need for zero
padding is somewhat reduced in Wiener filtering applications because the PSF ususally
has nonzero amplitudes only in a small area in the center of the PSF image. As a result,
the filter affects only a small band (depending on the width of the nonzero amplitudes,
that is, the beam width of the PSF) along the edge of the object estimate obtained by
Wiener filtering. Hence, the larger the beam diameter of the transducer, the wider will be
the 'corruption band' of the processed image when zero padding is not performed.

A third factor that affects the performance of a Wiener filter is the ranges of the
amplitude values of the PSF and the image being processed. It is necessary to normalize
the amplitudes of the PSF and the image so that they span the same range of values. This
is necessary because of the presence of the constant 'A' in the denominator of equation 2
(A is a fraction of H(0,0) of the PSF).

It can be observed from Figures 1c and 3c that the PSFs are Gaussian shaped (for
a transducer with a symmetrical beam). Hence, an analytically generated Gaussian beam
of appropriate variance (to conform to the azimuthal resolution of the transducer) can be
used for Wiener filtering if the transducer is known to have a symmetrical beam. Figures
5a, b, c and d are the processed images of those in Figures 1a, 2a, 3a and 4a, respec-
tively. The processing has been performed using PSFs generated by equation 3 below:

$$PSF = K \exp\left[-\frac{(x-\bar{x})^2}{2\sigma_x^2} - \frac{(y-\bar{y})^2}{2\sigma_y^2} \right] \tag{3}$$

748

A-68
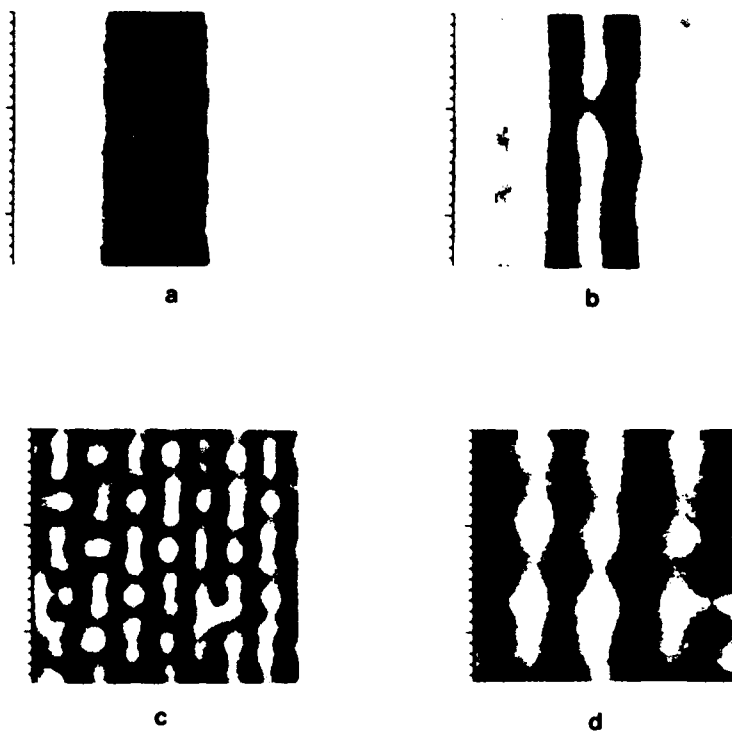
Figure 5 a Result of Wiener filtering the image in Figure 1 a using an analyti-
cally generated Gaussian PSF.

Figure 5 b Result of Wiener filtering the image in Figure 2 a using an analyti-
cally generated Gaussian PSF.

Figure 5 c Result of Wiener filtering the image in Figure 3 a using an analyti-
cally generated Gaussian PSF.

Figure 5 d Result of Wiener filtering the image in Figure 4 a using an analyti-
cally generated Gaussian PSF.

where, K is a constant. The results of using analytical PSFs are quite similar to that
obtained by using the actual PSFs.

CONCLUSIONS

Two dimensional pseudo-Wiener filtering has been shown to be an effective
resolution enhancement operator for ultrasonic NDE applications. The method provides
improved resolution in both surface images and internal images in materials such as
composite material and stainless steel. For a successful implementation of the technique,
it is necessary to remove any edge discontinuity by subtracting the average edge ampli-
tude from the entire image. The PSF and the image amplitudes should be normalized
toidentical ranges. Finally, if the transducer is known to have a symmetrical field, an
analytical Gaussian PSF can be used in place of the experimentally obtained PSF of the
transducer.

749

ACKNOWLEDGEMENTS

REFERENCES

1. Wells P.N.T., "Biomedical Ultrasonics", Academic Press, London, 1977.
2. Krautkramer J. and Krautkramer H., "Ultrasonic Testing of Materials", Springer-Verlag, Berlin, FRG, 1977.
3. Newhouse V.L., Bilgutay N.M., Saniie J. and Furgason E.S., "Flaw-to-grain Echo Enhancement", Ultrasonics International, Butterworth Scientific, U.K., pp:152-156, 1979.
4. Karpur P., "Split Spectrum Processing: Process Modeling and the Evaluation of Polarity Thresholding Algorithm for Material Noise Reduction in Ultrasonic NDE", Ph.D. Dissertation, Drexel University, Philadelphia, 1987.
5. Karpur P., Shankar P.M., Rose J.L. and Newhouse V.L., "Split Spectrum Processing: Determination of the Available Bandwidth for Spectral Splitting", Accepted for Publication in an upcoming issue of Ultrasonics, Butterworth Scientific, U.K.
6. Bhagat P.K., Chimenti D.E., Moran T.J. and Shimin K.D., "Effects of Deconvolution Procedures on Size Estimates in the Born Inversion Algorithm", Review of Progress in Quantitative Nondestructive Evaluation, Vol. 3A, pp:395-403, 1984.
7. Bhagat P.K. and Shimmin K.D., "Homomorphic Processing in Ultrasonic NDE", Review of Progress in Quantitative Nondestructive Evaluation, Vol. 3A, pp:351-358, 1984.
8. Burch S.F., "Comparison of SAFT and Two-Dimensional Deconvolution Methods for the improvement of Resolutoin in Ultrasonic B-scan Images", Ultrasonics, Butterworth Scientific, Vol. 25, pp:259-266, September, 1987.
9. Vollmann W., "Resolution Enhancement of Ulrasonic B-scan Images by Deconvolution", IEEE Transactions on Sonics and Ultrasonics, Vol. SU29, No.3, pp:78-83, March 1983.
10. Childers D.G., Skinner D.P. and Kemerait R.C., "The Cepstrum: A Guide to Processing", Proceedings if the IEEE, Vol. 65, No. 10, pp:1428-1443, October 1977.
11. Frock B.G., Martin R.W., Moran T.J. and Shimmin K.D., "Imaging of Impact Damage in Composite Materials", Review of Progress in Quantitative Nondestructive Evaluation, Vol. 7, 1987.
12. Burgoyne B., Pavkovich J. and Kino G.S., "Digital Filtering of Acoustic Images", Acoustical Imaging, Vol. 11, Plenum Press, New York, pp:181-166, 1981.
13. Andrews H.C. and Hunt B.R., "Digital Image Restoration", Prentice-Hall, Inc., 1977.
14. Gonzalez R. and Wintz P., "Digital Image Processing", Addison-Wesley Publishing Co., 1977.
15. Lee H., "Formulation of the Generalized Backward-Projection Method for Acoustical Imaging", IEEE Transactions on Sonics and Ultrasonics, Vol. SU-31, No.3, pp:157-161, May 1984.

750

BLUR REDUCTION IN ULTRASONIC IMAGES USING

PSEUDO THREE-DIMENSIONAL WIENER FILTERING

B. G. Frock and P. Karpur
University of Dayton
Research Institute
Dayton, Ohio 45469

INTRODUCTION

The ability to quantitatively image material anomalies with ultrasonic methods is severely restricted by the axial and lateral resolution of the interrogating transducer. Axial resolution is controlled by the pulse duration of the transducer with shorter pulse durations yielding better axial resolution. Lateral resolution is controlled by the width of the interrogating beam with narrower beams providing better lateral resolution.

Significant improvements in depth resolution have been achieved by collecting information from narrow software gates applied directly to the rf A-scans[1,2]. Further improvements have been obtained by using a one-dimensional Wiener filter to axially deconvolve the rf A-scans and then using the narrow software gates to collect information from the deconvolved A-scans[3,4]. Another study has shown that improvements in the lateral resolution of C-scan images can be achieved by using a two-dimensional Wiener filter to deconvolve the lateral point-spread function (psf) from the image[5]. That study has also shown that a Gaussian-shaped computer-simulated psf can be used in place of the actual psf to perform the Wiener deconvolution so long as the transducer's psf is symmetric.

This paper describes a method for improving both the depth resolution and the lateral resolution in C-scan images by serially combining the one-dimensional axial Wiener deconvolution, software gating and two-dimensional lateral Wiener doconvolution techniques. The method consists of first digitizing and storing rf A-scans. The rf A-scans are then axially deconvolved using a one-dimensional Wiener filter. Next, software gates are applied to the Wiener deconvolved A-scans to generate C-scan images at desired locations. Finally, the two-dimensional Wiener filtering technique is applied to the C-scan images to improve the lateral resolution.

WIENER DECONVOLUTION

One-dimensional axial Wiener deconvolutions were used to remove the "signature" of the ultrasonic transducer from the rf A-scans. The deconvolutions effectively reduce the pulse length of the transducer, thereby improving the depth resolution. The axial Wiener deconvolution

technique has been explained in previous publications and will not be discussed further here[3,6].

Two-dimensional Wiener deconvolutions were used to remove the lateral psf from C-scan images. As in the one-dimensional case, the measured image feature, $f(x,y)$ is assumed to be a convolution of the system response, $h(x,y)$, and the "true" image feature, $s(x,y)$[7]. Thus,

$$f(x,y) = h(x,y)*s(x,y) \qquad (1)$$

The system response, $h(x,y)$, for an ultrasonic transducer can be obtained from a C-scan image of a "small" spherical reflector. The Wiener deconvolution is most easily implemented in the Fourier domain using the relation

$$S(u,v) = \frac{[H^*(u,v)][F(u,v)]}{[H(u,v)]^2 + K} \qquad (2)$$

where $H^*(u,v)$ is the complex conjugate of $H(u,v)$ and "K" is a constant which is an estimate of the noise-to-signal ratio of the image. The constant also provides stability to the filter when $H(u,v)$ is small. Transformation of $S(u,v)$ back to the spatial domain yields an estimate of the "true" image feature.

SAMPLE

The sample used in this study is a 32-ply thick, quasi-isotropic graphic/epoxy composite. The separation between ply interfaces in this sample is approximately 0.14 mm. Prior to ultrasonic inspection, the sample had been intentionally damaged by a 5.4 Joule impact from a 12.7 mm diameter stainless steel ball on a pendulum impacter.

DATA COLLECTION

A computer controlled ultrasonic immersion scanning system was used to collect 256 point, 8-bit rf A-scans at each of 40,000 discrete points in a 20.3 mm by 20.3 mm square area surrounding the impact damage site. The spatial separation between data collection points was 0.10 mm in both planar directions. All 40,000 A-scan lines were stored in the computer memory for later processing. The rf A-scans were stored as 200 individual B-scan data files with 200 rf A-scans per B-scan file. Each individual A-scan within a B-scan file represented one step in the "X" direction, while each B-scan file represented one discrete step in the "Y" direction. A 3.5 MHz center frequency, 12.7 mm diameter, 50.8 mm focal length transducer was used for all data collection. Excitation for the transducer was a broadband spike pulse. A reference waveform (rf echo from the front surface of a flat plate) was collected and stored for the axial deconvolutions. The psf for the lateral Wiener deconvolutions was approximated by a computer-simulated Gaussian-shaped pressure profile.

AXIAL WIENER DECONVOLUTION

All 40,000 of the rf A-scans were axially deconvolved using a one-dimensional Wiener filter. These deconvolved A-scans were then stored as 200 separate B-scan files with 200 individual A-scans in each of the files. The improvement in depth resolution which results from deconvolution can be seen in Fig. 1. Figure 1a shows the rf B-scan image

across a delaminated region of the sample. The entry surface echo
appears as a broad dark region across the B-scan about one-third of the
way down from the top. Delaminations appear as lighter regions due to
a phase reversal of the echoes from the delaminated regions. The B-scan
image generated from axially deconvolved A-scans across the same region
of the sample is shown in Fig. 1b. The improvement in depth resolution
is clearly evident from the narrowing of the black entry surface echo and
the light delamination echoes. Such improvements in depth resolution are
in agreement with results published by other investigators[8,9].

C-SCAN IMAGE GENERATION

C-scan images were generated by applying narrow software gates to
the rf A-scans and to the Wiener deconvolved A-scans. The gates were
located to interrogate the second and third ply interfaces below the
entry surface. Since the round-trip distance between adjacent interfaces
in the sample was approximately 0.28 mm and the wavelength of the 3.5 MHz
interrogating beam was 0.86 mm, the gates were separated by about one-
third of a wavelength. Figure 2 shows an rf A-scan and a deconvolved A-
scan with four narrow gates on each. The minimum value in each gate was
used to generate C-scan images because the phase reversal at a ply
delamination results in a negative spike in echoes from each damage site.

C-scan images generated from the rf A-scans and from the Wiener
deconvolved A-scans are shown in Fig. 3. Figures 3a and 3b are images
of the second and third ply interfaces generated by software gating the
rf A-scans. Figures 3c and 3d are images of the second and third ply
interfaces generated by software gating the axially Wiener-deconvolved
A-scans. Note that the C-scan images generated from the axially Wiener-
deconvolved A-scans have better lateral resolution than the C-scan images
generated directly from the rf A-scans.

(a)   (b)
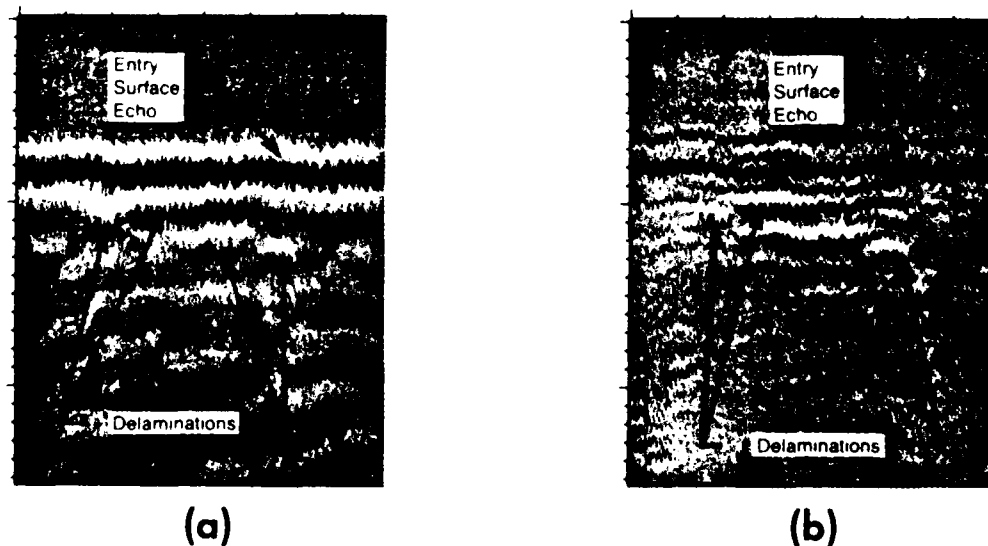
Fig. 1. B-scan images of impact damage site in graphite/epoxy
         composite: (a) from rf A-scans; (b) from axially Wiener-
         deconvolved A-scans.
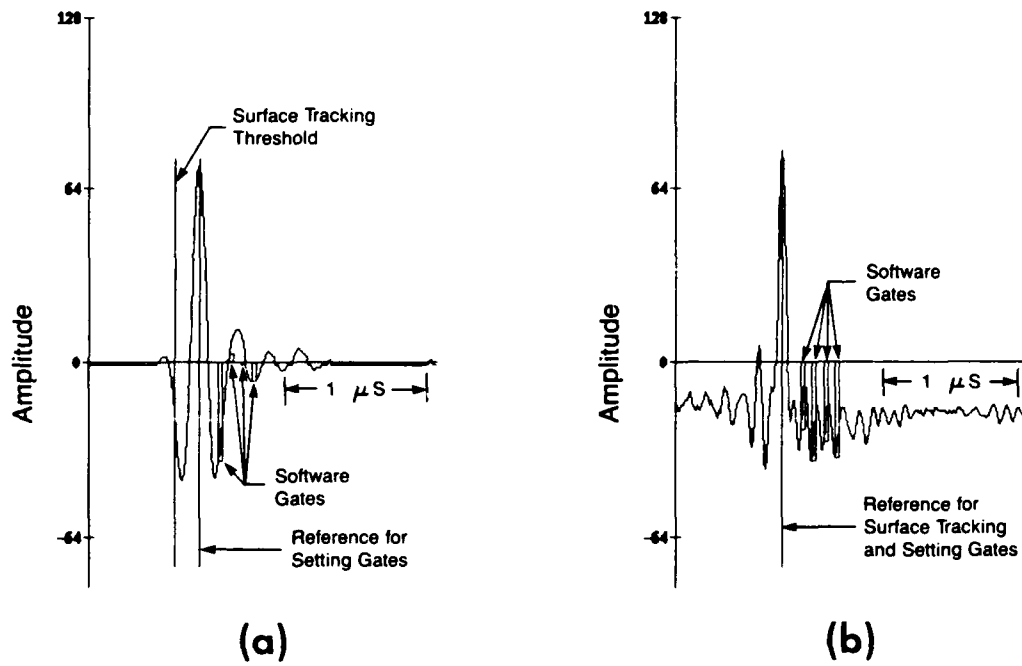
Fig. 2. A-scans showing four gates for C-scan image generation:
(a) rf A-scan and (b) axially Wiener-deconvolved A-scan.
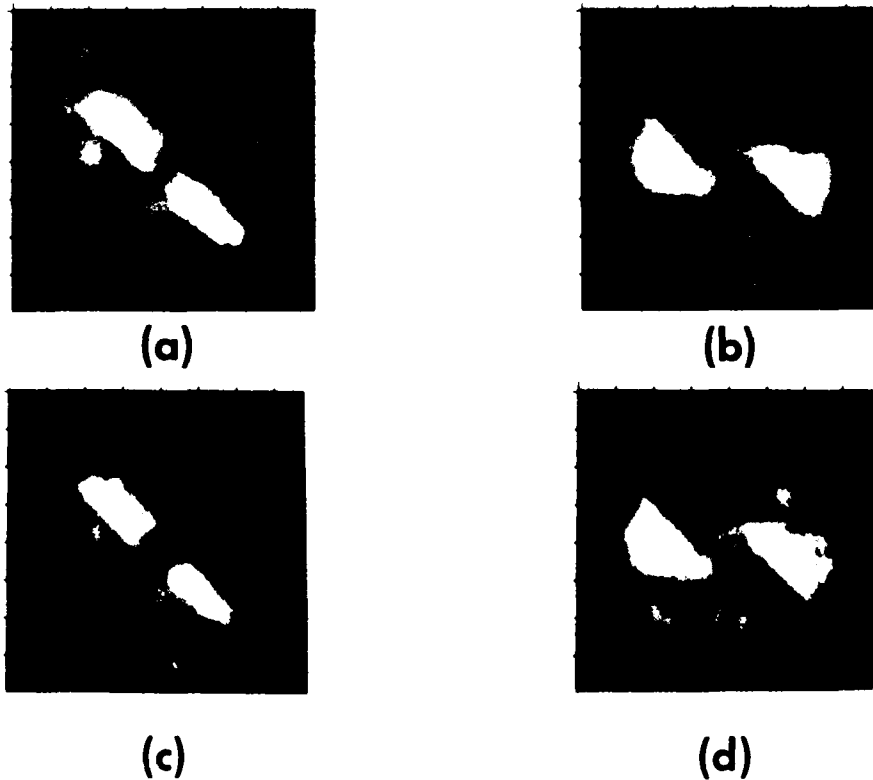
Fig. 3. C-scan images of impact damage at interfaces between:
(a) second and third plies (from rf A-scans); (b) third and
fourth plies (from rf A-scans); (c) second and third plies
(from axially Wiener-deconvolved A-scans) and (c) third and
fourth plies (from axially Wiener-deconvolved A-scans).

TWO-DIMENSIONAL LATERAL WIENER DECONVOLUTION

The psf used for two-dimensional lateral Wiener deconvolutions of the C-scan images was derived by fitting a two-dimensional Gaussian function to an experimentally determined psf[5].

The results of deconvolving the two-dimensional psf's from the C-scan images of Fig. 3 are shown in Fig. 4. Figures 4a and 4b result from two-dimensional Wiener deconvolutions of the C-scan images generated from the rf A-scans (Figs. 3a and 3b respectively). Figures 4c and 4d result from two-dimensional Wiener deconvolutions of the C-scan images generated from the axially Wiener-deconvolved A-scans (Figs. 3c and 3d respectively). It is evident from these images that the two-dimensional Wiener deconvolution operation improves the resolution of C-scan image features. It is also evident that the resolution in the two-dimensional Wiener-deconvolved C-scan images generated from one-dimensional axially Wiener-deconvolved A-scans is better than the resolution in the two-dimensional Wiener-deconvolved C-scan images which were generated directly from the rf A-scans.

During the course of this investigation, it was found that the psf required for deconvolving the C-scan images generated from axially deconvolved A-scans was narrower than that required for two-dimensional Wiener deconvolutions of the C-scan images generated from the rf A-scans. In fact, the variance of the Gaussian psf used for Wiener deconvolutions of the C-scan images in Figs. 3a and 3b (yielding the images in Figs. 4a and 4b) was 20 pixels, whereas the variance used for Wiener deconvolutions of the C-scan images in Figs. 3c and 3d (yielding the images in Figs. 4c and 4d) was 8 pixels. The reason for this difference in psf sizes is still under investigation.

(a)   **(b)**

(c)   **(d)**
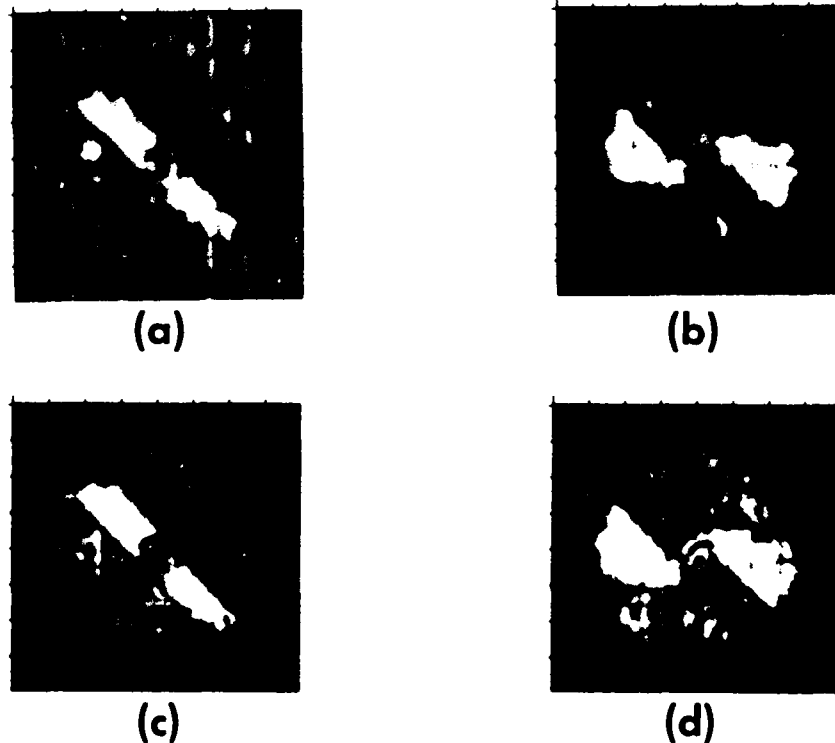
Fig. 4. Two-dimensional Wiener filtering of C-scan images in: (a) Fig. 3a; (b) Fig. 3b; (c) Fig. 3c and (d) Fig. 3d.

CONCLUSIONS

B-scan images generated from axially Wiener-deconvolved A-scans have been shown to have better depth resolution than B-scan images generated directly from rf A-scans. This improvement in depth resolution is due to the decrease in pulse length which results from the Wiener deconvolution process. Also, the C-scan images which have been generated by gating the axially Wiener-deconvolved A-scans exhibit better lateral resolution than do the C-scan images which have been generated by gating the rf A-scans. The reasons for this improvemnt in lateral resolution is still under investigation.

The use of two-dimensional lateral Wiener deconvolution significantly improves the resolution in C-scan images. This improvement in lateral resolution is primarily due to the partial removal of the point-spread function of the ultrasonic transducer from the C-scan images. The greatest improvement in lateral resolution has been achieved by applying two-dimensional lateral Wiener deconvolution techniques to C-scan images which have been generated from axially Wiener-deconvolved A-scans. The lateral resolution in those images is significantly better than that achieved by two-dimensional lateral Wiener deconvolution of C-scan images generated by gating rf A-scans.

Finally, the diameter of the psf used for two-dimensional lateral Wiener deconvolutions of C-scan images generated from one-dimensional axially Wiener-deconvolved A-scans is smaller than is the psf used for two-dimensional lateral Wiener deconvolutions of C-scan images generated directly from rf A-scans. The reasons for this difference in psf diameters is still under investigation.

ACKNOWLEDGEMENTS

REFERENCES

1. C. F. Buynak, T. J. Moran and R. W. Martin, "Delamination and Crack Imaging in Graphite/Epoxy Composites, "Materials Evaluation, Vol. 47, No. 4, April 1989, pp. 438-441.
2. C. F. Buynak and T. J. Moran, "Characterization of Impact Damage in Composites," in Review of Progress in Quantitative NDE, edited by D. O. Thompson and D. E. Chimenti (Plenum Press, New York, 1987), Vol. 6B, pp. 1203-1211.
3. B. G. Frock, R. W. Martin, T. J. Moran and K. D. Shimmin, "Imaging of Impact Damage in Composite Materials," in Review of Progress in Quantitative NDE, edited by D. O. Thompson and D. E. Chimenti (Plenum Press, New York, 1988), Vol. 7B, pp. 1093-1099.
4. B. T. Smith, J. S. Heyman, J. G. Moore, S. J. Cucura and S. M. Freeman, "Correlation of the Deply Technique with the Ultrasonic Imaging of Impact Damage in Graphite/Epoxy Composites," in Review of Progress in Quantitative NDE, edited by D. O. Thompson and D. E. Chimenti (Plenum Press, New York, 1986), Vol. 5B, pp. 1239-1244.

5. P. Karpur and B. Frock, "Two-Dimensional Pseudo-Wiener Filtering in Ultrasonic Imaging for Nondestructive Evaluation Applications," in *Review of Progress in Quantitative NDE*, edited by D. O. Thompson and D. E. Chimenti (Plenum Press, New York, 1989), Vol. 8A, pp. 743-750.

6. P. K. Bhagat, D. E. Chimenti, T. J. Moran and K. D. Shimmin, "Effects of Deconvolution Procedures on Size Estimates in the Born Inversion Algorithm," in *Review of Progress in Quantitative NDE*, edited by D. O. Thompson and D. E. Chimenti (Plenum Press, New York, 1984), Vol. 3A, pp. 395-403.

7. R. Gonzalez and P. Wintz, in *Digital Image Processing*, (Addison-Wesley Publishing Co., 1977), Chap. 5.

8. K. I. McRae and C. A. Zala, "Improved Axial Resolution of Ultrasonic B-scans by L1-Norm Deconvolution," in *Review of Progress in Quantitative NDE*, edited by D. O. Thompson and D. E. Chimenti (Plenum Press, New York, 1988), Vol. 7A, pp. 747-755.

9. W. Vollmann, "Resolution Enhancement of Ultrasonic B-scan Images by Deconvolution," *IEEE Transactions on Sonics and Ultrasonics*, Vol. SU29, No. 3, pp. 78-83, (March, 1983).

APPLICATION OF PATTERN RECOGNITION TECHNIQUES TO B-SCAN ANALYSIS

Richard W. Martin
University of Dayton Research Institute
Dayton, Ohio 45469

SUMMARY

Several pattern recognition techniques are utilized to identify defects in ultrasonic backscatter B-scans of composite materials. The goal is to aid inexperienced operators in identifying defects in composite materials. A threshold is applied to a rectified B-scan to produce a binary image. Then each unconnected component of the binary image is assigned a unique label. Various statistics such as area, integrated optical density, perimeter, axis angle, and x, z location are then computed for each labeled component. If-Then rules are applied in an expert system mode to these statistics to identify each component as front surface or back surface, delamination, front or back surface connected crack, noise or an unidentified feature. This technique has successfully identified both surface cracks and delaminations in graphite/epoxy laminates.

TEST SETUP

Two test samples were utilized in these experiments. The first sample (Figure 1) is a 16-ply graphite/epoxy laminate with a $[90_4/0_4]_s$ layup. It has several front and back surface cracks and the scan is 6 cm in length. The data acquisition procedure utilized an angle backscatter B-scan technique with a 10 MHz, 76.2-mm (3-inch) focus, 12.7-mm (1/2-inch) diameter transducer focused on the front surface and oriented at 20 degrees from normal to the surface. The second sample (Figure 2) is a 32-ply quasi-isotropic graphite/epoxy laminate damaged by a 20.2 joule (15 ft.-lb.) impact which caused delaminations within the material. The edges of the delaminations are seen as a series of steps radiating outward and downward from the central impact point. The steps occur because lower delaminations are partially shadowed by the upper level delaminations except where the lower delaminations cover a greater area. Data acquisition utilized a normal incidence B-scan technique with a 5 MHz, 101.6-mm (4-inch) focus, 19-mm (3/4-inch) diameter transducer. In both images, digitization of the rectified and filtered signal was at a rate of 100 MHz. Darker grey levels in both images indicate higher signal levels. Higher noise levels and digitizer mistriggers were introduced into the image of the second sample (Figure 2) to test noise rejection capabilities of the program.

FILENAME PAT005   500 PTS AT 5 MILS/PT   400 PTS AT 0.010 USEC/PT
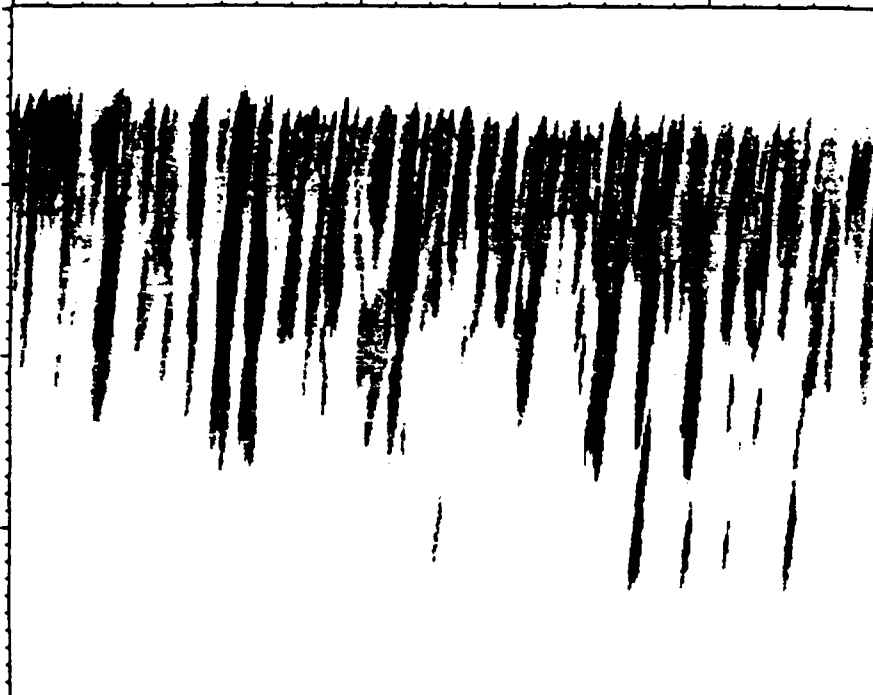
Fig. 1 Original backscatter B-scan image of crack sample.

FILENAME OLM3   350 PTS AT 10 MILS/PT   400 PTS AT 0.010 USEC/PT
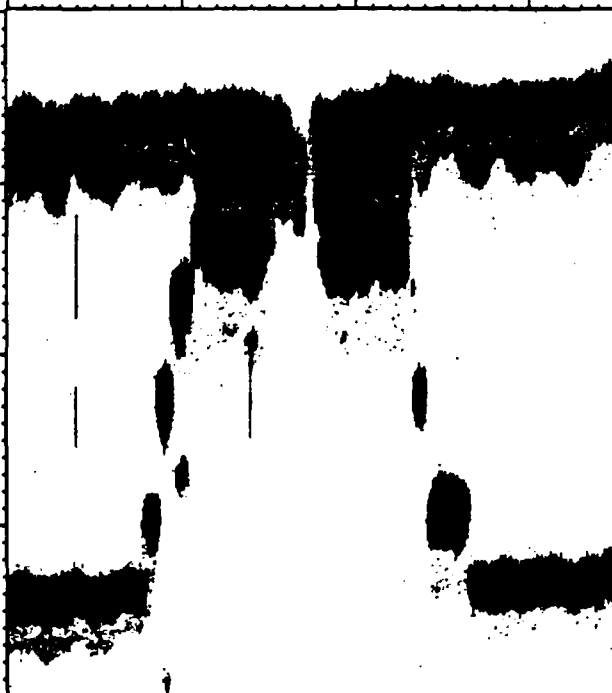
Fig. 2 Original normal incidence B-scan of delamination sample.
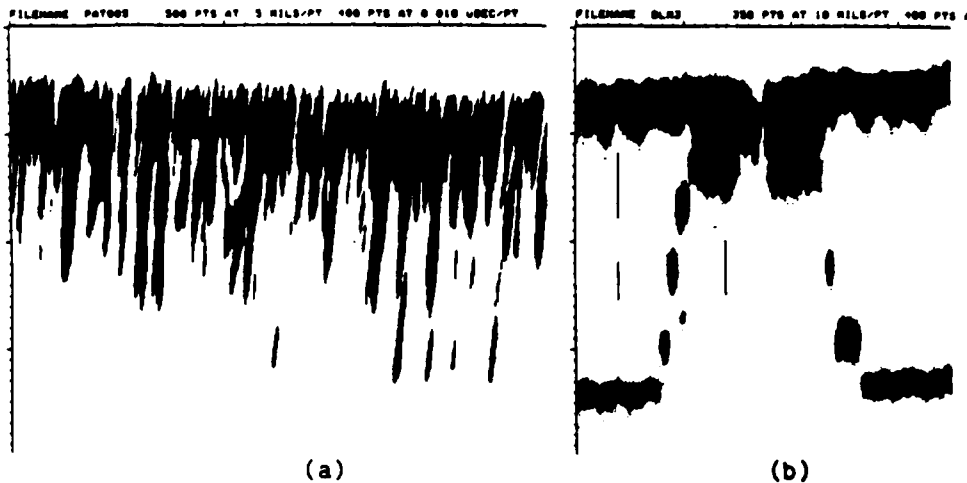
Fig. 3. Thresholded images of crack sample (a) and delamination sample (b).

LABELING THE IMAGE

The original B-scan images (Figures 1 and 2) have a range of 0-255 and are first thresholded to produce a binary image of 1's and 0's (Figures 3a and 3b). The test operator chooses the threshold value. The goal of the labeling program is to assign a unique label, which is a number, to each unconnected component of the binary image in order to identify it, so that statistics can later be computed on each component.

The front surface is located by first finding the horizontal row through the binary image with the largest number of 1's. This row is assumed to be within the front surface clutter of the image. Then a search is made above and below this row to find the first rows with only 65% as many 1's. The percentage may have to be altered for other images. These rows are defined as the top and bottom of the area of front surface clutter in the image. The bottom row of front surface clutter is seen in Figures 4, 5, 6, and 7 as an artificial dividing line between front surface components and components within the material. The back surface echo is found in a similar manner except that if none is found then it's location is estimated utilizing the known speed of sound in the material and the material's thickness.

In first pass labeling, a border of zeros is placed around the entire binary image. A 2x3 window is then moved down each A-scan (vertical) line, and 8 rules (Table 1) are applied to the pattern of 1's and 0's in the window. Rules must be applied in the predetermined order, and if any rule is executed then all of the remaining rules are skipped. The object of the labeling rules is to determine a label for pixel A in the moving window shown in Table 1. The first label (number) is 1 and additional labels are numbered consecutively. In first pass labeling 494 labels were assigned to the crack sample and 349 labels assigned to the delamination sample. Many image components will have multiple labels assigned to them due to the first pass labeling process. Multiple labels on parts of the same component are equivalent to each other. The rules (Table 1) have noted these equivalences [1].

In second pass labeling, all label equivalences noted during the first pass are resolved and labels are reassigned so that each image component has a unique label. Figure 4 indicates 54 labeled image components and Figure 5 has 191 labeled image components. These components are coded in a 7 level grey scale, and on Figure 4 are also marked with their label number.

Table 1. Rules for Image Labeling

WINDOW:

C	B
D	A
E	

1. If A = 0 (below threshold level), then A remains 0.
2. If C is labeled, (nonzero) then assign A the label in C, but if C not equal to E and E not equal to 0, then note equivalence of labels in C and E.
3. If B = 0, D = 0 and E is labeled, then assign A the label in E.
4. If B, C, D, and E equal 0, then assign new unique label to A.
5. If B = 0, then assign A the label in D.
6. If D = 0 and B is labeled, then assign A the label in B, but if B not equal to E and E not equal to 0, then note equivalence of labels in B and E.
7. If B and D have the same label, then assign A the label in B.
8. If B and D have different labels, then assign A the label in B and note the equivalence of labels in B and D.
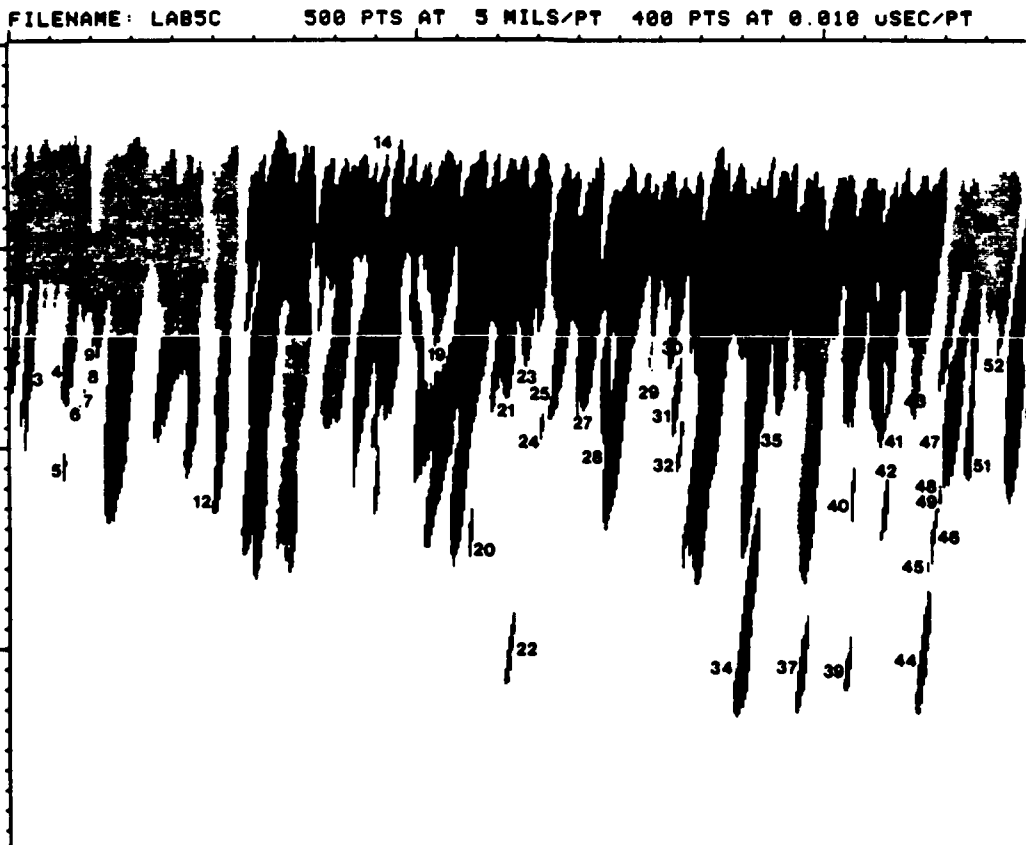
Fig. 4. 54-labeled image components of cracked sample.
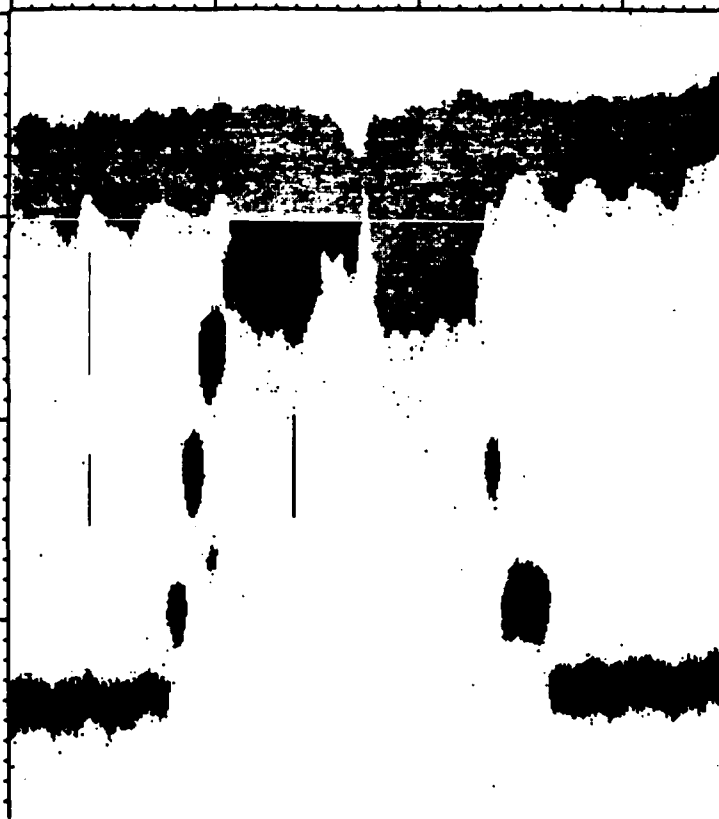
Fig. 5.   191-labeled image components of delamination sample.

STATISTICS

Several statistics [1] are computed for each component which will be utilized by a set of IF-THEN rules to identify the image components. The following is a list of definitions used to compute these statistics.

AREA is the sum of all "1" pixels within each binary component.

PERIMETER is the sum of all border pixels of a component.

BOUNDARIES Xmin, Zmin, Xmax, Zmax define the corners of a minimum sized rec-
        tangle which will enclose the entire image component.

SURFACE equals 1 if the boundaries of a component all lie above the row
        defined as the bottom of the front surface clutter.
        SURFACE equals 2 if the boundaries lie below that row.
        SURFACE equals 3 if the component lies across the estimated back
        surface row.

CENTER X, Z are the x, z coordinates of the center of a component. These
        are determined by computing the moment of each image component
        about each axis.
        X CENTER = (sum of all x component coordinates) / AREA
        Z CENTER = (sum of all z component coordinates) / AREA

AXIS ANGLE is the axis of least inertia of the component relative to the x
        axis (rotating counterclockwise) and limited to range of 0-180°.
            TAN 2θ = (2*B)/(A-C)

A-82

$$\text{WHERE:} \quad A = \sum_{i=1}^{n} \sum_{j=1}^{m} (Y_{i,j} - Y \text{ CENTER})^2$$

$$B = \sum_{i=1}^{n} \sum_{j=1}^{m} (X_{i,j} - X \text{ CENTER}) * (Y_{i,j} - Y\text{CENTER})$$

$$C = \sum_{i=1}^{n} \sum_{j=1}^{m} (X_{i,j} - X \text{ CENTER})^2$$

$$\text{ELONGATION} = \text{SQRT}(B^2 + A - C^2)/(A + C)$$

IOD (integrated optical density) or mass is the sum of all of the pixel amplitudes within the component in the original B-scan [2].

AVG LEVEL = IOD / AREA. The average grey level of a component [2].

COMPONENT IDENTIFICATION

Table 2 lists the set of IF-THEN rules utilized in an expert system mode to identify image components in both test samples. The statistics relating to each of the image components are examined by the rule base in an effort to identify the image component. The identification rules in Table 2 were determined by first examining the image component statistics of known cracks, delaminations, etc and choosing sets of typical values for each type of defect. The rules must be executed in the predetermined order and when any rule is executed all remaining rules are skipped. Figures 6 and 7 shows the results of the rule base application to these images. In Figure 6, 16 of the 54 image components were identified as noise and deleted (set to background color). In Figure 7, 180 of the 191 image components were identified as noise. Image components identifications are coded in grey scale to allow quick identification of surface cracks and other components. The original images were color coded, which further improved the clarity. The lightest grey level seen in Figure 6 is 8 front surface connected cracks. The next darkest level is the front surface clutter. The next darkest is 5 back surface connected cracks, while the darkest is 2 unidentified components. In Figure 7, the lightest grey level is 5 delaminations. Next darkest is front surface clutter, while the next darkest is the back surface. The darkest grey is 3 unidentified components. A black line can be seen traced across the front and/or back surfaces of Figures 6 and 7. This line represents a trace of the peak amplitudes in the front and back surface area and is meant to be an estimate of the actual surface location. The actual surface locations are often difficult to determine in an angle B-scan. The center (x, z) location of each front surface crack component is also marked by a black dot. Drawing a line through this dot, at the angle specified by the axis angle, to the front surface will provide a best estimate of the location of surface cracks where the line intersects the black front surface line trace. All components of the front surface can also be removed allowing even simpler identification of the surface cracks.

RESULTS

All known front and back surface cracks in the first sample (Figure 1) were identified by the program and shown in Figure 6. The two unidentified components are surface irregularities which caused a response close to that of a crack. The identification rules could be modified so that even these 2

Table 2. Identification Rules

1. If elongation is >0.99 then component is NOISE.
2. If angle is between 89.99 and 90.01 and elongation >0.7, then component is NOISE.
3. If angle >179.99 and elongation >0.7, then component is NOISE.
4. If area <30, then component is NOISE.
5. If surface = 1, then component is part of the FRONT SURFACE.
6. If surface = 2 and length (Zmax-Zmin) >50 and angle is between 82 and 89 degrees and elongation between 0.79 and 0.99 and IOD >36000 and average grey level >35, then compenent is a FRONT SURFACE CONNNECTED CRACK.
7. If surface = 2 and length >100 and angle between 82 and 89 degrees and elongation is between 0.79 and 0.99, then the component is a FRONT SURFACE CONNECTED CRACK.
8. If surface = 2 and length <75 and IOD <20000, then component is a part of the FRONT SURFACE.
9. If surface = 2 and IOD <20000, then component is a part of the FRONT SURFACE.
10. If angle is between 70 and 89.9 degrees and surface = 0 and IOD >8000, then component is a DELAMINATION.
11. If angle is between 90.1 and 110 degrees and surface = 0 and IOD >8000, then component is a DELAMINATION.
12. If surface = 3 and angle is between 82 and 86 degrees and length >25 and elongation >0.95 and average grey level >26, then component is a BACK SURFACE CONNECTED CRACK.
13. If surface = 0 and angle is between 82 and 89 degrees and elongation is >0.8, then component is NOISE.
14. If surface = 3 and angle is between 82 and 89 degrees and elongation >0.8, then component is NOISE.
15. If surface = 3 and (angle >150 degrees or angle <30 degrees), then component is the BACK SURFACE.
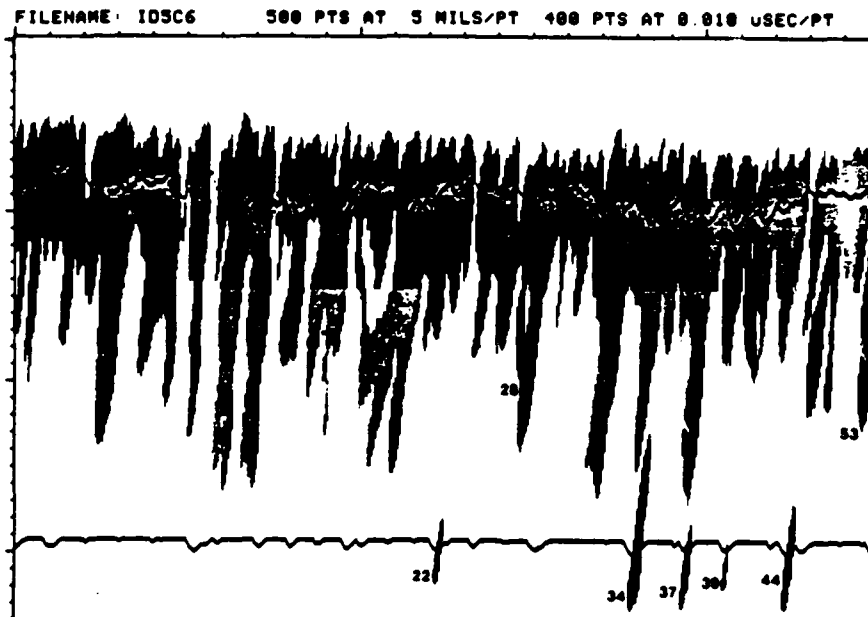
Fig. 6. Identified components in crack sample.

FILENAME: ID1DLM   350 PTS AT 10 MILS/PT   400 PTS AT 0 010 uSEC/PT

Fig. 7.   Identified components in delamination sample.

components could become defined as part of the front surface instead of
unidentified. Most of the delaminations in the second sample (Figure 2)
were correctly identified and all noise in the image was eliminated (Figure
7). The two unidentified components near the front surface are
delaminations. These were not identified as delaminations because the rules
presently assume that a delamination will not be connected to any feature of
the front surface. Higher resolution transducers and different binary
thresholding could better isolate these near front surface delaminations,
and then they would be identified correctly. The remaining unidentified
area is a secondary reflection from the delamination directly above it.

This paper has shown that pattern recognition programs can be utilized
to aid in identification of surface cracks and delaminations (due to impact)
in graphite/epoxy laminates and that noise can be eliminated from the image.
Rule bases could also be constructed to examine an image for other types of
defects and for defects in other kinds of materials.

ACKNOWLEDGEMENTS

REFERENCES

1. Winston, P. H. and B. K. P. Horn, LISP, Second Edition, 1984, Addison-
    Wesley Publishing Company, pp. 151-167.

2. Castleman, K. R., Digital Image Processing, 1979, Prentice-Hall, Inc.,
    pp. 76-78.

A-85

LEAKY PLATE WAVE INSPECTION OF BIAXIAL COMPOSITES

Richard W. Martin
University of Dayton Research Institute
Dayton, Ohio, 45469-0001

Dale E. Chimenti
Materials Laboratory
Wright Patterson AFB, Ohio, 45433-6533

INTRODUCTION

The utilization of leaky plate waves in a scanning arrangement has exhibited improved reliability and increased sensitivity to important defects in unidirectional material [1,2,3]. The application of frequency modulation to the usual tone burst signal used to generate plate waves has also been shown to enhance defect discrimination [2,3]. In the current work, leaky plate wave techniques have been applied to the inspection of biaxially laminated graphite-epoxy composites. Test samples having 8, 16, and 24 plies, respectively, are studied. Test specimens contain several types of defects - simulated delaminations, porosity, and ply cuts. In addition, a series of impact-damaged samples are examined to study the method's sensitivity to this type of delamination. All simulated defects were detected, and comparisons with conventional normal-incidence C-scan measurements have shown that the plate wave technique is more sensitive to both porosity and ply cuts, consistent with our observations on uniaxial composites [3]. Novel gating methods have been applied to the plate wave spectra to improve defect detection in biaxial composites.

LEAKY PLATE WAVE GENERATION

Leaky plate waves are generated by a beam of ultrasound propagating to the sample and striking the plate at an incident angle. If conditions of beam width and frequency are favorable, the reradiated field appears distorted and displaced in the direction of propagation of the plate wave. In our application transmitter excitation is provided by a swept frequency tone burst which is generated by frequency modulating the RF tone burst with a triangular waveform at audio rates in the range of 5-20 Hz. Previous publications describe modulated tone-burst leaky wave generation in greater detail [1,2,3].

DATA ACQUISITION SYSTEM DESCRIPTION

The incident ultrasonic beam consists of a series of swept frequency tone bursts through the range of 0.8 to 4.5 MHz [3]. The received signal is amplified, video-detected, and sampled with a gated integrating amplifier. The experimental output is then a time-varying signal, most of whose power is concentrated at an audio frequency equal to twice the product of the modulation frequency with the number of plate modes subtended by the modulation bandwidth. The resulting signal of plate wave modes is then bandpass filtered at 700 Hz on the high frequency end for anti-aliasing and at 25 Hz on the low frequency end to remove the fundamental of the 56 ms sweep period and D.C. components from the signal. Removal of the D.C. and low frequency (<20Hz) components from the received signal is required to prevent degradation of the resolution of the spectral calculations described in later paragraphs. The plate wave signals are digitized over the entire 56 ms sweep period at a rate of 2064 samples per second with a total of 128 points recorded. Data are then sent to a microcomputer for processing and image generation [3,4].

TEST SAMPLES

The characterized samples utilized in this study are 6 biaxial graphite/epoxy laminates of 8, 16, and 24 plies in thickness constructed from AS4/3501 type material. The stacking sequences are $[0_2/90_2]_s$, $[0_2/90_2]_{2s}$, and $[0_2/90_2]_{3s}$, respectively. The size of each sample is 3 inches wide by 4 inches in length. Simulated defects are embedded in samples of three different thicknesses. Delaminations are simulated with 0.5 and 0.25 inch diameter teflon wafers (0.5 mil thick) and porosity is simulated with a very light scattering of 40 micron diameter microballoons. There are also single-layer ply cuts. Three samples of different thicknesses have also been subjected to low velocity impacts with a 12.7 mm diameter stainless steel ball on a pendulum impacter to produce true delaminations.

PLATE WAVE DATA SPECTRAL PROCESSING

While the detected RF envelope of the received signal shows minima at various frequencies, some characteristic of this signal is needed to distinguish between defects and defect-free material. Our method is to utilize spectral processing. Data processing software first calculates a 256 point Fast Fourier Transform (FFT) on the filtered low frequency detected RF envelope of the received signal. In this case only the 0-500 Hz frequency range of the FFT spectrum is of interest. In the general case, the spectral frequency range of interest depends upon the modulation frequency introduced by the sweep, the RF frequency range and the thickness of the panel under test. The median frequency of the area under the Fourier amplitude spectrum is computed for each sampling point on the panel using integration techniques. This median frequency measures the overall frequency shifts in the mode data as mode structure changes when passing over defects in the panel. High median frequencies are generated in defect-free material as the plate wave propagates through the entire thickness of the panel (many modes), while lower median frequencies are generated over a defect area of the panel because the panel thickness is effectively decreased and produces fewer modes. Median frequency thus provides a measure of relative defect depth. Figures 1, 2 and 3 depict these stages in signal processing. In each figure, the (a) plots are of the detected RF envelope which can be viewed as either amplitude versus frequency or amplitude versus time data. The (b) plots are the result of applying a 25-700 Hz bandpass filter plus a Hamming window to the signal

in (a), while (c) is the FFT of waveform (b). Note the shift toward lower
frequencies in the FFT spectra (c) progressing from Figure 1 to Figure 3
(effectively thicker to thinner material). The median frequency at each
measured point (x,y) on the sample is stored as one data value in a C-scan
image. An advantage of using the median frequency technique is that no
prior knowledge of defects or their resulting frequency responses is
required to produce a high quality image. Also, median frequency spectral
processing provides a wide dynamic range of response to defects while
preserving sensitivity to small or weak flaws. The depth information is
accurate as long as the frequency difference representing defects close to
the same depth is equal to or greater than the resolution of the FFT. In
the case presented, the FFT resolution is 8.9 Hz, but it could be improved
by utilizing any of several methods. A previous publication describes
leaky plate wave spectral processing in greater detail [3].

TEST RESULTS

Figure 4a shows a C-scan image of a 24-ply test panel with simulated
defects. Data for the image was generated by applying the median
frequency signal processing technique to the leaky plate wave data
acquired from the panel. The column of defects on the left is located
between layers 8 and 9 in the panel while the column of defects on the
right is between layers 16 and 17. In each column, the top defect is a
0.5 inch diameter delamination, the second from top is a 0.25 inch
diameter delamination, the third is a 0.5 inch diameter area of porosity,
while the bottom defect is a 0.5 inch wide ply cut with a 0.125 inch gap.

A pair of 2.5 MHz unfocused transducers with 0.375 inch diameter
elements are utilized to acquire data. The incident angle of the beam to
the panel is 15 degrees from surface normal, and the swept frequency tone
burst covers the range of 0.8-4.4 MHz in a 56 ms sweep time (17.9 Hz
modulation). In the image of Fig. 4a, increasing median frequency is
proportional to defect depth. Progressively darker shades of gray in the
image represent greater defect depth. Thus, the two simulated
delaminations on the left are shown as white because they are closer to
the entry surface of the panel while the deeper delaminations on the right
appear as darker shades of gray. The porosity and ply cuts do not conform
to the same gray scale because only partial signal reflections are
possible from these structures due to the width of the beam. Defect-free
areas of the panel are black because they represent the maximum panel
thickness, and thus the highest median frequency.

Figure 4b shows a C-scan image of the same panel utilized for
comparison purposes. Data for this image was acquired with a 10 MHz, 4-
inch focused transducer with a 0.25 inch diameter element at normal
incidence to the panel. Software gating and front surface tracking were
used to acquire the image data [5]. Not all defects are shown (especially
porosity and ply cuts) and of course no depth information is indicated.

Figs. 1, 2 and 3 depict representative waveforms recorded to generate
the median frequency image of Fig. 4a. The median frequency for the
defect-free FFT of Fig. 1c is 128 Hz, while median frequency for the layer
8 delamination of Fig. 2c is 112 Hz and for the layer 16 delamination of
Fig. 3c is 73 Hz. The most notable difference between these waveforms and
the previously reported waveforms obtained with unidirectional material
[3] is the increased waveform complexity; however, the median frequency
algorithm still correctly encodes depth information. Another finding of
this investigation is that the beam direction should be parallel to the
orientation of the top surface plies to optimize mode structure and
therefore the defect contrast potential. Incident beam angles between 10
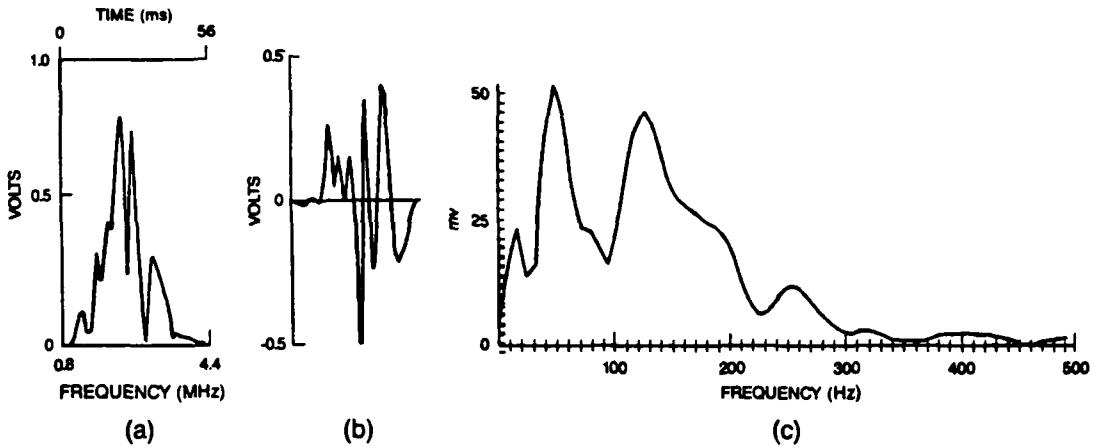
Fig. 1. (a) Plot of plate wave modes of a defect-free area showing
envelope of detected ultrasonic signal. (b) Bandpass filtered
and windowed version of signal in (a). (c) FFT spectrum of the
signal shown in (b).
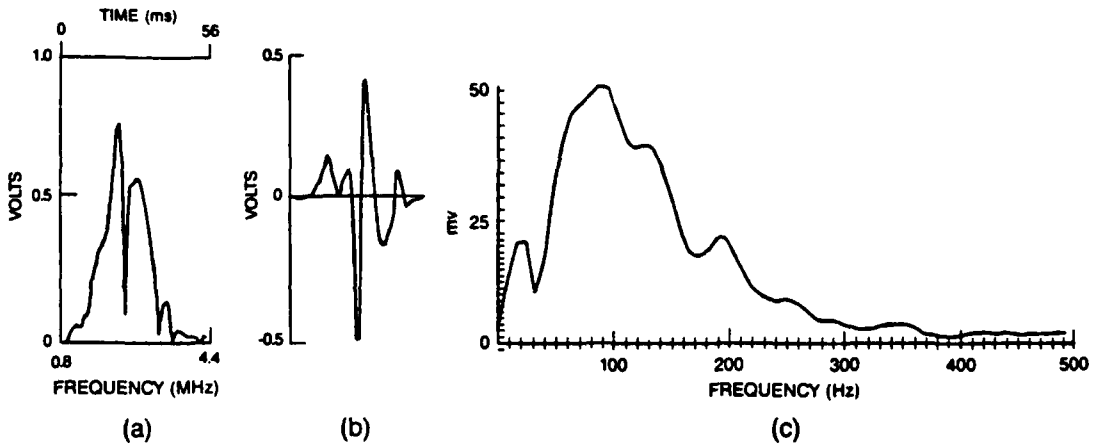
Fig. 2. (a) Plot of plate wave modes of a lower level defect showing
envelope of detected ultrasonic signal. (b) Bandpass filtered
and windowed version of signal in (a). (c) FFT spectrum of the
signal shown in (b).
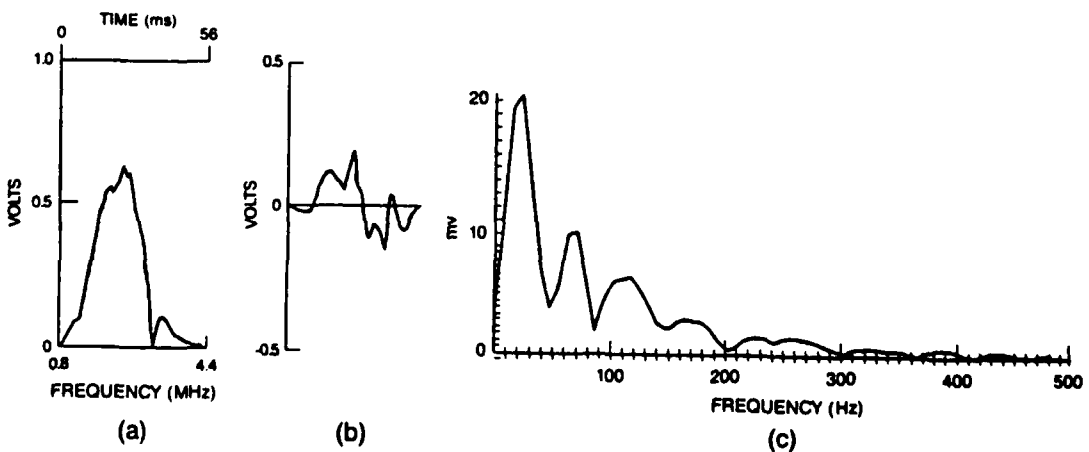
Fig. 3. (a) Plot of plate wave modes of an upper level defect showing
envelope of detected ultrasonic signal. (b) Bandpass filtered
and windowed version of signal in (a). (c) FFT spectrum of the
signal shown in (b).

A-89

**(a)**   **(b)**
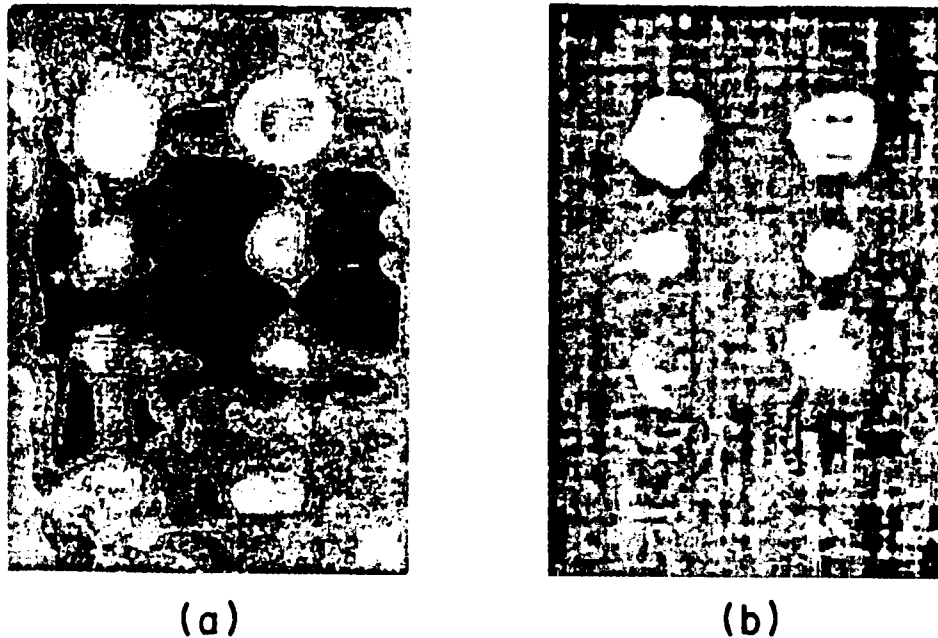
Fig. 4. (a) C-scan image of 24-ply panel utilizing median frequency,
         proportional to defect depth. Dark areas are defect-free: gray
         scale correlates with distance of defect from surface.
         (b) Normal incidence C-scan of same panel gated on back surface.

and 30 degrees have been investigated. Acceptable mode structure was
generated only at angles close to 15 degrees.

    Figures 5a and 5b are also images of the 24-layer panel but have been
acquired by measuring the depth of specific nulls in the detected swept-
frequency RF envelope waveform. Two software gates, each of which detects
the minimum data value within the gate, have been utilized. Their location
and typical amplitudes at two specific panel areas are indicated by the
position and heights of the rectangular gates shown in Fig. 6. Minimum
values detected in gate #1 result in low amplitudes that selectively image
the deeper delaminations (white areas) in Fig. 5a, while minimum values
detected in gate #2 (Fig. 6) result in high amplitudes (dark areas) for
all defect areas and low amplitudes for defect-free material (Fig. 5b).
The null in gate #2 is at a frequency characteristic of defect-free
material. The contrast and definition of defect areas in Figs. 5a and 5b
are superior to those in the median frequency image of Fig. 4a, but the
resulting signal has no depth information encoded.

    A median-frequency processed image of an 8-ply thick panel which has
been impacted with an energy of 1 joule is shown in Figure 7a. The RF
sweep frequency range is 1.2 to 4.0 MHz in a 56 ms time period.
Delaminations from an impact generally are small in plies near the impact
surface, but grow in area outward and downward from the impact and overlap
each other in successively deeper plies. This morphology is verified by
performing a software gated normal incidence C-scan with gates set at the
depth of each ply interface within the material. Figure 7b is taken from
such a scan and is an image from a gate on the back surface of the sample
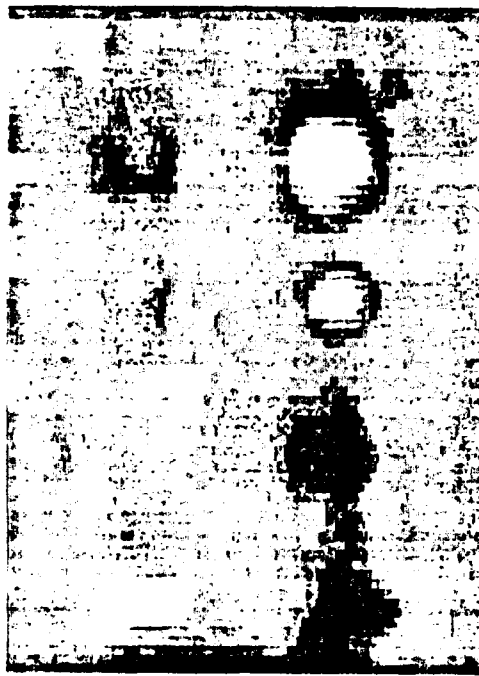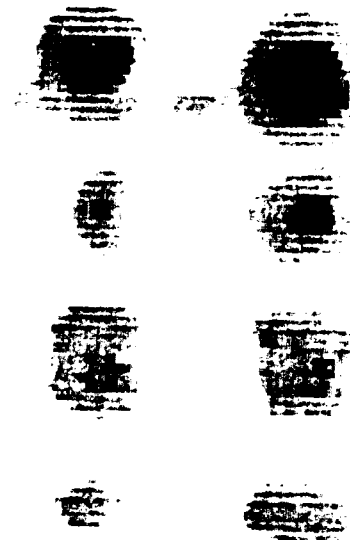
(a) (b)

Fig. 5. (a) Image formed by measuring minima in gate #1. Deeper
         delaminations are selectively imaged in white. (b) Image formed
         by measuring minima in gate #2. All defects are imaged in darker
         shades of gray.
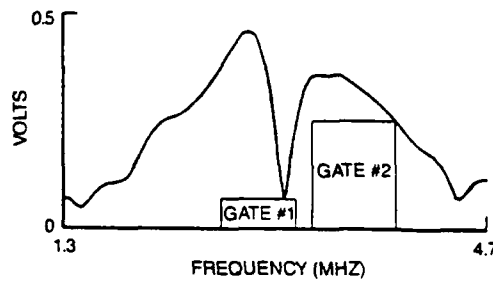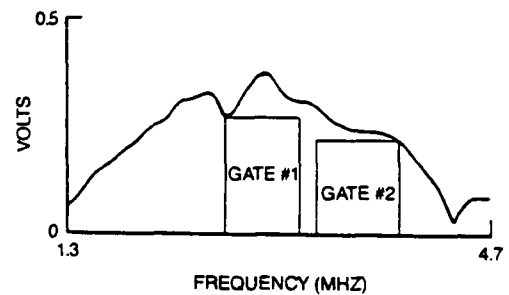
(a) (b)

Fig. 6. Positions and amplitudes of two minimum value software gates on
         the leaky plate wave mode spectrum. (a) lower level defect. (b)
         upper level defect.

showing the cumulative damage of all levels of delaminations. A 10 MHz
focused transducer has been utilized. Figure 7a shows two areas of damage
near the top surface (white areas), and then larger areas of damage at
greater depths within the material, shown by increasingly darker shades of
gray. Black indicates undamaged material. Figure 7b verifies the damaged
area, but encodes no depth information. The wide acoustic beam and larger
x,y step size of Figure 7a result in lower spatial resolution than the
image in Figure 7b. Note that the leaky plate wave median-frequency
processing of a real delamination (Fig. 7a) is much better than that of
the simulated delamination in Figure 4a. The improvement is apparently
due to a greater acoustic impedance mismatch in the real delamination.

(a)   (b)
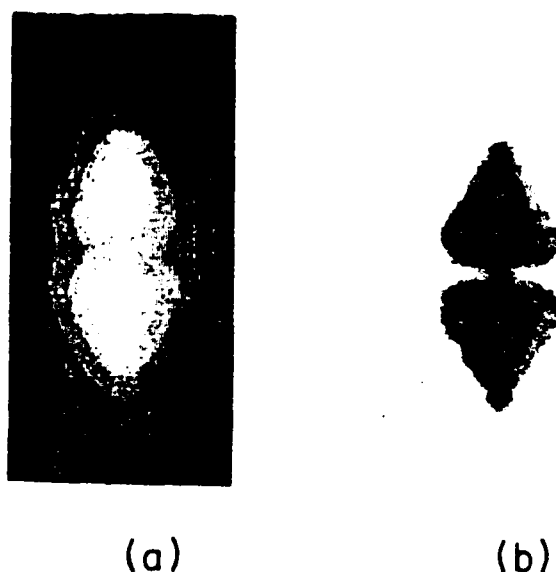
Fig. 7. (a) C-scan image of 8-ply impact damaged panel utilizing median
         frequency processing of the plate wave mode spectrum. (b) Normal
         incidence C-scan of same panel gated on the back surface.

An energy of 6 joules has been utilized to impact a 24-ply thick
panel. A normal incidence 10 MHz C-scan is performed with a software gate
at every ply interface and at the back surface to verify delamination
damaged areas. The back surface gated image is shown in Figure 8a.
Delaminations are generated in both the 0 and 90 degree ply directions and
they enlarge in area outward and downward from the impact site. A leaky
plate wave scan is performed utilizing a frequency sweep range of 0.8-4.4
MHz in a 56 ms period. A very wide software gate is then placed on the
received RF envelope of the leaky plate waves. This gate will detect the
minimum amplitude value that falls within the time interval of the gate.
The gate covers the sweep over the time of about 10ms (1.4 MHz) to 44ms
(3.6MHz). The resulting image is shown in Figure 8b and has the
interesting effect of outlining the edges of the many levels of
delaminations. The effect might be caused by a very deep null being
created when the acoustic beam is on the edge of a delamination and
partially covering both delaminations. Although this technique does not
provide depth information, relative depth of the delamination areas can be
easily inferred by prior knowledge of the manner in which impact
delaminations are formed. The width and location of the wide gate is not
critical, but experimentation has shown that the best images are produced
with a gate width of 0.5 to 0.75 of the sweep time and nearly centered in
the sweep band.

CONCLUSIONS

Swept frequency leaky plate wave techniques have been shown to
provide reliable detection of simulated delaminations, porosity, and ply
cuts in biaxial laminates. Also, the extent and relative depth of
delaminations due to impact damage can be determined. Spectral processing
techniques avoid the problems associated with tracking the amplitude of a
specific null because the entire mode signal is utilized. Medi᾿n
frequency processing of the mode spectra provides a good general purpose
processing technique for defect detection and relative depth
determination, since median frequency is related to depth. Specific
minimum value gating techniques have also been shown to provide important
information and defect detection capabilities.

(a)   (b)
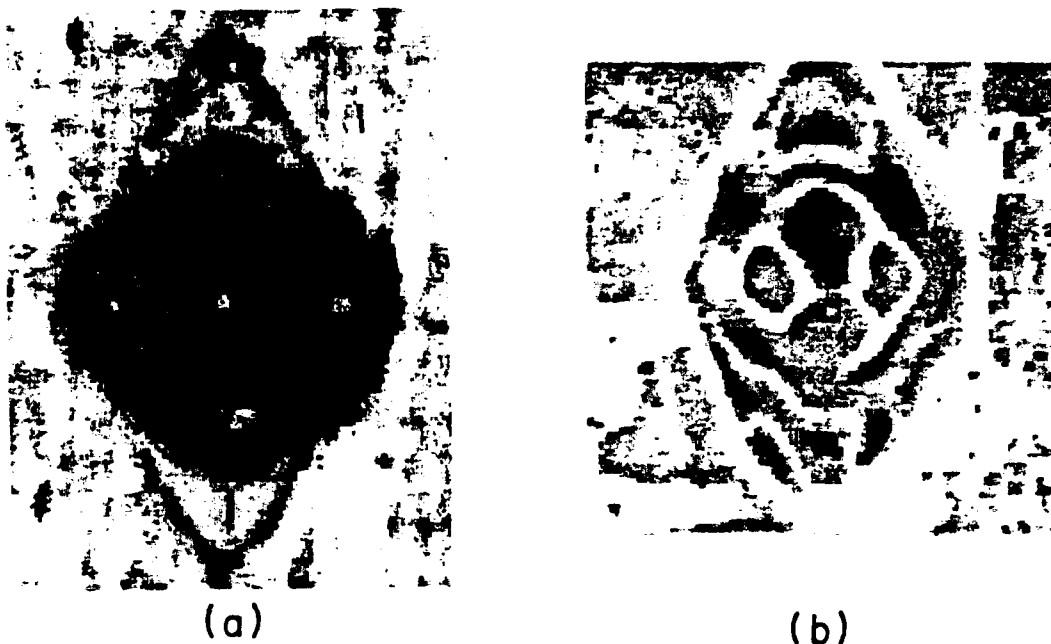
Fig. 8.   (a) Normal incidence C-scan of same panel gated on the back
          surface. (b) C-scan image of 24-ply impact damaged panel
          utilizing a wide minimum value software gate on the leaky plate
          wave modes.

ACKNOWLEDGEMENTS

REFERENCES

1. D.E. Chimenti and Y. Bar-Cohen, 1985 IEEE Ultrasonic Proceedings,
    B.R. McAvoy, ed., New York, (1986), p 1028
2. D.E. Chimenti and A.H. Nayfeh, J. Appl. Phys. 58, (1985), 4531.
3. R. W. Martin and D. E. Chimenti, "Signal Processing of Leaky Lamb
    Wave Data for Defect Imaging in Composite Laminates", Review of
    Progress in QNDE, Vol. 6A, D. O. Thompson and D. E. Chimenti, eds.,
    Plenum Press, New York, 1987, pp 815-824.
4. R.W. Martin and R.J. Andrews, "Backscatter B-scan Images of Defects
    in Composites", Review of Progress in QNDE, Vol. 5B, D. O. Thompson
    and D. E. Chimenti, eds., Plenum Press, New York, 1986, pp 1189-1198.
5. B. G. Frock, R. W. Martin, T. J. Moran, and K. O. Shimmin, "Imaging
    of Impact Damage in Composite Materials", Review of Progress in QNDE,
    Vol. 7B, D. O. Thompson and D. E. Chimenti, eds., Plenum Press, New
    York, 1988, pp 1093-1099.

APPENDIX B

DESCRIPTION OF EXPERIMENTAL CAPABILITIES

APPENDIX B
DESCRIPTION OF EXPERIMENTAL CAPABILITIES

This appendix describes the laboratory facilities which were utilized in the performance of the research efforts reported in Section 2 and upgrades which were incorporated into the facilities in order to perform advanced technique development. The appendix is divided into a section describing ultrasonic scanning systems and another section describing the computer systems.

ULTRASONIC SYSTEMS DESCRIPTION

Ultrasonic NDE technique development efforts were primarily conducted using two automated scanning systems, each containing an immersion tank. The high precision, small tank system was described in detail in AFWAL-TR-87-4007 and will not be described in this report. A photograph of this system is shown in Figure B-1. A second ultrasonic scanning system was installed as part of this research effort and has been named the large tank scanning system. This system is described in the paragraphs below.

Large Tank Scanning System Hardware

The large tank automated ultrasonic scanning system is an ULTRASCAN System 664 manufactured by California Data Corporation (see Figure B-2). This high precision system consists of a stainless steel immersion tank 1.22 m (48 in.) wide by 1.83 m (72 in.) long by 1.14 m (45 in.) deep. The x-y translation carriage is constructed on a bridge and gantry above the tank. The bridge consists of a dual lead-screw x-axis, a single lead-screw y-axis, and a kinematically mounted z-axis search tube and manipulator, with dual gimbal (Model 1048). System control is performed manually using a DIGISCAN 6000 controller from California Data Corporation or computer controlled using a DEC MicroVax III with a VR290 workstation. Scan speeds of up to 152 mm/sec (6 in/sec) are possible with a step size resolution of 0.025 mm (0.001 in).

Several modifications were made to the system to improve its performance and versatility. Optical encoders were mounted on the x and y axes of the translation system to accurately keep track of transducer position. Gortiflex

Figure B-1. Small tank ultrasonic scanning system.
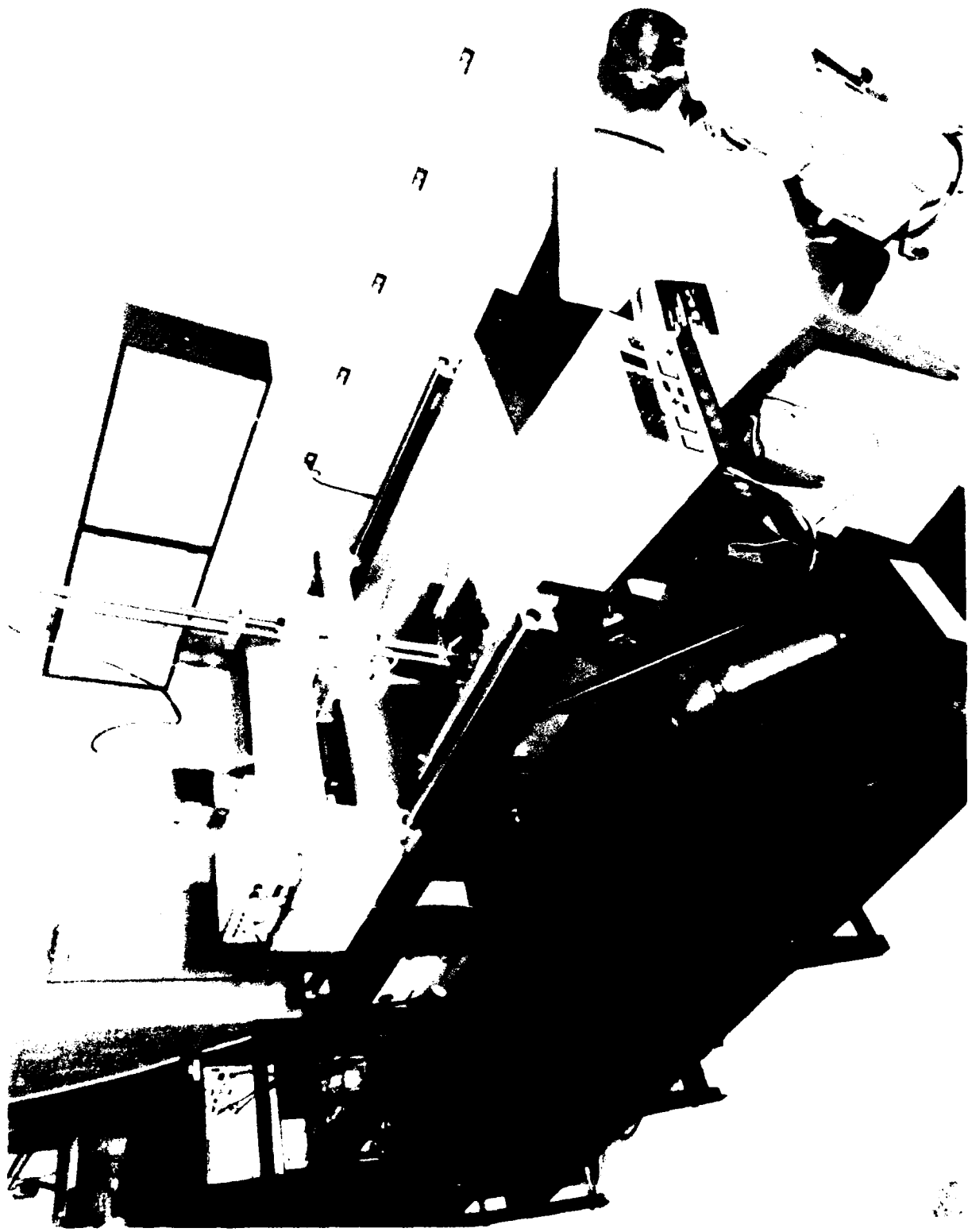
Figure B-2. Large tank ultrasonic scanning system.

roundway covers were designed and installed to protect the carriage support rods and prevent a corrosion problem. Because the top of the immersion tank is 1.3 m (51 in.) above the floor, a mezzanine walkway was designed, fabricated, and installed around the tank, providing easier working distances for the experimenters. Also, an immersion platform was fabricated and installed in the tank to allow flexibility in sample placement. The platform consists of six adjustable stainless steel legs, three rubber encapsulated aluminum I-beams, and a 25.4 mm (1.0 in.) thick PVC top. A unique sample holder was designed and fabricated for the large tank. It consists of four square stainless steel bars 0.71 m (28 in.) long, that are grooved so each bar slides on the other allowing for adjustment to any size square or rectangle. This is done by simply releasing tension on four screws, adjusting the holder to the desired size, and tightening the four screws. Hold down clamps which may be placed anywhere along the top of the bars are used to hold and also to flatten the samples. Once the holder is adjusted, samples can be removed and replaced in the same location.

The California Data System forms the core of the large tank ultrasonic system. Figure B-3 is a block diagram of the entire system including ultrasonic instrumentation. Motion control and data acquisition are performed under control of a MicroVax III computer. A Panametrics 5052PR Pulser/Receiver generates the rf signal to drive the ultrasonic transducer. The received signal is sent from the Panametrics 5052PR to a LeCroy transient waveform recorder which digitizes the signal at rates up to 200 megasamples per second. The digitized signal is stored on the MicroVax. Data analysis, including image enhancement and analysis is performed on the MicroVax using a VR290 workstation. Access to the data files from other computers in the laboratory is possible through the local area network DECNET.

Currently, the large tank system can be used to perform C-scans but not B-scans. B-scan capabilities are, however, available on the smaller scanning system. The capability for B-scans is recommended as a future upgrade for the large tank system to increase the overall versatility of this system. C-scan data is collected by digitizing the rf signal from the receiver and storing user-specified values from software-gated regions of the digitized signal. Digitizing is performed by a LeCroy analog-to-digital (A/D) converter shown in
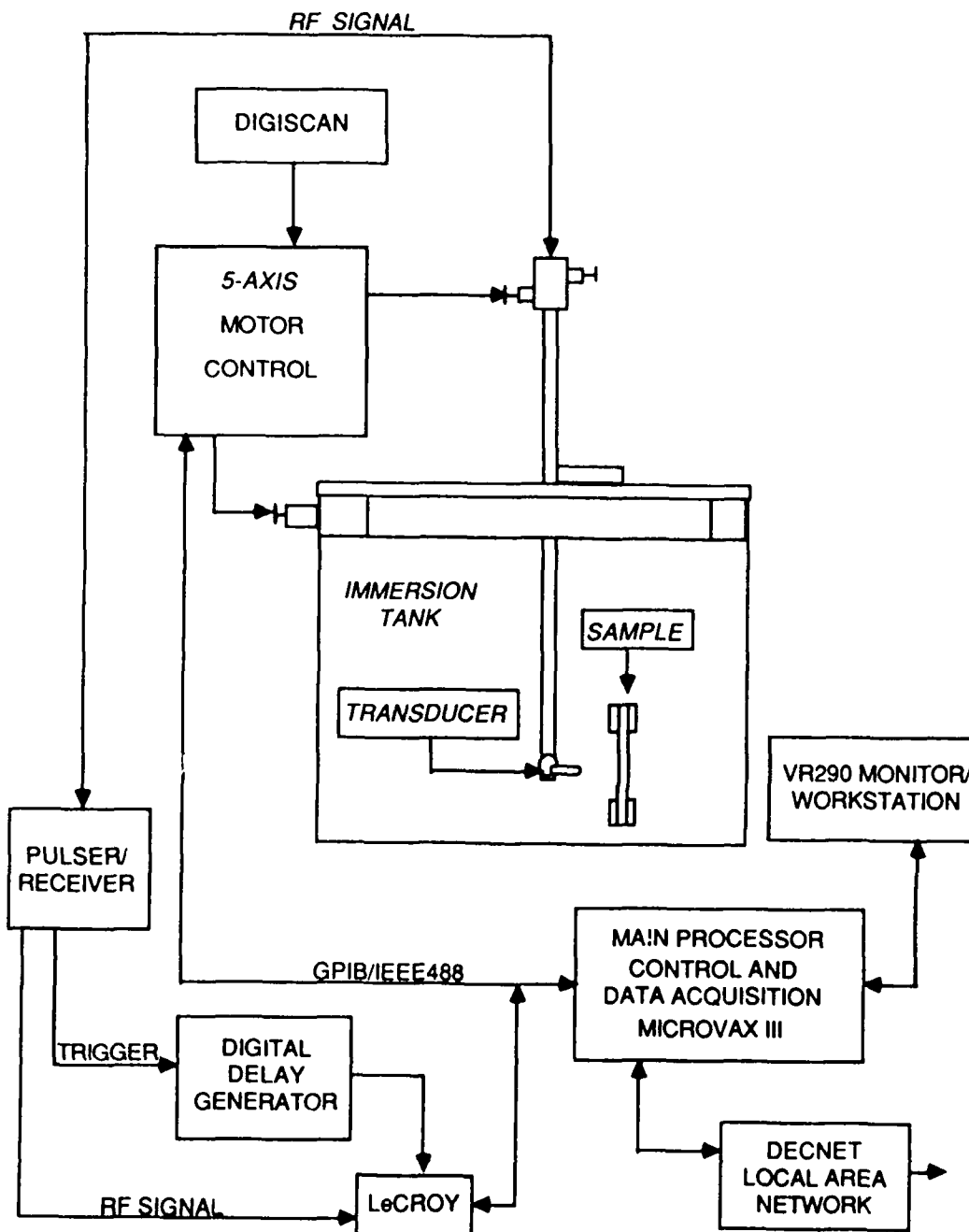
Figure B-2.   Schematic diagram of large tank system.

Figure B-3 and interfaced to the MicroVax through the IEEE-488 interface. Motion control is accomplished under computer control by sending commands over the IEEE-488 interface to the motor controllers. These commands include the starting point of the scan, the step size, the number of points on a line and the number of scan lines. Scans may be performed using any two of the three axes (x-y, x-z, y-z) with step increments of 0.025 mm (0.001 in.) to 25.4 mm (1.0 in.) per step. The controlling program for these C-scans is called BCSIS and resides on the MicroVax III.

LeCroy model TR8828B and TR8818 A/D converters are used to digitize the rf signal. The model TR8828B is an 8-bit A/D converter which digitizes a maximum of 32,000 points at a rate of 200 MHz (5 nanoseconds per point) and transfers the data to the collection system computer. The model TR8818 is an 8-bit A/D converter with a variable digitizing rate from 1 Hz to 100 MHz which may be specified by an external clock. The user-selected digitizer is interfaced to the data collection system computer through a high speed IEEE-488 interface. Commands to the LeCroy and digitized data from the LeCroy are sent through this interface. The digitized A-scan data are assembled into data files by the computer. The data collection program, BCSIS, which operates the LeCroy is described in detail in the following paragraph.

Large Tank Scanning System Software

The following paragraphs describe the software library which supports the large tank ultrasonic scanning system. The library includes routines for data collection and analysis of C-scans. It also includes specialized routines for software gating, image analysis and enhancement. Table B-1 contains a short functional description of each program in the library.

The C-scan data collection program, BCSIS, collects data from the LeCroy digitizer. Multiple-level software gates are generated by BCSIS to produce multiple C-scan files from rf A-scans. Software gating provides a more precise method for setting and tracking a gate and has a higher signal-to-noise ratio than do analog methods such as those which use a boxcar integrator.

Rf A-scan data is acquired by the LeCroy digitizer and displayed on the screen to allow the operator to define the positions and widths of up to 80

gates. Each digitized A-scan may be up to 1024 points in length and the C-scan size may be up to 1024 x 1024 points. The operator may also specify software rectification of the signal and may specify the signal integration time if low-pass filtering is needed. Integration time is defined as the number of consecutive pixels which are included in each average of a moving average sequence.

The operator may also specify the type of processing for data within each gate. Processing options are: mean value, peak value, minimum value, peak-to-peak value, and time-of-flight (TOF) to either a positive or negative peak within a gate. Data from each gate is stored in a separate C-scan file for later analysis.

A front surface tracking routine is provided to ensure that each gate is kept at the correct position (depth) during the course of a scan and also provides for detection and correction of any mistriggers that may otherwise result in erroneous data collection. One of eight different front surface tracking options may be selected.

Major advancements in image display and analysis were incorporated in the C-Scan Analysis System software, CSAS. CSAS was converted from operation on an LSI-11/23 computer to the MicroVax computer. The LSI-11/23 version of CSAS used only 16 colors and levels of gray and a 512 x 512 pixel color monitor. The MicroVax computer with the Graphics workstation can display up to 248 colors simultaneously and has a resolution of 1024 x 864 pixels. The conversion primarily involved removal of graphic subroutine calls and implementing workstation supported UIS graphic subroutine calls throughout CSAS.

When CSAS was implemented on the MicroVax, many new color features were added to provide flexibility during image analyses. CSAS provides the user access to either the full range of 248 colors available on the workstation, or subsets of that range assigned to various C-scan data files being analyzed. After a color mode is selected, the user may "custom tailor" the color map to the current image. This is accomplished by selecting a specific color or range of colors from the color map and assigning it (them) to a certain data value or range of values in the image. In addition to the original color map of 248 colors, expanded color maps are also available to the user. These maps

are: 1) black/white, 2) red/blue, 3) HLS (hue, lightness, saturation), and 4) HLV (hue, lightness, value). The expanded color maps may also be used to custom tailor the current image.

When a specific color map is selected, the chosen colors can be displayed in the histogram, line plot, and scaled images. This is particularly useful in the histogram, since certain data value ranges in the histogram may be colored to highlight specific features in the image. CSAS now has the capability to plot horizontal or vertical lines of the image.

The Versatec color printer and its corresponding "screen grabber" hardware are used with the MicroVax to make color copies of images and plots on the CSAS workstation screen in up to 248 colors. Black and white (or gray scale) images and plots can also be produced using an LN03 Plus laser printer.

A computer program called CSAS_BATCH was created which has the same functions as CSAS, but will perform the same set of CSAS procedures on multiple C-scan files.

TABLE B-1

SOFTWARE LIBRARY

PROGRAM NAME   PROGRAM DESCRIPTION

BCSIS   BCSIS is a real-time ultrasonic C-scan control and digital
               data acquisition program which uses software gating tech-
               niques to generate digital ultrasonic C-scan image files.
               A maximum of 80 software gates can be simultaneously ap-
               plied to digitized rf A-scans to generate the C-scan files.
               Types of digital data which can be acquired from each gate
               are: minimum amplitude, peak amplitude, peak-to-peak
               amplitude, mean amplitude and time-of-flight values. The
               maximum C-scan image file size which the program can gener-
               ate is 1024 X 1024 pixels. An entry surface tracking
               feature is included.

BTOC   BTOC is a digital C-scan data generation program which ap-
               plies software gating techniques to previously digitized
               and stored rf ultrasonic A-scans. A maximum of 80 software
               gates may be simultaneously applied to the stored A-scans
               which may be up to 1024 points in length. Data from each
               gate are stored in separate C-scan data files. Types of
               digital data which can be acquired from each gate are: min-
               imum amplitude, peak amplitude, mean amplitude, peak-to-
               peak amplitude and time-of-flight values. An entry surface
               tracking feature is included. The maximum C-scan image
               file size which the program can generate is 1024 X 1024
               pixels.

MLAMB   MLAMB is a real-time ultrasonic C-scan control and digital
               data acquisition program which collects and processes leaky
               Lamb wave data and generates C-scan image files. It col-
               lects amplitude data as a function of frequency from video-
               detected and filtered swept-frequency ultrasonic tone
               bursts. A 128 point Fourier-domain representation of the
               data is generated and the spectrum is divided into 5 fre-
               quency bands by digital band-pass filtering techniques.
               Each frequency band corresponds to a different depth in the
               test sample. The median frequency of the spectrum is also
               calculated to encode the depth of defects in different gray
               levels in a single C-scan data file. A total of 6 C-scan
               data files are stored by the program; one from each of the
               five band-pass filter outputs, and one from the median fre-
               quency value.

TABLE B-1 (continued)

SOFTWARE LIBRARY

PROGRAM NAME	PROGRAM DESCRIPTION
CONVOLVE	CONVOLVE is a collection of digital image enhancement subroutines which operate on digitized C-scan image files of any size up to 1024 X 1024 pixels. The subroutines use spatial-domain moving-window convolution operators to enhance the image data files. Window sizes are user selectable in the range 3 X 3 to 63 X 63 pixels. Specific enhancement operations available are: Gaussian first derivative and Marr-Hildreth edge enhancers, median and Gaussian smoothing, fixed and variable gain filtering and constant variance filtering.
CSP	CSP is a collection of digitial image enhancement subroutines which operate on digitized C-scan image files of any size up to 1024 X 1024 pixels. These subroutines use spatial-domain moving-window convolution operators with a fixed window size of 3 X 3 pixels to enhance the image data.
BMUNCH	BMUNCH is a collection of digitial image enhancement subroutines which operate on digitized B-scan image files of any size up to 1024 X 1024 pixels. These subroutines use spatial-domain moving-window convolution operators with a fixed window size of 3 X 3 pixels to enhance the image data files.
AXWIENER	AXWIENER is a one-dimensional Fourier-domain Wiener filter which sequentially deconvolves all rf A-scan lines in a series of digitized rf B-scan files. The deconvolved rf B-scan files are scaled to the global maximum and minimum. Inputs for AXWIENER are a digitized reference rf A-scan and a series of digitized rf B-scans. The output is a series of B-scan files consisting of deconvolved A-scans.
REFSUB	REFSUB enhances rf B-scan images of near-entry-surface defects by subtracting a digitized rf reference entry- surface echo from each A-scan in the B-scan file. The residual A-scans are rescaled and stored in another B-scan file. The user specifies a multiplicative constant to scale the reference entry-surface echo to those of the B-scan file. The program automatically shifts the reference entry surface echo prior to each subtraction to account for variations in entry-surface echo location in each A-scan of the B-scan.

TABLE B-1 (continued)

SOFTWARE LIBRARY

PROGRAM NAME	PROGRAM DESCRIPTION
TRANS_SIM	TRANS_SIM models the acoustic field of broadband, focused ultrasonic transducers. The output is a B-scan image file which can be used to illustrate the effects of center frequency, pulse length, element diameter and focal length on the output beam diameter, focal spot size, depth of field and acoustic pulse shape.
NOLAP	NOLAP generates a composite C-scan image from a series of binary C-scan images of delamination damage at different interfaces within a sample. NOLAP removes regions of overlap by assigning higher priority to C-scan images from the upper planes in the sample. The gray shades in the composite image are proportional to the depths of the delaminations. NOLAP operates on C-scan files of up to 512 X 512 pixels in size.
COLORS	COLORS ia an interactive color map program for modifying displayed colors in a C-scan or B-scan image on the MicroVax/GPX screen. It can be run simultaneously with any of the image display programs. Over 4 million colors are available, but only 248 colors can be displayed at any one time. The program uses RGB, HSV, and HLS color schemes and allows adjustment of any of the variables in these schemes utilizing the cursor and mouse input device.
CONVRT	CONVRT reformats digital C-scan and B-scan data files so that they may be transferred between the RT-11 and MicroVax computer systems utilizing the file transfer utility, KERMIT. Data files can be converted to or from 8-bit direct access and 16-bit sequential formats, or to or from 8-bit ASCII and 8-bit direct access formats. The program allows the user to choose to run either interactively or in batch mode.
SCREEN	SCREEN copies the entire MicroVax/GPX screen display to a disk file for storage. Anything which is displayed on the GPX screen can be copied. One major application of this program is saving the display of an rf A-scan with superimposed gates, surface-tracking marker and reference marker in the manner in which they were set up for specific C-scan data collections with BCSIS. Stored screen files can also be recalled from disk for display at any time by SCREEN.

TABLE B-1 (concluded)

SOFTWARE LIBRARY

PROGRAM NAME   PROGRAM DESCRIPTION

BLABEL   BLABEL is an artificial intelligence (AI) program which
                separates features in a digitized B-scan image and then
                labels, computes statistics and attempts to identify each
                feature based on a set of rules. The features may be
                surface-connected cracks, delaminations or noise. BLABEL
                operates on B-scan files of up to 512 X 512 points in size
                and outputs a B-scan file in which the identified features
                are color coded.

COMPUTER SYSTEM DESCRIPTION

The computing resources within the NDE group have been significantly upgraded during the past three years. In September 1986 the computing system consisted of a Digital Equipment Corporation (DEC) PDP-11/44 and several DEC LSI-11 based computers. The PDP-11/44 was used as a general group resource and also controlled the ultrasonic leaky Lamb wave experimental system. One LSI-11/23 controlled the small ultrasonic scanning system. There have been four DEC workstations and a DEC MicroVAX III added during this contractual period. All five VAXes are connected by DECnet; Figure B-4 shows the network layout.

The DEC MicroVAX III is used as the UDRI NDE group and MLLP branch computer resource. The MicroVAX III computer system consists of a powerful 3000 series central processing unit (CPU) with 16 Mbytes of main memory, two 456 Mbyte RA81 disk drives (one RA81 is used as the system disk drive and the second RA81 is used as the main user disk drive). This system has two additional disk drives, a 71 Mbyte RD53 and a 205 Mbyte RA60. The RA60 is a removable drive used for the Computed Tomography database and as a fast backup device. Two magnetic tape drives are on this system, a 95 Mbyte cartridge tape unit and a 1600/6250 BPI reel-to-reel tape unit. There are 12 asynchronous serial ports; two are connected to printers and the other 10 ports are connected to a variety of video terminals. One of the two printers connected to the serial ports is an LN03 Plus laser printer with graphical output capabilities. The other printer is an LA120 DECwritter III which can accommodate paper sizes up to 11 by 17 inches. A Hayes 1200 baud modem is connected to a serial port for remote access.

Three of the four workstations are DEC VAXstation III/GPXs. Each of these three workstations is connected to and controls an experimental system. The fourth workstation is a DEC VAXstation II/GPX and is used as a software development platform for control, acquisition and display software and also serves as the general purpose analysis workstation.

The three experimental systems that are controlled by the VAXstation III/GPXs are the thermal wave, the ultrasonic leaky Lamb wave and the large ultrasonic scanning system (Cal Data Ultrascan System 644). The thermal wave
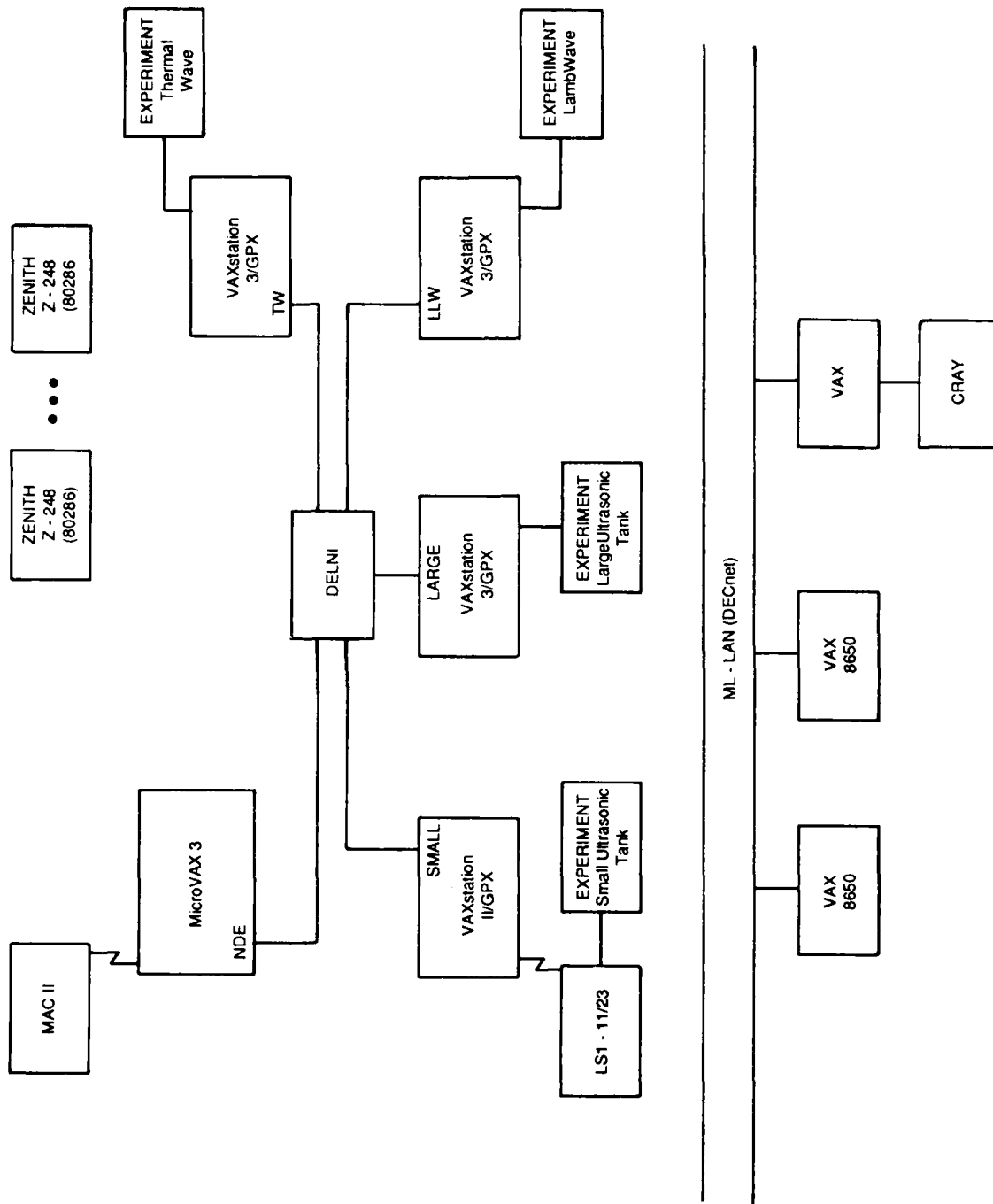
Figure B-4. Schematic diagram of WRDC/MLLP computing system.

and the ultrasonic leaky Lamb wave VAXstations have the same system configuration, that is, a DEC 3000 series CPU with 8 Mbytes of main memory, two 71 Mbyte RD53 disk drives (one used as the system disk drive and the second as the user disk drive), a dual 400 Kbyte RX50 floppy disk drive and a 95 Mbyte cartridge tape unit. Both systems contain a National Instruments IEEE-488 interface that connects the experiment to the computer system. These workstations have a 19 inch color-graphics display unit that serves as the console terminal and main output unit. The resolution of the display unit is 1024 by 864 pixels with 256 simultaneously displayable colors which are user-selectable from a palette of 16.7 million. Each workstation has four asynchronous serial ports used to connect a VT320 video terminal and other general laboratory RS-232 devices. The ultrasonic leaky Lamb wave workstation also has an LN03 Plus laser printer attached.

The workstation that controls the large tank ultrasonic scanning system consists of a DEC 3000 series CPU with 8 Mbytes of main memory, three 71 Mbyte RD53 disk drives (one used as a system disk drive, one used as a software development disk drive and one used entirely as a data disk drive) and a 95 Mbyte cartridge tape unit. This system has a National Instruments IEEE-488 interface that connects the experiment to the computer system. Like the other two VAXstations this system has a 19 inch color display unit and four asynchronous serial ports.

The VAXstation II/GPX consists of a MicroVAX II CPU with 9 Mbytes of main memory and three 318 Mbyte System Industries SI-55 disk drives (one used as the system disk drive, one used as the user disk drive and one used as storage for data being analyzed). This system also has a 95 Mbyte cartridge tape unit and eight asynchronous serial ports. An LN03 Plus laser and a Versatec thermal transfer color plotter are used as output devices. The color plotter can generate plots on standard A, B, A3, and A4 size paper and transparency film. A Versatec frame grabber can also be used to copy the contents of the VAX VR290 color display to the Versatec color plotter.

A DEC LSI-11/23 system is used to control the small ultrasonic scanning system. This system consists of 256 Kbytes of main memory, one 30 Mbyte disk, an RGB color monitor interface and a National Instruments IEEE-488 interface

that controls the experiment. The LSI-11/23 and the VAXstation II/GPX communicate over a 19.2 Kbaud serial link.

The software on the DEC MicroVAX III system consists of the VMS V4.7a operating system, DECnet, a FORTRAN-77 compiler, RS-1, a database package, WordMarc, a word processing package, and DISSPLA, a graphics software package. The software on the thermal wave VAXstation III/GPX system consists of the VMS V4.7a operating system, DECnet, VAX windowing V3.3, a FORTRAN-77 compiler and INTERLEAF, a technical publishing package. The software on the ultrasonic leaky Lamb wave VAXstation III/GPX system consists of the VMS V4.7a operating system, DECnet, VAX windowing V3.3, a FORTRAN-77 compiler and DISSPLA, a graphics software package. The software on the large ultrasonic scanning system VAXstation III/GPX system consists of the VMS V4.7a operating system, DECnet, VAX windowing V3.3 and a FORTRAN-77 compiler. The software on the software development platform VAXstation II/GPX system consists of the VMS V4.7a operating system, DECnet, VAX windowing V3.3, a FORTRAN-77 and an ADA compiler, the VAX MACRO assembly language, a source code management package, CMS, and DISSPLA, a graphics software package. This system's software also includes the International Mathematical and Statistical library (IMSL) and the public domain data communication program, KERMIT.

The UDRI NDE group has an Apple MAC II with a 40 Mbyte disk, a high resolution color monitor, an Apple LaserWriter Printer and an AST scanner. This system is used mainly for desktop publishing. The system has the following software: PageMaker, Microsoft Word, PowerPoint and Excel. The MAC II also has a terminal emulation package, VersaTerm, and general purpose drawing package, Super Paint.